Jonas Deuermeier

Diplom-Ingenieur der Materialwissenschaft
(equiv. Master of Science in Materials Science)
born in Kassel, Germany

Origins of limited electrical performance of polycrystalline Cu_2O thin-film transistors

Thesis approved by the Department of Materials Science of Universidade NOVA de Lisboa in fulfillment of the requirements for the degree of Doctor in Nanotechnologies and Nanosciences and by the Department of Materials and Earth Sciences of the Technische Universität Darmstadt in fulfillment of the requirements for the degree of Doctor in Engineering (Dr.-Ing.).

Date of submission: 23rd September 2016
Date of exam: 9th December 2016

Supervisors: Dr. Elvira Fortunato, Professor, Faculdade de Ciências e Tecnologia, Universidade NOVA de Lisboa
Dr. Andreas Klein, Associated Professor, Technische Universität Darmstadt

Examination Committee

Chairperson:	Prof. Dr. Rodrigo Martins
Rapporteurs:	Prof. Dr. Lambert Alff
	Prof. Dr. Florinda Mendes da Costa
Members:	Prof. Dr. Andreas Klein
	Prof. Dr. Wolfgang Donner
	Prof. Dr. Luís Rebouta

D 17 – Darmstadt, 2017

Origins of limited electrical performance of polycrystalline Cu_2O thin-film transistors

Dissertation of Jonas Deuermeier from Kassel

Doctoral research in joint supervision conferring a dual-degree

The Doctor in Nanotechnologies and Nanosciences is conferred by the Department of Materials Science, Faculty of Science and Technology, Universidade NOVA de Lisboa, Portugal

The Doctor in Engineering (Dr.-Ing.) is conferred by the Department of Materials and Earth Sciences, Technische Universität Darmstadt, Germany

Primary Referee: Prof. Dr. Andreas Klein
Secondary Referee: Prof. Dr. Lambert Alff

Für Yassna

ABSTRACT

In this thesis, cuprous oxide Cu_2O was investigated concerning its ability to function as p-type channel in thin-film transistors. The material was chosen for its promising electronic characteristics as bulk single crystal. In order to be competitive with other technological solutions for flexible thin-film electronics, the temperature during fabrication has to remain below 200 °C. Following this approach, a tremendous gap between potential and actual electrical performance of Cu_2O thin-film transistors is encountered. The aim of this thesis is to show the reasons for this discrepancy.

Relevant stages during the fabrication process of a thin-film transistor were analyzed with respect to their impact on the cation oxidation state. These stages included thin film deposition, the study of interface formation to the dielectric layers as well as post-deposition annealing. Semiconducting and dielectric layers were deposited by reactive magnetron sputtering (Cu_2O, Cu_4O_3, CuO, Bi_2O_3, Al_2O_3) and atomic layer deposition (Al_2O_3). An innovative approach for a thickness-dependent characterization of thin films was conducted by a combination of in situ X-ray photoelectron spectroscopy with in situ conductance measurement. Electrical properties of Cu_2O films and thin-film transistors were analyzed in dependence of film thickness, temperature, oxygen partial pressure and time.

It is shown, that the primary cause for the limited electrical performance is the poly-crystalline morphology in conjunction with the material-inherent tendency to oxidation and reduction of the metal cation. On the one hand, metallic Cu(0) depletes the material from hole carriers and causes Fermi level pinning. On the other hand, a high conductivity in the grain boundary is caused by the presence of Cu(II). A model is presented to describe the conductivity at different film thicknesses as a function of grain size.

Resumo

Nesta tese foi investigado o óxido de cobre Cu_2O e a sua habilidade para funcionar como semicondutor do tipo p em transistores de filme fino. Este material foi escolhido devido às promissoras características electrónicas no estado monocristalino. De modo a poder vir a ser uma alternativa competitiva face a outras tecnologias utilizadas na electrónica flexível, a temperatura de fabrico deverá ser inferior a 200 °C. No entanto esta abordagem levou a um fosso enorme entre o desempenho elétrico potencial e o desempenho real manifestado nos dispositivos. O objectivo desta tese é explicar as causas desta discrepância.

Foram analizadas as etapas relevantes no processo de fabrico dos transístores de filme fino tendo em conta o seu impacto no estado de oxidação do catião metálico. Estas etapas incluem a deposição de filmes finos, o estudo da formação das interfaces com as camadas dielétricas assim como os tratamentos de recozimento efectuados após a deposição. As camadas semicondutoras e dielétricas foram depositadas recorrendo à técnica de pulverização catódica assistida por magnetrão (Cu_2O, Cu_4O_3, CuO, Bi_2O_3, Al_2O_3) e *atomic layer deposition* (Al_2O_3). Foi desenvolovida uma nova abordagem na caracterização de filmes finos dependente da espessura dos mesmos, combinando medidas *in-situ* de espectroscopia de raios-X com medidas de condutancia *in-situ*. As propriedades eléctricas dos filmes de Cu_2O e dos transístores foram analizadas em função da espessura dos filmes, temperatura, pressão parcial de oxigénio e tempo.

Conclui-se que a principal razão para o fraco desempenho elétrico observado é a morfologia policristalina do óxido de cobre combinada com a tendência inerente para oxidar e reduzir o catião. Por um lado o cobre metálico Cu(0) deplete o filme de buracos e fixa o nível de Fermi. Por outro lado, nas fronteiras de grão é formado um estado de elevada condutividade devido à presença de Cu(II). É apresentado um modelo que descreve e correlaciona a condutividade com a espessura dos filmes e o tamanho de grão.

Überblick

Diese Dissertation befasst sich mit dem Kupferoxid Cu_2O bezüglich seiner Anwendbarkeit als p-leitender Kanal in Dünnschichttransisitoren. Die Auswahl des Materials liegt begründet in den vielversprechenden elektrischen Eigenschaften als Einkristall. Um konkurrenzfähig zu sein mit anderen Technologien zur Implementierung von elektronischen Schaltungen auf flexiblen Substraten, muss die Temperatur während der Herstellung unter 200 °C bleiben. Die elektrischen Eigenschaften dünner Schichten, die auf diese Weise abgeschieden werden, weichen stark von denen eines Cu_2O-Einkristalls ab und verhindern das Auftreten des erwarteten Schaltverhaltens, basierend auf den Eigenschaften des Einkristalls. Das Ziel dieser Arbeit ist, die Gründe für diese Diskrepanz aufzuzeigen.

Verschiedene Schritte des Herstellungsprozesses eines Cu_2O-Dünnschichttransistors wurden analysiert, insbesondere in Bezug auf den Oxidationszustand des Kations. Diese Schritte umfassten die Dünnschichtabscheidung, die Analyse von Grenzflächen zum Isolatormaterial sowie Temperaturbehandungen nach der Abscheidung. Halbleitende und isolierende Schichten wurden mittels reaktiver Magnetron-Kathodenzerstäubung (Cu_2O, Cu_4O_3, CuO, Bi_2O_3, Al_2O_3) und Atomlagenabscheidung (Al_2O_3) hergestellt. Eine in-situ Analyse der Materialeigenschaften in Abhängigkeit der Schichtdicke mittels Röntgenphotoelektronenspektroskopie wurde gepaart mit der in-situ Messung des elektrischen Leitwertes. Weiterhin wurden die Eigenschaften von Cu_2O-Dünnschichten und Dünnschichttransistoren in Abhängigkeit der Schichtdicke untersucht, der Temperatur, des Sauerstoffpartialdrucks sowie der Verweilzeit unter bestimmten Bedingungen.

In dieser Dissertation wird aufgezeigt, dass die Limitierungen im Schaltverhalten der Transistoren ihren Ursprung hat in der Polykristallinität des Materials, kombiniert mit einer inhärenten Tendenz zu Oxidation und Reduktion der Kationen. Zum einen führt ein Auftreten von metallischem Cu(0) zu einer Verarmung der Ladungsträger durch die Fixierung der Fermienergie an der Cu/Cu_2O Schottky-Barriere. Zum anderen sind die Korngrenzen stärker elektrisch leitfähig als als das Innere der Cu_2O-Körner, was durch das Auftreten von Cu(II) in den Korngrenzen verursacht wird. Ein mathemtisches Model zur Beschreibung der schichtdickenabhängigen Leitfähigkeit unter Berücksichtigung der Korngröße wird beschrieben.

Contents

CHAPTER 1

INTRODUCTION

1.1 Motivation

1.1.1 Why p-type oxide thin-film transistors?

This work is thematically situated in the field of oxide-based electronic circuits. As one of the fundamental building blocks of an electronic circuit, thin-film transistors (TFT) are investigated. The technology based on the semiconductor silicon is mature and provides high performance. However, a few characteristics limit this technology. For certain applications a potential alternative to silicon are organic semiconducting layers. Table 1.1 shows which properties distinguish TFTs based on amorphous oxide semiconductors (AOS) from devices using silicon and organics.[1, 2]

Table 1.1: Comparison of properties of TFTs using different semiconductors. The following abbreviations are used: poly-Si – polycrystalline silicon, a-Si:H – hydrogenated amorphous silicon, AOS – amorphous oxide semiconductors.

property	poly-Si	a-Si:H	organics	AOS
optical transparency	↓	↓	(↑)	↑
production temperature (°C)	450	300	< 200	200
large scale uniformity	↓	↑	↓	↑
field-effect mobility ($cm^2V^{-1}s^{-1}$)	> 100	1–2	≈ 1	10–100
conduction type	ambipolar	ambipolar	ambipolar	n-type

A fundamental difference between silicon and oxide semiconductors is the optical transparency in the visible range of many oxides. When all parts of a circuit are made of oxides, including the transparent conductive oxides (TCO) and the insulating oxides, *invisible electronics* are possible. Transparency of organic semiconducting layers is possible but generally causes a degradation of the electrical properties.[3] The comparatively

low maximum temperature during production of both organics and oxides allows the usage of flexible organic substrates. This opens up a broad field of new applications of electronic circuits, for example on plastic foils or wearables. For an application in flat-panel displays, uniformity on a large area is required. Amorphous inorganic films (silicon and oxides) have an advantage over polycrystalline silicon and organics in this respect. However, the charge carrier mobility and thus the field-effect mobility of silicon devices is decreased in the amorphous state. Here, AOS show mobilities which are high despite the structural disorder in the amorphous state. Organics cannot compete with oxides in terms of carrier mobility. A major drawback of oxide semiconductors with respect to the other classes of materials of Table 1.1 is, that the listed properties only apply for n-type materials.

The above mentioned advantages of n-type oxide electronics are exploited by commercially available products. At the time of writing, several high-resolution displays employ pixel driver circuits based on amorphous indium-gallium-zinc oxide (IGZO), e.g. a 77 inch active matrix organic light-emitting diode (AMOLED) display by LG or an 80 inch liquid crystal display (LCD) by Sharp and even a 55 inch transparent AMOLED display by Planar.[4–6]. These examples show that the AOS-based driver backplane technology does not require a p-type oxide in order to be commercially successful.

The integration of more complex circuits into a display may be referred to as *system-on-panel* and typically requires complementary circuits, since they are considerably more power efficient than non-complementary designs. In order to realize transparent complementary oxide circuits, a p-type AOS is required. Although the first report of a p-type TCO marked the starting point of the transparent electronics development,[7, 8] the realization of products based on this technology is primarily held back by the lack of a p-type oxide semiconductor with good TFT performance. Compared to most n-type AOS, the p-type oxide semiconducting thin films known today generally have a lower band gap and exhibit a lower charge carrier mobility. In addition, the most common p-type oxides in TFTs (Cu_2O and SnO) are not amorphous.[1] Hence, many of the advantages which n-type oxide semiconductors have over silicon and organics (optical transparency, high field-effect mobility and film uniformity on large areas) do not apply for p-type oxides.

1.1.2 Challenges with Cu_2O in thin-film transistors

This thesis is focused on the p-type oxide semiconductor Cu_2O. A Hall mobility of up to $100\,cm^2V^{-1}s^{-1}$ is reported for single crystals and $90\,cm^2V^{-1}s^{-1}$ for epitaxial thin films.[9, 10] The corresponding carrier concentrations are 10^9–$10^{12}\,cm^{-3}$ (single crystal) and $10^{14}\,cm^{-3}$ (epitaxial film). These electrical properties are favorable to obtain a TFT operation with low drain current in the OFF state and a high field-effect mobility. The intrinsic electrical properties of the material are the main stimulation for research in the field of TFTs.

Apart from a band gap, which is too low for transparency in the entire visible range

and the crystalline structure, the main factor which limits TFT properties is the pronounced discrepancy between bulk electrical properties and device characteristics. The field-effect mobilities reported in literature are often in the range of $10^{-3}\,cm^2V^{-1}s^{-1}$ and in a few cases above $1\,cm^2V^{-1}s^{-1}$ (see Section 2.6.2). The reported ON/OFF drain current ratios are usually not higher than 10^4. For comparison, n-type AOS-TFTs typically show ON/OFF ratios above 10^7.[11] Both the low field-effect mobility and the low drain current modulation can be explained by a high concentration of defects, which increase the concentration of hole charge carriers and decrease the hole mobility.

At room temperature and in ambient air, Cu_2O is thermodynamically unstable, but the eutectoid decomposition into Cu and CuO below 375 °C is kinetically hindered.[12] A structural stabilization has been reported by (110) stacking faults in minerals of Cu_2O, which are understood as a missing plane of copper ions and give rise to a formal increase in copper valence of the adjacent cations.[13] Grain boundaries in general have been shown to present regions of increased conductivity with respect to monocrystalline material[14] and act as a sink for intrinsic defects.[15] Apart from segregation of intrinsic defects, inhomogeneity may also exist in the form of oxidation states different from the parent material. In Cu_2O, precipitate phases containing either Cu(0) or Cu(II) might be present.[12] Cu(0) is metallic and forms a Schottky barrier to Cu_2O.[16, 17] Cu(II) occurs in another stable p-type oxide, CuO, which generally exhibits a higher charge carrier concentration and a lower Hall mobility than Cu_2O.[9, 18, 19]

Already one year after the first report on epitaxial Cu_2O as active channel in a TFT,[10] the interpretation of bulk properties has led to the conclusion that the low ON/OFF drain current ratio and field-effect mobility can be either due to a secondary phase of CuO or due to the ionization of intrinsic donors (oxygen vacancy).[20] In the case of high-quality epitaxial films, either of both defects are localized at interfaces and/or surfaces. Apart from a well known surface oxidation of Cu(I) in Cu_2O to Cu(II),[21] a porosity of Cu_2O at the interface between the semiconductor and the dielectric substrate has been discussed to cause the deteriorated transport properties.[22, 23]

1.2 Objectives and structure of this thesis

The objectives of this thesis are firstly to investigate the possible presence of Cu(II) and Cu(0) oxidation states in polycrystalline Cu_2O thin films. The influences of the deposition conditions, post-deposition annealing as well as the formation of interfaces to other materials are analyzed. Secondly, the effects of Cu(II) and Cu(0) on the electrical properties of thin films are discussed and evaluated for an application of Cu_2O in p-type TFTs.

An overview on fundamentals, material and device properties as well as methodology related to Cu_2O TFTs is given in Chapters 2 and 3. The presentation and discussion of results obtained during the preparation of this thesis begins with Chapter 4 with an explanation of the efforts undertaken to deposit stoichiometric Cu_2O by reactive radio-frequency sputtering as a starting point for further investigations. Emphasize is put on

the influence of the oxygen partial pressure during deposition and on differences between thin films produced at the two institutes at Universidade NOVA de Lisboa and Technische Universität Darmstadt, which have been involved in this work.

With the growth of Cu_2O on a variety of substrates, the inhomogeneous electrical properties of the material are analyzed in Chapter 5. Evidences are provided, which show a contribution of Cu(II) to the grain boundaries of polycrystalline Cu_2O, causing highly conductive grain boundaries in the material. The analysis is based on a combined in situ study by X-ray photoelectron spectroscopy and conductance measurements at various film thicknesses. Data on conductivity, carrier concentration and carrier mobility is discussed by using model descriptions for the inhomogeneous electrical properties. In Chapter 6, the energy band alignments of selected material combinations of the preceding chapter are presented. A novel usage of the Auger parameter for determination of the valence band offset between the substrate and an ultra-thin layer is discussed.

The limits of chemical stability during further processing of Cu_2O films are explored in Chapter 7. The reduction and oxidation at the Cu_2O surface due to the deposition of Al_2O_3 by two different techniques (atomic layer deposition and sputter deposition) is described. The main focus is put on the occurrence of metallic copper at the interface and its influence on electronic properties of the Cu_2O film. This is followed by results on the influence of oxygen partial pressure and time on Cu_2O during post-deposition heat treatments. The relaxation of electrical properties was monitored by Hall effect measurements. The analysis was complemented by X-ray diffraction measurements. In Chapter 8, the properties of Cu_2O TFTs after post-deposition annealing in air are discussed, comprising a study of gate voltage stress in depletion at different temperatures.

Part I

Fundamentals and methodology

Chapter 2

Fundamentals

The fundamental concepts, which are presented in this chapter have been taken from the following main references, grouped roughly by topics: General solid state physics,[24] semiconductor physics and interfaces,[25] semiconductor device physics,[26] electrical characteristics of thin-film transistors,[27] intrinsic defect equilibrium in solids,[28] thin-film growth.[29]

The terminologies *concentration* and *density* are used interchangeably to refer to the amount of defects in the material in units of cm^{-3}. The same holds for Fermi energy and Fermi level in units of eV. Due to the relevancy to Cu_2O, the mechanisms are discussed mainly for p-type materials. Equivalent equations however exist for n-type semiconductors.

2.1 Device functionality of a transistor

The electronic function of a transistor is the one of a variable resistance between two terminals, which is controlled by a voltage applied to a third terminal. Since the current through the third terminal is ideally low compared to the other terminals, power amplification can be achieved when this device is placed in a proper circuit. In digital signal processing, a transistor serves as a volatile switch from a high resistance *OFF* state to a low resistance *ON* state. The switching allows for logic operations of binary code in a computer processor or controlling the pixels of a flat panel display, for instance. While a processor typically uses integrated circuits of silicon-based metal-oxide-semiconductor field-effect transistors (MOSFET), the pixels of a display are usually controlled by thin-film transistors (TFT).[2] Both device types use the semiconductor as a variable resistance. The resistance is controlled by an electric field, which is applied to the semiconductor through an insulating layer.

Figures of merit of transistors are primarily related to the speed of switching between OFF and ON state (field-effect mobility μ_{FE}, subthreshold swing S), the operating voltages (threshold voltage V_{th}, turn-on voltage V_{on}) and the involved currents (ON/OFF current ratio, leakage current). Before discussing how these values are influenced by material and device characteristics, a brief introduction to semiconductors is given, followed by a presentation of intrinsic and extrinsic defects, which lead to non-ideal device behavior.

2.2 A very brief introduction to electrons in semiconductors

Tightly bound electrons are localized close to the atomic nucleus. Their binding energy is high and they are referred to as core level electrons. Due to the strong localization close to the core, the broadening of the binding energy is defined by the Heisenberg uncertainty principle.[30] Less tightly bound electrons may also be present close to the boundaries of an atom. They are referred to as valence electrons. Due to the weak spatial localization, the corresponding energy level is sharp. When a solid is formed, individual atoms are approximated until an equilibrium between attraction and repulsion is reached. Valence electrons interact with each other. The occupancy of energy levels by an electron is limited by the Pauli principle.[31] This means that a spatial vicinity of energetically similar orbitals leads to a dispersion in energy. This dispersion is the origin of the formation of what is referred to as an energy band.

Under some circumstances, valence electrons enable charge transport and electrical current, which is why they are further discussed in the following. The solution of the Schrödinger equation for a quasi-free electron in the periodic potential of a crystal leads to degeneracy at the Brillouin zone boundaries.[1] This degeneracy is forbidden by the Pauli principle. An adequate correction to the calculation results in energies, for which no eigenvalues exist. This energy range is thus referred to as the *forbidden* energy band gap E_{g}. In a perfect crystal, the change in density of states at the band edges is described by a step function.

The energetically highest occupied band is referred to as the valence band, whereas the lowest (completely) unoccupied band is called the conduction band. If a band is partially occupied, it can allow a transport of charges, which is the case for a metal. The band gap is defined as the energy difference between the valence band maximum E_{VB} and the conduction band minimum E_{CB}. Insulators and semiconductors are characterized by a fully occupied valence band and a fully unoccupied conduction band at a temperature $T = 0\,\mathrm{K}$. In general, a material is called a semiconductor when the band gap is greater than 0 eV but does not exceed 3 eV.

The Fermi energy E_{F} is defined as the energy E at which the probability for occupation with electrons is equal to $1/2$. So in the ideal case (meaning no states inside the forbidden band gap and equal density of states at E_{VB} and E_{CB}) it lies in the middle of the band gap.

[1] The wave function used for the solution is referred to as Bloch states and describes an electron wave function, which is modulated by the periodic potential of the lattice.

The Fermi-Dirac distribution is defined by Equation 2.1, in which k is the Boltzmann constant.[32, 33]

$$f(E) = \frac{1}{1 + \exp(\frac{E - E_F}{kT})} \tag{2.1}$$

At 0 K, $f(E)$ is a step function. At $T > 0$ K, it becomes smoother with higher temperature. The energy interval around E_F, which is effected by the smoothening is $\approx 6kT$. A fundamental property of a semiconductor is the possibility to change its conductivity from insulating to conducting. This is governed mainly by the distance of the Fermi energy from one of the band edges E_{VB} and E_{CB}, which modulates the free charge carrier concentrations p of holes and n of free electrons, according to Equations 2.2 and 2.3.[2]

$$p = \int_{-\infty}^{E_{VB}} N(E)(1 - f(E))\mathrm{d}E \tag{2.2}$$

$$n = \int_{E_{CB}}^{\infty} N(E) f(E)\mathrm{d}E \tag{2.3}$$

Here, $N(E)$ is the density of states. If E_F is more than $3kT$ from the band edges,[3] Equations 2.2 and 2.3 can be simplified by the Boltzmann statistics, resulting in Equations 2.4 and 2.5. Moreover, $N(E)$ is approximated by the density of states at the valence band maximum VBM and the conduction band minimum CBM, respectively.

$$p = 2\left(\frac{2\pi m_h^* kT}{h^2}\right)^{3/2} \cdot \exp\left(\frac{-(E_F - E_{VB})}{kT}\right) \tag{2.4}$$

$$n = 2\left(\frac{2\pi m_e^* kT}{h^2}\right)^{3/2} \cdot \exp\left(\frac{-(E_{CB} - E_F)}{kT}\right) \tag{2.5}$$

Here, h is the Planck constant, m_e^* is the effective mass of an electron and m_h^* the effective mass of a hole. It should be noted, that the effective mass of charge carriers plays an important role for carrier transport, since it is inversely proportional to the charge carrier mobility of the material μ. It is essentially determined by the degree of spatial localization of valence electrons in the solid. In thermodynamic equilibrium, charge neutrality is obeyed, which means $n = p$. If $m_e^* \approx m_h^*$, the Fermi energy is found in the middle of the band gap.

2.2.1 General definitions of energy parameters

In order to discuss the energetic properties of valence electrons, which are relevant for charge carrier statistics, some useful variables have been defined. They are summarized in Figure 2.1 and the equations therein.

[2] A hole may be seen as equivalent to an unoccupied electronic state.
[3] This is referred to as a nondegenerate semiconductor.

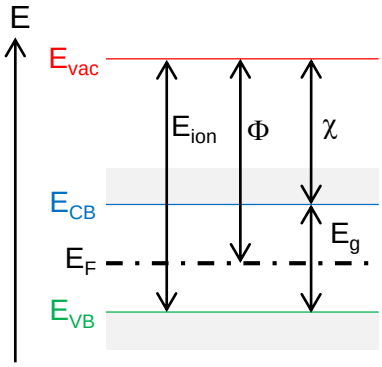

$$\text{electron affinity} \qquad \chi = E_{\text{vac}} - E_{\text{CB}} \tag{2.6}$$

$$\text{ionization potential} \qquad E_{\text{ion}} = E_{\text{vac}} - E_{\text{VB}} \tag{2.7}$$

$$\text{work function} \qquad \Phi = E_{\text{vac}} - E_{\text{F}} \tag{2.8}$$

$$\text{band gap} \qquad E_{\text{g}} = E_{\text{CB}} - E_{\text{VB}} \tag{2.9}$$

Figure 2.1: Important definitions of energies of valence electrons. E_{vac} is the energy of the vacuum level.

2.3 Field-effect devices

2.3.1 Metal-insulator-semiconductor capacitor

The carrier concentration of a semiconductor may be significantly altered by external stimuli which induce excess charge carriers. Such stimuli can be light with an energy higher than E_{g} (like in a solar cell) or the application of an external electrostatic potential φ, like in a transistor. The latter is referred to as the *field-effect*. The simplest field-effect device is the metal-insulator-semiconductor capacitor (MIS). It consists of the following sequence of layers, shown in Figure 2.2 (a): a bottom electrode, a dielectric (insulating) layer, a semiconductor and an ohmic top contact. In this example there shall be no difference between the work functions of the metal electrode and the semiconductor. The voltage at the bottom contact can be set to any given value V, whereas the top contact is grounded.

A spatially inhomogeneous charge distribution $\rho(z)$ along a coordinate z is described by the Poisson equation, given in its 1-dimensional form in Equation 2.10.

$$\frac{\rho(z)}{\epsilon_{\text{r}}\epsilon_0} = \frac{\mathrm{d}\mathcal{E}(z)}{\mathrm{d}z} = -\frac{\mathrm{d}^2\varphi(z)}{\mathrm{d}z^2} \tag{2.10}$$

Here, $\mathcal{E}$ is the electric field, φ the electrostatic potential, ϵ_{r} the relative permittivity and ϵ_0 the permittivity of vacuum.

The ratio between the potential drops in the dielectric and in the semiconductor is primarily governed by the corresponding dielectric constants and film thicknesses. The Fermi energy in the dielectric is sufficiently far from the band edges, so that free charge carriers can be neglected and the potential changes linearly over the dielectric thickness. The linear potential is represented by the slope of the band edges of the dielectric in Figure 2.2 (b).

The potential which reaches the semiconductor at $z = 0$ is $\varphi(0)$. Along $z > 0$ over the thickness of the semiconducting film d, the value of the potential decreases from $\varphi(0)$ to $\varphi(d) = 0$ at the top contact. If the semiconductor was free of charges, the potential

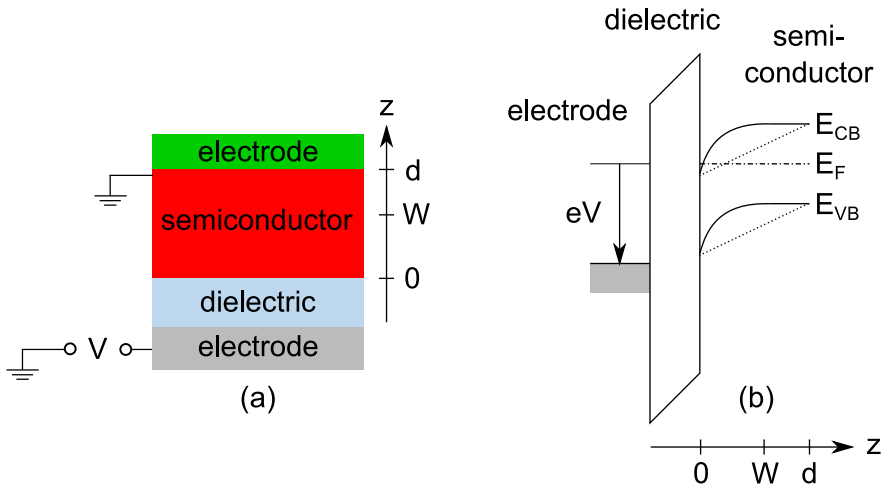

Figure 2.2: Schematic representation of a MIS. The semiconductor film thickness is d and the width of the space charge region is W. (a) Cross-sectional view of the layer sequence. (b) Energy band diagram under application of a voltage V, represented by the potential eV, where e is the elementary charge. The potential drop in a semiconductor without charges would be described by the broken line.

would simply change linearly, as illustrated by the dotted line in Figure 2.2 (b). However compared to the dielectric, the Fermi energy in a semiconductor lies closer to the band edges due to the smaller band gap.[4] The smaller difference between the Fermi energy and the band edges means (by Equations 2.4 and 2.5), that with a sufficiently high external voltage V, a significant increase in the free charge carrier concentration of the semiconductor can be induced. The result is an inhomogeneous charge distribution $\rho(z)$, which affects the variation of the potential along z according to Equation 2.10.

The relation between the inhomogeneous charge carrier concentration and the potential can be rationalized by the concept of screening. In the case of a metal, the high carrier concentration is able to screen the electric field and prevent it from penetrating from the interface into the bulk of the metal. Screening happens also in the semiconductor, when a considerable amount of charge carriers is induced by the field-effect. As the carrier concentration decreases towards the bulk semiconductor and the top contact at ground potential, the screening ability is reduced. So the slope of $\varphi(z)$ continuously decreases with increasing z until it asymptotically approaches charge neutrality ($\varphi(W) = 0$) at $z = W$, which defines the width of the space charge region W. With $W < d$, the ground potential applied to the top contact extends into the semiconductor. The higher the free charge carrier concentration, the more effective is the screening of the potential and the smaller is W.

It will be shown later in this chapter, that charges in a semiconductor are not exclusively free inside the valence band and conduction band. Dopants and defects can cause charges at the nuclei, which in turn affect the free charge carrier concentration due to

[4] A dopant-free semiconductor is considered here.

charge neutrality and thus the width of the space charge region.

2.3.2 Thin-film transistor

The most widely applied device which benefits from the field-effect is the thin-film transistor (TFT), first described by Lilienfeld in 1925/1926.[34] Figure 2.3 shows the architecture of a typical bottom-gate top-contact thin-film transistor (TFT). The structure

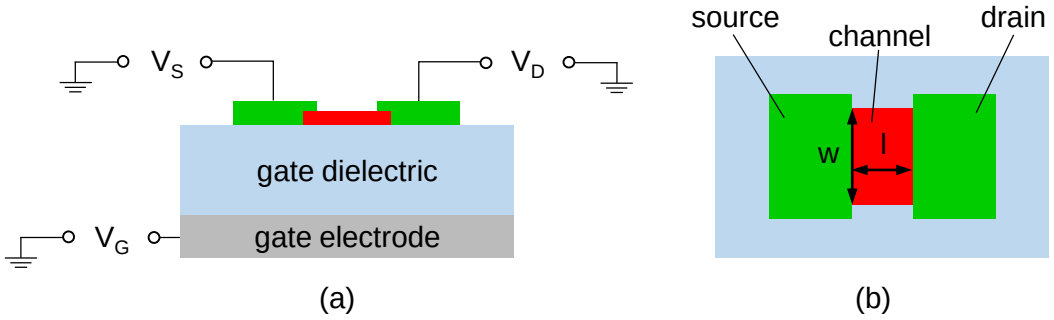

Figure 2.3: Schematic representation of a TFT: (a) Cross-sectional view, showing the voltage application to gate, drain and source (b) drain and source layout in top-view, showing channel width w and l.

is very similar to an MIS with the difference, that two top contacts are used. Between these contacts a current can flow through the semiconducting film in planar geometry. The top contacts are referred to as source and drain, whereas the bottom contact is the gate. The channel has a length l and a width w. V_G is the gate voltage, V_S the source voltage and V_D the drain voltage. V_S is usually at ground potential, V_G induces the field-effect and V_D is set to obtain the desired device operation, which is explained further below. The accumulation of charges, as it has been described for the MIS, leads to an increase in current from source (I_S) to drain (I_D). If the semiconductor is little conductive at $V_G = 0\,V$, which means it has a relatively low intrinsic charge carrier density, the device works in *enhancement mode*. If the semiconductor is conductive at $V_G = 0\,V$ and has to be depleted by V_G in order to become insulating, the device works in *depletion mode*. The following description of TFT characteristics is valid for a semiconductor film thickness, which exceeds the width of the space charge region.

Typical characteristics of a TFT are graphically illustrated in Figure 2.4, together with the band alignment across the gate dielectric for the different working conditions. Figure 2.4 (a) shows *transfer characteristics*, which refers to a change in gate voltage V_G at constant drain voltage V_D while measuring the drain current I_D. In the linear representation of I_D, the onset of conduction at a specific value of V_G is observed, which corresponds to the turn-on voltage V_{on}. Since $V_{on} > 0\,V$, an enhancement mode TFT is displayed here.

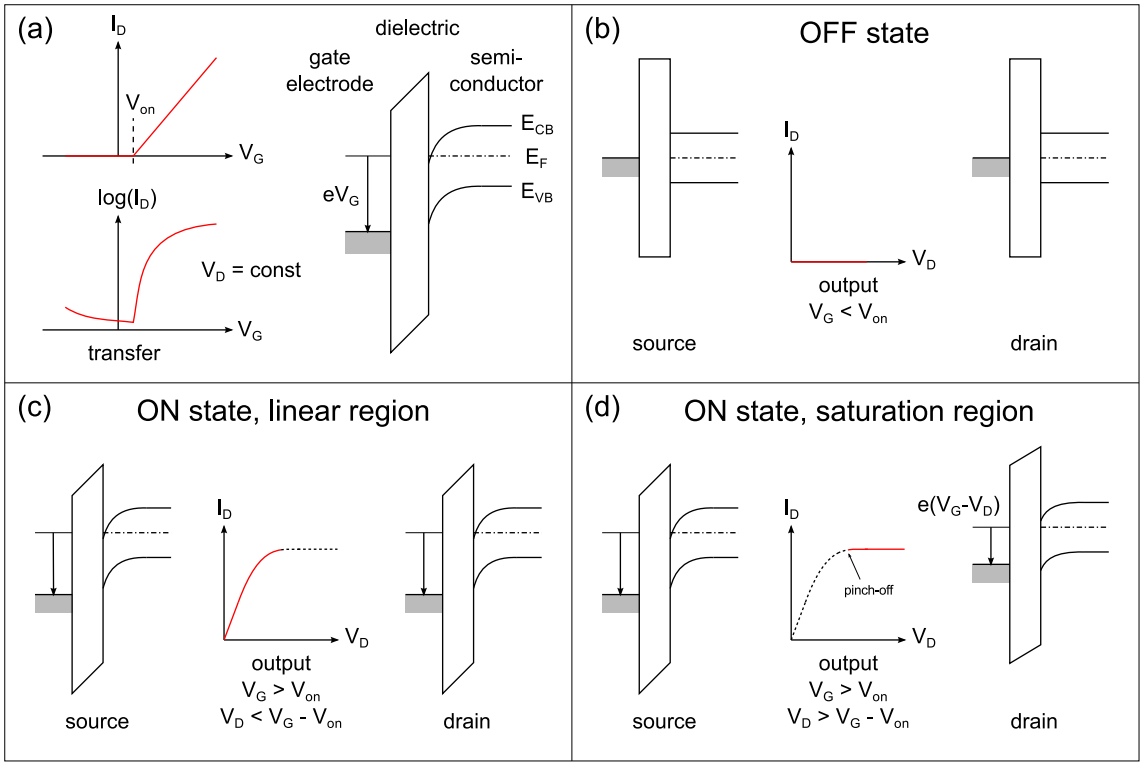

Figure 2.4: The working principle of a TFT in terms of the correlation of current-voltage characteristics and Fermi energy in the band gap. (a) Transfer characteristics and energy band diagram, (b) OFF state, (c) linear regime of ON state, (d) saturation regime of ON state.

The turn-on voltage is often referred to as threshold voltage V_{th}.[5] For $V_{\mathrm{G}} < V_{\mathrm{on}}$, the transistor is in the OFF state and for $V_{\mathrm{G}} > V_{\mathrm{on}}$ it is ON. Due to non-ideal effects, which are covered in Section 2.4, the transition between OFF and ON state is not perfectly sharp, which appears as a drain current $I_{\mathrm{D}} > 0\,\mathrm{V}$ at $V_{\mathrm{G}} < V_{\mathrm{on}}$. Referred to as subthreshold region, the slope of the logarithmic representation of I_{D} can be evaluated for this range of V_{G} to obtain the subthreshold swing S.

In the band picture of Figure 2.4 (a), the change in I_{D} with V_{G} can be rationalized as follows: When increasing V_{G} over the turn-on voltage, an accumulation of charge carriers at the interface to the dielectric takes place, which is schematically represented by the entry of the Fermi energy into the conduction band. This mechanism is equivalent to the field-effect in a MIS structure.

In general, the drain current of a transistor is used in a circuit for further processing while it is controlled by the gate voltage. Therefore, the *output characteristics* I_{D} *vs.* V_{D} need to be discussed in reference to Figure 2.4 (b)–(d). At first, the OFF state is shown in which ideally no drain current flows at any V_{D} while $V_{\mathrm{G}} < V_{\mathrm{on}}$. Assuming no difference in work function between the metallic gate electrode and the semiconductor, the bands

[5] See further comments on the threshold voltage terminology and its applicability to oxide TFTs in Section 2.4.3.

of the semiconductor are not subjected to any band bending at $V_G = 0\,V$, neither at the source nor at the drain.

Figure 2.4 (c) schematically shows what happens in the device at $V_G > V_{on}$ and for small drain voltages $V_D < V_G - V_{on}$. An accumulation of charge carriers at the interface to the dielectric takes place, which is uniform with respect to source and drain. At higher drain voltages above $V_G - V_{on}$, the drain voltage begins to influence the drain current significantly by counteracting the field-effect, since both voltages are positive (see Figure 2.4 (d)). Consequently at the drain electrode, the semiconductor is not accumulated anymore, which results in the effect referred to as *pinch-off* in the output characteristic and a saturation of drain current. The saturation regime begins once V_D surpasses $V_G - V_{on}$.

In order to describe the drain current as a function of the drain and gate voltage, equations for the ideal TFT have been developed by Borkan an Weimer.[27, 35] Equation 2.11 shows an expression for the drain current, which is valid in the linear region (i.e. for any $V_D < V_G - V_{on}$). C_{di} is the capacitance of the insulator and μ_{lin} is the linear field-effect mobility.

$$I_{D,lin} = \frac{C_{di}\, w\, \mu_{lin}}{l} \left[(V_G - V_{on})\, V_D - \frac{V_D^2}{2} \right] \tag{2.11}$$

To describe the mobility conveniently, the transconductance g is introduced by

$$g = \frac{\partial I_D}{\partial V_G}. \tag{2.12}$$

This leads to a simplified expression at constant V_D. It allows for a direct measure of the linear field-effect mobility from the slope of a transfer curve in the linear region g_{lin}.

$$\mu_{lin} = \frac{l\, g_{lin}}{w\, C_{di}\, V_D} \tag{2.13}$$

Equation 2.11 predicts a decrease in drain current for $V_D > V_G - V_{on}$. However, this does bot correspond to the measured characteristics. The drain current remains essentially constant with the value at pinch-off $V_D = V_G - V_{on}$. V_D can be substituted in Equation 2.11, resulting in Equation 2.14, which defines the field-effect mobility in saturation μ_{sat}.

$$I_{D,sat} = \frac{C_{di}\, w\, \mu_{sat}}{l} \frac{(V_G - V_{on})^2}{2} \tag{2.14}$$

Due to this dependency of $I_D(V_G)$ in the saturation regime, the formalism is sometimes referred to as the *square-law*.

2.4 Electronically active defects in semiconductors

Instead of having the Fermi energy at mid-gap $E_g/2$ and $n = p$, many semiconductors applied in devices have majority and minority charge carriers. If electrons are the majority

they are called n-type semiconductors, whereas p-type semiconductors when holes are predominant. This is generally caused by localized impurities or defects, which have charge transition states inside the band gap. During the switching of the TFT, part of the induced potential is consumed for the charging/discharging of the impurities of defects. In turn, part of the charge calculated by $\int_0^d \rho(z)\mathrm{d}z$ is not *free* (either contributing to n or p) but is bound at atomic nuclei. The impact of impurities or defects on TFT characteristics is discussed in this section.

2.4.1 Dopants

In general, dopants are intentionally introduced impurities which influence the charge carrier statistics of a semiconductor. This is governed by charge neutrality

$$p - n = \sum_i N_{\mathrm{Ai}}^- - \sum_j N_{\mathrm{Dj}}^+ = \sum_i N_{\mathrm{Ai}} f(E_{\mathrm{Ai}}) - \sum_j N_{\mathrm{Dj}} (1 - f(E_{\mathrm{Dj}})), \tag{2.15}$$

here shown for an arbitrary number of acceptors with a density N_A and donors with a density N_D. For each dopant, the density of ionized dopants N_A^- and N_D^+ with respect to the total dopant density N_A and N_D is governed by the distance of the Fermi energy to the respective dopant level E_A and E_D according to Equations 2.16 and 2.17.

$$N_\mathrm{A}^- = \frac{N_\mathrm{A}}{1 + g_\mathrm{A} \exp \frac{(E_\mathrm{A} - E_\mathrm{F})}{kT}} \tag{2.16}$$

$$N_\mathrm{D}^+ = \frac{N_\mathrm{D}}{1 + g_\mathrm{D} \exp \frac{(E_\mathrm{F} - E_\mathrm{D})}{kT}} \tag{2.17}$$

The symbols g_A and g_D are the respective ground-state degeneracy of the impurity level. These shall be shortly explained for a monovalent dopant: Such a level can be occupied by electrons with two types of spins, so it appears as two available sites in carrier statistics while it is unoccupied. However once occupied, it holds its maximum charge and appears in carrier statistics as a single level. Consequently g_D for donors becomes $1/2$ whereas g_A for acceptors is equal to 2.[36]

Shallow dopants have a charge transition state within $3kT$ from one of the band edges, so that the electron or hole is contributing to the free carrier density. An active donor is positively charged, when an electron has been ionized from the donor state to the CBM. An active acceptor is negatively charged, when an electron has been ionized from the VBM to the acceptor state. *Deep* dopants cannot directly contribute to free charge carrier density, but they have an influence as *compensating* defect. To illustrate charge neutrality and free charge densities in a semiconductor with different types of defects, charge densities (free and localized) are graphically displayed with respect to the Fermi energy in the band gap in Figure 2.5. Table 2.1 summarizes the doping conditions and the resulting hole carrier density and Fermi energy with a band gap of 2 eV.

Since the only shallow dopant in the example is an acceptor, the material is p-type in all four cases. A rather high hole concentration is present in the uncompensated case (a).

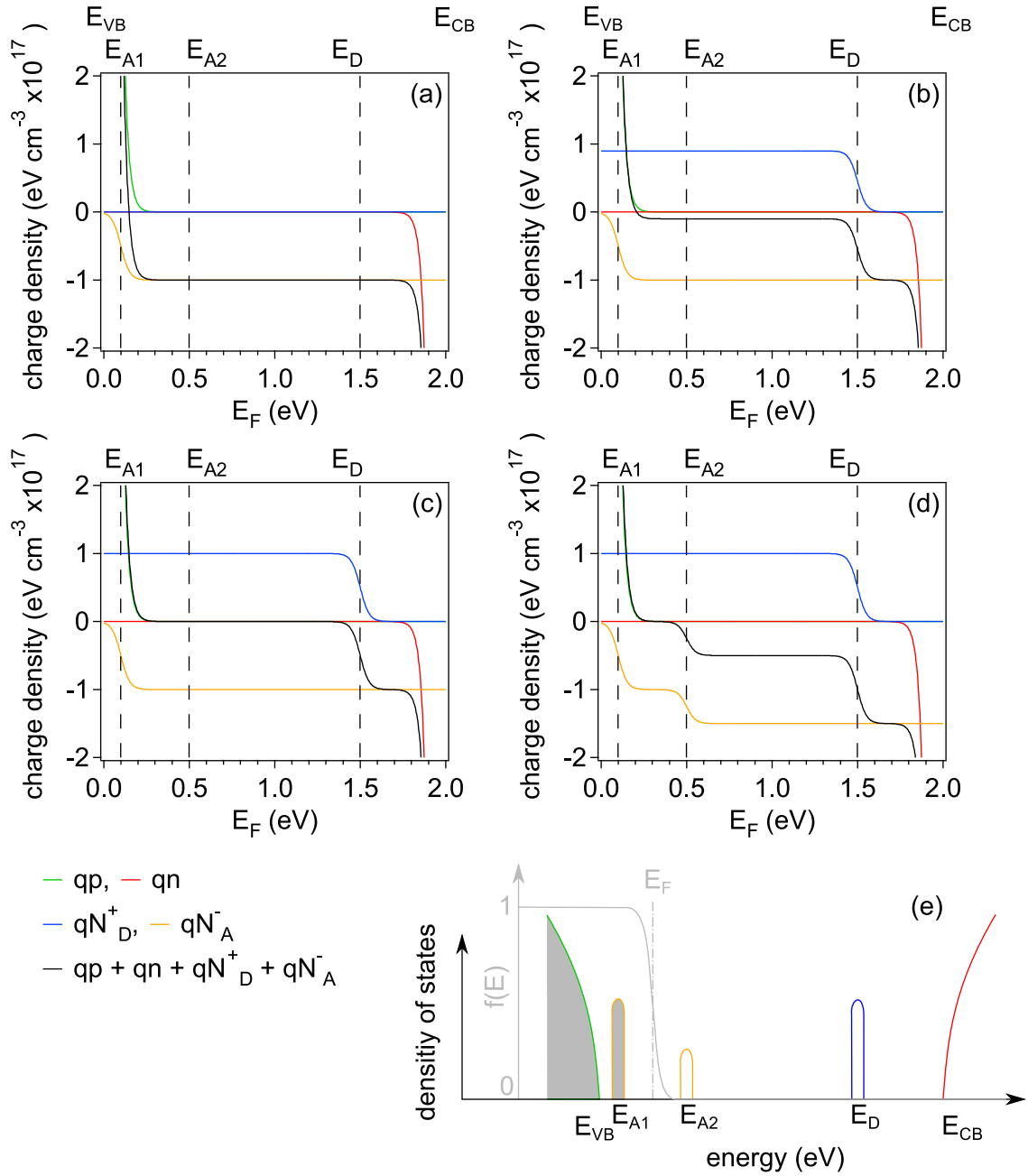

Figure 2.5: Charge densities multiplied by the respective charge q of a semiconductor with a band gap of 2 eV at 300 K and different dopant densities are displayed with respect to the Fermi energy: (a) A shallow acceptor at E_{A1}, (b) plus a deep compensating donor at E_D with $N_{A1}/N_D = 0.9$, (c) a shallow acceptor and a deep compensating donor with $N_{A1}/N_D = 1$, (d) plus a deep acceptor E_{A2}. (e) The occupation of the respective states equivalent to (d) is shown by superposition of band and dopant density of states (black) and the Fermi distribution (gray, after Equation 2.1).

Table 2.1: Values of free hole concentration and Fermi energy obtained from Figure 2.5.

	(a)	(b)	(c)	(d)
N_{A1} ($cm^{-3} \times 10^{17}$)	1	1	1	1
N_{A2} ($cm^{-3} \times 10^{17}$)	-	-	-	0.5
N_D ($cm^{-3} \times 10^{17}$)	-	0.9	1	1
p (cm^{-3})	9×10^{16}	9×10^{15}	4×10^{5}	6×10^{13}
E_F (eV)	0.15	0.21	0.83	0.33

n is negligibly small, so Equation 2.15 becomes $p = N_{A1}^-$. With the occurrence of a deep donor in case (b), p decreases one order of magnitude. Now, the hole concentration rather depends on $N_{A1} - N_D$ than on the absolute value of N_{A1}. Even though the donor state is too deep to produce free carriers (electrons), it has significant influence on charge neutrality by compensating part of the acceptors. Since all donors are fully ionized at the Fermi energy of 0.21 eV, Equation 2.15 can be simplified to $p = N_{A1}^- - N_D$. Case (c) shows a compensation ratio of $N_{A1}/N_D = 1$. This practically eliminates all free charge carrier and puts the Fermi energy close to mid-gap.[6] From these characteristics, the behavior of the material should be similar to a defect-free band gap. However, a large concentration of charged defects ($2 \times 10^{17}\,cm^{-3}$) is present in the material, which on the one hand act as scattering centers and reduce carrier mobility and on the other hand restricts the allowed range of the Fermi energy by a mechanism referred to as *Fermi level pinning*. This is further explained in case (d), where an additional deep acceptor is introduced. Without contributing directly to p, it adds additional negative charge to Equation 2.15 by $p = N_{A1}^- + N_{A2}^- - N_D$ and thus shifts the Fermi energy towards the VBM, which allows more holes to be created by the acceptor A1. Furthermore, the high negative total charge for $E_F > 0.4$ restricts the Fermi energy to lower values. If the Fermi level is artificially increased, for example by using the semiconductor shown in case (d) in a MIS capacitor and putting it under positive bias, a space charge region of ionized defect is developed at the interface to the dielectric, which counteracts an increase in Fermi energy. The higher the density of ionized defects with respect to the free charge carrier density for a given Fermi energy, the more effective is this pinning mechanism.

Figure 2.5 (e) illustrates the occupancy of states according to Equations 2.2 and 2.3 (however using the Boltzmann approximation 2.4 and 2.5 for the intrinsic charge carriers) and will be used for the explanation of trap states in the following subordinated section. Discrete defect levels are displayed with a finite energy distribution, for the purpose of a more comprehensive graphical representation.

[6] The Fermi energy is not exactly at mid-gap since $E_{A1} - E_{VB} \neq E_{CB} - E_D$.

2.4.2 Effects of defects under external bias

In thermodynamic equilibrium, the density of states in the band gap is responsible for the generation of free charge carriers, according to the mechanisms outlined in Section 2.4.1. When excess charge carriers are generated, for example by the field-effect, states in the band gap can capture free charge carriers, acting as *trap states*. This shall be outlined for hole charge carriers.

Any defect (shallow or deep), which can be oxidized can act as a hole trap. This means an occupied (neutral) donor can capture a hole as well as an occupied (negative) acceptor. The charge state is mediated by the Fermi energy, the temperature and the trap state energy, whereas the capture cross-section of the defect determines the efficiency of the process.[37] As an example, the situation in Figure 2.5 (d) and (e) is considered. The only defect, which is capable of capturing a hole is A1. However, when this material is used as a p-type channel, majority charge carriers are accumulated and the Fermi level is moved below E_{A1}, which means, that some of the positive charge is consumed to neutralize A1. Consequently, a higher gate voltage is required to induce a the free charge density, which would be present in a defect-free channel material. Hence, the presence of trap states has a negative effect on field-effect mobility.

A high density of charged acceptors A1 in the unbiased state implies, that the semiconductor has a rather high intrinsic charge carrier density, causing a high OFF current and a negative V_{on}. However, if the material is highly compensated, the intrinsic free charge density may be low. Nevertheless, a large amount of localized charges is present in the material, which deteriorates the drain current modulation of the device.

2.4.3 Intrinsic point defects

In Section 2.3, the field-effect has been described for a semiconductor, which does not constrain changes of the Fermi energy within the band gap. This is the case for elemental semiconductors like silicon and germanium. Also GaAs behaves like this, which is ascribed to its small band gap. The carrier type and concentration can be almost deliberately chosen by the introduction of extrinsic dopants. Compound semiconductors of higher band gap often have rather high equilibrium defect concentrations, which are of intrinsic nature. High defect concentrations induce *Fermi level pinning*, according to the mechanism described in Section 2.4.1. Furthermore, defect formation energies are dependent on Fermi energy, once a defect is charged. Consequently, the equilibrium defect concentration is dependent on Fermi energy, which is referred to as *self-compensation*. Intrinsic defects are the reason that a certain majority carrier type is associated to most semiconductors with a high band gap, which is particularly encountered in oxide semiconductors.[38] In such materials it is impossible to induce minority charge carriers by a field-effect, which is the typical working principle of silicon-based transistors, for example. Oxide semiconductors in a TFT can only be switched from a partially depleted state to majority charge carrier accumulation. For this reason, the terminology *threshold*

voltage (see Section 2.3.2) technically is of no relevance to oxide-based devices, since it is defined as the gate voltage necessary to induce a band bending in inversion of twice the flat-band voltage.[26] In an ideal accumulation-type device, no band bending exists and the channel region can even be treated as a two-dimensional layer.[39]

The mechanism of self-compensation shall be described in more detail. Compound semiconductors are able to form intrinsic point defects by the creation of vacancies, interstitials, anti-site defects or even complex combinations of the these. Under thermodynamic equilibrium, the change in Gibbs free energy ΔG_f upon introduction of an intrinsic defect to the solid is used to obtain information on its concentration c. The Gibbs free energy depends on a few quantities of which the most relevant ones are given in Equation 2.18.

$$c \propto \exp\left(-\frac{\Delta G_\mathrm{f}}{kT}\right) \propto \exp\left(-\frac{\Delta E_\mathrm{f} - \sum_i n_\mathrm{i}\mu_\mathrm{i} + q\,(E_\mathrm{F} - E_\mathrm{defect})}{kT}\right) \tag{2.18}$$

The dominant contribution to ΔG_f in a closed system at low temperature and low pressure is the defect formation energy ΔE_f.[28] When the number of particles is not conserved upon defect creation, then ΔG_f depends furthermore on the sum of chemical potentials μ_i of the components i and the respective number of exchanged particles n_i. In oxides, the chemical potential of oxygen is closely related to the oxygen partial pressure. This is why the latter plays an important role for defect properties of oxide semiconductors.

If a defect has a charge transition state in the band gap, it can carry the charge q. Then the energy difference between the Fermi energy and the charge transition state of the defect E_defect adds another contribution to ΔG_f. The relation of ΔG_f to the Fermi energy is schematically illustrated in Figure 2.6 for the same doping as in Figure 2.5 (d) and (e).

It can be observed in the figure how ΔG_f becomes dependent on E_F once a defect is charged ($q \neq 0$). In order to represent the defect concentrations used in Figure 2.5, ΔG_f has to correspond to the concentrations $N_\mathrm{A1} = N_\mathrm{D} = 10^{17}\,\mathrm{cm}^{-3}$ and $N_\mathrm{A2} = 0.5 \times 10^{17}\,\mathrm{cm}^{-3}$. These two values of the Gibbs free energy are shown by the broken lines. However, at charge neutrality the acceptors A1 are negatively charged and the donors D positively charged. Consequently, ΔG_f at charge neutrality is lower than for the neutral defects A1 and D. The reduction of ΔG_f is in each case given by $q\,(E_\mathrm{F} - E_\mathrm{defect})$.

For certain Fermi energies, ΔG_f becomes negative, which is unphysical. However, $\Delta G_\mathrm{f} = 0\,\mathrm{eV}$ may be interpreted as a spontaneous formation of the corresponding defect. Using the example shown in Figure 2.6, this means that self-compensation limits the Fermi energy to values below 1 eV by the creation of additional acceptor defects A1.

Defects are not necessarily homogeneously distributed inside the material. ΔG_f at grain boundaries, surfaces and interfaces are most probably different from the bulk material. Any boundary of a grain represents a finite border to the periodic lattice. Consequently, the formation energy ΔE_f may be significantly altered. Also the chemical

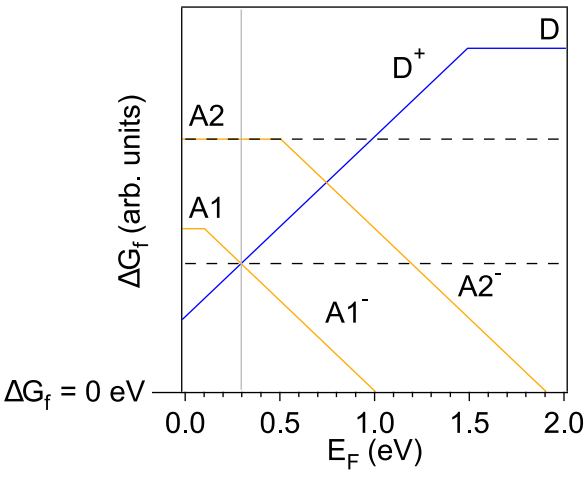

Figure 2.6: Gibbs free enthalpy ΔG_f of defect formation is shown with respect to Fermi energy according to Equation 2.18. The doping is equivalent to Figure 2.5 (d) and (e). The broken lines represent ΔG_f corresponding to N_{A1} and N_D ($10^{17}\,cm^{-3}$) as well as to N_{A2} ($0.5 \times 10^{17}\,cm^{-3}$). The horizontal gray line represents charge neutrality.

potential μ_i can be different, for example if the diffusivity of one component of the material is significantly enhanced along the grain boundary. The result is a different defect concentration in the grain boundary than in the grain interior. Depending on the charge of the segregated defects, changes of the electrostatic potential around the boundary occur.[40–42]

2.4.4 Extrinsic defects by oxidation/reduction

A compound is thermodynamically stable when the chemical potential of each component i lies within a certain range $\mu_i \leq \mu_i^{max}$. Beyond this range, oxidation or reduction may occur provided the components allow more than one oxidation state. In oxides, the oxygen partial pressure plays an important role for the oxidation state of the metal species, similar to the intrinsic defect formation energies. For example, in a binary oxide at μ_O close to μ_O^{max}, a rather high concentration of metal vacancies or oxygen interstitials may be present. When μ_O surpasses μ_O^{max} and in case higher cation oxidation states exist, metal cations get oxidized. Similar to intrinsic defects, oxidation (or reduction) may occur preferentially at crystallographic defects, grain boundaries, interfaces or surfaces, due to the dependency on the chemical potential.

2.5 Morphology

At first, the mechanisms which can lead to an influence of morphology on charge carrier transport are presented. Then, the ones which are specifically relevant for Cu_2O are discussed in more detail.

A *monocrystal* consists of one crystallite which expands up to the macroscopic delimitations of the sample. Apart from intrinsic point defects, 1-dimensional line defects may occur, which are stacking faults such as edge or screw dislocations. Strictly speaking, interfaces and surfaces are also defects, since they represent a disturbance to the periodic lattice, which is the basis for the discussion of the quasi-free electron in a periodic

potential, presented in Section 2.2. A *polycrystal* consists of differently orientated grains, which are connected by grain boundaries, a 2-dimensional crystallographic defect. Morphology, also referred to as microstructure, describes the shape, size and orientation of crystallites in a polycrystalline material. If orbital geometries at the VBM and/or CBM are anisotropic, electronic properties in this case will be different for current passing through a grain boundary, than for current inside the grain. However, this only has influence on respective charge carriers mobilities, if the mean free path of electrons λ_e exceeds the distance between scattering centers, which in case of grain boundaries is equivalent to the grain size. The mean free path of electrons can be calculated with the following equation.[40, 43]

$$\lambda_e = \tau \cdot v_{therm} = \frac{m_h^* \mu_{grain}}{e} \cdot \sqrt{\frac{8kT}{\pi m_h^*}} \tag{2.19}$$

The symbol τ is the time between individual scattering processes, v_{therm} the thermal velocity of charge carriers and m_h^* the effective charge carrier mass (here shown for holes).

Another mechanism, which can cause additional scattering at grain boundaries is related to a *potential barrier* at the boundary. This is formed when majority carriers are captured at defect states in the grain boundary. Due to charge neutrality, a depletion region is consequently formed around the boundary, which represents a barrier for majority charge carrier transport.[44] Depending on grain size and width of the depletion, this can also have significant influence on charge carrier concentration. The original model to describe this type of scattering was given by Seto.[45]

A third type of mechanism is encountered, when the grain boundary contains fixed charges of the opposite sign as the majority charge carriers. Then, an accumulation of the latter results from charge neutrality. The accumulation itself does not form a potential barrier for the charge carrier. However, the *ionized impurities* in the barrier still act as scattering centers.[46, 47]

The origin of the defects, which cause a fixed charge in the grain boundary may simply be the broken symmetry at the boundary. A covalent semiconductor like silicon ends up with dangling bonds in the middle of the band gap. If the material is doped, dangling bonds always capture majority charge carriers and cause a barrier at the grain boundary. In a more ionic compound like a metal oxide, the sign of the fixed charge with respect to the majority charge carriers depends on the defect structure at the interface between the grains.

Structural disorder and mobility of n-type and p-type oxides

The meaning of structural disorder for amorphous oxide semiconductors shall be shortly commented here, as this technology has significantly stimulated research on p-type oxide materials for transparent electronics.[48] If a material has no long-range order, it is referred to as *amorphous*. The lack of a periodic structure implies, that the band model cannot be applied for these types of materials. However, the electrical properties of an

amorphous material may be similar to the respective monocrystal if the current-carrying energy band is primarily of isotropic geometry.[49] For example, this is the case of a strong contribution of metal s-orbitals to the conduction band minimum.[50] Due to orbital isotropy, the missing spatial order is partially compensated and a Gaussian-distributed distance to neighboring atoms is found. The equivalent to a band edge is then also rather Gaussian-distributed. The consequence is a certain amount of states "tailing" exponentially into the band gap, which are referred to as *tail states*. Their density is inverse to the degree of isotropy of the current-carrying orbital.

The high electron mobility in the amorphous state of n-type AOS is mainly due to the orbital configuration at the conduction band minimum,[7] dominated by metal ions of $(n-1)\mathrm{d}^{10}n\mathrm{s}^{0}$ configuration.[48, 50] When the quantum number n is at least equal to 5, the radius of the spherical s-orbital is sufficiently large to create a continuous[8] path for conducting electrons by the overlap between neighboring atoms.[49] The result is a high electron mobility. Another consequence of the strong s-orbital overlap is the low density of tail states, which enables a fast switching between the ON and OFF states of a TFT.

Quite contrasting, the valence band maximum in a metal oxide is typically dominated by the oxygen 2p character, based on the molecular orbital theory. These orbitals are anisotropic and rather localized, compared to metal s-orbitals and thus do not allow for a continuous conduction of holes. Only when there is a comparatively strong contribution of metallic orbitals to the valence band maximum, the necessary orbital overlap for continuous conduction may occur. This is the case in oxides, which contain Cu(I) or Sn(II), for example.[8, 51]

2.5.1 The structure zone model

The relations between growth conditions and morphology and available models for including inhomogeneities to the analysis of electrical properties are presented in the following paragraphs. The information on thin film morphology is to large extend taken from a book by Ohring.[29]

The factors which determine film morphology by deposition from the vapor phase have lead to structure zone models (SZM), which relate morphology to the deposition conditions. The significant processes are shadowing, surface diffusion, bulk diffusion and desorption. The first one is purely geometric, involving amongst other influences the surface roughness of the substrate. The other three processes depend on the temperature at the substrate surface T_s in relation to the melting point of the film material T_m.

The first structure zone model has been developed by Movchan *et al.* for evaporated metallic and oxide thin films.[52] The main parameter, which determines the growth zone is $T_\mathrm{s}/T_\mathrm{m}$. A more refined model has been developed by Thornton for metallic thin films

[7] Note that the band theory based on Bloch states in fact does not apply in a non-periodic lattice. Instead of bands, the term *mobility edge* may be used.[24]

[8] The word "continous" here means, that the conduction is not accomplished by hopping between localized states.

by sputter-deposition.[53] This model includes additionally the inert gas pressure during deposition, which is influencing the particle energy. Both authors identified three main zones of distinct grain growth, however with slightly different transition temperatures. Consequently, when a rough estimation of the three zones is needed, the original SZM by Movchan *et al.* is sufficient, as has been recently published for samples of Cu_2O.[46]

Three zones have been identified by Movchan *et al.*:

- Zone 1 at $T_s/T_m < 0.3$ features "cauliflower-type" grains with voids in the grain boundaries. Shadowing effects are pronounced due to low adatom diffusion.
- Zone 2 at $0.3 < T_s/T_m < 0.45$ features rather columnar grains without voids in the boundary. Surface diffusion now influences the growth and grains become larger with increasing temperature.
- Zone 3 at $T_s/T_m > 0.5$ features comparatively large grains of isotropic dimensions as the growth is dominated by bulk diffusion.

In addition, Thornton described a transition zone between zone 1 and 2, consisting of rather fibrous grains, which however was later characterized as a sub-zone of zone 1.[54]

In order to find a relationship between the growing lateral grain size in zone 1 and the increasing thickness, computer simulations have been performed by Messier *et al.*.[54–56] The authors started with a random distribution of seeds on the substrate surface. A power-law dependency was used to describe the shape of each grain growing, given by Equation 2.20.

$$d \propto L_{\text{grain}}^{n} \tag{2.20}$$

In this way, the thickness d increases along the y-direction as the lateral grain size L_{grain} increases along x. Since the macroscopic dimensions along x are fixed, some cones stop growing as their boundaries insect with other grain boundaries. If various values of n are used during the simulation, the cones with higher exponent preferentially stop growing on the expense of others. If a uniform n is used, the competition between grains is random. Figure 2.7 shows cone shapes for different exponents n and an example for a morphology predicted with $n = 1$.

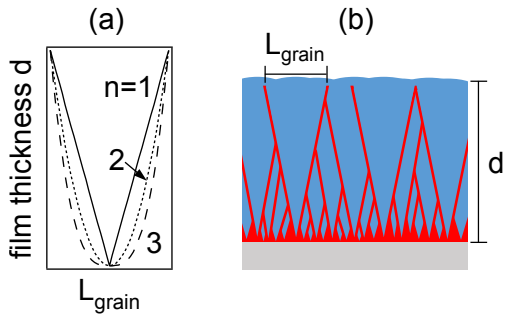

Figure 2.7: (a) The shape of individual grain cones is shown for different exponents n. (b) A model morphology for $n = 1$ is suggested.

2.5.2 Models for inhomogeneous electrical properties

In polycrystalline semiconductors, generally the morphology has an effect on electrical properties, when the ratio of conductivity inside the grains σ_{grain} and conductivity in the grain boundary σ_{GB} is different from unity. Most literature intends to model highly resistive boundary layers, a rather common situation in polycrystalline thin films.[40] Most geometrical models to describe the macroscopic electronic properties of systems consisting of two components make use of approximations due to $\sigma_{GB} << \sigma_{grain}$.[40] However, this limitation cannot be applied in the case of polycrystalline copper oxide.[14, 15, 57] Hence, in the following paragraphs selected literature is presented, which is not limited to the case $\sigma_{GB} << \sigma_{grain}$. Most of the information presented here is taken from a comprehensive review by Orton *et al.*, as well as from a book by Shik.[40, 58]

The first model described by Volger was based on the assumption of cubic grains, surrounded by a grain boundary medium.[59] Lipskis and Heleskivi further developed the original formalism, based on the same geometry.[60, 61] A schematic representation of the model morphology is shown in Figure 2.8 (a). There is an important limitation to the applicability of the cubic matrix model. If $L_{GB} << L_{grain}$, an unrealistic edge effect occurs in region 4. If $L_{GB} >> L_{grain}$, the edge effect occurs in region 1. The problem can be solved by limiting the analysis to either of the two cases. Volger, Lipskis and Heleskivi have analyzed the case $L_{GB} << L_{grain}$ by including region 4 into region 3. Furthermore, they limited their analysis to the case $\sigma_{GB} << \sigma_{grain}$, which allowed certain simplifications.

The Orton model

An effective resistivity, which is valid for any ratio of $\sigma_{GB}/\sigma_{grain}$ is provided by Orton *et al.*.[40] It is based on the equivalent circuit shown in Figure 2.8 (b).[40] The resistances R and currents I in the regions 1, 2 and 3 are given by the following equations, where V_i is the applied voltage in each individual cell of the periodic structure. As the equivalent

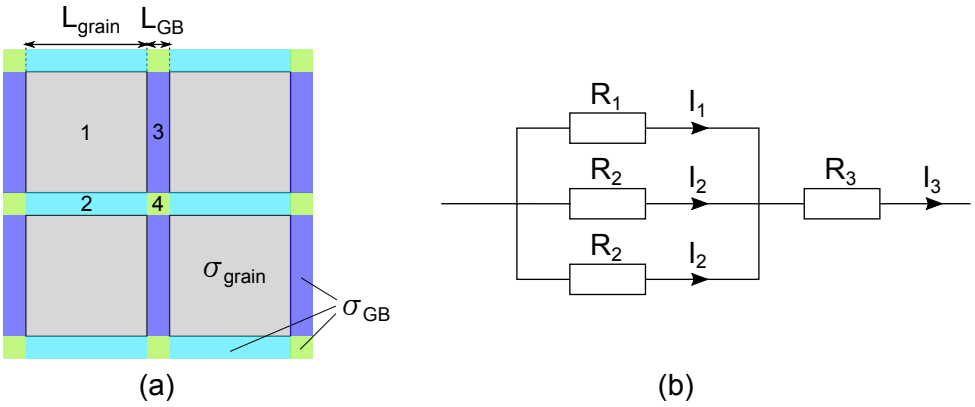

Figure 2.8: (a) The cubic matrix model morphology. The numbers indicate the different regions. (b) The equivalent circuit used by Orton *et al.*. The subscripts refer to the regions of (a).

circuit serves to derive also equations for Hall effect measurements, there are two resistors R_2, one perpendicular and one parallel to the magnetic field.

$$R_1 = \left[\sigma_{\text{grain}} L_{\text{grain}}\right]^{-1} \tag{2.21}$$

$$R_2 = \left[\sigma_{\text{GB}} L_{\text{GB}} \left(L_{\text{grain}} + L_{\text{GB}}\right)/L_{\text{grain}}\right]^{-1} \tag{2.22}$$

$$R_3 = \left[\sigma_{\text{GB}} \left(L_{\text{grain}} + L_{\text{GB}}\right)^2/L_{\text{GB}}\right]^{-1} \tag{2.23}$$

$$I_1 = V_{\text{i}} \left[R_1 + \frac{R_3\,(2R_1 + R_2)}{R_2}\right]^{-1} \tag{2.24}$$

$$I_2 = V_{\text{i}} \left[R_2 + \frac{R_3\,(2R_1 + R_2)}{R_1}\right]^{-1} \tag{2.25}$$

$$I_3 = V_{\text{i}} \left[R_3 + \frac{R_1 R_2}{2R_1 + R_2}\right]^{-1} \tag{2.26}$$

The effective conductivity σ^* is then

$$\sigma^*_{\text{Orton}} = \frac{I_3}{V_{\text{i}}\left(L_{\text{grain}} + L_{\text{GB}}\right)} = \left[\frac{1+\beta}{\sigma_{\text{grain}}\left[1 + 2\alpha\beta\,(1+\beta)\right]} + \frac{\beta}{\sigma_{\text{GB}}\,(1+\beta)}\right]^{-1}, \tag{2.27}$$

with $\alpha = \sigma_{\text{GB}}/\sigma_{\text{grain}}$ and $\beta = L_{\text{GB}}/L_{\text{grain}}$. Orton *et al.* then derived an equation which predicts the effective Hall coefficient R^*_{H}, based on the same equivalent circuit. However, only the limiting case of a much less conductive grain boundary with respect to the grain interior is regarded in order to simplify the equations. For this reason, their equation for R^*_{H} cannot be applied to the case of copper oxide.

The Mathew model

An alternative to the cubic matrix model has been provided by Mathew *et al.*.[62] The equation for the effective conductivity of this model is equivalent to the one of the cubic matrix model (Equation 2.27) as long as $L_{\text{GB}} << L_{\text{grain}}$. However, the authors developed the basic equations for σ^* and R^*_{H} without any limitations regarding $L_{\text{GB}}/L_{\text{grain}}$ and $\sigma_{\text{GB}}/\sigma_{\text{grain}}$.[40, 62]

The derivation of the equations is relatively complex, which is why only the concept is presented here. The model considers a mixture of spheres, which all have a core of a certain conductivity and a shell of another conductivity. In order to fill voids between the spheres, various diameters are considered simultaneously. The authors have shown, that as long as the ratio of core and shell radius is the same for all spheres, the potential in one sphere is independent of the potential of the spheres surrounding it. Hence, they could represent the effective conductivity and Hall coefficient by calculating it for a single

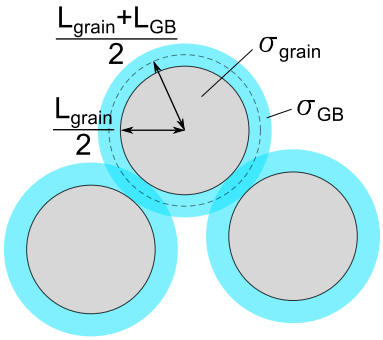

Figure 2.9: Schematic illustration of the composite sphere model.

sphere. The geometry of the sphere is schematically shown in Figure 2.9. For convenience, the same terminology is used as above, which means the core is referred to as the grain interior and the shell is equivalent to the grain boundary. Then the radius of the core is $L_{\text{grain}}/2$ and the radius of the core plus the shell is $(L_{\text{grain}} + L_{\text{GB}})/2$. The symbol X means the volume fraction of grain boundary (or shell) phase.

$$\sigma^*_{\text{Mathew}} = \frac{2\left(\sigma^2_{\text{GB}} - \sigma_{\text{grain}}\sigma_{\text{GB}}\right)X + 3\sigma_{\text{grain}}\sigma_{\text{GB}}}{3\sigma_{\text{GB}} + X\left(\sigma_{\text{grain}} - \sigma_{\text{GB}}\right)} \tag{2.28}$$

$$R^*_{\text{H}} = \frac{27\sigma^2_{\text{grain}}\sigma^2_{\text{GB}}R_{\text{H,grain}}\,(1-X) + 9R_{\text{H,GB}}X\sigma^3_{\text{GB}}\left(\sigma_{\text{GB}} + 2\sigma_{\text{grain}}\right)}{A\sigma^* + B\sigma^{*2} + C} \tag{2.29}$$

$$A = 9\sigma_{\text{grain}}\sigma^2_{\text{GB}} + 3X\left(2\sigma^3_{\text{GB}} - 3\sigma_{\text{grain}}\sigma^2_{\text{GB}} + \sigma^3_{\text{grain}}\sigma_{\text{GB}}\right) \tag{2.30}$$

$$B = 9\sigma^2_{\text{GB}} + 6X\left(\sigma_{\text{grain}}\sigma_{\text{GB}} - \sigma^2_{\text{GB}}\right) \tag{2.31}$$

$$C = 9\sigma^2_{\text{grain}}\sigma^2_{\text{GB}} + 12X\left(\sigma_{\text{grain}}\sigma^3_{\text{GB}} + \sigma^2_{\text{grain}}\sigma^2_{\text{GB}}\right) \tag{2.32}$$

The Nakamura model

An experimental study of an insulator-conductor composite has been reported, which had a structure of rather large insulating particles in a matrix of conductive material.[63] This had been achieved by dispersing graphite powder into molten wax, which then was solidified under stirring. The resulting structure consists of wax particles surrounded by a comparatively fine-grained layer of conductive graphite. The experimentally obtained conductivity of the composite of different volume fractions of conductive material has been reported. The model by Mathew was not applied by the authors. Instead, an analysis using the finite-element method (FEM) has been reported by Nakamura.[64] The author modeled a two-dimensional network of conductive channels around a periodic lattice of non-conductive grains with an idealized geometry (triangles, squares and hexagons). Since the solution was obtained numerically, no analytic equation for the effective conductivity could be provided. Further below, the model will be graphically compared to the other ones.

The Göbel model

More recently, cerium oxide has been shown to have an increased grain boundary conduction, when deposited on SiO_2.[65] Data had been obtained by measuring the films conductance in planar geometry at different thicknesses. The conductance *versus* thickness curves showed a positive ordinate intercept. A model has been developed to account for an increased grain boundary conduction, which is represented in Figure 2.10.

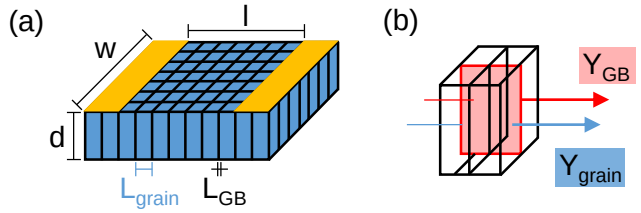

Figure 2.10: (a) The model of the film morphology is shown, as used by Göbel *et al.*.[65] The symbols w and l are the width an length, defined by the electrodes, L is the grain size and d the film thickness. (b) The two parallel currents through the grain boundary (red arrow) and through the grains (blue arrow) are illustrated, together with the respective reduced conductances Y.

Due to $\sigma_{\text{grain}} < \sigma_{\text{GB}}$, only the grain boundaries parallel to the current flow are assumed to contribute to conduction, as long as the lateral grain size L_{grain} is significantly higher than the grain boundary width L_{GB}.

To build up the model, the number of parallel grain boundaries N_{GB} is counted according to the width of the planar contacts w and the grain size L_{grain}. Note, that here each grain counts one grain boundary of a width L_{GB} whereas, the original article considered two space charge regions on each side of the grain.

$$N_{\text{GB}} = \frac{w}{L_{\text{grain}}} \tag{2.33}$$

The conductance G is calculated as a parallel connection of the monocrystalline conductance G_∞ and all grain boundary conductances G_{GB}. This implies, that G_∞ is assumed to be unaffected by the grain boundaries.

$$G = G_\infty + N_{\text{GB}} G_{\text{GB}} \tag{2.34}$$

Furthermore, the reduced conductances $Y_\infty = G_\infty l/w$ and $Y_{\text{GB}} = G_{\text{GB}} d/l$ are used, which lead to the final equation:

$$Y = Y_\infty + Y_{\text{GB}} \frac{d}{L_{\text{grain}}} \tag{2.35}$$

The grain sizes have been found to be a function of film thickness and can be approximated by linear dependency. This is valid for the investigated thickness range between 40 nm and 200 nm. In order to compare this model to the others, which are presented in

this section, it is useful to derive an equation for σ^*, based on the same equivalent circuit of a simple parallel connection. Then each grain has a contribution coming from the grain interior and from the boundary. Each one simply scales with the respective fraction. This is expressed by Equation 2.36.

$$\sigma^*_{\text{Göbel}} = \sigma_{\text{grain}} \frac{L_{\text{grain}}}{L_{\text{grain}} + L_{\text{GB}}} + \sigma_{\text{GB}} \frac{L_{\text{GB}}}{L_{\text{grain}} + L_{\text{GB}}} \tag{2.36}$$

A comparison of the models

At this point, three different expressions for σ^* have been presented. In order to visualize to which extend the analysis by Orton, Mathew and Nakamura differ from each other, the predicted dependencies are graphically illustrated in Figure 2.11. The grain boundary width was fixed to $L_{\text{GB}} = 0.5\,\text{nm}$, which is within the range suggested by Göbel for an accumulated boundary layer, with respect to the grain interior.[65] A normalization of σ^* is done by $\left(\sigma^* - \sigma_{\text{grain}}\right)/\left(\sigma_{\text{GB}} - \sigma_{\text{grain}}\right)$ in order to compare the models by Orton, Mathew and Göbel to the data published by Nakamura. With the normalization, any ratio of $\sigma_{\text{GB}}/\sigma_{\text{grain}} > 1$ can be used.

For the analysis by Orton and Mathew, the volume fraction X relates to the grain size and grain boundary width according to Equations 2.37. Note, that the grain boundary volume fraction is displayed on reversed axis in Fig. 2.11 (a) and (b) to facilitate the comparison to grain size in (c) and (d).

$$X = 1 - \left(\frac{L_{\text{grain}}}{L_{\text{grain}} + L_{\text{GB}}}\right)^3; \qquad L_{\text{grain}} = \frac{L_{\text{GB}}\,(1-X)^{1/3}}{1-(1-X)^{1/3}} \tag{2.37}$$

In the analysis by Göbel, the grains are cuboid, extending in the direction perpendicular to the surface over the entire film thickness. Consequently, X is calculated with a different exponent, given in Equation 2.38. Note, that grain boundaries perpendicular to the current flow are considered in the volume fraction, even though their effect on conductivity is neglected.

$$X = 1 - \left(\frac{L_{\text{grain}}}{L_{\text{grain}} + L_{\text{GB}}}\right)^2; \qquad L_{\text{grain}} = \frac{L_{\text{GB}}\,(1-X)^{1/2}}{1-(1-X)^{1/2}} \tag{2.38}$$

Figure 2.11 (a) shows, that the results of Nakamura are very similar to the ones obtained by Mathew. As Nakamura changes the grain geometry from triangles, to squares and hexagons (not shown here) the curve moves towards the results obtained by the composite sphere model by Mathew *et al.*. This is reasonable, since the grains successively become more spherical. Note, that the analysis by Nakamura was conducted in two dimensions but the results are similar to the three-dimensional model by Mathew *et al.*. The analysis described by Orton deviates considerably from the other two calculations at high volume fractions of grain boundaries. This is most likely due to the limitation of the model to $L_{\text{grain}} << L_{\text{GB}}$.[40] The model by Göbel produces similar results as the one by

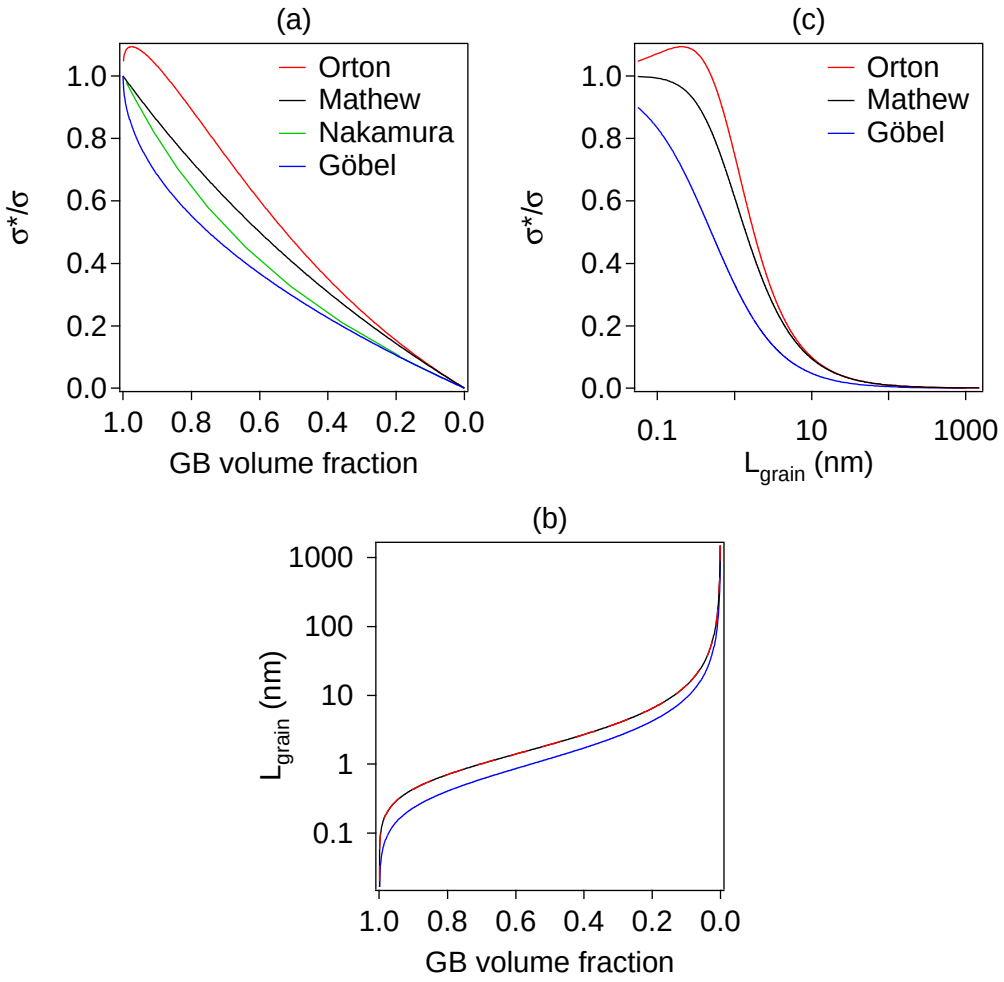

Figure 2.11: Effective conductivity models are comparatively displayed with respect to (a) grain boundary volume fraction and (c) grain size, following the relation volume fraction–grain size shown in (b).

Nakamura. However, an underestimation of conductivity at high grain boundary volume fractions is observed in comparison to the other models, which may be expected since the model neglects grain boundaries perpendicular to the current flow. Figure 2.11 (b) shows how L_{grain} relates to the grain boundary volume fraction for the models by Orton and Mathew, as well as by Göbel. This gives rise to the representation in Figure 2.11 (c), illustrating the range of grain size, within which a strong effect on the effective conductivity is observed.

Considerations on applicability of the models to experimental data of Cu_2O thin films

In Chapter 5, data from two types of electrical measurements of inhomogeneous Cu_2O thin films are presented. First, the in situ conductance of thin films between < 1 nm and

250 nm thickness is analyzed with respect to thickness. Then, results from Hall effect measurements of Cu_2O samples with different grain sizes are discussed.

In the analysis of conductance with respect to film thickness, a grain size in a similar range as the film thickness may potentially be encountered at the lowest thicknesses. Consequently, the model described by Orton may not be applied to interpret such data. Due to the columnar morphology of the growing thin film, the model by Göbel *et al.* is more adequate than the one by Mathew *et al.*. Firstly, the model by Mathew *et al.* requires a constant ratio between the core and shell radii for all spheres. The constant ratio means the grain boundary grows simultaneously with the grains. This is in contrast to the morphology of polycrystals, which typically features a constant grain boundary width. Secondly, the absolute size of the sphere is not restricted for a certain volume fraction of conductive phase. This is also in contrast to the morphology of polycrystals, which typically have an average grain size with a deviation from the mean value in the range of 20–40 %, when determined by scanning electron microscopy.[46]

In the model by Göbel *et al.*, the grain size is assumed to be uniform for a certain thickness. The authors could make this simplification to the grain growth model by Messier *et al.*, since their films where rather thick and indeed showed a uniform lateral grain size throughout the whole thickness.[65] In order to apply the model by Göbel *et al.* to a film of non-uniform grain size, an integration step has to be included. The complete calculation is described in Section 5.1.4.

The interpretation of results by Hall effect measurements of samples with different grain sizes is tentatively done using the model by Mathew *et al.*. In the limiting case of $\sigma_{GB} > \sigma_{grain}$, it is the only model which includes an analytic expression for the Hall coefficient. However, the model geometry the equations are based on differs significantly from the morphology of Cu_2O. Whether or not the model can be applied to interpret the experimental data is discussed in Section 5.2.2.

2.6 Cu_2O material properties and state of the art of thin-film transistors

The rectification of the Cu/Cu_2O junction and hence the semiconducting nature of Cu_2O is known since 1926.[66] Since then, numerous scientific reports have been published to elucidate the material's properties. Most relevant literature is summarized in the PhD thesis of Francesco Biccari,[67] and in a comprehensive review by Bruno Meyer *et al.*.[19] Together they provide a good overview on the current understanding of this material. Since a full review on this material is available in literature, Section 2.6.1 focuses on the electrical properties and their correlation to (intrinsic and extrinsic) defects.

The development and state of the art of p-type TFTs from Cu_2O has been recently reviewed by Al-Jawhari *et al.*.[68] A recent, more general review on p-type oxide TFTs can also be found in literature.[69] Section 2.6.2 focuses on the development of TFTs with Cu_2O by physical vapor deposition. A comparison of a few general properties of copper and copper oxides from literature is given in tables 2.2 and 2.3.

Table 2.2: General properties of copper and copper oxides (part 1), *sputter-deposited. The structural data is taken from the respective ICDD entries; Cu: PDF 00-004-0836, Cu_2O: PDF 00-005-0667, Cu_4O_3: PDF 01-083-1665, PDF CuO: 00-045-0937

	Cu	Cu_2O
oxidation state	Cu(0)	Cu(I)
name	Copper	Cuprite cuprous oxide
crystal structure	cubic	cubic
lattice constant (Å)	$a = 3.615$	$a = 4.2696$
band gap (opt.) (eV)	-	2.17[70] (2.45)[71]
dielectric constant	∞	≈ 7[72]
conductivity* ($S\,cm^{-1}$)	5×10^5[71]	$10^{-5} - 3 \times 10^{-3}$[19, 71]

Table 2.3: General properties of copper and copper oxides (part 2).

	Cu_4O_3	CuO
oxidation state	Cu(I) and Cu(II)	Cu(II)
name	Paramelaconite	Tenorite cupric oxide
crystal structure	tetragonal	monoclinic
lattice constants (Å)	$a = 5.837$ $c = 9.932$	$a = 4.6853$ $b = 3.4257$ $c = 5.1303$ $\beta = 99.549°$
band gap (eV)	1.34 or 2.47[71]	≈ 1.5[57]
dielectric constant	-	5.8 – 10.5[18]
conductivity* ($S\,cm^{-1}$)	10^{-3}[19, 71]	$10^{-2} - 1$[18, 19, 57]

2.6.1 Defects in Cu_2O

Probably the most important figures of merit, which determine whether a semiconductor has chances to be successfully applied in a majority charge carrier device like a TFT, are the respective charge carrier concentration and the mobility.[9] As described in Chapter 2, the carrier concentration is related to the band gap and doping. The modulation of the carrier concentration by external influences has to obey charge neutrality (Equation 2.15), which is intimately linked to the concentration of defects and their charge state. The highest reported mobility of a monocrystalline Cu_2O is $\mu = 100\,\mathrm{cm^2V^{-1}s^{-1}}$,[9] which is associated to an effective hole mass of $m_h^* = 0.58 \cdot m_0$ in units of the free electron mass m_0.[73] According to Equation 2.19 of Section 2.5, the mean free path of hole charge carriers at room temperature is $\lambda_e = 4.7\,\mathrm{nm}$. In a polycrystalline material, scattering at grain boundaries due to the broken crystal symmetry would occur for grain sizes below this value. However, high-resolution transmission electron microscopy showed a grain diameter of at least 10 nm, when thin films have been deposited by magnetron sputtering at room temperature.[74] Hence, scattering at grain boundaries is not a dominant mechanism in such samples. Instead, the mobility is limited by charge carrier scattering at phonons and charged defects (i.e. ionized impurities).[10, 22, 46, 75] The possible defects in the material are the subject of the following subordinated sections.

Intrinsic point defects in Cu_2O

Many experimental studies and theoretical calculations have been published, which try to resolve the point defects structure of Cu_2O. Experimental data on point defect formation enthalpies has been mainly obtained by gas volumetric analysis,[76] chemical analysis of quenched samples,[77] coulometric titration[78, 79] and thermogravimetry.[80–82]. The intrinsic defects are widely discussed for being responsible for self-diffusion.[83–86] Electronic defect properties have been predominantly investigated by conductivity[14, 82, 84, 87, 88] and Hall effect measurements at different temperatures.[9, 17, 46, 74, 75, 89–91] The list of cited works does not intend to be exhaustive, but it is sufficient to outline the current understanding on this material. As representative studies, the works by Brattain and Bloem on bulk samples shall be presented in more detail below.

As early as 1951, the important work by Brattain has shown Cu_2O to be a compensated material.[17] He analyzed the activation energy for temperatures between 170 K and $\approx 700\,\mathrm{K}$. A fit to the data had to reproduce not only the slope, but also the saturation of majority charge carriers at high temperature. In case of an uncompensated material of the same carrier concentration, he found the saturation value would have to be in the order of $N_A = 10^{20}\,\mathrm{cm^{-3}}$. However, the experimentally observed saturation is in the range of 10^{14}–$10^{15}\,\mathrm{cm^{-3}}$. This can be explained by a compensated situation, in which the saturation value gives $N_A - N_D$. Brattain further analyzed the depletion layer capacitance

[9] Minority charge carrier life time and diffusion length are only important when electron-hole pairs are created during device operation, like in a solar cell.

of a Cu/Cu_2O Schottky barrier and obtained the same value of $N_A - N_D$. By comparison of a set of different samples, he found the dopant density to vary between $10^{14}\,cm^{-3}$ and $10^{16}\,cm^{-3}$. The energy level of the main acceptor is found at 0.3 eV above the valence band maximum. The potential drop in the semiconductor due to the Schottky barrier to metallic copper is 0.5 eV.

A few years later, Bloem confirmed the main acceptor state to be due to copper vacancies and introduced the concept of oxygen vacancies as dominating donor.[92, 93] His conclusions were based on photoluminescence measurements at low temperature. The assignment of the three main signals in the spectrum due to V_{Cu} (1.36 eV), V_O^+ (1.51 eV) and V_O^{++} (1.72 eV) are consistently used in photoluminescence studies.[19, 94] Based on this result, a hole trapping level in Cu_2O transistors was assigned to oxygen vacancies.[20, 22]

As a complement to experimental results, several theoretical calculations by density functional theory (DFT) have helped to obtain a better understanding of the nature of dopant point defects in Cu_2O.[95–100]: The main acceptor type defect is the copper vacancy V_{Cu}, which may also exist in a paired configuration, referred to as split-vacancy V_{Cu}^{split}. The formation energy of V_{Cu}^{split} is slightly higher[96] or equal to the one of V_{Cu}.[98] A common result from the reported DFT calculations is, that the Gibbs free enthalpy of copper vacancy formation becomes negative at Fermi energies above 0.5–1 eV. This shows the self-compensation of the material, which constrains the semiconductor to p-type conduction. The split-vacancy V_{Cu}^{split} has a deeper charge transition state than the simple vacancy. It should be noted, however, that in the presence of doubly-positive metal ions, for example Mg(II) and Sr(II), a complex is formed with two copper vacancies, which has a comparatively low acceptor level of 0.1 eV.[101–103]

The donor-type defect with the lowest formation energy, which has a transition energy inside the band gap is the copper interstitial. Only at Fermi energies close to the valence band maximum and under copper rich conditions, the formation energy becomes similar to the one of copper vacancies. Oxygen vacancies V_O are present, even with similar concentrations as the main acceptor in some conditions.[99] However, their charge transition level lies within the valence band, which means they do not contribute any charge to the system and cannot cause hole capture.[38, 98] By considering hydrogen as an omnipresent element in ambient atmosphere[104], a donor level in the band gap with a reasonably low formation energy is found, more precisely hydrogen at an oxygen site H_O.[100] The formation of this defect requires a vacant oxygen site and is thus related to the concentration of V_O. Besides hydrogen, another possibility of a stable donor state is given by the formation of defect complexes, which is addressed in the next section. Note, that the exact energetic level of the donor defect is not relevant for the analysis, since it is ionized under all conditions. Figure 2.12 (a) schematically illustrates the charge transition levels in the band gap, as obtained from selected calculations (see references in the figure caption).

Carrier concentration and mobility show some changes, when the material is deposited as thin film ($\leq 1\,\mu m$). Recent experimental results from reactively sputtered Cu_2O thin films,[46, 74] as well as of epitaxial thin films by pulsed laser deposition, shall be considered.[10] As general trend in polycrystalline thin films, hole concentration increases and hole mobility decreases with decreasing grain size.[74] Accordingly, the acceptor concentration increases and the compensation ratio decreases.[46] In epitaxial films a similar trend is found in dependence on the domain size.[10] The acceptor density of sputter-deposited polycrystalline thin films can exceed $10^{18}\,cm^{-3}$. Furthermore, the Arrhenius plot is not linear anymore for lower grain sizes, which suggests the existence of more than one acceptor defect level.[46] The activation energies of Cu_2O thin films from the here discussed literature are summarized in Figure 2.12 (b).

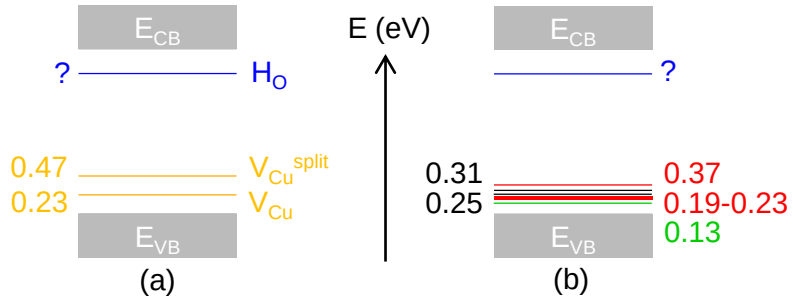

Figure 2.12: (a) Schematic illustration of the main defect levels in Cu_2O, responsible for the equilibrium charge carrier concentration as adopted from DFT calculations.[98–100] (b) Schematic compilation of results on activation energies from assorted references (green,[74] red,[46] black.[10])

Apart from intrinsic defects in their simple form, the formation of defect complexes can lead to new energetic levels in the band gap. Such complexes have been regarded to explain experimental observations of electrical conductivity, in particular persistent photoconductivity (PPC).[93, 105, 106] Here, the association of two copper vacancies and of a copper vacancy with an oxygen vacancy were considered. In a recent study,[106] a deep donor level is associated to the donor-acceptor complex. According to the authors, this complex is stable when positive $V_{Cu}^{-} + V_{O}^{++} \longrightarrow [V_{Cu}V_O]^{+}$, but unstable when neutral $[V_{Cu}V_O]^{0} \longrightarrow V_{Cu}^{-} + V_{O}^{+}$. This is in accordance with the absence of a stable oxygen vacancy donor level in the band gap of Cu_2O. Under illumination, the complex captures an electron and dissociates, forming V_{Cu}^{-} and a *metastable* V_{O}^{+} state. This increases the hole carrier concentration. By calling the oxygen vacancy level metastable, conflicts with results from DFT calculations are avoided, which locate the oxygen vacancy donor level inside the valence band. Hole capture by the V_{O}^{+} state is thus not possible. Equilibrium is only restored when V_{Cu}^{-} re-associate with V_{O}^{+} upon simultaneous hole capture, forming a positively charged stable $[V_{Cu}V_O]^{+}$ complex. This process involves diffusion, which accounts for the temperature and time dependences of persistent photoconductivity observed by the authors.[106] The fastest diffusing intrinsic defect in Cu_2O is the copper

vacancy.[86]

The possible donor state of a $[V_{Cu}V_O]$ complex under equilibrium has been addressed by DFT.[99] It is calculated to lie below the acceptor state of copper vacancies. Hence a neutral (supposingly unstable)[106] complex would capture a hole, when the material is forced into accumulation, eg. in a thin-film transistor. However, the formation enthalpy of this defect complex is too high to explain the strong compensation in Cu_2O. In the light of these results, hydrogen is most probably responsible for the high concentration of compensating donors in the material.[100]

Intentional doping of Cu_2O

With the deliberate addition of impurities to Cu_2O, an intentional doping can be performed. Due to the large amount of reports in literature, only a few examples are given here. Experimental studies on n-type doping are not considered, since n-type Cu_2O is against the rules of thermodynamics.[99] The existing literature may be categorized by the aim of the doping. An increase of the conductivity is typically desired for an application as absorber material in solar cells, for example.[102, 107–110] In addition, an increase of the photoconductivity is beneficial, which can be achieved by a passivation of trap states.[101, 111] For a potential application as p-type TCO, the band gap would have to be increased.[103, 112, 113] All the cited experimental studies have in common, that the conductivity is never decreased by the doping with respect to the undoped material.[10] Furthermore, the mobility of the doped material is usually below the mobility of undoped Cu_2O. Also when comparing Cu_2O to multi-component p-type oxides based on Cu(I), the highest mobility is reported for Cu_2O.[115] Since p-type TFTs based on Cu_2O typically suffer from a high OFF current and a low field-effect mobility, intentional doping was not considered in this thesis.

Thermodynamic stability of Cu_2O

The temperature during the experimental analysis of defect formation enthalpies presented in the previous paragraphs has generally been in the range of 1000 °C, the oxygen partial pressure was controlled to remain in the stability region of Cu_2O. Just like in DFT calculations, thermodynamic stability is fulfilled. Figure 2.13 shows the stability region of Cu_2O.[116] At RT and an oxygen partial pressure corresponding to air of 213 mbar, CuO is the thermodynamically stable phase. Many deposition techniques for thin films of Cu_2O are carried out at RT or below 300 °C (sputtering, pulsed laser deposition, spray pyrolysis etc.), conditions under which Cu_2O is thermodynamically unstable. However,

[10] An exception is the doping with hydrogen, which is reported to decrease the hole carrier concentration due to the passivation of acceptor defects.[100, 114] However, the role of hydrogen is not clear, since it may also act as compensating donor, as mentioned earlier. Furthermore, it can cause cation reduction, which also results in a lower carrier concentration of Cu_2O and can easily be confused with an effect due to the presence of hydrogen. Since hydrogen is not detectable by the analytical techniques used in this thesis, a doping with this element was not considered.

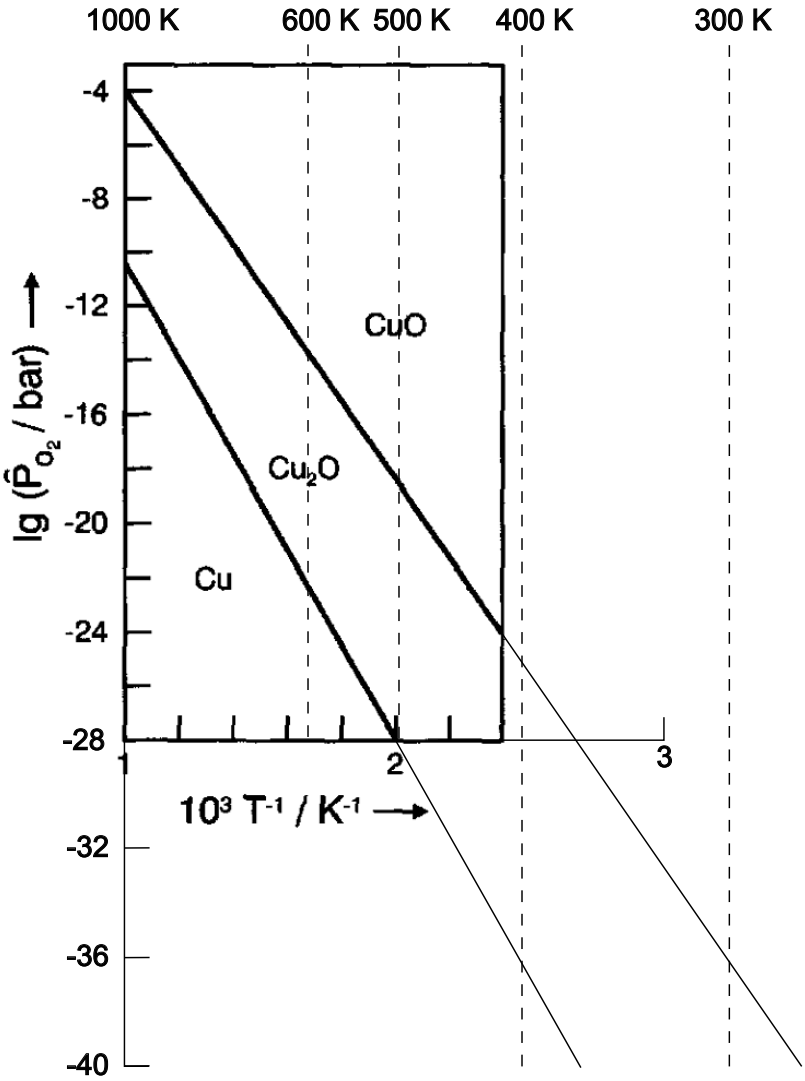

Figure 2.13: Oxygen partial pressure and temperature of different copper and copper oxide phases, reprinted from Maier.[116] The range is graphically extended to 300 K.

the eutectoid decomposition of Cu_2O to Cu and CuO[117] is kinetically hindered at temperatures below 400 °C.[118] A 2-dimensional lattice fault of a missing plane of copper ions along (110) direction has a stabilizing effect on the phase.[13] This corroborates with a first-principle study, which found a low-energy surface structure of Cu_2O(110):CuO under oxygen-rich conditions.[119]

The existence of any secondary copper oxidation state impacts free carrier statistics, either by hole depletion at the Cu/Cu_2O Schottky barrier,[120] or by an introduction of additional free carriers due to Cu(II).[20] There are examples from literature, where a change in the cation oxidation state was originally not considered, but could explain observations of previously published results: Fortin and Weichman as well as McKinzie *et al.* reported a decrease of carrier concentration in monocrystalline Cu_2O over more than two orders of magnitude after annealing at 300 °C in vacuum.[9, 89] 16 years later, Weichman

elaborated on the impact of copper inclusions and copper forming on the surface of Cu_2O by heating in vacuum and the changes in the electrical properties by means of depletion at the Cu/Cu_2O Schottky barrier.[120] Apart from the charge carrier concentration also the activation energy is affected by the metallic copper: The measurement of a non-constant activation energy, following the Meyer-Neldel rule is common for samples with conductivities below $10^{-4}\,S\,cm^{-1}$.[121, 122] Noguet *et al.* interpreted this by assuming a broad acceptor band. However, with the knowledge of the presence of Cu(0) precipitates, the respective Schottky-barrier is likely to cause the variation in the measured activation energy.[120] In fact, thin-film transistors, which have been reported to obey the Meyer-Neldel rule, included a metallic copper phase, detected by XRD.[123]

The electrical properties of Cu_2O, which is depleted by the internal Schottky barriers to metallic copper, are similar to a highly compensated material as long as no percolation path is formed between the metallic particles. The minimum ratio of copper to oxygen for metallic conduction is $Cu/O \approx 2.3$.[124]

2.6.2 State of the art of Cu_2O thin-film transistors

The development of p-type TFTs based on Cu_2O by physical vapor deposition is shortly reviewed. For additional information, the reader may consult two recent reviews, which cover all types of deposition techniques that have been used to fabricate TFTs with Cu_2O.[68, 69] Figure 2.14 is shown for graphical illustration of the literature results. The figure highlights the influence of the fabrication temperature on field-effect mobility and ON/OFF drain current ratio. Other important factors which affect the TFT performance are mentioned in the text.

The first works on TFTs applying Cu_2O as channel material employed pulsed laser deposition (PLD) and focused on producing a material with defect concentrations as low as possible in order to preserve the promising properties of single crystals ($\mu_H \approx 100\,cm^2V^{-1}s^{-1}$ and $p = 10^9$–$10^{12}\,cm^{-3}$) [9]. The material was deposited epitaxially on a MgO(110) single crystal, which required substrate temperatures of 850 °C and a top-gate approach.[10] The film showed almost a Hall mobility as high as the single crystal, but the field-effect mobility μ_{FE} in the device was between two and three orders of magnitude lower. As already stated in the original paper, defects at the interface to the dielectric are made responsible for this discrepancy, since the channel is formed within the first few nanometers of the semiconductor in contact with the dielectric. The effect of a secondary CuO phase on TFT properties was discussed one year after the presentation of the first Cu_2O-based TFTs.[20] These devices were annealed at 750 °C, which resulted in worse TFT properties. CuO was shown to introduce states below the Fermi energy with a density of $> 10^{20}\,cm^{-3}$, which pin the Fermi energy inside the band gap of Cu_2O. This secondary phase was detected under oxidizing conditions. Under reducing conditions, oxygen vacancies were assumed to cause Fermi level pinning. The assumption that oxygen vacancies cause the main donor state was based on results from photoluminescence

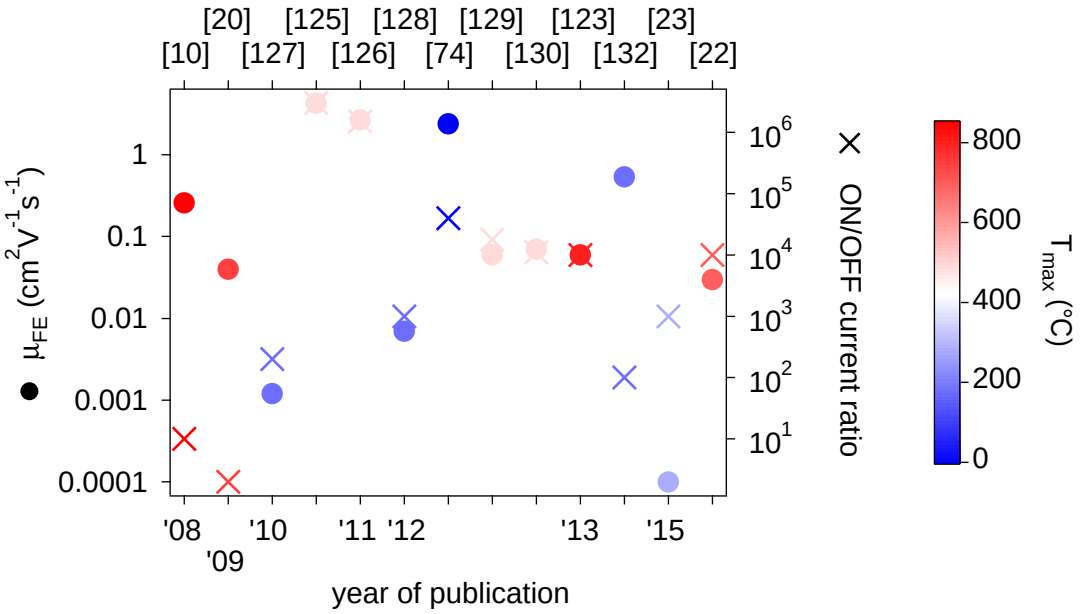

Figure 2.14: Overview on properties of Cu_2O TFTs by physical vapor deposition. Field-effect mobilities μ_{FE} and ON/OFF current ratios are plotted chronologically with respect to year of publication (starting in 2008) and reference number. The colors coding indicates the maximum substrate temperature during processing.

measurements.[19, 94]

Only two years after the first report, much improved properties could be achieved by PLD at lower temperatures (500 °C, top-gated as well as bottom-gated), omitting the need for epitaxial films.[125, 126] Starting also in 2010, first bottom-gated TFTs emerged, which were produced by a technique more widely used in industry – radio-frequency magnetron sputtering – and with a maximum post-deposition annealing temperature not exceeding 200 °C.[127, 128] As bottom-gate stack the layer sequence ITO/ATO was used. ITO is indium-tin oxide and ATO a commercially available nano-laminate structure of AlO_x and TiO_x, prepared by atomic layer deposition (ALD) at 500 °C. Other devices fabricated by magnetron sputtering but on Si/SiO_2 as bottom-gate stack showed higher μ_{FE} and ON/OFF ratios than the transistors made by the Fortunato group, but also needed higher annealing temperatures: A device based on a CuO film, which was converted to Cu_2O by annealing in vacuum at 500 °C is reported in 2012.[129] Later, devices with comparable performance were published, based on a similar fabrication process including the post-deposition annealing in vacuum, partially using rapid thermal annealing.[123, 130, 131] At low Cu_2O thicknesses, metallic copper was found after vacuum annealing.[129] The study of charge transport mechanism and sub-gap density of states employed a device which also exhibited metallic copper in the semiconducting channel material.[123] Multiple trap levels in accordance with the Meyer-Neldel rule where found in these devices. The likely existence of Fermi level pinning at the Cu_2O/Cu Schottky barriers and a corresponding depletion of the material was not commented by the respective authors.

From the device characteristics reported in the literature mentioned above it is clear, that an increased temperature during film deposition or post-deposition annealing usually leads to an increased structural order and a lower concentration of defects in thin Cu_2O films. The carrier mobilities and ON/OFF current ratios of the devices produced with a maximum temperature of 200 °C were lower than when higher temperatures were applied (≥ 500 °C). Despite the generally high temperatures during fabrication, it is possible to process the material completely at room temperature, if the right substrate dielectric is used: TFTs from Cu_2O deposited by sputtering on AlN exhibit a field-effect mobility of $2.4\,cm^2V^{-1}s^{-1}$ and an ON/OFF ratio of 4×10^4,[74] which is comparable to transistors processed at high temperature. Exploring rather uncommon dielectrics was further shown to be beneficial for TFT properties by sputter-deposition of Cu_2O on strontium titanate (STO).[132] In 2015, two articles have been published, which confirm the correlation of the use of temperature during fabrication with improved TFT properties.[22, 23] These devices were made by PLD on conventional SiO_2 dielectric substrates.

In the last few years, a number of reports on Cu_2O by cost-effective solution-based processes have been published.[133–135] Similar to physical vapor deposition, the device performance is enhanced when high deposition or annealing temperature is used. Among the best results are a mobility of $\mu_{FE} = 0.3\,cm^2V^{-1}s^{-1}$ and an ON/OFF ratio of 10^4 after post-deposition annealing in vacuum at 600 °C.[135]

CHAPTER 3

METHODOLOGY

The experimental procedures applied for the preparation of this thesis are described in this chapter. Section 3.1 addresses the techniques for thin film deposition. For electrical characterization and fabrication of TFT devices, the thin films had to be patterned, which is described in Section 3.2. At last, the analysis of the thin films is described in Section 3.3.

The experimental work has been carried out at two different institutes. Some techniques have been used only at one of them, whereas others were common to both. Table 3.1 shows how the experimental work has been divided between the involved universities. The techniques/processes which were used at both institutes (rRF-MS and shadow masks) inevitably had to use partly different parameters, which will be explained in detail

Table 3.1: The experimental techniques and processes are shown, ordered by the corresponding institute. UNL is Universidade NOVA de Lisboa and TU Darmstadt is Technische Universität Darmstadt. The following abbreviations have been used: rRF-MS – reactive radio-frequency magnetron sputtering, EBE – electron beam evaporation, ALD – atomic layer deposition, XPS – X-ray photoelectron spectroscopy, XRD – X-ray diffraction, SEM – scanning electron microscopy, EDS – energy-dispersive X-ray spectroscopy, AFM – atomic force microscopy.

	UNL	TU Darmstadt
deposition	rRF-MS EBE	rRF-MS ALD
patterning	shadow masks photolithography	shadow masks
analysis	electrical XRD SEM/EDS AFM	electrical (in situ) XPS (in situ)

in the respective subordinated sections. At TU Darmstadt, electrical and XPS analysis was carried out in situ by sample transfer in UHV conditions. Details on this procedure are explained in Section 3.3.2.

3.1 Thin film deposition

In this work, rRF-MS has been used for the deposition of the semiconducting copper oxide films. Samples for general thin film analysis as well as for fabrication of TFTs have been deposited by this technique. Furthermore at TU Darmstadt, Al_2O_3, Bi_2O_3 and gold electrical contacts were deposited by rRF-MS. Atomic layer deposition (ALD) has been used for deposition of Al_2O_3. Electron beam evaporation (EBE) was used at UNL for deposition of gold contacts for TFTs, involving a thin layer of nickel as adhesion promoter.

3.1.1 Reactive radio-frequency magnetron sputtering

Working principle

Reactive radio-frequency magnetron sputtering (rRF-MS) is a physical vapor deposition (PVD) technique for fabrication of thin films, which is widely used in industry for its capability of fast and reliable deposition on large areas. In research it is widely applied, since it offers a precise control over process parameters. Most information in this section has been adapted from the book *Materials science of thin films* by Ohring.[29]

Sputtering is a deposition technique, in which positive ions of sufficient kinetic energy are used to eject material from the surface of a *target*. A high electric field is used to create a plasma of a noble gas species (typically argon). The first observations of cathode erosion under such circumstances have been described by Grove, Faraday and Plücker in the mid-1850's.[136] The deposition in its simplest form consists of the subsequent condensation of the ejected material on a substrate surface. A direct current (DC) can be used to create the necessary electric field. High sputtering rates at relatively low power are achieved due to the acceleration of the argon ions towards the cathode surface. However, only conductive materials can be sputtered by this technique. The use of alternating current (AC) at radio frequency (13.56 MHz[1]) is a way to deposit also insulating and semiconducting materials by sputtering. The geometry of a typical magnetron sputtering system is schematically shown in Figure 3.1.

The sputter yield is the number of incident particles divided by the number of ejected particles. A metal usually has a higher sputter yield than the corresponding oxide, due to the ionic bonds in the oxide. Since the sputter yield of each element in a compound target is different, it may be assumed that there is no direct transfer of stoichiometry from target to substrate. Preferential sputtering of one of the elements may occur. However, by lowering the surface concentration of the preferentially sputtered element during

[1] 13.56 MHz has been reserved for plasma applications by the US Federal Communication Commission.

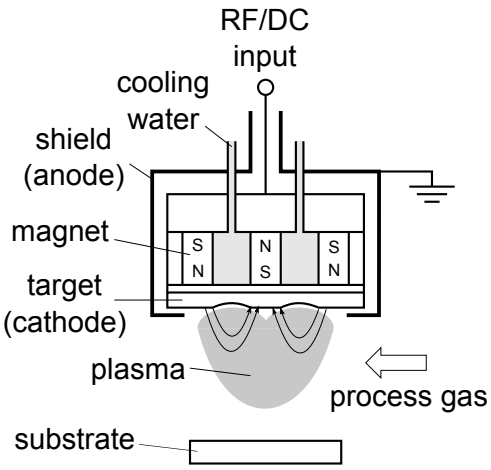

Figure 3.1: The assembly of a magnetron sputtering system is schematically shown. The arrows indicate the magnetic field lines. The figure was partially adapted from literature.[137]

target conditioning, a steady state on the target surface is reached at some point. Then the lower surface concentration compensates for the higher sputter yield of one of the elements and the stoichiometry is transfered to the substrate.[29] In practice, sputter deposition of an oxide target without the addition of a small amount of oxygen to the process gas may result in the growth of a rather oxygen deficient film. For example, an n-type transparent conductive oxide (TCO) will grow in a highly conductive state. To achieve a lower conductivity, oxygen may be added to the process gas, which is referred to as reactive sputtering and is described in the next paragraph.

In general, the introduction of reactive gas species to the process gas provokes chemical reactions in the plasma, which alter the deposited film with respect to the target material. For example, a metallic target may be sputtered while oxygen is added to the process gas in order to form an oxide. Since the reactive component becomes partially ionized by the plasma, the ejected metal particles react either with ions or neutral molecules of the reactive gas component. The partial pressure of the reactive component has strong impact on the stoichiometry of the resulting compound. A way to control this is the ratio of the volumetric gas flow rate in units of standard cubic centimeters per minute (sccm). Usually the flow of one component is expressed relative to the total gas flow. However, the relationship between the partial pressure of the reactive species and the gas flow ratio is not simply linear. This applies to metal and compound targets alike. Figure 3.2 schematically shows the relationship between partial pressure and gas flow of the reactive gas component. First the case of pure argon is discussed, which is shown by the broken

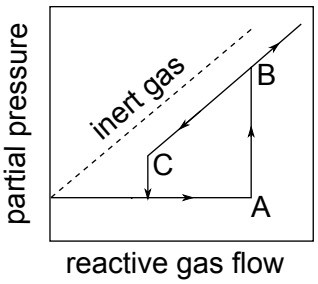

Figure 3.2: The relation between partial pressure and gas flow of a reactive gas component during sputtering is illustrated schematically. The broken line shows the case of an inert gas (after [29]).

line. An increase in gas flow results in a linear increase of pressure. It is a reversible process. If however the gas flow of a reactive component like oxygen is increased, its partial pressure does not increase immediately. The oxygen first reacts with the target surface and with the metal particles prior to film growth, forming the respective oxide. All reactive gas is consumed in the chemical reaction. This happens up to point A, at which all metal particles forming the deposited film are fully oxidized and the target surface oxidation has reached a steady state. Then the partial pressure increases drastically upon further increase of gas flow (point B). The target surface is now essentially an oxide. Due to the constant consumption of the reactive species to form the oxide film, the partial pressure remains however somewhat lower than in the case of an inert gas. When decreasing the reactive gas flow again, the partial pressure decreases linearly. This is due to a lower sputter yield obtained from the oxidized target surface compared to the metallic one. Consequently, less reactive species is consumed for the reaction. The target surface remains oxidized up to point C. A further decrease in gas flow reduces the target surface again and reverts the partial pressure back to the initial behavior.

The partial pressure of the reactive gas component determines the degree of oxidation of the deposited film. If the process is controlled by the gas flow ratio, special care needs to be taken to avoid unintentional results due to insufficient knowledge on the target oxidation state. With metallic targets, it is most convenient to choose to always approach the hysteresis region by a reduced target surface. Therefore, a sufficient target conditioning by pre-sputtering in pure argon is essential to obtain reproducible results.

Experimental conditions used in this work

Due to the hysteresis effect in reactive sputtering, the plasma was always ignited in pure argon atmosphere, followed by a conditioning step using the same parameters as in the subsequent film deposition. If the same process had been run before, 5 min of pre-sputtering was sufficient. If a different material had been sputtered in the same chamber, but from a different magnetron, 15 min of pre-sputtering was performed. If the chamber had been vented or if a process in strong oxidizing atmosphere had been run before, the target was sputtered in pure argon for another 15 min prior to roughly 45 min of pre-sputtering. This procedure was applied at both institutes.

At UNL, a commercial ATC Orion 8 stand-alone UHV sputtering system by AJA International was used. A schematic representation is given in Figure 3.3. The system combined three confocal 2 inch (diameter, 5.08 cm) sputtering sources with a rotating substrate holder. Each sources provided an individual shutter and an extended anode ring, resembling a chimney, in order to avoid cross-contamination between the sources. The base pressure of the chamber was in the upper 10^{-8} mbar range. The pressure was monitored by a capacitive gauge for $> 10^{-4}$ mbar and a cold-cathode ionization gauge for lower values. There were gas inlets for argon at the source, whereas the reactive component oxygen was introduced through a separate inlet on the chamber side wall.

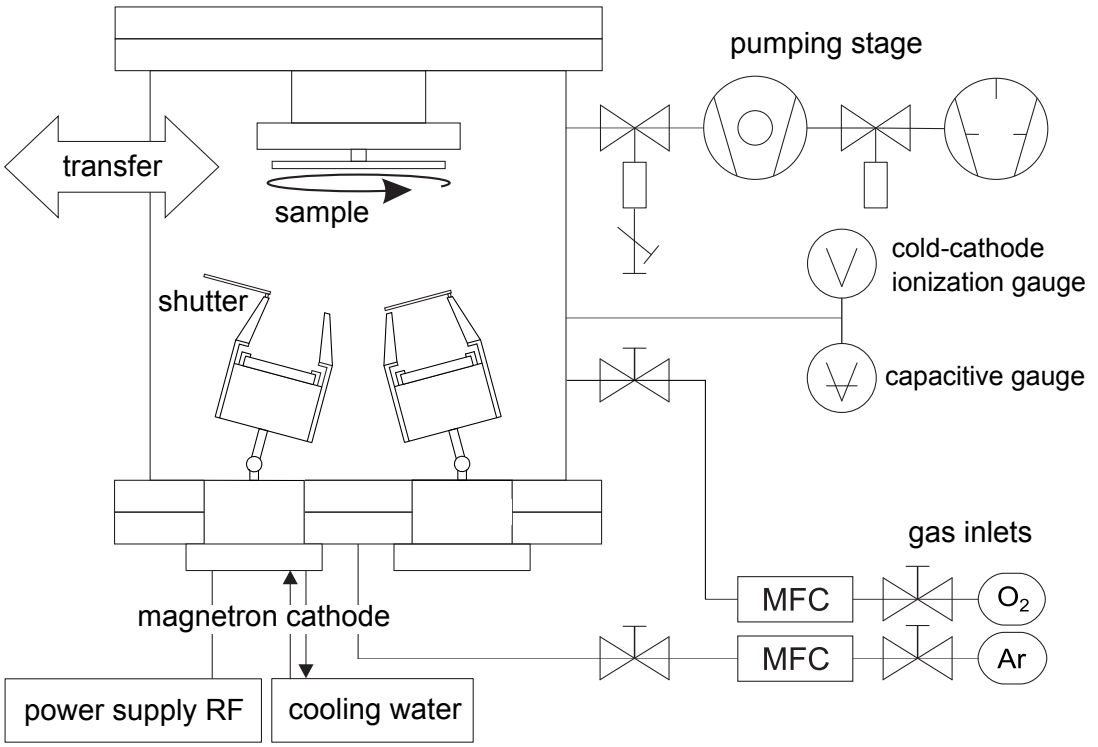

Figure 3.3: Schematic representation of the sputtering chamber at UNL. The layout was adapted from previous works.[138, 139]

The gas flow was controlled by mass flow controllers (MFC) with a maximum range of 20 sccm. The substrate was top-mounted and the holder was equipped with a radiative heater on the back of the substrate support. Substrate sizes up to $10 \times 10\,\mathrm{cm}^2$ were supported. The system was equipped with a load lock and most of its functions could be controlled by a computer. Pre-sputtering (target conditioning) was done with a closed shutter.

At TU Darmstadt, a custom-made sputtering chamber was used, which was connected to the DAISY-MAT cluster tool by a UHV transfer stage (see Figure 3.13). A schematic representation is given in Figure 3.4. It was equipped with four top-down 2 inch sputtering sources by the company Thin Film Consulting. The base pressure of the chamber was in the upper 10^{-8} mbar range. The pressure was monitored by a capacitive gauge for $> 10^{-4}$ mbar and a cold-cathode ionization gauge for lower values. There were gas inlets at each source and one at the chamber side wall for the reactive gas species. It was possible to choose whether the reactive gas should be introduced separately or directly at the source together with argon. For the sake of a compact graphical representation, the reactive gas inlet is drawn on the same chamber side as the pumping stage in Figure 3.4, although it was actually located opposite to the pumping stage to allow a reasonable spatial distribution of the reactive gas component. The gas flow was controlled by mass flow controllers with a maximum range of 20 sccm. In addition to oxygen, a mixture of 90 %

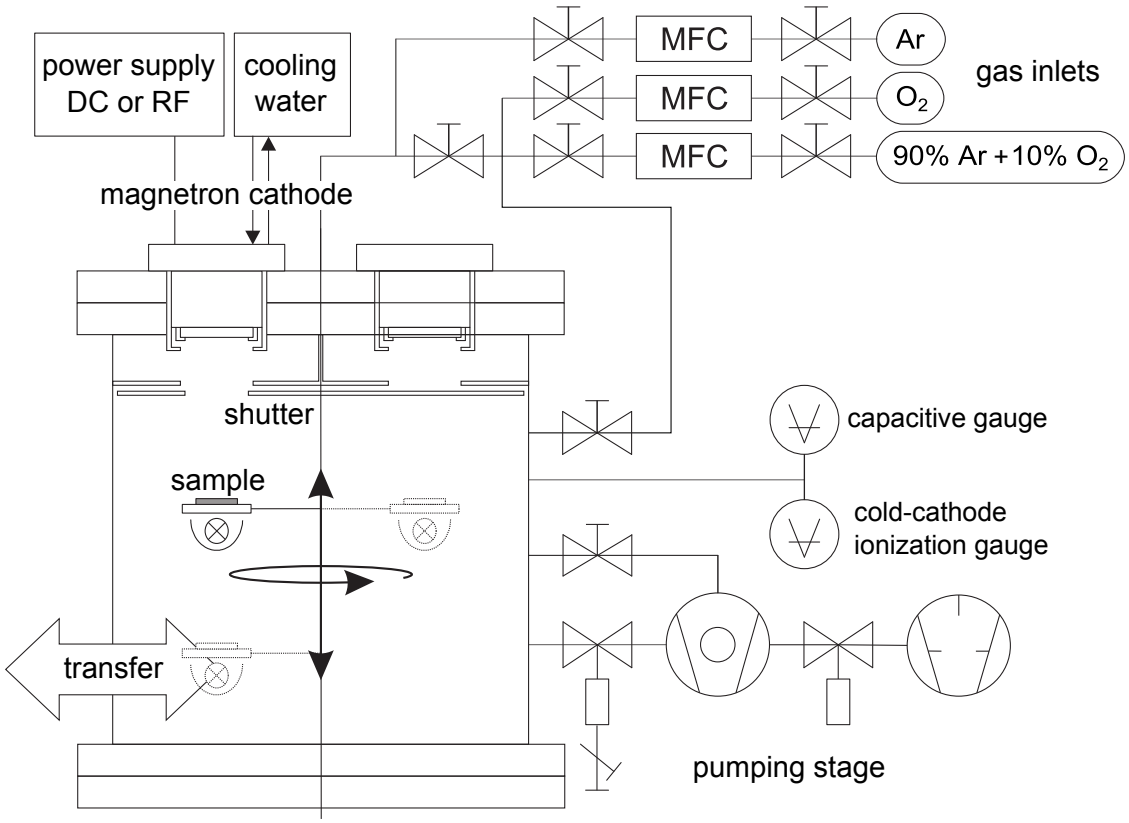

Figure 3.4: Schematic representation of the sputtering chamber at TU Darmstadt, adapted from previous works.[138, 139]

argon with 10 % oxygen was available to gain a more precise control when low amounts of oxygen were required. The sample holder was capable of a maximum substrate size of $2.5 \times 2.5\,\mathrm{cm}^2$, with a halogen light bulb installed below the substrate holder for sample heating. After introduction of the sample into the chamber, it was brought to the height of deposition and rotated out of the line of sight of the magnetron cathode. Pre-sputtering (target condictioning) was then done with an open shutter, to avoid particles from falling onto the substrate by vibrations introduced by the rotation of the shutter. To start and stop the deposition, the substrate was rotated below and away from the area below the magnetron, respectively.

The deposition parameters for both sputtering systems are summarized in Table 3.2. For the deposition of electrical contacts at TU Darmstadt, the commercial sputter coater Q300T D of the company Quorum was used. Thin gold films were deposited by direct current sputtering up to a thickness of at least 100 nm. Shadow masks were used for patterning.

3.1.2 Atomic layer deposition

Atomic layer deposition is a chemical vapor deposition (CVD) technique, which in an idealized picture grows inorganic thin films monolayer by monolayer. It is based on

Table 3.2: Conditions for sputter-deposition at UNL and TU Darmstadt (AMT: Alineason Materials Technology).

	UNL	TU Darmstadt			
material	Cu_2O	Cu_2O	CuO	Al_2O_3	Bi_2O_3
target	Cu	Cu		Al	Bi
target purity (%)	99.99	99.999		99.9995	99.99
manufacturer	Plasmaterials	Kurt Lesker			AMT
temperature	RT	RT	RT	RT	RT
RF power (W)	50	25	25	40	15
RF power density ($W\,inch^2$)	5.06	2.53	2.53	4.05	1.52
pressure ($mbar \times 10^{-3}$)	5	5	5	5	5
gas flow ratio (%)	3.3-5.0	3.7-4.3	10	15	10
target-substrate (cm)	16.6	9	7	9	9
deposition rate ($nm\,min^{-1}$)	2.4-2.8	6.2-8.5	12.2	0.26	14

self-terminated chemical surface reactions of precursors, which are individually brought into contact with the substrate or the growing film. The highly conformal coverage even on rough substrates is an advantage for the deposition of electrically insulating layers, such as the dielectric in a TFT.[140] The possibility to grow dense films of $\leq$ 1 nm thickness made this technique favorable for the incorporation of buffer layers in photovoltaics[141] and more recently for the fabrication of resistive memory devices.[142, 143] A comprehensive compilation of its manifold applications is available in literature and shows the relevance to many different fields of technology.[144]

The first published works on this technique date back to a contribution by Shevyakov et al. in 1965[145] and a patent by Suntola from 1977.[146] In the 1990s, the scientific interest started to grow significantly, which is an ongoing trend still today. A typical and extensively studied process is the deposition of Al_2O_3 by ALD from the precursors trimethylaluminum (TMA) and water, which will be discussed here to explain the working principle. Most of the information in this section has been taken from the review on Al_2O_3 by ALD by Puurunen.[147]

Working principle

In order to explain the mechanisms of ALD, a schematic representation is given in Figure 3.5. In the initial stage, the substrate surface should ideally be terminated by hydroxyl groups (–OH). The presence of oxygen at the surface may be intrinsic to the substrate in case of an oxide or has to be induced by adequate surface treatment. Prior to the deposition, the substrate is brought to a temperature, which provides enough energy to overcome the activation enthalpy for adsorption. At the same time it should not provoke thermal decomposition of any of the involved materials, including the precursors.[147] The substrate is either kept in vacuum or under an inert gas flow, for example of nitrogen, in order to avoid a reaction of the precursors in the gas phase rather than on the surface.

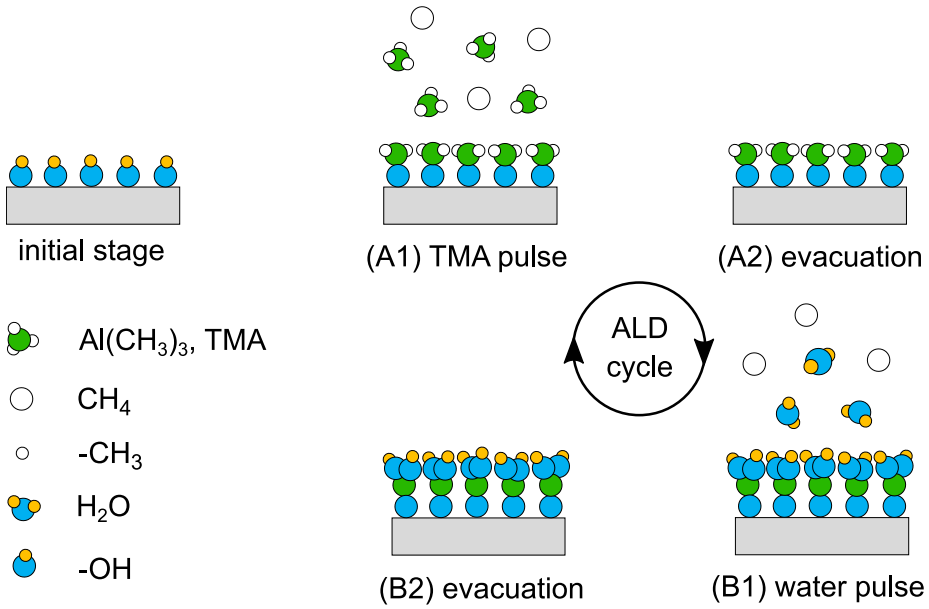

Figure 3.5: A schematic representation of the ALD process is shown. (A) represents the first half-cycle and (B) the second one. The layout of the figure has been inspired to a large extent by a PhD thesis from TU Darmstadt.[148]

The first step of an ALD cycle for Al_2O_3 deposition comprises an introduction of a controlled amount of TMA. The chemical reaction taking place on the surface is given in Equation 3.1 and is schematically shown in Figure 3.5 (A1). The symbol || represents the solid surface of the sample.

$$||\text{–O–H} + \text{Al(CH}_3)_3 \longrightarrow ||\text{–O–Al(CH}_3)_2 + \text{CH}_4\uparrow \tag{3.1}$$

The amount of adsorbed TMA molecules depends on the available hydroxyl groups on the surface. Once the adsorption is irreversibly saturated, no further reaction occurs. This is referred to as a *self-terminated* reaction, which is one of the prerequisites for a substance to work as an ALD precursor.[144] To conclude the first half-cycle, remaining precursor material as well as the by-product methane are removed from the chamber by purging with an inert gas or evacuation of the chamber, as shown in Figure 3.5 (A2).

The second half-cycle initiates with the introduction of water to the chamber. The following reaction occurs, which in Figure 3.5 is step (B1):

$$||\text{–O–Al(CH}_3)_2 + 2\,\text{H}_2\text{O} \longrightarrow ||\text{–O–Al(OH)}_2 + 2\,\text{CH}_4\uparrow \tag{3.2}$$

The remaining methyl groups react with water to form the by-product methane and leave the surface terminated by hydroxyl groups again. Subsequently, by-products and remaining precursor molecules are removed from the chamber again by purging/evacuation (see Figure 3.5 (B2)). This completes the full ALD cycle, resulting in a monolayer of Al_2O_3, according to the theory. However, the availability of surface sites is limited by steric hindrance of the involved molecules. Consequently during one ALD

cycle, typically less than one monolayer is deposited.[147] The pulse times need to be carefully calibrated to ensure a complete surface coverage without loading the pumping stage with too much precursor material. The same applies to the purge/evacuation time, during which all remaining precursor needs to be removed before the subsequent pulse.[149]

Provided there is a uniform availability of hydroxyl groups on the surface, the chemical nature of the adsorption process ensures a uniform coverage after each cycle even on structures of high aspect-ratio.[150] The uniformity is guaranteed once the cycles simply reproduce Al_2O_3 on top of a closed Al_2O_3 surface. Then, a typical *growth per cycle* (GPC) of $\approx 0.09\,\text{nm/cycle}$ is achieved by this process.[147, 151, 152] In the initial steps however, before a closed film of Al_2O_3 is deposited, there might be strong changes to the GPC, which depend essentially on the availability of adsorption sites on the surface:[147] A *surface-inhibited initial growth* is observed when the availability of adsorption sites is lower on the substrate material, than for the material grown by ALD, which can be related to the amount of hydroxyl groups at the substrate surface, as mentioned above. A *surface-enhanced initial growth* occurs, when there are more adsorption sites available on the substrate surface than on the film grown by ALD. These terminologies have been developed for substrates which do not react with either of the ALD precursors, except through the hydroxyl groups at the surface.[153]

If additional reactions with the substrate occur, the initial growth may be increased due to oxygen which diffuses from the substrate to the film surface. As long as the ALD film is not dense enough to inhibit oxygen diffusion during the first cycles, additional adsorption sites are provided.[152, 154, 155] Such an extraction of oxygen from the substrate can lead to a reduction of the substrate material. On GaAs, this phenomenon is referred to as "self-cleaning" and describes the reduction of a native oxide surface layer.[156] Some oxide surfaces which have been reported to be reduced by the precursor TMA are CuO, thin Cu_2O on Cu, RuO_2, indium tin oxide (ITO) and Fe_2O_3.[152, 154, 155, 157, 158]

Experimental conditions used in this work

The ALD chamber used in this work was part of the DAISY-MAT system at TU Darmstadt. It was a custom-made chamber which had been planned and set up during the diploma thesis of Thorsten Bayer.[149]. Due to the integration into a UHV system, the removal of the precursor after each pulse was accomplished by evacuation via a turbo molecular pump. The base pressure of the deposition chamber was $10^{-8}\,\text{mbar}$. The optimized substrate temperature for this system was found to be 200 °C. Lower temperatures resulted in a relatively high amount of carbon in the films, which were ascribed to an incomplete reaction of the TMA precursor.[149] During the temperature calibration, a substrate of glass coated with indium tin oxide (ITO) was used. The enhancement of the growth for the initial cycles, which was observed on this substrate, was significantly higher at 300 °C

than at 200 °C.[152]

The amount of TMA and water was controlled by setting the pulse length of two individual ALD 3 series valves by Swagelok. Electronic grade TMA was purchased from SAFC Hitech. To achieve highest purities of the water precursor, Millipore water was evaporated and condensed several times in alternate arms of a double arm glass vessel. A hair dryer and dry ice was used for this procedure. The pulse length for TMA was set to 80 ms and for water to 150 ms, the evacuation time between pulses was set to 5 min, which reduced the pressure down to 4×10^{-6} mbar. These values were taken from the already mentioned previous works on the deposition process.[149, 152]. Prior to deposition, the substrate was brought to the deposition temperature of 200 °C by radiative heating from the backside of the substrate holder. The deposition parameters are summarized in Table 3.3.

Table 3.3: Overview on the conditions for atomic layer deposition.

substrate temperature (°C)	200
TMA pulse time (ms)	80
evacuation (min)	5
water pulse time (ms)	150
evacuation (min)	5
base pressure (mbar)	10^{-8}
pressure between pulses (mbar)	4×10^{-6}

3.1.3 Electron beam evaporation

Electron beam evaporation carried out at UNL to deposit top-contacts for TFT fabrication and for other electrical characterization, which is described in Section 3.3.3.

Working principle

The deposition by evaporation is a vacuum process, which comprises the evaporation of a material from a heated crucible and the subsequent condensation on a substrate at a certain distance. Conventionally, the source is heated electrically by resistive heating. As an alternative, a focused electron beam may be used, as it has been the case in this work. The advantages over evaporation from a resistively heated crucible are a higher input power and less contamination from the crucible and heater parts, since the crucible itself is water-cooled is this case.[29] Electrons are generated by thermionic emission from a filament. To avoid the deposition of evaporated material on the electron source, it is located next to the crucible and slightly below it. The electron beam is then deflected by magnetic lenses and focused on the material to be evaporated. A shutter is placed between the evaporation source and the substrate to ensure uniform conditions throughout the whole duration of the deposition.

Experimental conditions used in this work

The base pressure of the system at UNL was 10^{-5}–10^{-6} mbar. It used an electron acceleration voltage of 6 keV. The current was controlled to achieve a deposition rate of ≈ 0.2 nm/s. Gold was deposited to form an Ohmic contact to Cu_2O.[159]. However, since the adhesion of gold on most inorganic substrates is rather poor, a 5 nm thick layer of nickel was always deposited prior to gold, without interrupting the vacuum conditions between the depositions. The thickness was controlled by a crystal oscillator film thickness monitor. For the fabrication of TFTs, top-contacts of ≈ 100 nm were deposited and subsequently patterned by lift-off (see Section 3.2.1). For other electrical characterization and in case the pattering could be conducted by shadow masks, the gold thickness was occasionally higher.

3.1.4 General substrate cleaning

The substrate cleaning procedure was general for depositions at UNL and TU Darmstadt. The main objective was to remove organic contaminants from the surface. The first step was an ultrasonic bath in acetone for 10 min. After a short rinse with fresh acetone when taking the substrate out of the solvent, it was put into an ultrasonic bath of isopropyl alcohol for another 10 min. The main objective of this second step was to remove acetone, which otherwise may have remained on the substrate surface. After this, the substrate was again rinsed with fresh isopropyl alcohol upon taking it out of the bath and subsequently thoroughly rinsed in deionized water. Immediately after, the substrate was blown dry with pressurized nitrogen.

3.2 Thin film pattering

For electrical thin film characterization, the fabrication of certain structures is required, which allow for an electrical contact to the semiconductor and the application of electrical fields in a well defined geometry. This is mostly accomplished by the use of shadow masks. This patterning approach has the advantage that it is easy to handle and does not involve chemicals, which may attack certain materials in the sample. However, geometric design limitations exist due to the nature of the mask being one piece of solid material. Furthermore, the feature size is limited to ≈ 200 µm, which is to a large extend due to shadowing effects during deposition: There is always an unavoidable gap between mask and substrate due to the mechanic nature of the process. Since the incident angle of particles on the substrate during a vapor-based deposition is never exclusively 90° to the surface, there is always some material deposited in the areas which should be covered by the mask. If smaller feature sizes are required, photolithography (PL) can be used, enabling a minimum feature size of 2 µm. In order to be pattered by photolithography, a sample needs to be inert towards the involved chemicals and methods are required to selectively remove parts of the film from the substrate.

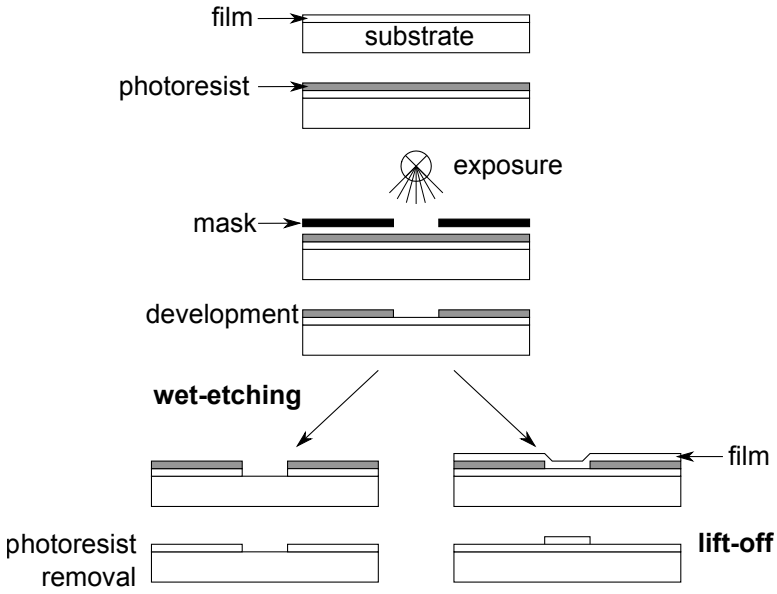

Figure 3.6: Photolithography process steps.

3.2.1 Pattering of common-gate TFTs by photolithography

A common-gate TFT is a device in which the gate electrode and dielectric cover the complete surface of the sample. Only the channel and the source and drain are individualized (i.e. patterned). The disadvantage of such devices is a higher gate leakage current and parasitic capacitance due to the large contact overlap area with respect to the channel area. The advantages lie in the shortened sample production process and the possibility to use commercially available bottom-gate substrates. The latter was the decisive factor to use common-gate substrates, since this work was not focused on the optimization of the gate dielectric and high quality materials could be used.

As a bottom-gate stack, the layer sequence ITO/ATO was used, where ITO is indium-tin oxide and ATO a commercially available nano-laminate structure of AlO_x and TiO_x, prepared by atomic layer deposition (ALD) at 500 °C. The substrates were supplied by Benq, formerly Planar Systems. The thickness of the dielectric was 250 nm. In order to access the gate electrode on these substrates, a small area of ATO could be removed by dissolving the amphoteric Al_2O_3 in a saturated solution of NaOH in water at around 80 °C. Other devices were fabricated on n-type silicon with a thermal SiO_2 layer of 100 nm. In this case, access to the gate electrode was provided through the backside of the wafer, placed on a conductive surface.

The channel layer as well as source and drain electrodes of TFTs in this work were patterned by photolithography (PL). This process involved the application of a chemical mask of thin photoresist onto the material surface, which was illuminated in selected areas and subsequently developed to expose parts of the underlying surface. The process steps are illustrated in Figure 3.6 (a). Most of the information described here was taken from a booklet by the company MicroChemicals, which provides all necessary

chemicals for PL.[160] The positive photoresist used in this work was the AZ 6632 by the same company. The resin is a cresol, synthesized from phenol and formaldehyde. The solvent was propylene-glycol-mono-methyl-ether-acetate (PGMEA). It is a photoresist optimized for dry-etching with an increased softening point of $\approx 130\,^{\circ}\mathrm{C}$, allowing for steep sidewalls after baking. However, it accepts a broad window of process parameters and is thus usable for wet-etching and lift-off, as well. The resist was applied on the sample surface by spin-coating, resulting in a typical thickness of 3.2 µm. At this point, it still contained 10–35 % solvent, which was reduced in a subsequent soft-bake step at $\approx 110\,^{\circ}\mathrm{C}$. Then the sample was introduced into a Karl-Suss MA6 mask aligner. If the sample already contained structures from previous patterning steps, alignment marks existed which helped to align the subsequent patterns to the already existing ones. Exposure through the chromium-coated glass mask was done with UV light from a mercury lamp. The sensitivity of the photoresist was matched to the emission spectrum of the lamp. The photoactive compound in the resist was DiazoNaphtoQuinone-sulfonate (DNQ-sulfonate). Upon exposure, it looses a nitrogen molecule and reacts with water to form a carboxylic acid. This acid has a significantly increased alkaline solubility over the non-exposed photoresist. Consequently, when the exposed sample was developed in a tetramethylammonium hydroxide containing solution of pH = 13 (AZ 726 MIF)[2] for a few seconds, the exposed areas of the photoresist were dissolved, while the unexposed areas remained. This concludes the patterning of the photoresist.

The channel material was structured by wet-etching in diluted hydrochloric acid ($HCl/H_2O = 1/70$) and using distilled water as etch-stopper.[161] The areas which were not supposed to be attacked by the acid were the one which had been covered with photoresist prior to the etching. After complete etching, the remaining photoresist was dissolved in acetone.

The source and drain electrodes were patterned by *lift-off*. Here, the photoresist was applied and patterned before layers of 5 nm nickel and 55 nm gold were deposited by electron beam evaporation. To initiate the lift-off process, the sample was then immersed in acetone for approximately 2 h. In this way, all the photoresist was dissolved, including the area below the gold layer. By a careful application of ultrasonic treatment, occasionally with the aid of a soft manual brush, this layer was detached from the sample surface. In order to prevent gold particles floating in the solution from sticking to the sample surface when removed from the acetone, a second acetone bath followed, as well as two baths of isopropyl alcohol and rinsing in distilled water with subsequent blowing-off with nitrogen, similar to the general substrate cleaning procedure.

The schematic cross-sectional view of the TFT structure is given in figure. 2.3. In Figure 3.7, the source-drain electrode and channel layout is shown by a photograph from an optical microscope. It includes two common-gate structures with channel width-to-length ratios of 160/160 and 80/80 (in µm). These are examples for the largest channel

[2]Safety data sheet of AZ 726 MIF Developer in accordance with 2001/58/EC, substance key SXR054682, version 1–6/EU

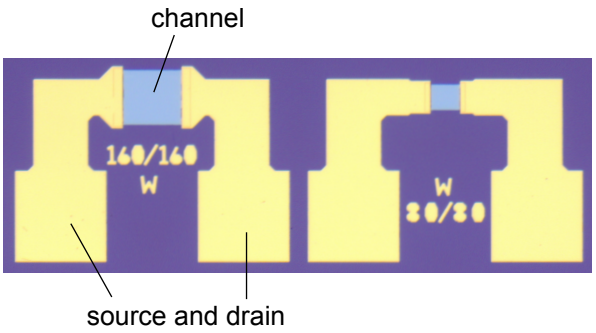

Figure 3.7: Example of TFT layout from optical microscopy.

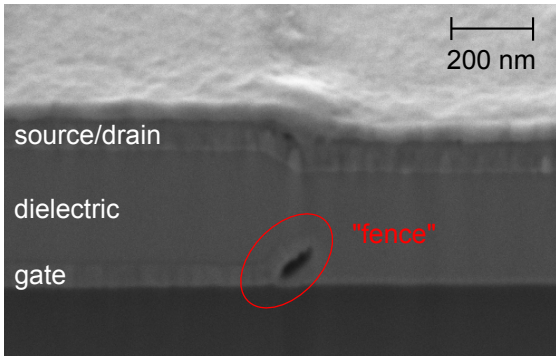

Figure 3.8: SEM-FIB cross-section of a TFT with patterned gate electrode. "Fences" appear on the edges of the gate layer due to the lift-off process. The image was kindly provided by Asal Kiazadeh and Daniela Nunes.

geometries possible with the PL masks. Both channel width and length can theoretically reach 2 µm. However, the not fully optimized fabrication process limits the lowest achievable channel dimension to about 5 µm.

A typical problem encountered after lift-off is the development of "fences" on the sidewalls of the deposited film.[160] This is film material, which has not been detached from the patterned layer and has been bent up during lift-off. An example of this is shown by an SEM cross-section cut by focused ion beam (FIB). The problem is minimized, when film deposition on the resist sidewalls is prevented. A unidirectional deposition is beneficial in this respect (like evaporation rather than sputtering) as well as steep sidewalls, which is one of the characteristics of the photoresist AZ 6632. However, possibly higher temperatures than the softening point at 130 °C are reached at the sample surface during deposition by electron beam evaporation. Furthermore, gold is a rather ductile metal, which may cause material at the sidewalls to bend rather than break during lift-off.

3.3 Thin film analysis

The analysis of thin films deposited during the preparation of this thesis had the objective to provide the basis for a discussion of electrical device properties. Some of the applied analysis techniques are sensitive to bulk properties (XRD, EDS, Hall effect measurement), whereas others probe the sample surface (XPS, SEM, AFM). The properties of a TFT may be dominated by interface effects, however the bulk properties of a material define the boundaries for what is feasible on a device level. Special attention is drawn to the method

of in situ XPS, which allows to obtain thickness-dependent spectroscopic data without the drawbacks of conventional sputter depth profiling (e.g. preferential sputtering of compounds) or the limited available range of angle resolved XPS. Finally, the incorporation of conductance measurement into the in situ XPS analysis provides the necessary link between electronic and chemical information from XPS and electrical properties. This allows for the sound interpretation of interface effects, such as energy band alignment or chemical reactions between substrate and the growing film, which are of actual relevance for device characteristics.

3.3.1 Photoelectron spectroscopy

Photoelectron spectroscopy is a technique in which light of a certain energy is used to excite the electrons of a material. When the excitation energy is high enough, the *photoelectric effect* is induced, which has been first observed by Hertz in 1887 and later been described by Einstein in 1905.[162, 163] Due to the atomic orbitals, electrons have discrete[3] binding energies in a solid, as has been described in Section 2. The number of emitted electrons is detected with respect to their kinetic energy, which is dependent on their binding energy. The spectroscopic use of the photoelectric effect has first been reported by Siegbahn in 1956.[164] At that time, the technique was referred to as *electron spectroscopy for chemical analysis* (ESCA) for the ability to distinguish between elements and their oxidation states by characteristic sets of binding energies. The detection limit of XPS is 0.1–1 at.%.[29] However, since the binding energy can also be referenced to the Fermi energy, spectroscopic information can be related to electronic properties such as carrier concentration in a material. For this reason, the more general term photoelectron spectroscopy is widely used today.

Instrumentation

X-rays provide sufficient energy to excite electrons from core levels. The method is referred to as X-ray photoelectron spectroscopy (XPS). Valence electrons are probed with a higher intensity and higher energy resolution if ultraviolet light is used for excitation, which is then referred to as ultraviolet photoelectron spectroscopy (UPS). However, core levels cannot be probed by UPS and the information depth d_i is reduced with respect to XPS. This is related to the mean free path of electrons λ_e in a solid, which is mainly limited by inelastic scattering and depends on the kinetic energy $E_\mathrm{kin} \leq h\nu$. The mean free path λ_e reaches a minimum value of $\approx 4\,\mathrm{nm}$ for kinetic energies of ≈ 10–$100\,\mathrm{eV}$, which corresponds to the ultraviolet region, and increases both for lower and higher energies, with a more pronounced increase at lower energies. At low energies ($< 5\,\mathrm{eV}$), electrons scatter mainly at phonons and at high energies electron-electron scattering limits λ_e.[165] A typical X-ray source uses the Kα emission of an aluminum anode with a photon energy

[3] There is in fact a finite natural line width associated to each energy level, which is explained in more detail further in this section.

of 1486.6 eV. At kinetic energies corresponding to a binding energy range of 0–1000 eV, λ_e in inorganic compounds lies between 4–2 nm.[166] A rather detailed description of the mean free path of photoelectrons and the relation to information depth has been given by Mirko Weidner in his PhD thesis.[167] Further considerations on this topic will be given in Section 3.3.1 on the photoelectron intensity.

Ultrahigh vacuum conditions with a pressure in the order of 10^{-10} mbar are required for common photoelectron spectrometers. On the one hand, this reduces scattering of low energy photoelectrons at gaseous species in the space between the sample surface and the detector. On the other hand, the adsorption of molecules on the surface is greatly reduced at UHV, compared to higher pressures. This is essential to keep the number and type of adsorbates at the sample surface constant throughout the measurement. Samples which have been introduced into the analysis chamber from an air atmosphere and are not cleaned prior to the measurement, unavoidably are covered with contaminants like hydrocarbyl groups and water. For this reason, some spectrometers are equipped with a preparation chamber to allow annealing in controlled atmospheres in order to remove surface contaminants. The surface of elemental samples can be easily cleaned by the irradiation with argon ions of a few keV from a sputter gun, incorporated into most modern spectrometers. An in situ measurement of a sample deposited by a vacuum-based process however is only possible when a transfer from preparation chamber to analysis chamber in UHV is provided.

The analyzer of a photoelectron spectrometer is commonly a concentric hemispherical analyzer, consisting of two hemispheres of different radii, which are kept at different electrical potentials. An electron entering through the entrance slit is deflected on its way trough the space between the hemispheres according to its kinetic energy. After passing the exit slit, the electrons are counted by one or multiple channeltron(s). The energy resolution of the analyzer is dependent on the kinetic energy of the electron. In order to measure with a constant energy resolution throughout the whole kinetic energy range, the electrons are retarded to a constant pass energy at the entrance slit to the analyzer, while the potentials of both hemispheres are kept constant. A scan of all kinetic energies is possible by varying the retardation voltage at the entrance slit. With a trade-off between intensity and energy resolution, higher pass energies allow for higher count rates, whereas lower pass energies increase the energy resolution.

Other important factors influencing the energy resolution of the spectrum are the natural line width of the X-ray source and the natural line width of the orbital form which photoemission occurs. The line widths of common X-ray sources range from 0.5 to 1.7 eV.[168] If intensity is not crucial, the use of a monochromator between source and sample can reduce the line width significantly. For example, the line width of Al Kα is reduced from 0.85 eV to 0.26 eV upon monochromatization, involving a decrease in intensity by a factor of 40.[169]. The natural line width of emission from an orbital however cannot be influenced. The Heisenberg uncertainty principle demands, that the product of

energy and time is at least $\hbar/2$.[4][30] The photohole state of core levels is generally rather short-lived, compared to valence states.[165] Ag $3d_{5/2}$ for example exhibits a natural line width of 0.35 eV.[170]. The line width of valence states in gaseous species are an order of magnitude lower. In solids however, the eventual overlap of valance state leads to a broadening of energy levels due to the Pauli exclusion principle.[31]

Due to the limited mean free path of electrons, a variation of the emission angle with respect to the sample surface θ provides a way to enhance emissions originating from the surface without a variation of excitation energy. The information depth scales approximately with $\sin\theta$.[171] Eventual surface contributions are minimized at $\theta = 90°$ and increase with lower angles. Angle resolved measurements are commonly incorporated by the possibility to tilt the sample stage.

The principle of photoelectron spectroscopy

The fundamentals of photoelectron spectroscopy are explained in reference to the supporting schematic representation in Figure 3.9. In this example, a solid semiconducting sample shall be measured. Figure 3.9 (a) shows the photoelectric effect. The excitation energy is constant and the kinetic energy of photoelectrons E_{kin} depends on their binding energy in the material E_{B}. E_{B} may be defined with respect to the vacuum level E_{vac}. However in photoelectron spectroscopy, a reference to the Fermi energy is common. This is due to the possibly different work functions of the sample Φ_{sample} and the instrument $\Phi_{\mathrm{instrument}}$. In thermodynamic equilibrium however the Fermi energy of sample and the instrument are the same. Since the energy is measured inside the instrument (Figure 3.9 (b)), the binding energy is related to $\Phi_{\mathrm{instrument}}$ and not Φ_{sample} according to Equation 3.3.

$$E_{\mathrm{B}} = h\nu - E_{\mathrm{kin}} - \Phi_{\mathrm{instrument}} \tag{3.3}$$

The detector of a photoelectron spectrometer counts the electrons of a certain kinetic energy. A scan through different energies allows the representation of the data as a spectrum, as shown in Figure 3.9 (b) and (c). In order to understand the relation between the material energy levels and the spectrum, the excitation energy $h\nu$ (the blue arrow) may be imagined to be shifted up and down in the representations (a) and (b). As the common reference, the binding energy of the Fermi energy is defined as $E_{\mathrm{F}} = 0$ and appears at the origin of the photoelectron spectrum. Since the example shows a semiconductor, there are no electronic states at the Fermi energy. By moving the blue arrow $h\nu$ downwards (i.e. by decreasing the detected kinetic energy to access signals from higher binding energies), occupied electronic states are encountered at the valence band maximum E_{VB}. Consequently, an intensity of photoelectrons is detected in the spectrum, which arises from delocalized states due to the solid state of the sample. The valence band maximum can be estimated by a linear extrapolation towards high kinetic/low binding energy.[172]

[4] $\hbar$ is the Planck constant h divided by 2π.

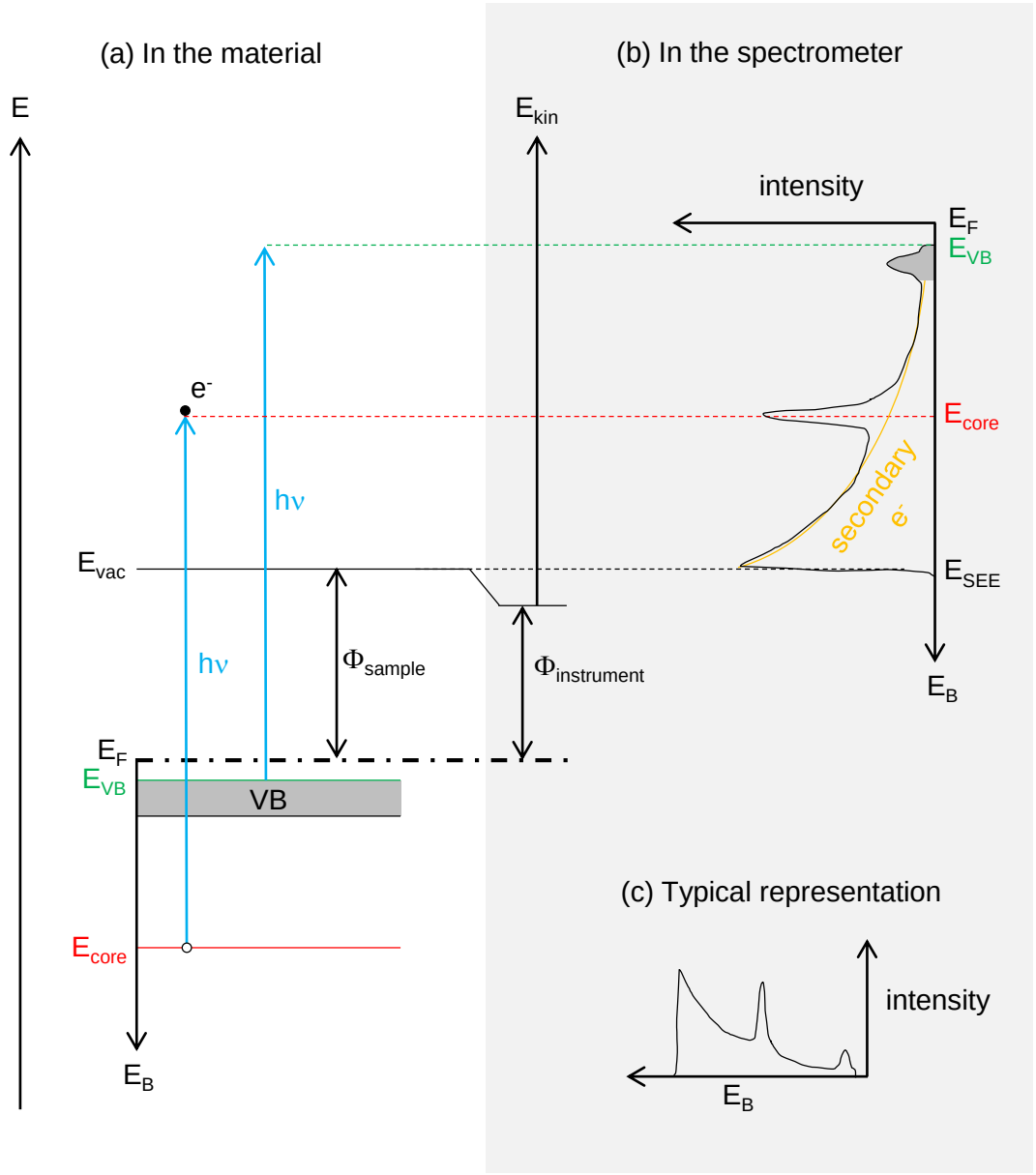

Figure 3.9: It is schematically illustrated (a) how energy levels in a material give rise to a kinetic energy of photoelectrons, (b) how this kinetic energy is translated into an intensity with respect to the electron binding energy, which is (c) the typical representation of data from photoelectron spectroscopy. Note, that core level measurements and the secondary electron edges are show in the same representation, though such data is typically obtained using different excitation energies (XPS and UPS, respectively).

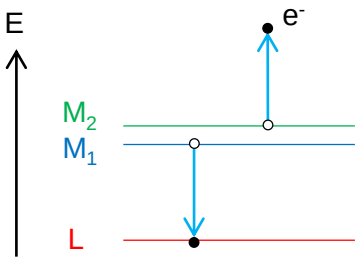

Figure 3.10: The emission of an LM_1M_2 Auger electron is schematically shown.

Towards lower kinetic energies, additional peaks appear in the spectrum corresponding to electrons emitted from more localized occupied electronic states, which are referred to as core levels. The electrons from a core level, shown in red, result in a rather sharp emission line associated to a characteristic binding energy. However, even without peaks due to photoemission, the electron intensity continuously increases towards lower kinetic energy due to the emission of secondary (i.e. inelastically scattered) electrons. Their contribution to the total intensity is referred to as the background of the photoelectron spectrum and is schematically represented by the yellow line in Figure 3.9 (b). At the point where $E_{\text{kin}} = \Phi_{\text{instrument}} - \Phi_{\text{sample}}$, photoelectrons do not have sufficient kinetic energy anymore to leave the sample surface. Consequently, the intensity drops sharply at an energy E_{SEE} referred to as the *secondary electron edge*. Φ_{sample} can be determined from this value according to Equation 3.4.

$$\Phi_{\text{sample}} = h\nu - E_{\text{SEE}} \tag{3.4}$$

It should be noted, that the secondary electron edge can only be detected when $h\nu - \Phi_{\text{sample}}$ is smaller than the maximum energy range of the detector. In general, UPS is used to determine the work function and a small negative bias is applied to the sample to facilitate the extraction of the electrons with $E_{\text{kin}} = 0$ from the sample surface.

The relaxation from the excited state after photoemission back to the ground state involves the filling of the photo hole with an electron. This electron can originate from a state higher in energy. The energy the electron emits when falling into a lower state is either emitted as a fluorescent X-ray photon or is transfered to another electron, which is subsequently emitted from the material and counted by the photoelectron detector. This process is referred to as *Auger emission* and is schematically depicted in Figure 3.10. The kinetic energy of the Auger electron is solely defined by the energy difference of the states L, M_1 and M_2[5] and is independent on excitation energy of the original photoemission process. Note, that the Auger electron may or may not originate from the same energy level as the electron which recombines with the photo hole. The example shown in Figure 3.10 would be referred to as a LM_1M_2 Auger emission.

Depending on the electronic configuration of a material, a finite probability may exist, that an ion after photoemission remains in an excited state, rather than directly returning to the ground state.[171] The result in the spectrum is an additional emission at a specific,

[5]The nomenclature of the Auger process uses orbital quantum numbers.

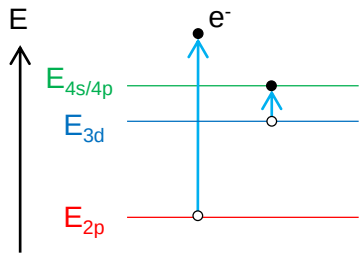

Figure 3.11: The origin of a shake-up satellite emission in a Cu(II) compound is schematically illustrated.

higher binding energy (i.e. lower kinetic energy), corresponding to the energy difference between (the intermediate) excited state and the ground state. This process is referred to as *shake-up satellite emission* and is schematically illustrated in Figure 3.11. The example shown is of a Cu(II) compound. The photoemission process from the 2 p orbital excites the transition of the unpaired 3d electron to the 4 s or 4 p energy level. The loss in kinetic energy of the photoelectron is observable as an additional satellite emission at a characteristic lower kinetic energy (higher binding energy) in the spectrum.[173] The intensity of satellite lines in such paramagnetic compounds can reach that of the main emission line.[171]

Binding energy shifts

Due to the specific number of electrons, photoelectron spectra are characteristic to each element. Many compounds can be identified by the interaction of valence electrons. However, due to a strong overlap of emissions in solid samples, it is generally not the analysis of signals from valence states which is conducted to identify compounds but the *chemical shift* of core levels. The interaction and exchange of valence electrons causes electrostatic forces with respect to the elemental state, which affect core levels of high binding energy. With empirical data at hand,[171] the oxidation state of an atom can be determined from the core level binding energy shift.

The binding energy as calculated from the kinetic energy according to Equation 3.3 is at first a function of the electron density at the atom.[174] It is the difference between ground state and excited state of the photoemission process.[175] *Shifts* in binding energy of a photoelectron core level $\Delta E_B(\mathrm{PE})$ typically occur due to changes in chemical environment or effects at interfaces to other materials, with respect to an isolated state. The reason for these shifts can be of several type, but are generally categorized as initial and final state effects, $\Delta\epsilon$ and ΔR, according to Equation 3.5.[174, 176, 177]

$$\Delta E_B(\mathrm{PE}) = \Delta\epsilon - \Delta R \tag{3.5}$$

The initial state ϵ refers to the electron shell in the ground state, so $\Delta\epsilon$ is caused by a change in the chemical environment of the atom.[174]. As explained by Egelhoff, the electron density, giving rise to the initial state remains "frozen" upon creation of a photohole. However, it has an effect on the final state relaxation R by the screening of the photohole, which is correlated to the electron density.[175] Put simple, the final state R

accounts for any kind of relaxation after the creation of the photohole, which is generally extra-atomic.[174][6] It is important to note that not all final state effects are included in ΔR, as for example charging during the measurement does not affect the Auger parameter, but can strongly alter the binding energy, although it is not an initial state effect. For this reason, it is useful to follow a terminology inspired by Hollinger and Iwata *et al.*.[178, 179] Hollinger modified Equation 3.5 to account for changes in Fermi energy ΔE_F due to electrostatic interactions at an interface between two materials.[7] Iwata furthermore added the term $e\Delta\Phi$ in order to account for effects of charging, where e is the elementary charge. Charging due to photoemission of electrons always increases the binding energy, which is why its sign should be positive. Including both effects results in Equation 3.6. [8]

$$\Delta E_B(\mathrm{PE}) = \Delta\epsilon - \Delta R - \Delta E_F + e\Delta\Phi \tag{3.6}$$

With this extended formalism, ΔR does not include all final state effects but only extra-atomic relaxation.[9] If all terms of Equation 3.6 are different from zero, it is impossible to individualize the contribution of each effect. However, if the chemical state of two materials which are put into contact remains constant ($\Delta\epsilon = 0$), charging artifacts are excluded ($e\Delta\Phi = 0$) and extra-atomic relaxation can be neglected ($\Delta R = 0$) the energy band alignment at an interface can be deduced as described in Section 3.3.2.

Practically, $\Delta R \neq 0$ when thin films with a thickness in the nanometer range are measured. The experimental value of the total change in relaxation energy ΔR is defined as half the change of the Auger parameter $\Delta\alpha'$, according to Equation 3.7.[174, 180] The Auger parameter itself is the sum of the binding energy of the photoelectron $E_B(\mathrm{PE})$ and the kinetic energy of the Auger electron $E_{kin}(\mathrm{AE})$ according to Equation 3.8.[174, 177]

$$\Delta R = \frac{\Delta\alpha'}{2} \tag{3.7}$$

$$\alpha' = E_B(\mathrm{PE}) + E_{kin}(\mathrm{AE}) = E_B(\mathrm{PE}) - E_B(\mathrm{AE}) + h\nu \tag{3.8}$$

The Auger parameter is sensitive to a change in polarization energy, since emission of a photoelectron involves a singly ionized excited state, whereas the Auger emission results in a doubly ionized state.[177] Polarizability is mainly related to electron density. Therefore, tabled values of α' are a widely used tool to obtain chemical state information from a material.[171] Other than by a change in oxidation state, a shift in α' can occur due to different coordinations of a metal cation (as it is the case of Al^{3+} in Al_2O_3, deposited

[6] A clear distinction between initial and final state effects is difficult and shall not be an objective of this thesis.

[7] If thermodynamic equilibrium is assumed at a junction, it is of course the energy bands which change with respect to a constant Fermi energy. However, as the Fermi energy is used as reference energy in XPS, a parallel shift of energy bands may technically be expressed as a change in Fermi energy with opposite sign.

[8] Instead of talking about a "true chemical shift" as Iwata *et al.* did, the conventional term $\Delta\epsilon$ as used by Hollinger is kept here.

[9] This is only true when local relaxation can be neglected. Cu(I) does not show a local relaxation process.[180]

on SiO_2).[181] Furthermore, bridging oxygen between cations of two different metals affects α'.[180] Significant in the context of this thesis is the shift of α' due to effects from interfaces to other materials. Changes in coordination number and bridging oxygen at an interface are rather short-ranged phenomena, whereas an additional final state contribution due to different dielectric constants of substrate and film materials extends further than the next neighboring environment.[180] Hence, a decrease in $\Delta\alpha'$ can be gradually observed with increasing film thickness.[182, 183] According to the Kirkwood model, the polarization energy $U(d)$ due to a difference in dielectric constant of substrate ϵ_s and film ϵ_f approximately depends on film thickness d in the following way: [181, 184, 185]

$$U(d) \approx \frac{\pi e^2}{8d}\left(\frac{1}{\epsilon_f} - \frac{1}{\epsilon_s}\right) \tag{3.9}$$

In Chapter 6, the role of extra-atomic relaxation is discussed for a number of energy band alignments, which have been experimentally obtained during the preparation of this thesis.

Photoelectron intensity

The intensity of an emission line I_i (after the removal of the background contribution from secondary electrons) depends on several factors, which are listed in the following:

- concentration of atoms i (c_i)
- X-ray flux
- photoeletric cross-section of an atomic orbital
- angular efficiency of the instrument
- efficiency of the photoelectric effect
- mean free path of electrons λ_e (function of E_{kin})
- sample area
- detection efficiency

In order to estimate c_i at the surface of the sample, the other factors have to be known and taken into account. This is done by dividing I_i by the empirical, relative atomic sensitivity factor of the respective emission line. A list of these factors is provided for a specific instrument, excitation energy (Al or Mg anode) and emission angle.[171]

The thickness of a thin film on a substrate can be determined by evaluating the damping of the intensity of a substrate emission, due to the additional layer on the surface according to Equation 3.10.[186]

$$I_d = I_0 \cdot e^{-d/(\lambda_e \sin\theta)} \tag{3.10}$$

I_d is the substrate core level intensity measured through the additional layer on the surface, I_0 is the corresponding intensity of the clean substrate, d is the thickness of the

layer, λ_e is the mean free path of photoelectrons in the film material and θ the emission angle. For this analysis to be valid, the film has to grow in a layer-by-layer fashion, also referred to as Frank van der Merwe growth.[29]

The intensity depends exponentially on the sinus of the emission angle. This is related to the information depth d_i, which is limited by an exponential increase in inelastic scattering probability as the thickness increases. Since there is no definite limit to the information depth, a common practice is to use a thickness range of $3 \cdot d_i$, which includes 95 % of emitted photoelectrons (at an emission angle of 90°).[169, 186, 187] Taking into account the influence of the emission angle, the exact relation is given by the following equation.

$$d_i = \sin\theta \cdot 3\lambda_e \tag{3.11}$$

This relation is the basis of angle-resolved photoelectron spectroscopy, where surface sensitivity is modulated by measurements at different θ. In this thesis, the method is used in Section 7.1 to obtain qualitative information on the location of a certain chemical state with respect to the distance from the surface into the bulk.

XPS on copper oxide

Some lines do not exhibit a strong chemical shift: For example, if a change in oxidation state occurs by altering the d electron density, then the electrostatic potential change is effectively shielded by the large electron density in this energy band. This is the case e.g. for Cu(I) and Cu(II) as well as Sn(II) and Sn(IV), respectively. The chemical shift is well below 1 eV, which is close to the instrument resolution. Cu_2O is a good example for a successful application of spectral information other than chemical shifts in order to determine the cation oxidation state. On the one hand, a reliable indicator of the presence of Cu(II) is a shake-up satellite emission associated to the Cu 2p line.[173] On the other hand, the Cu LMM Auger emission provides a binding energy difference of 2.3 eV between the peak of Cu(I) and Cu(0).[188] Figure 3.12 is taken from previously published results to illustrate changes in both the Cu 2p satellite structure and the Cu LMM Auger emission, when copper oxide is deposited under slightly reducing and oxidizing conditions, with respect to Cu_2O stoichiometry.[189] The difference between Fermi energy and valence band maximum $E_F - E_{VB}$ has been found an even more sensitive indicator for the presence of metallic copper than the shoulder in the Auger emission. Due to the formation of a Schottky barrier at the Cu/Cu_2O interface,[120] $E_F - E_{VB}$ increases in the presence of nanocrystalline copper precipitates from typical values of 0.25–0.30 eV to 0.5–0.6 eV.

Spin orbit splitting occurs at all lines except emissions from s orbitals. This is due to a coupling of the electron spin (which can be either +1/2 or −1/2) to the angular momentum of the emitting orbital.[187] The most intense emission of copper arises from the 2p line.[171] Referring to Cu 2p technically includes both lines Cu $2p_{1/2}$ and Cu $2p_{3/2}$.[10] In

[10] The index refers to the sum of angular momentum and spin momentum.

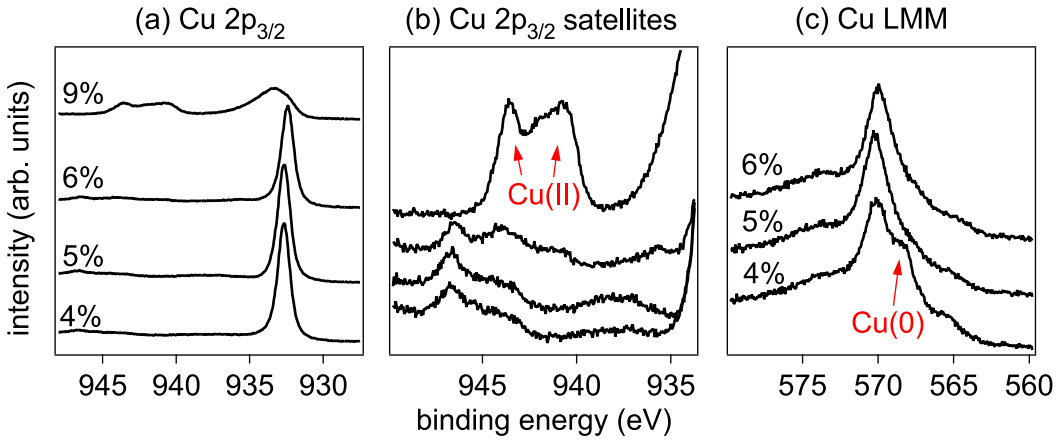

Figure 3.12: XP spectra of (a) the Cu $2p_{3/2}$ emission, (b) its satellite lines and (c) the Cu LMM emission, taken from previous work.[189] The films were deposited by reactive magnetron sputtering at RT and various oxygen contents in the process gas, which are indicated in the graphs. The spectral features related to Cu(II) and Cu(0) are indicated in red.

this thesis it is sufficient to only consider the more intense Cu $2p_{3/2}$ emission. Throughout the text however, this is either correctly referred to as Cu $2p_{3/2}$, or just Cu 2p for the sake of simplicity.

It is important to note, that the surface of Cu_2O is partially oxidized to Cu(II) containing species. The associated satellite intensity can be reduced by heating in vacuum at 200 °C.[21, 190] A comparative study of the reduction of partially oxidized copper (having approximately 1 nm CuO and 2 nm Cu_2O at the surface) and fully oxidized CuO by annealing in vacuum (30 min at 10^{-8} mbar) showed, that 100 °C is enough to reduce the 1 nm CuO at the surface of Cu_2O. At 300 °C, the surface of thick CuO is reduced to Cu_2O.[191] When the temperature is not supposed to increase above room temperature, which such heating in vacuum would require, Cu_2O has to be measured by XPS in an in situ approach without breaking the vacuum between deposition and analysis. This is described in the following Section 3.3.2.

Experimental conditions used in this work

XPS measurements have been carried out with a Physical Electronics PHI 5700 multi-technique surface analysis unit, using monochromatic Al Kα radiation with an energy of 1486.7 eV, an emission angle $\theta = 45°$ and a pass energy of 5.85 eV, resulting in an overall energy resolution of less than 0.4 eV. Angle resolved measurements have been performed in the range of $15° \leq \theta \leq 85°$. Binding energies are reported with respect to the Fermi energy, which was calibrated measuring a metallic silver sample after cleaning during 5 min with an argon sputter gun. This standard sample is stored in vacuum at 10^{-9} mbar.

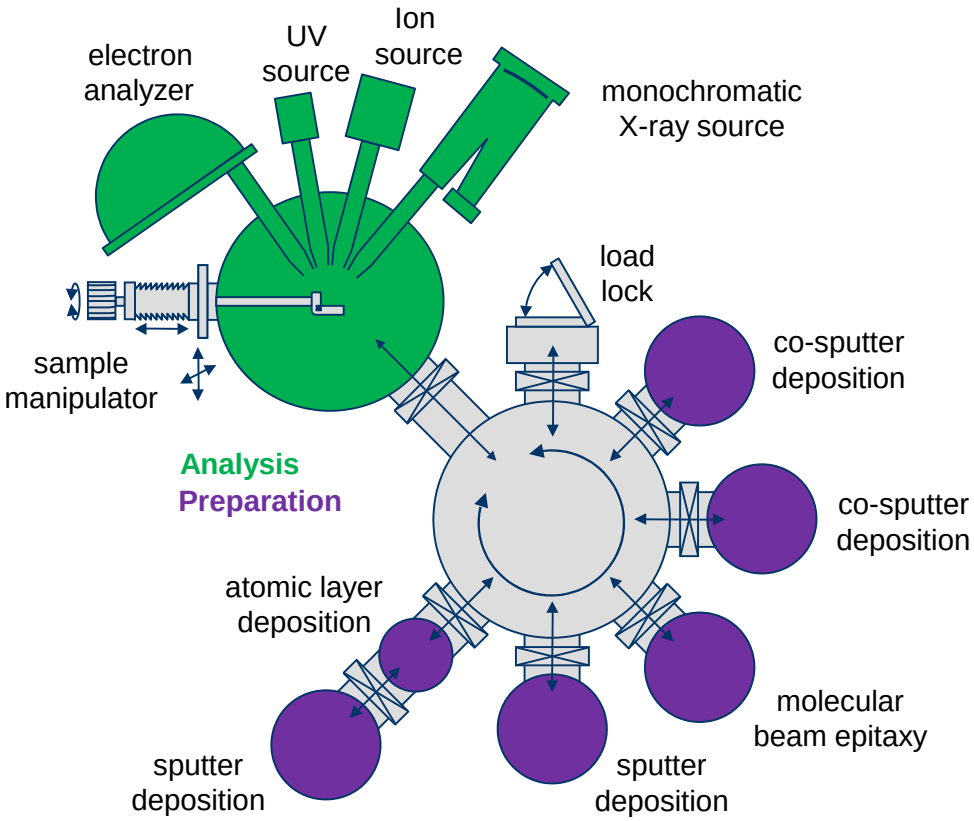

Figure 3.13: Schematic representation of the cluster tool DAISY-MAT.

3.3.2 In situ XPS measurements

In situ measurements have been performed at the cluster tool DArmstadt Integrated SYstem for MATerial research (DAISY-MAT), which is schematically depicted in Figure 3.13. It provides a central distribution chamber, connecting a Physical Electronics PHI 5700 multi-technique surface analysis unit to several home-made preparation chambers, allowing for rapid sample transfer between preparation and analysis chambers without interrupting UHV conditions. The base pressure of the transfer stage is 10^{-9} mbar.

A deposition by magnetron sputtering and simultaneous measurement by XPS or by means of electrical characterization is not possible due to the presence of plasma inside the deposition chamber. With the DAISY-MAT it is however possible to interrupt the film deposition at any given moment and measure XPS and electrical properties, such as resistance, without any alteration to the film surface induced by air contamination.

Energy band alignment

The energy band alignment between two planar materials can be measured by stepwise thin film deposition and subsequent photoelectron spectroscopy as outlined by Waldrop, Kraut and co-workers.[172] The knowledge of the band gaps of the involved materials results in the proposition of an alignment of the respective valence band and conduction

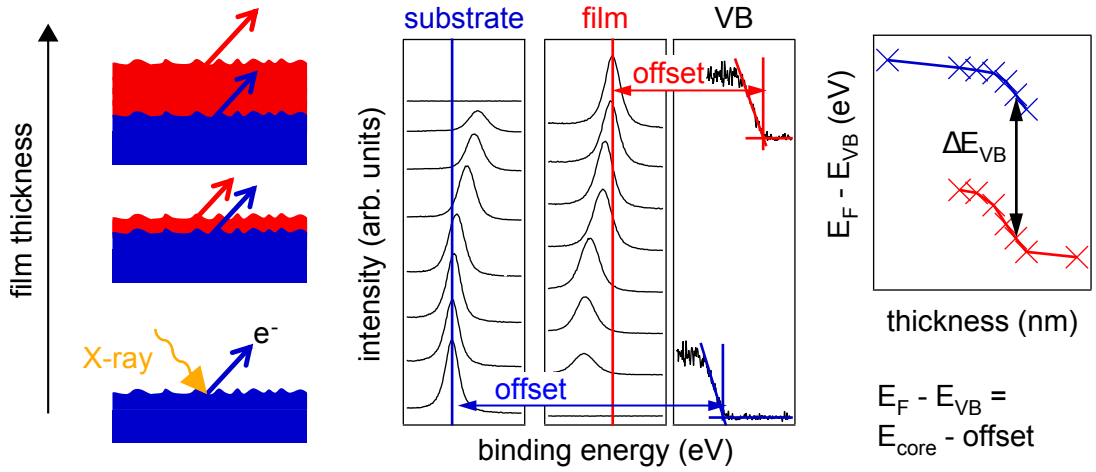

Figure 3.14: The procedure for obtaining the valence band discontinuity ΔE_{VB} is schematically illustrated. An explanation of the figure can be found in the text.

band edges. A schematic representation of the determination of the valence band discontinuity ΔE_{VB} with XPS is provided in Figure 3.14. The materials shown in Fig. 3.14 are either semiconductors of insulators due the existence of band gaps.

When the thickness of a thin film on a substrate material is below the information depth of XPS, both materials contribute to the photoelectron spectrum. Usually the valence band spectra overlap and individual contributions cannot be distinguished from each other. This is why $E_{\mathrm{F}} - E_{\mathrm{VB}}$ is constructed from core level binding energy shifts: Before film deposition, the clean substrate surface is measured and the offset between core level binding energy E_{core} and valence band maximum E_{VB} is determined for the substrate. Successive film deposition leads to the reduction of substrate intensity and the appearance of emissions from the film. When the thickness is high enough, so that the substrate has no influence on the film emissions anymore, the offset is calculated for the film material. With the subtraction of the offsets from the corresponding core level signal, an indirect evolution of $E_{\mathrm{F}} - E_{\mathrm{VB}}$ with film thickness is constructed. The valence band discontinuity ΔE_{VB} is extracted in the thickness range in which both material show similar binding energy shifts. In order to achieve a measurement of the band bending in the film material, a second experiment with an inverted layer sequence usually needs to be done. This is mainly due the effects described in Section 3.3.1, occurring in the vicinity of the substrate interface.

One uncertainty encountered in this procedure is related to the determination of the valence band maximum by linear extrapolation, being of up to ±0.1 eV.[172] The chemistry at the interface can further affect the value of valence band alignment. Whether or not the surface is polar influences the formation of a dipole at the interface.[192] Interface reaction, in some cases introduced by the deposition process, also affect the alignment and can be observed for example when reverting the layer sequence.[172, 193]

In order to measure Schottky barrier heights Φ_{B}, the metallic layer is deposited onto

the semiconductor up to a thickness which allows the measurement of both substrate and film emissions. The valence band maximum in a p-type semiconductor with respect to the Fermi energy in the contacting metal is a direct measure of the Schottky barrier height. In case of an n-type semiconductor, the difference between conduction band minimum (according to the band gap of the material) and the Fermi energy in the metal has to be calculated.

The significance of extra-atomic relaxation on the measurement of an energy band alignment according to the concepts described in Section 3.3.1 will be discussed together with the relevant data in Section 6.2. To the best of the author's knowledge, the effect of extra-atomic relaxation in the vicinity of a substrate interface has not been investigated in the light of an analysis of energy band alignment at the interface. In Chapter 6 of this thesis, such a correlation is tentatively established, based on XPS data of Cu_2O, deposited on different types of substrates.

Energy alignments which are solely determined by bulk properties and not by the local environment at the interface follow the rules of *commutativity* and *transitivity*, given in Equation 3.12 and 3.13, respectively.[172, 194]

$$\Delta E_{\mathrm{VB}}(A,B) = -\Delta E_{\mathrm{VB}}(B,A) \tag{3.12}$$

$$\Delta E_{\mathrm{VB}}(A,C) = \Delta E_{\mathrm{VB}}(A,B) + \Delta E_{\mathrm{VB}}(B,C) \tag{3.13}$$

Using the terminology of Equation 3.6, this implies that the binding energy shift is equal to ΔE_{F}, whereas all other terms are zero. The commutativity rule means that the layer sequence does not change the alignment. When transitivity can be ensured, the energy alignment between the materials A/C can be predicted from the energy alignment between A/B and B/C. In Chapter 5 the valence band discontinuity between Cu_2O and CuO is determined in this way. A sufficiently large number of data sets ensures the validity of transitivity.[172] Another transitive model is the electron affinity rule. However, it uses the vacuum level as common energy reference and not the Fermi energy.[195]

In situ conductance measurement

On some samples, in situ measurement of 2-point conductance have been performed prior to XPS analysis. The Physical Electronics PHI 5700 chamber provides two electrical feed-throughs, which have been connected to the terminals of a Keithley 6487 picoammeter/voltage source. They are individually contacted to two parts of a specially designed sample holder. Two lateral gold electrodes on the sample surface are contacted with screws and metallic tips. An image of the sample assembly before introducing it into the vacuum chamber is shown in Figure 3.15.

Since especially at low film thicknesses the measured currents have been in the range of picoamperes, the current measurement was conducted by applying a constant bias voltage of 1 V until the current reached a steady state. Then the bias voltage was set to

Figure 3.15: A photography of the sample holder for in situ conductance measurement is shown. The inner circle is insulated from the outer rim. The sample for conductance measurement can be recognized by the two planar gold contacts. The second sample serves as an additional substrate for XPS characterization.

zero and the current was read until again steady state was reached. The difference of both steady-state currents was used for calculation of the conductance.[196]

3.3.3 Current-voltage characterization of transistors

Two different semiconductor parameter analyzers were available at CENIMAT for the measurement of current-voltage characteristics of TFT devices and other test structures. An Agilent 4155C SPA was connected to a Cascade M150 microprobe station, which was placed in a metallic box for electrostatic shielding and measurement in the dark. It offered fast and easy handling by using an optical microscope for sample and tip positioning. General TFT characterization by measurement of transfer and output curves was usually performed with this instrument.

The other available instrument was a Keithley 4200-SCS connected to a Janis ST-500-UHT microprobe station. The Janis probe station offered a cryostat for temperature control between 78.2 K and 675 K. A continuous flow of liquid nitrogen was used for cooling a solid copper sample holder. The holder was resistively heated, controlled by a Lakeshore 336 temperature controller. The cryostat was enclosed in a vacuum chamber, connected to a turbo molecular pumping stage. The setup is capable of chamber pressures down to 10^{-4} mbar. Since this equipment offered more possibilities than the Agilent setup at the expense of an easy sample handling, it was rather used for specific test purposes, like characterization in temperature and under gate voltage stress.

3.3.4 Hall effect measurement

By the Hall effect technique, it is possible to determine the majority charge carrier type, its carrier concentration and carrier mobility. When the measurement is conducted under variation of the temperature, information on dopant states and concentrations can be obtained by evaluating the activation energy of free carrier concentration. Furthermore, the temperature-dependent mobility may reveal the dominant scattering mechanisms.

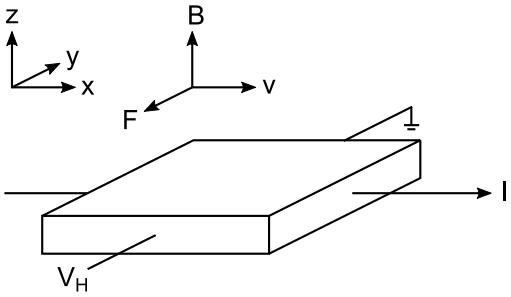

Figure 3.16: Geometrical relations relevant for equations of the Hall effect measurement (adapted for positive charge carriers from [197]).

Working principle

The information on the working principle of Hall effect measurements is adapted from a book by Marius Grundmann.[197] In 1879, Edwin Hall described for the first time a force acting on a charge carrier in an electric field by a transversal magnetic field.[198] It may be described by considering the geometry shown in Figure 3.16, assuming an isotropic material. The magnetic field along z induces an electric field in the x and y plane according to the Lorentz force, which is described by Equation 3.14.

$$\mathbf{F}_\mathrm{L} = q\,(\mathbf{v} \times \mathbf{B}) \tag{3.14}$$

A current density $j_x = \sigma \mathcal{E}_x$ is flowing due to an applied voltage in x-direction. Consequently, the Lorentz force acts along y, leading to charge accumulation, which results in the Hall voltage V_H. After Equation 3.14, the field along y is given by $\mathcal{E}_y = v_x B_z = \mu_\mathrm{H} \mathcal{E}_x B_z$. This results in the following expression for the Hall coefficient R_H for the case of a p-type material.

$$R_\mathrm{H} = \frac{\mathcal{E}_y}{j_x B_z} = \frac{\mu_\mathrm{H}}{\sigma} = \frac{1}{ep} \tag{3.15}$$

Thus the quantity directly obtained from the measurement of the Hall coefficient is the carrier concentration p. Typically prior to the Hall effect the conductivity σ is measured. This value is then used to determine the Hall mobility μ_H according to Equation 3.15.

This simplified approach assumes the same mobility for charge carriers moving along x due to the electric field as for carriers moving along y due to the magnetic field in z. This means the mobility is proportional to a uniform, average scattering time τ. However, this is only true at very large magnetic fields, which are typically not encountered in laboratory-based Hall effect equipment. When considering the ensemble averages of the scattering time it can be shown that $< \tau^2 >$ is different from $< \tau >^2$. This results in a more general expression for the Hall coefficient.

$$R_\mathrm{H} = \frac{\mu_\mathrm{d}}{\sigma} = \frac{r_\mathrm{H}}{ep} \tag{3.16}$$

The Hall factor $r_\mathrm{H} = < \tau^2 > / < \tau >^2$ may vary between 1 and 1.93 depending on the dominant scattering mechanism. The knowledge of r_H allows for calculation of the mobility which determines the conductivity, also referred to as drift mobility μ_d. Nevertheless,

the Hall mobility is widely used in literature since it does not require the knowledge of the dominant scattering process.

The presence of charged defects causes *ionized impurity scattering*. This mechanism becomes dominant when the temperature decreases, due to a decreased probability of phonon scattering. Due to the relevance to Cu_2O,[10, 22, 46] the mechanism will be shortly described in the next paragraphs, mainly based on the book "Solid State Physics" by Blakemore.[199]

Ionized impurity scattering

Scattering at ionized impurities happens when a charge carrier is deflected by attraction to or repulsion from the localized charges of impurities. The formalism is based on the one Rutherford developed for describing the scattering of alpha particles at atomic nuclei.[200] Conwell and Weisskopf adapted it to the case of electron scattering by limiting the effective Coulomb force for scattering at low angles to a certain distance to the ionized impurities, which in turn depends on the total impurity concentration.[201] The resulting expression for the mobility limited by ionized impurity scattering μ_I with respect to the temperature is given in Equation 3.17. A quantum mechanical approach has been followed by Brooks and Herring leading to roughly the same formalism.[202]

$$\mu_\mathrm{I} = \frac{128\sqrt{2\pi}\left(\epsilon_\mathrm{r}\epsilon_0\right)^2 (kT)^{3/2}}{\sqrt{m_\mathrm{h}^*} N_\mathrm{i} Z^2 e^3} \left[\ln\left(1 + \frac{12\pi\epsilon_\mathrm{r}\epsilon_0 kT^{\,2}}{Ze^2 N_\mathrm{i}^{1/3}}\right)\right]^{-1} \tag{3.17}$$

The variable N_i is the ionized impurity concentration and Z charge state of the scattering center. The numerator predicts a $T^{3/2}$ dependence. Only at very low temperature and high ionized impurity concentrations, the denominator changes the dependence to $T^{-1/2}$. The total ionized impurity concentration in a p-type semiconductor, which is compensated by a fully ionized single donor, is $N_\mathrm{i} = p + 2N_\mathrm{D}$.[46] When ionized impurity scattering is the dominant mechanism, the Hall factor is 1.93.

Description of equipment

The commercial system at UNL was a HL5500PC by the company Accent. The description is taken from the respective user manual. The magnetic field of 0.32 T was provided by a permanent magnet. The system was equipped with a buffer amplifier for measurement of high impedance, involving source currents down to 1 pA. Furthermore, it provided a cryostat enabling measurements between 90 K and 550 K by cooling with liquid nitrogen. During the measurement at various temperatures, the sample space was continuously evacuated by a rough vacuum pump. Below a pressure of a few millibar, water condensates directly from the gas phase at a transition temperature between 273 K and 200 K, which is decreasing with lower pressure.[203] This eventually influenced the electric properties of a samples, which resulted in a significantly reduced activation energy from the Arrhenius plot below the phase transition temperature of water. In order to avoid the

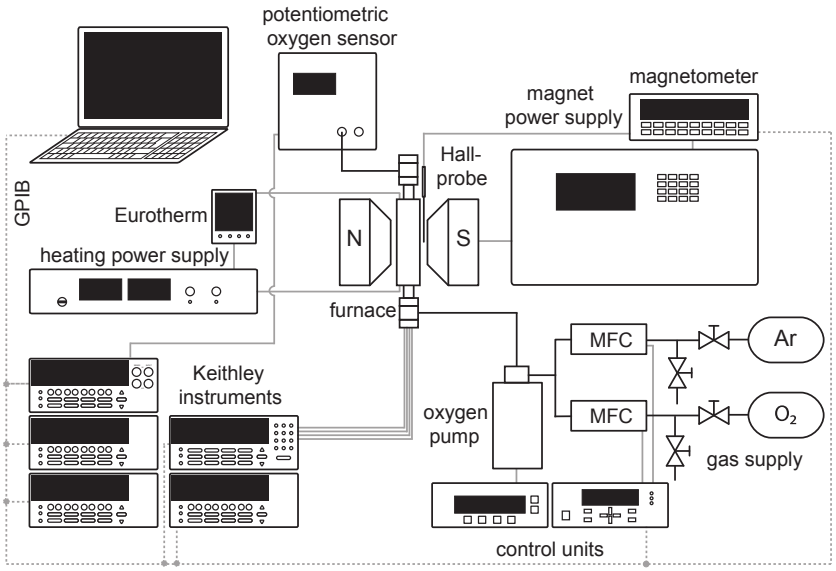

Figure 3.17: Schematic representation of the Hall effect set-up at TU Darmstadt, taken from previous works.[205]

influence of water on measurements below the phase transition temperature, the sample was heated above 400 K during a few minutes in the rough vacuum prior to cooling down. All samples were measured in van der Pauw geometry.[204]

The custom-made Hall effect system at TU Darmstadt is described in a respective publication.[205] The experimental set-up has been elaborated during preparation of the PhD theses of André Wachau and Mareike Frischbier.[44, 206] Figure 3.17 shows a schematic representation of the setup. The sample in van der Pauw geometry is installed inside a quartz tube, which may be evacuated through a turbo molecular pump down to a pressure of 10^{-8} mbar. Alternatively, a gas flow at atmospheric pressure of an argon-oxygen mix may be chosen by separate mass flow controllers and an optional oxygen pump. The gas mixture at the outlet is monitored by a potentiometric oxygen sensor. The quartz tube is fit into a furnace, which allows for measurement at temperatures up to 600 °C. The furnace with quartz tube carrying the sample is then placed between the pole shoes of a electromagnet (Type EM4-HVA, Lake Shore Cryotronics), capable of a maximum magnetic field of 1 T. A Hall probe serves to monitor the actual magnetic field in the vicinity of the sample. Several Keithley instruments are responsible for supplying the measurement current, measuring the Hall voltage and performing the permutation among the four contacts of the sample in van der Pauw geometry. A buffer amplifier is included in order to measure high impedance samples. A LabView routine controls the Keithley instruments and the magnet power supply to perform conductivity and Hall effect measurement.

3.3.5 Transmittance spectroscopy

Transmittance spectroscopy enables to determine the optical band, which is one of the characteristic quantities of a semiconducting or insulating material. Photons of a comparatively high energy eventually give rise to the photoelectric effect, which was covered in Section 3.3.1. A lower energy leads to other kinds of interactions. One of them is absorption. In case the absorbing material is a semiconductor or an insulator, photons are only strongly absorbed when their energy is higher than the optical band gap. By measuring the portion I_T of the unattenuated light intensity I_0 which is transmitted through the sample as well as the reflected intensity I_R, the absorption coefficient α can be estimated, following the Lambert-Beer law.[20] Equation 3.18 shows the respective formalism, in which d is the sample thickness (i.e. the distance the light is traveling through the sample).

$$\alpha = -\frac{\ln\left(\frac{I_T/I_0}{1-I_R/I_0}\right)}{d} \tag{3.18}$$

The transmittance I_T/I_0 as well as the reflectance I_R/I_0 can be readily measured with commercial spectrophotometers like the Perkin Elmer Lambda 950, available at UNL. However, the sample area of films deposited at TU Darmstadt was limited to 2x2 cm^2. In the case of a simultaneous deposition on several substrates, it often had to be below 1x1 cm^2. It was found that such small sample sizes led to an overestimation of reflectance with the equipment available at UNL. The usage of a mask covered with Spectralon (the same white coating found on the inside of the sphere) at the exit port of the integrative sphere was necessary. Due to the lack of focusing optics at the entrance port, reflected light intensity which was rather coming from the mask than from the sample was recorded. When calculating the absorption coefficient upon taking into account an overestimated sample reflectance, a negative absorption coefficient was obtained at low light energies. In order to avoid this error, the absorption coefficient was calculated neglecting the reflectance. As a consequence, interference fringes which appeared in transmittance data are included in the calculated absorption coefficient. However, since the Tauc plot applied for the estimation of the band gap involves the product of α and the photon energy $h\nu$,[207] this effect is of minor concern for the determination of the band gap.

3.3.6 X-ray diffraction

The basics of X-ray diffraction are taken from references [208] and [209]. Light is diffracted by means of coherent, elastic scattering at periodic structures and interference of the scattered rays. The process is described by the Bragg equation, here 3.19.[210]

$$2 \cdot d_{hkl} \cdot \sin\theta_{hkl} = n \cdot \lambda \tag{3.19}$$

The symbol d_{hkl} is the spacing of periodic planes, θ_{hkl} the angle with respect to the planes, λ the wave length of the light and n the order of interference. The condition $\lambda \leq 2/n \cdot d_{hkl}$ needs to be fulfilled. After the discovery of X-rays by Röntgen (Nobel Prize in 1901), it had been found that their wavelength range gives rise to diffraction at lattice planes of a crystal (Laue, Nobel Prize in 1914). These planes are commonly indicated by *Miller* indices *hkl*. However, they are not physically existing planes inside the crystal but rather arise from the periodic stacking of atoms. It is further not a reflection in a macroscopic analogy to a mirror, but rather based on the excitation of electrons. By means of Hertz dipoles, each atom emits light of the same wavelength as the incident beam.[11] The periodicity of atoms in a crystal consequently gives rise to interference effects within the emitted radiation, governed by Equation 3.19.

By variation of θ_{hkl} and/or λ and recording the intensity of the diffracted beam, information on structural properties and composition of phases of a sample can be obtained. As X-ray tubes are a common radiation source available in a laboratory environment, a popular method involves the use of monochromatic[12], divergent X-rays and a variation of θ_{hkl}. The *Bragg-Brentano* diffraction method is performed in reflexion at the sample surface. By varying both the incident and the emitted beam optics by the same value, the lattice planes parallel to the sample surface are measured, which is referred to as $\theta/2\theta$ scan. In the case of measuring thin films deposited on a substrate, *Bragg-Brentano* is preferred towards a measurement in transmission, since less substrate intensity is recorded.

The goniometer geometry with a radius r is schematically shown in Figure 3.18. With a fixed divergence angle γ defined by slits in the incident (and scattered) beam path, the length L along the sample surface, which is illuminated (and detected) changes with the diffraction angle θ according to Equation 3.20 (for a circular sample).[208, 211]

$$L = \frac{r \tan \gamma}{\sin \theta} \tag{3.20}$$

This means the measured sample area decreases with increasing diffraction angle. Together with the penetration depth of X-rays, the measured sample volume is defined. The penetration depth generally increases with increasing diffraction angle, which counteracts the effect of Equation 3.20.[208] However, in a thin film sample the penetration depth may be larger than the sample thickness for a given diffraction angle. Under these circumstances, the measured sample volume within the film is predominantly defined by the illuminated area.

[11] This is referred to as Thomson scattering in the framework of the kinematic scattering theory.[208]

[12] The incident beam is actually not monochromatized, since this would mean a significant intensity loss. The Kα_1 and Kα_2 X-ray lines are used, as the Kβ line can be filtered be a metallic absorber.

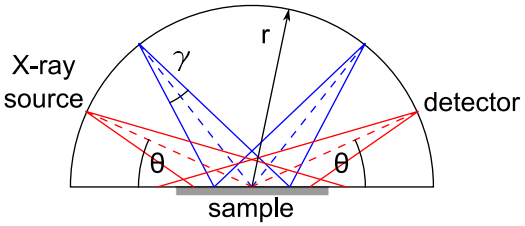

Figure 3.18: Schematic representation of the goniometer half-circle in Bragg-Brentano geometry.[208] Two different diffraction angles θ are shown in blue and red with fixed goniometer radius r and divergence angle γ.

Qualitative phase analysis

The obtained XRD data was analyzed with the software HighScore Plus, which was provided by the manufacturer of the instrument.[13] The information in this subsection is mainly taken from the respective manual version 4.1. An algorithm for automatic background removal is used.[212] Bragg reflections are automatically detected from the second derivative of the data, which is calculated by applying a polynomial filter.[213] Although an evaluation of the first derivative provides a higher accuracy in diffraction angle, the second derivative allows for a better detection of overlapping reflections. In order to obtain refined line profile parameters, a Pseudo-Voigt profile fitting routine is used. The fitting considers the $K\alpha_2$ component.[214, 215] The most important parameters from the line profile analysis are diffraction angle, areal intensity and full width at half maximum (FWHM). A list containing these parameters is matched to a database of powder diffraction files of the International Center of Diffraction Data (ICDD). The possible phases are first limited by selecting the containing elements, and allowing the software to search for any possible phases formed by the defined list of elements. A score is created to sort the most probable database entries by their likelihood of occurrence in the sample. In a manual selection step, the patterns which best fit to the experimental data are chosen. The XRD results presented in this thesis are shown together with the patterns from the corresponding powder diffraction files. Distances between lattice planes d_{hkl} are compared to the database entry in a relative fashion. The FWHM is occasionally evaluated using the Scherrer formula. Equation 3.21 gives the grain size L_{grain} of monodisperse cube-shaped crystallites of a powder. In case of polycrystalline thin films, where cube-shaped grains are the exception, it may only serve to provide a lower boundary of grain size.[209]

$$L_{\text{grain}} = \frac{\lambda}{\text{FWHM} \cdot \cos\theta_{hkl}} \tag{3.21}$$

3.3.7 Scanning electron microscopy

Most information on the technique is obtained from the book by Ohring.[29] A scanning electron microscope (SEM) uses a focused electron beam, which scans the sample surface and analyzed primarily secondary electrons (SE) and elastically backscattered electrons (BSE). The primary electrons of an energy between a few keV and 50 keV are usually

[13] HighScore Plus software version 4.1, year 2014, PANalytical B.V., Almelo, The Netherlands

created either by thermionic emission from a filament or by a field emission gun and focused to a spot size of ≈ 1 nm through a column of electromagnetic lenses. They interact with the sample up to a depth of 1 µm from the surface.

Secondary electrons (SE) have an energy a factor of a thousand lower than the primary electrons. This implies, that they are emitted only from a region of a few angstroms from the sample surface. Secondary electrons provide a topographical contrast, since the SE yield depends on slope and curvature of the surface: A tilted surface with respect to the primary beam emits more secondary electrons, than a surface at 90°. Furthermore, the yield from convex surfaces is higher than from concave ones. The resolution of an SE image is in the order of 2 nm.

Backscattered electrons have a kinetic energy similar to the primary electrons and are obtained up to a depth of a few tenths of a micrometer. Since the interaction volume increases with the depth from the surface, a lower lateral resolution is obtained from BSE. The probability for backscattering is roughly proportional to the square root of the atomic number, so elemental contrast can be obtained, if the atomic numbers are sufficiently different in the sample. When detecting electrons which are emitted from the sample under different angles between the primary beam and the surface, BSE can be detected which have undergone Bragg diffraction by the crystal lattice of the samples. This technique is called electron backscatter diffraction and is able to provide crystallographic information for individual grains. In addition to SE and BSE, Auger electrons and X-ray fluorescence are produced in the samples as competing processes. Due to the relatively low kinetic energy of Auger electrons, as described in Section 3.3.1, they are emitted only from the top few nanometers of the surface. Fluorescent X-rays are emitted from up to a depth of 1 µm. Both provide elemental information, but it is most commonly the fluorescent X-rays, which are detected by energy dispersive spectroscopy (EDS).

In this work, secondary electrons were analyzed for topographical contrast with a Carl Zeiss Auriga. To obtain cross-sectional images of the films, the samples have been manually broken prior to the measurement.

3.3.8 Atomic force microscopy

Like in the previous section, the information on the technique is taken from the book by Ohring.[29] An atomic force microscope (AFM) measures attractive and repulsive forces between surface atoms and an ideally atomically sharp cantilever tip. It is mostly used to obtain topographical images of a sample surface with sub-nm resolution. As a successor of scanning tunneling microscopy, it extends the range of measurable surfaces from conductors to semiconductors and insulators.

The cantilever acts as a soft spring with respect to the interatomic forces of the samples and becomes deflected upon sensing the surface. In *non-contact mode*, attractive van der Waals forces between tip and sample surface are sensed by a vibrating cantilever, while the tip is not in physical contact with the sample. These forces are small, so they are

detected by an amplitude or frequency change in the cantilever vibration. Alternatively, the *contact mode* enables to sense repulsive forces between the surface and the tip without the need of a vibrating cantilever. Having the advantage of being a simpler procedure, the contact mode provokes more abrasion between tip and surface compared to the non-contact mode and is not suited for soft materials. In both modes, the cantilever deflection is measured by the alignment of a laser beam, which is reflected from the backside of the cantilever. While a micrometer-sized area of the surface is scanned, the distance between tip and surface is piezo-controlled, coupled to the deflection (contact mode) or amplitude/frequency change (non-contact mode) of the cantilever. The height contrast of the sample area is the most common type of data acquired by AFM. However by measuring a current or electrostatic forces between the tip and the surface, other types of contrast can be obtained by this technique.

In this work, an Asylum Research MFP-3D atomic force microscope was used to obtain surface roughnesses and average grain sizes at the surface in non-contact mode. Furthermore, data from conductive atomic force microscopy (CAFM) is included in Chapter 5, showing current maps in contact mode of an area of $1 \times 1\,\mu m^2$ with a voltage of 2 V applied to the tip[14].

[14] Asylum Research PPP-CONTPt

Part II

Results and discussion

Chapter 4

Deposition of stoichiometric Cu_2O

With the knowledge on defects in Cu_2O outlined in Section 2.6.1, it is important to ensure the material to be as stoichiometric as possible in order to benefit from the low hole carrier concentration and the high carrier mobility of Cu_2O. In the process of reactive sputtering, the most important parameter for the oxidation state of the deposited material is the oxygen partial pressure. For convenience, the oxygen partial pressure was indirectly controlled by the argon and oxygen gas flow, while maintaining the total system pressure constant. In previous works, in situ XPS has already been shown to be a suitable technique for the detection of small amounts of copper ions in oxidation states other than Cu(I), whereas XRD requires the formation of the corresponding secondary crystallographic structures.[189]

The first section of this chapter contains a summary of bulk properties of thin Cu_2O films when deposited with different oxygen content in the process gas. This intends to emphasize the impact of stoichiometry and oxidation state on the electrical properties of Cu_2O. It shall also highlight the importance of XPS as an analytical tool to ensure the optimum deposition conditions in order to obtain the desired cation oxidation state. Since XPS is not readily available at UNL, Section 4.2 introduces transmittance spectroscopy as common benchmark for samples from both institutes. To conclude the analysis of bulk properties, Hall effect measurements as a function of temperature and atmosphere composition are presented in Section 4.3.

In order to distinguish the samples deposited at TU Darmstadt, the Cu/O ratio is used, which was obtained from in situ XPS data. This allows to easily relate observations from other measurements to deviations from Cu_2O stoichiometry. Since the Cu/O ratio from in situ XPS could not be measured for the samples deposited at UNL, they are referred to by the letters **A, B, C, D, E**. Higher letters in the alphabet correspond to a higher amount of oxygen gas flow in the process gas during sputter-deposition. The percentage of oxygen

in the total gas flow has been varied from 4.5 % to 6.5 % in steps of 0.5 %.

4.1 Fermi energy and resistance with respect to the stoichiometry of in situ samples

Slight variations in oxygen content in the process gas lead to changes in the stoichiometry and the Fermi energy of copper oxide. Figure 4.1 (a) graphically depicts the relation between Fermi energy and Cu/O ratio of samples of > 200 nm thick films obtained during calibration of the oxygen content for deposition of Cu_2O at room temperature. Figures 4.1 (b) and (c) show corresponding values of the conductivity σ and the activation energy E_a. The activation energy was obtained from conductance measurements in planar geometry in a temperature range of $-50\,° < T < 130\,°$ at a total pressure of 10^{-4}–10^{-3} mbar. More results and details on activation energies are included in Section 5.2.1. Relevant XP spectra of selected samples are displayed in Figure 4.1 (d) and (e).

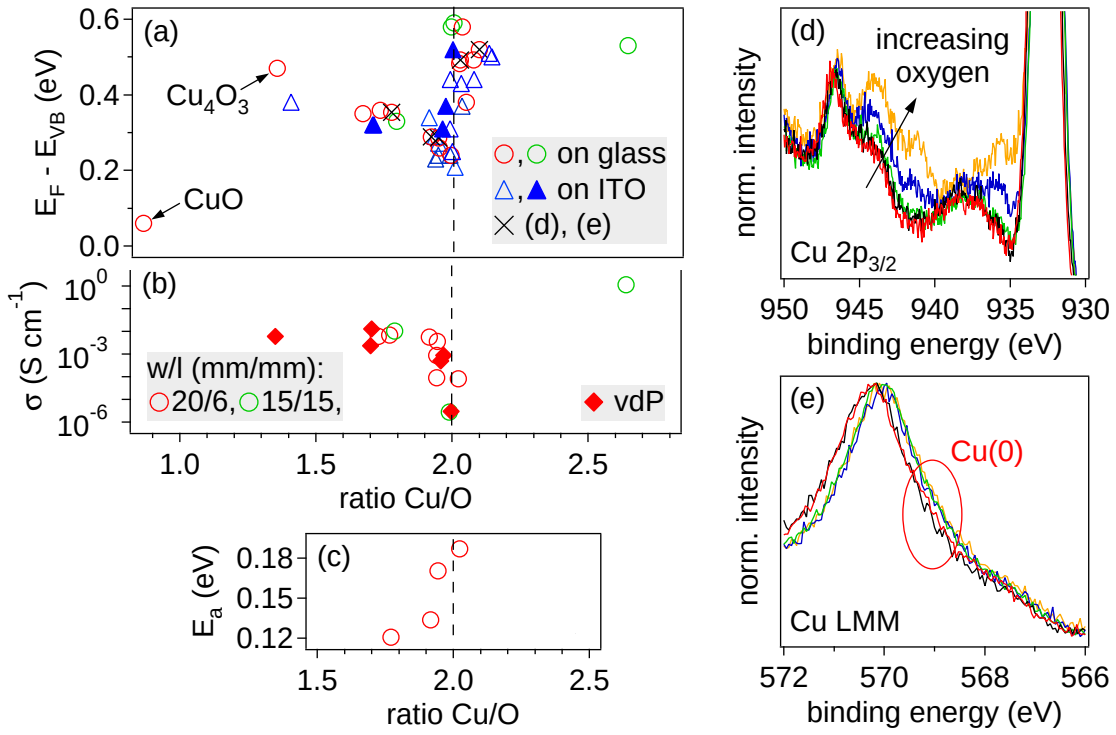

Figure 4.1: (a) Fermi energy of copper oxide films (> 200 nm) with respect to stoichiometry as deduced from XPS data. The films were deposited on corning glass and ITO-coated corning glass. (b) Conductivity σ from planar geometry (circles) and van-der-Pauw geometry (vdP, squares) with respect to stoichiometry. The full symbols in (a) and (b) show data obtained from the same deposition. The green circles are taken from previous work.[189] (c) Activation energy between -50 °C and 130 °C of a few representative samples. (d), (e) XP spectra of selected samples at binding energies of the Cu $3p_{3/2}$ satellite emission and the Cu LMM Auger emission.

The Fermi energy of stoichiometric Cu_2O is found at 0.21–0.24 eV above the valence band maximum. When increasing the oxygen content in the process gas to more oxygen-rich conditions, the XP spectra presented in (d) show a gradual increase in Cu 2p satellite intensity, which corresponds to an increased amount of Cu(II) in the sample. Simultaneously, a gradual increase in Fermi energy and an increase in conductivity as well as a decrease in activation energy is observed. At first, it is contradicting how a sample can show increased conductivity together with an increased Fermi energy, especially since a sample of CuO stoichiometry exhibits a Fermi energy of 0.06 eV above the valence band maximum. If a homogeneous materials is assumed, the mobility would have to increase tremendously to compensate for the lower carrier concentration. Since such an observation is not reported in literature, the increasing conductivity is rather an indication for the presence of a highly conductive secondary phase. The Fermi energy does not decrease with more oxygen-rich conditions in Fig. 4.1 (a), whereas the conductivity in (b) increases and the activation energy in (c) decreases. This indicates, that the more conductive phase is found in the depth of the film and not at the in situ surface. Motivated by these findings, the possibility of an increased conductivity at grain boundary and interface layers is analyzed in Chapter 5.

Going towards copper-rich conditions, an increase of $E_F - E_{VB}$ to 0.4–0.6 eV is observed at Cu/O $\approx$ 2. The conductivity drops accordingly. In order to conclude whether metallic copper is present in the copper-rich material, the Cu LMM Auger emission can be considered, as it was mentioned in Section 3.3.1. When looking closely at the differences of the normalized intensity of the red (Cu/O = 2.09) and the black curve (Cu/O = 2.02) in Figure 4.1 (e), a slightly increased intensity is observed around the typical binding energy of the metallic Cu LMM emission at 568.5 eV. Consequently, the high Fermi energy of the copper-rich Cu_2O is ascribed to metallic precipitates, which cause Schottky barriers to the Cu_2O in the bulk of the material and deplete the semiconductor.[120][1] As long as the metallic precipitates do not form a continuous conductive path, the conductivity is the one of the depleted semiconductor. This corresponds to the range $2 \leq$ Cu/O < 2.3.[124] The data point in Fig. 4.1 (b) at Cu/O = 2.64 confirms, that metallic conduction occurs for Cu/O > 2.3.

4.2 Transmittance spectroscopy as common benchmark

Since XPS is only available at TU Darmstadt, other experimental techniques were needed to compare samples from both institutes. In previous work,[189] XRD was show to be insensitive to small changes of oxygen content in the process gas during reactive sputtering at room temperature. The Fermi energy and conductivity of the material is strongly affected, which was presented in the preceding section. In order to investigate similarities between samples from UNL and TU Darmstadt, one option was Raman spectroscopy.[19]

[1] The formation of metallic copper at the interface to another material is covered in Section 7.1.

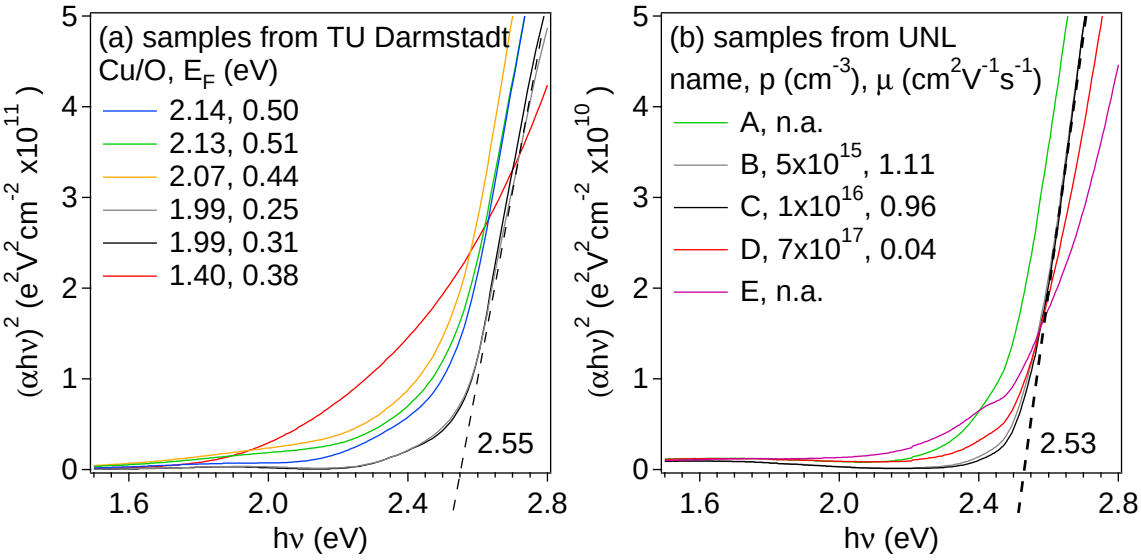

Figure 4.2: Absorption data from optical transmittance of (a) samples from TU Darmstadt, including in situ XPS data and (b) samples from UNL, including data from Hall effect measurements (n.a. means *non applicable*, since these samples were not measurable by the Hall effect method). The TU Darmstadt samples were deposited on ITO-coated glass substrates, whereas the UNL samples were grown on corning glass. The value of the optical band gap of stoichiometric Cu_2O films is indicated in the lower right corner of each graph.

However, it was found that this technique could not detect the small differences in oxygen content, probably due to a high degree of disorder in the material deposited at room temperature. Furthermore, a Raman system was available only by collaboration with other groups, like the Chemistry Department of UNL or the Physics Department of the University of Aveiro.

The technique which was found most sensitive to compare the films of the different institutes was transmittance spectroscopy. This is due to the fact that on the one hand, Cu_2O exhibits the onset of optical absorption at the lowest energy of all possible compounds, which can be formed with oxygen (Cu_3O_4 and CuO).[19] On the other hand, metallic copper also introduces additional absorption for energies below the band gap of Cu_2O, which is readily detected by this technique. Figure 4.2 shows a comparison of absorption coefficients (a) of samples deposited at TU Darmstadt, which were analyzed by in situ XPS and (b) of samples from UNL, which were measured by the Hall effect method. The data is represented in order to be evaluated for optical band gap determination as direct, allowed transition according to the Tauc method.[207] From top to bottom, the legend of each plot refers to samples deposited with an increasing oxygen amount. The increase of oxygen amount in the process gas is particularly clear in Figure 4.2 (a) from the decreasing Cu/O ratio. The colors are chosen to approximately show similarities between samples from the different universities.

The absorption spectra are not identical, which is partly due to the different substrates (ITO-coated glass for TU Darmstadt samples and corning glass for UNL samples). However, with a band gap of 2.8–2.9 eV,[216] ITO does not have a significant influence on the absorption at the energies represented in the figure and is consequently neglected in the calculation of the absorption coefficient. The important part of the data is the onset of light absorption: In Figure 4.2 (a), the onset occurs at the highest energies for the most stoichiometric Cu_2O films. In Figure 4.2 (b), a similar trend is seen with respect to the lowest carrier concentration and the highest mobility. Similar to the samples of (a), these films were deposited with increasing oxygen content in the process gas (from green to purple). No data on electrical properties are available for the samples deposited at the extreme oxygen contents (sample A: 4.5 % and sample E: 6.5 %), since the Hall coefficient had alternating signs during the measurement (see Section 4.3). Judging from the highest observed onset of adsorption, the samples represented by the gray and black lines in both figures exhibit the lowest amount of copper-containing materials other than Cu_2O. The comparison to the Cu/O ratio in Figure 4.2 (a) confirms this. The values included in Figure 4.2 (b) show the comparatively high hole mobility and low concentration in these samples. The band gap for stoichiometric Cu_2O may be estimated, which produces almost identical values of 2.53 eV and 2.55 eV for films deposited at TU Darmstadt and UNL, respectively. This is in accordance with literature.[217–220]

Transmittance spectroscopy was used throughout the preparation of this thesis to ensure optimum stoichiometry, also of samples which could not be checked by in situ XPS. In this way, results of films produced at TU Darmstadt and at UNL may be safely correlated, as far as the oxygen content and the copper oxidation state of stoichiometric Cu_2O is concerned.

4.3 Hall effect measurements

The results from the Hall effect measurement of films deposited with different amounts of oxygen in the process gas have already been included in Figure 4.2 (b). The same results are shown in a different graphical representation in Figure 4.3 (a) for improved clarity. The average of at least 15 measurements has been calculated for each sample.

The conductivity increases with increasing oxygen content in the process gas. For an oxygen flow of 5 % and higher (samples B–E), the conductivites are similar to the in situ samples fabricated at TU Darmstadt, which were shown in Figure 4.1 (b). At the extreme oxygen contents (sample A: 4.5 % and sample E: 6.5 %) the measured average concentration had a negative sign, which indicates, that hole conduction is obstructed. Note that the negative Hall sign is not an indication for Cu_2O to be an n-type conductor, since this is thermodynamically impossible.[99] The highest mobility and lowest carrier concentration were obtained for sample B, which had been deposited at 5 % oxygen flow. A further increase in oxygen flow leads to a decrease in mobility and an increase in hole concentration. With a higher oxygen content, the electrical properties of the material

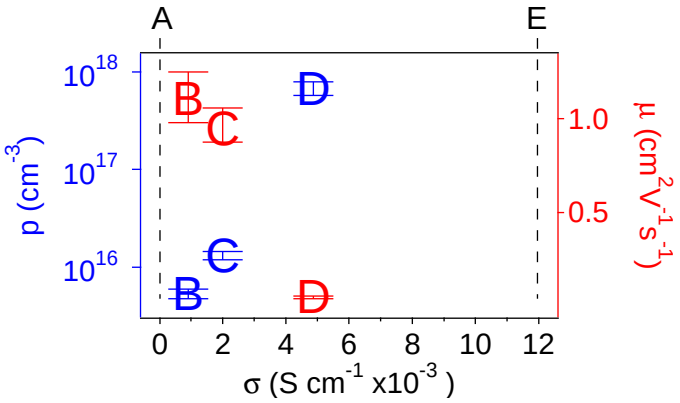

Figure 4.3: Results from Hall effect measurements of ≈ 100 nm Cu_2O on glass, deposited at UNL with different gas flow ratios of oxygen between 4.5 % and 6.5 % (samples A–E). Errors obtained from several repetitions of the measurement are indicated by error bars.

increasingly resemble the ones of CuO,[18] rather than of Cu_2O. With a hole mobility in CuO of $< 10^{-2}\,cm^{-3}$, the significant contribution of Cu(II) is most probably the reason, why at 6.5 % oxygen flow (sample E) a stable Hall voltage could not be obtained. The eventual formation of secondary crystallographic structures is investigated by XRD measurements in Section 4.4.

Results of stoichiometric Cu_2O samples deposited at TU Darmstadt are summarized in Table 4.1. The values as deposited are in a similar range as for the samples of UNL. A significant improvement of the mobility is obtained after a post-deposition annealing step at 200 °C in air, whereas the carrier concentration is not strongly affected. The change is smaller for the samples from UNL: The Hall mobility of samples B and C increases to 2.1 and $2.5\,cm^2V^{-1}s^{-1}$ and the carrier concentration to 3.7×10^{16} and $2.5\times10^{16}\,cm^{-3}$, respectively. The observed alterations due to the annealing suggest, that structural defects which cause carrier scattering are healed-out by the annealing, whereas an oxidation to Cu(II) does not appear to be significant during only 1 h of annealing. A detailed discussion of the influence of the temperature and the atmosphere on the hole mobility and the concentration can be found in Section 7.2.

Table 4.1: Hall effect measurements of > 1 µm thick samples on glass, produced at TU Darmstadt.

	σ (S cm^{-1})	μ ($cm^2V^{-1}s^{-1}$)	p (cm^{-3})
as deposited	4×10^{-4}	0.5	5×10^{15}
as deposited	3×10^{-2}	-	-
annealed (1h, 200 °C, air)	1×10^{-2}	33	2×10^{15}

Films deposited at TU Darmstadt had to be an order of magnitude thicker than the samples from UNL in order to be measurable by the Hall effect method. This influence of film thickness is likely a result of a change in grain size with thickness, according to

the growth model by Messier described in Section 2.5.1. Structural differences between the films from each institute, which are described in the following section, may cause the observed difference in electrical properties.

4.4 X-ray diffraction measurements

In order to confirm the crystallographic structure of the samples, X-ray diffraction is used. Figure 4.4 shows the diffraction patterns of films deposited at UNL (a) and at TU Darmstadt (c). Fig. 4.4 (b) features data from Powder Diffraction Files (PDF) of the respective phases (see figure caption). Generally, database entries of the highest quality (designated as "star") were used. If such was not available, like in the case of Cu_4O_3, a calculated pattern was used. Both the samples from UNL and TU Darmstadt were deposited at different oxygen contents in the process gas. The data shown in Fig. 4.4 (a) was obtained on the same samples as represented in Figure 4.2 (b) and Fig. 4.3 (a). Fig. 4.4 (c) shows a part of the samples, which are included in Figure 4.1 (b) as filled symbols.

The occurrence of a phase other than Cu_2O due to oxygen-poor deposition conditions can be observed in sample A of Figure 4.4 (a) by the presence of reflections of metallic copper, most prominently at the (111) planes under a diffraction angle of 43.298°. In the samples of pure Cu_2O phase from both institutes, a shift of the most intense Cu_2O reflections towards smaller diffraction angles is observed, when slightly oxidizing deposition conditions are applied. This has been observed in previous works and was interpreted as a manifestation of an increased copper vacancy concentration.[189] Interestingly, Cu_2O films at UNL exhibit compressive strain, whereas samples at TU Darmstadt are under tensile strain with respect to values from the database. The different deposition chamber geometries as well as differences in the deposition parameters (e.g. sputtering power, total pressure) are most probably responsible for this. The importance of strain for charge carrier mobility and the release of strain after post-deposition annealing are discussed in Section 7.2.

An important difference between samples deposited at UNL and TU Darmstadt is the orientation perpendicular to the sample surface. Even though the diffractometer at UNL was not equipped for rocking curve measurements, a qualitative conclusion is possible from the $\theta/2\theta$ scans. When confining the analysis to the angular range of the (111) and (200) reflections (36.419° and 42.298°, respectively), the change in sampling volume related to the illuminated surface area is in the range of 13 %, according to Equation 3.20. The intensity ratio (111)/(200) from the respective PDF is $100/37 \approx 2.7$. With this as a reference, the Cu_2O samples deposited at UNL show no significant preferential orientation along the surface normal, whereas samples from TU Darmstadt exhibit a dominance of (200) orientation. It is possible, that the preferential orientation in (200) of the samples from TU Darmstadt causes lower in-plane mobilities when compared to the rather isotropically oriented samples from UNL. In epitaxially grown samples, a dependence of the mobility on the orientation has been reported.[10] However, the samples were of

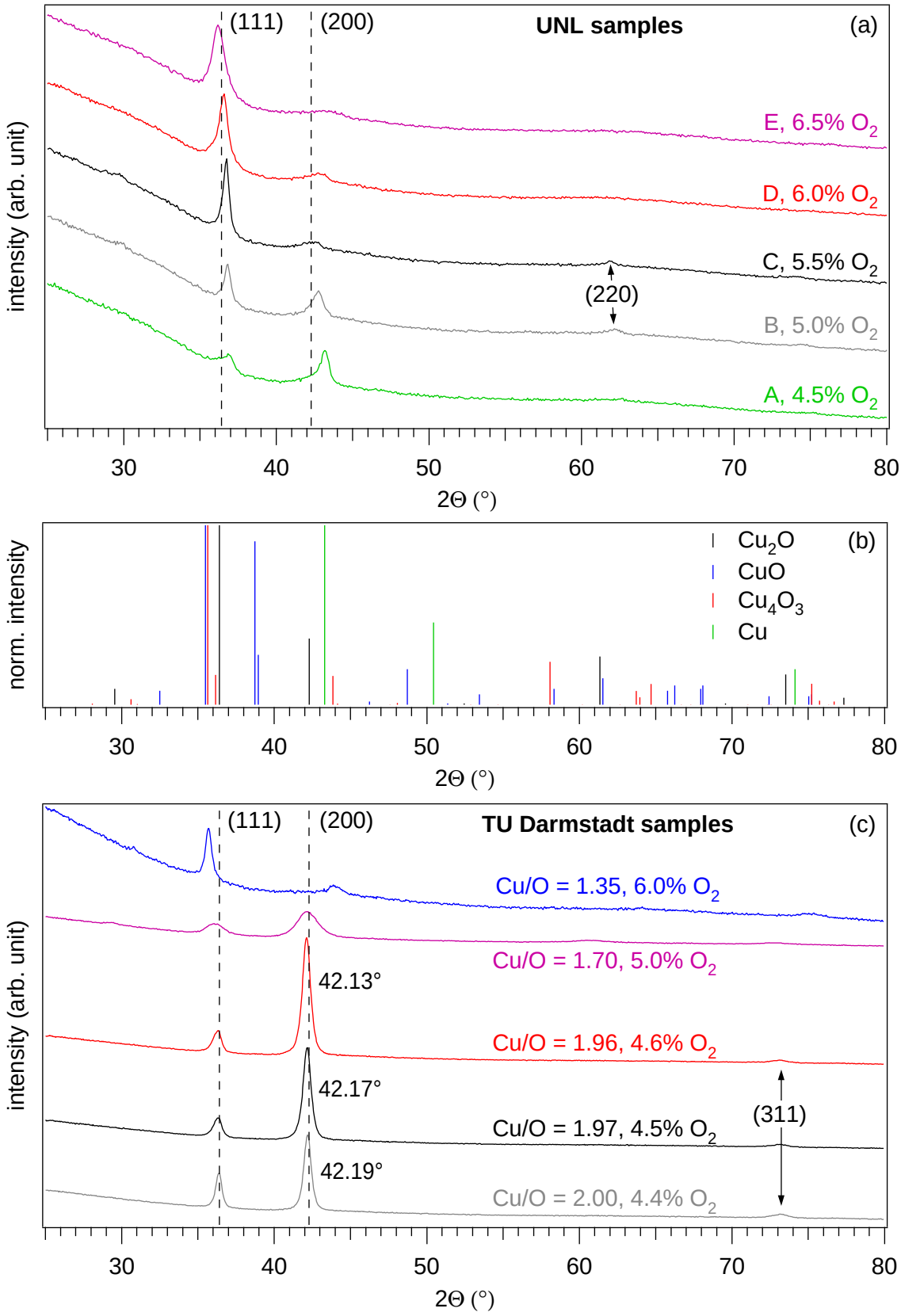

Figure 4.4: Diffraction pattern of samples (a) deposited at UNL and (c) at TU Darmstadt; (b) values from database entries, Cu: PDF 00-004-0836, Cu_2O: PDF 00-005-0667, Cu_4O_3: PDF 01-083-1665, PDF CuO: 00-045-0937.

different domain size, showing lower mobility at lower domain size. Indeed it is shown in Section 5.2.2, that the grain size plays a decisive role for Hall mobility and carrier concentration, since Cu(II) is segregated inside the grain boundary.

Increasing the oxygen content in the process gas during sputtering beyond the range, which leads to the deposition of a singular Cu_2O phase, results in the formation of Cu_4O_3, since the CuO (111) reflection at 38.731° is absent in Figure 4.4. This is valid for the samples deposited at both institutes. [2] The results reported in Chapter 5 suggest, that Cu(II) is segregated in the grain boundary of Cu_2O. Hence, the formation of a corresponding secondary phase might preferentially occur in the grain boundary. However, based on the XRD patterns it cannot be concluded here whether the secondary Cu_4O_3 phase is predominantly formed at the grain boundaries of Cu_2O.

4.5 Deposition rates analyzed by profilometry

The thickness of copper oxide thin films was measured with a profilometer. Divided by the duration of deposition, this results in the deposition rate. The deposition rate is an important factor for the interpretation of the thickness-dependent analyses of Chapters 5 and 6. As the deposition conditions were kept constant once the calibration for deposition of stoichiometric Cu_2O had been finished, a general deposition rate is calculated for the chambers at UNL and at TU Darmstadt. To obtain reliable results from the thickness measurements, an average of several point at different locations on the sample surface was calculated for each sample. Furthermore, the measured data from the profilometer was calibrated by using a standard sample, provided with the instrument. A large set of samples with thicknesses ranging from 250 nm to 1500 nm led to the average deposition rates as shown in Table 4.2. The uncertainty in the thickness measurement of a 1500 nm thick film is estimated to be of ±25 nm, which affects the value of deposition rate by ±0.15 nm/min. An uncertainty in the time measurement is assumed to be negligible with respect to the error in thickness determination.

Table 4.2: Deposition rates as determined by profilometry.

(nm/min)	Cu_2O	CuO
UNL	2.80	n.a.
TU Darmstadt	8.45	12.17

[2] Both Cu_4O_3 and CuO have their most intense reflection at slightly lower diffraction angles than the Cu_2O (111) planes (Cu_4O_3 (202) at 35.654° and CuO (002) at 35.496°). Even though these angles are close to the most intense Cu_2O reflection, the Cu_4O_3 (220) reflection at 43.834° and the CuO (111) reflection at 38.731° allow to distinguish a simple change in Cu_2O reflection angles from the formation of either of both secondary phases, provided the respective material is not textured.

4.6 Conclusion

The results presented in this chapter had the purpose to compare the film properties of copper oxide deposited at the two different institutes at which the work of this these was conducted. Samples deposited at UNL and TU Darmstadt behave similar to each other in terms of optical and (to a large extend) electrical properties, which were determined by optical transmittance spectroscopy and the Hall effect method, respectively. This allows a correlation of findings obtained by techniques exclusively available at either of both institutes, notably the in situ characterization by XPS at TU Darmstadt, which enables the measurement of the Fermi energy with respect to the valence band. However, the samples from the two institutes also showed differences, most importantly in the crystallographic orientation and residual strain. The Cu_2O samples from UNL had no preferential orientation and were compressively strained, whereas the samples from TU Darmstadt grew predominantly in (200) direction perpendicular to the film surface and under tensile strain. The differences in strain indicate that the films from TU Darmstadt are less dense compared to the samples from UNL. Tensile strain may be associated to the presence of voids inside the material, which are detrimental for charge carrier mobility.[22] A low density may explain why the samples from TU Darmstadt could not be measured by Hall effect prior to post-deposition annealing. Post-deposition heat treatments are investigated further in Section 7.2. When deposited at higher oxygen amount in the process gas, films from both institutes grow in a Cu_4O_3 structure.

By comparing the film properties of the samples from the two institutes, this chapter described correlations between stoichiometry and electrical properties, as well as optical and structural properties, which are general to polycrystalline Cu_2O. The findings were mainly interpreted by considering reduction or oxidation of the metal cation, since this could be observed by in situ XPS on films deposited with different oxygen amounts. The consequences for electrical properties of the resulting inhomogeneous semiconductor were put into focus. Metallic copper in contact with Cu_2O causes a depletion, whereas Cu(II) leads to an increase in carrier concentration and a decrease in carrier mobility. The important question of localization of these defects is addressed in the remainder of this thesis. Most importantly, in Chapter 5 it is shown that Cu(II) is contained in the grain boundaries of nominally stoichiometric Cu_2O.

Chapter 5

Partial oxidation in the grain boundaries of Cu_2O

This chapter is concerned with the cation oxidation state inside thin polycrystalline Cu_2O films, grown on different kinds of substrates. Section 5.1 presents results from in situ conductance measurements at thicknesses from sub-nm to around 250 nm with parallel X-ray photoelectron spectroscopy. An enhanced conductivity at low thicknesses is explained by the occurrence of Cu(II), which is segregated in the grain boundary and locally causes a conductivity similar to CuO, although the surface of the thick film has Cu_2O stoichiometry. Since grains grow with increasing film thickness, the effect of an apparent oxygen excess is most pronounced in vicinity to the substrate interface. Electrical properties of Cu_2O grains are at least partially short-circuited by this effect. The study focuses on properties inherent to copper oxide, although interface effects cannot be ruled out. This non-destructive, bottom-up analysis reveals phenomena which are commonly not observable after device fabrication, but clearly dominate electrical properties of polycrystalline thin films. The results of this section have been published in the *Journal of Applied Physics*.[221]

In Section 5.2, data from Hall effect measurements at low temperatures and of samples with different grain sizes are presented. The evaluation of the activation energies supports the existence of Cu(II) in the material. The comparison of charge carrier concentrations and mobilities of samples with different grain sizes (mainly obtained from literature) proves the existence of a higher charge carrier concentration and a lower carrier mobility in the grain boundary of Cu_2O with respect to the grain interior. An attempt is made to represent the experimental data with the composite sphere model by Mathew *et al.*.

5.1 Highly conductive grain boundaries in thin films

The samples were prepared and analyzed in the DAISY-MAT system at TU Darmstadt. SiO_2 (quartz glass),[1] Al_2O_3 by ALD and Bi_2O_3 by sputter-deposition were used as substrates for the deposition of Cu_2O. Substrates of either 25 nm Al_2O_3 or 45 nm Bi_2O_3 deposited on quartz glass are referred to as **q/Al_2O_3** and **q/Bi_2O_3**, respectively. The plain ATO substrate (with the conductive ITO back contact) was used in two different runs of the experiments, referred to by **ATO (1)** and **ATO (2)**. Substrates with 45 nm Bi_2O_3 deposited on ATO were also analyzed twice, designated as **ATO/Bi_2O_3 (1)** and **ATO/Bi_2O_3 (2)**. Additionally, a CuO film was measured on ATO.

5.1.1 Electrical film properties

The different types of insulating substrates investigated in this study are referred to by the names shown in Table 5.1. Stoichiometry, Fermi energy and in situ conductivity σ from planar geometry of thick Cu_2O and CuO are reported. The conductivity is calculated according to Equation 5.1, where Y is the reduced conductance, corrected for the electrode geometry.

$$\sigma = \frac{l}{w}\frac{G}{d} = \frac{Y}{d} \tag{5.1}$$

The film thickness of the samples listed in Table 5.1 was generally 254 nm, except for sample ATO (1) (42 nm) and for CuO on ATO (366 nm). All surfaces of thick Cu_2O films are stoichiometric within an error of 5 %. Accordingly, they were free of the characteristic

Table 5.1: Stoichiometry, Fermi energy and conductivity (estimated from planar geometry).

substrate	ratio Cu/O	$E_F - E_{VB}$ (eV)	σ ($S\,cm^{-1} \times 10^{-3}$)
quartz (q)	1.98	0.26	0.3
q/Al_2O_3	2.13	0.23	2.2
q/Bi_2O_3	1.93	0.24	4.4
ATO (1)	1.89	0.27	10.2
ATO (2)	1.99	0.33	3.4
ATO/Bi_2O_3 (1)	2.05	0.29	8.6
ATO/Bi_2O_3 (2)	2.05	0.28	15.3
CuO on ATO	0.86	0.06	166.6

spectral features described in Section 3.3.1, which indicates the absence of Cu(0) and Cu(II). However, the conductivities at 254 nm film thickness are quite different according to the type of substrate. Cu_2O on quartz shows the lowest value, followed by the Al_2O_3 substrates. The low conductivity on quartz is not due to a measurement artifact, since a similarly low value was obtained on a sapphire substrate (not shown here). The highest conductivities in Cu_2O are obtained on Bi_2O_3 with further increase when deposited on

[1] The quartz glass substrates were provided by CrysTec.

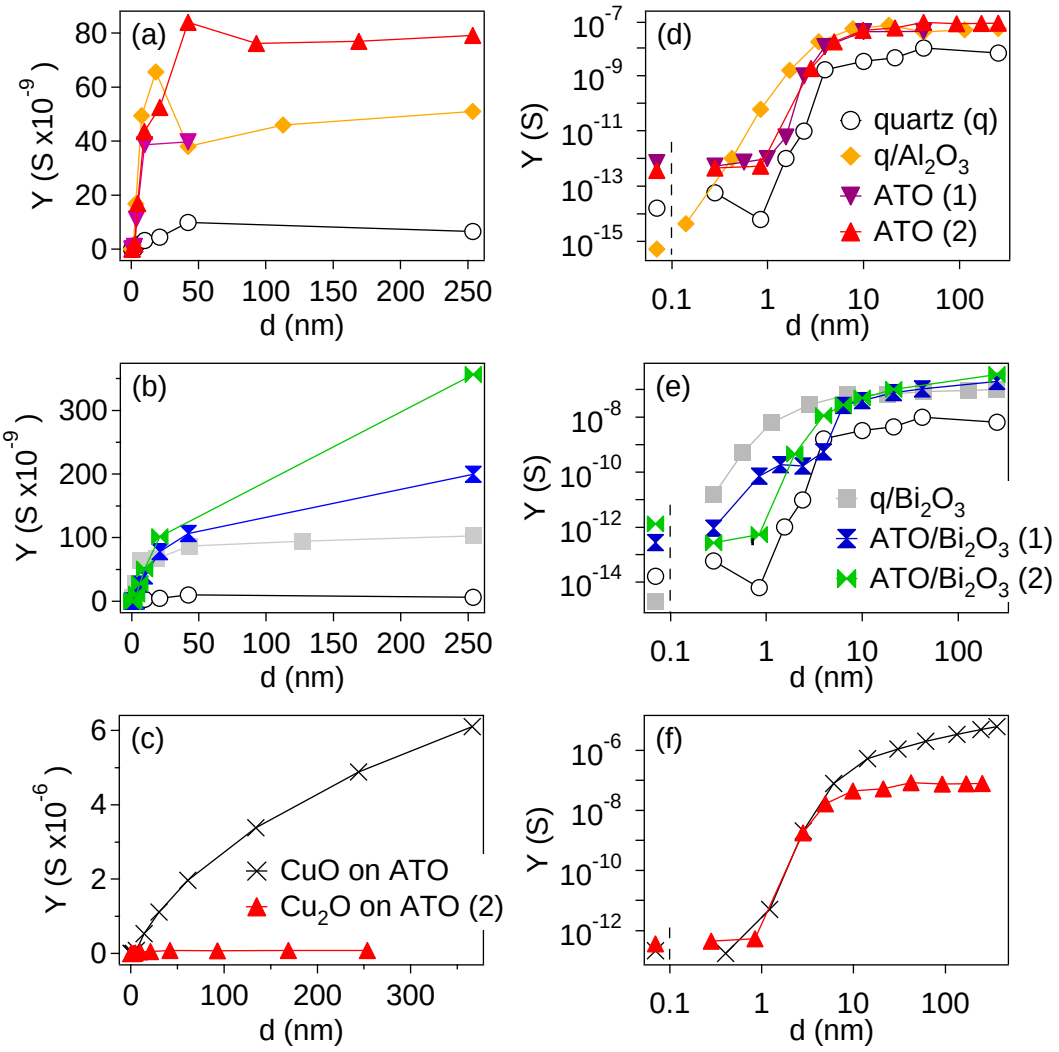

Figure 5.1: In situ reduced conductance data are shown with respect to increasing copper oxide thickness (a)–(c) on linear and (d)–(f) on double-logarithmic scale. The type of substrate is indicated, using the same nomenclature as in Table 5.1. (c)–(f) The data on CuO in shown, in comparison to Cu_2O on ATO (2). The values left of the broken line correspond to the uncoated substrate (at arbitrary thickness).

ATO/Bi_2O_3. In CuO, the conductivity is comparatively high in accordance with the low Fermi energy. The remainder of this article is concerned with the wide range of conductivities observed in Cu_2O by evaluating the data with respect to film thickness.

Figure 5.1 shows the change in reduced conductance with increasing copper oxide thickness on a linear scale and in double-logarithmic representation. The value of Y before any film deposition is at least five orders of magnitude lower than the final reduced conductance for all experiments. As the measurements were performed in the vacuum system directly after deposition, this observation is related to the film properties and not to an extrinsic surface effect, which may be caused, for example, by adsorbates. The most striking observation from Fig. 5.1 (a)–(c) is the strong initial increase of conductance at

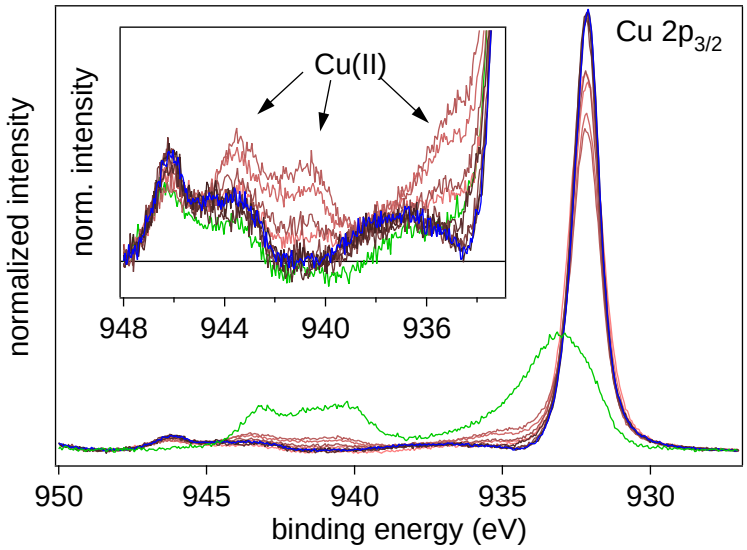

Figure 5.2: Spectra of the Cu $2p_{3/2}$ satellite region of copper oxide on q/Al_2O_3 are shown as example to illustrate the thickness-dependent amount of Cu(II) satellite emission and the procedure for semi-quantification. The blue curve is the spectrum after the final deposition step, which is supposed to represent pure Cu_2O. The dark brown to light brown curves are the spectra at intermediate thicknesses. The green curve represents data of CuO.

thicknesses below 10 nm, compared to the slope at higher thicknesses. This is found both for Cu_2O and CuO. Fig. 5.1 (d)–(e) reveal the different thicknesses, at which the onset of conduction occurs. The root mean square (RMS) roughness of ATO-based substrates is about 5 nm, which explains the observed higher conduction onset thickness compared to q/Al_2O_3 and q/Bi_2O_3. The quartz-based substrates have a similar RMS roughness of 0.4 nm. The reason for the relatively high onset thickness on quartz compared to q/Al_2O_3 and q/Bi_2O_3 is therefore most likely related to a different substrate-film interaction. In Figure 5.1 (f), it is noteworthy, that for thicknesses below 5 nm, the conductance of Cu_2O is nearly identical to CuO.

5.1.2 XPS analysis

Depending on the film thickness, systematic changes in Cu $2p_{3/2}$ satellite intensity from the Cu_2O films could be identified by XPS. Figure 5.2 shows the Cu $2p_{3/2}$ spectra of all Cu_2O thicknesses on q/Al_2O_3 as representative example. In order to obtain a semi-quantification of the relative amount of satellite emission with respect to film thicknesses, the following procedure was applied to each experiment: The background was removed according to the method of Shirley in the binding energy range of Cu $2p_{3/2}$ including the satellite region (around 927 eV–948.5 eV). Then the integral intensity of this region was calculated and the spectra were normalized to the respective area. The difference between the spectra of each thickness and of the final film was then calculated and integrated in

the region, where Cu $2p_{3/2}$ satellites typically appear (around 938.3 eV–945.8 eV). The relative satellite sensitivity of Cu_2O is zero by definition and around 0.3, when calculated for CuO.

The relative intensity of the Cu $2p_{3/2}$ satellite emission with respect to the main line intensity is plotted against Cu_2O film thickness in Figure 5.3 (a). In order to compare the data to the conductance results, the conductivity σ is shown in Figure 5.3 (b). A general accordance of Cu(II) satellite intensity and conductivity is observed. However, the maximum satellite intensity is generally observed at lower thicknesses than the maximum conductivity. Note that the substrate ATO (1) had been heated at 200 °C in 5×10^{-3} mbar oxygen for 2 h prior to film deposition. This additional surface cleaning step may be the reason for the lower satellite intensity compared to that of Cu_2O on ATO (2). However, this does not affect the film conductivity, which is similar for both samples.

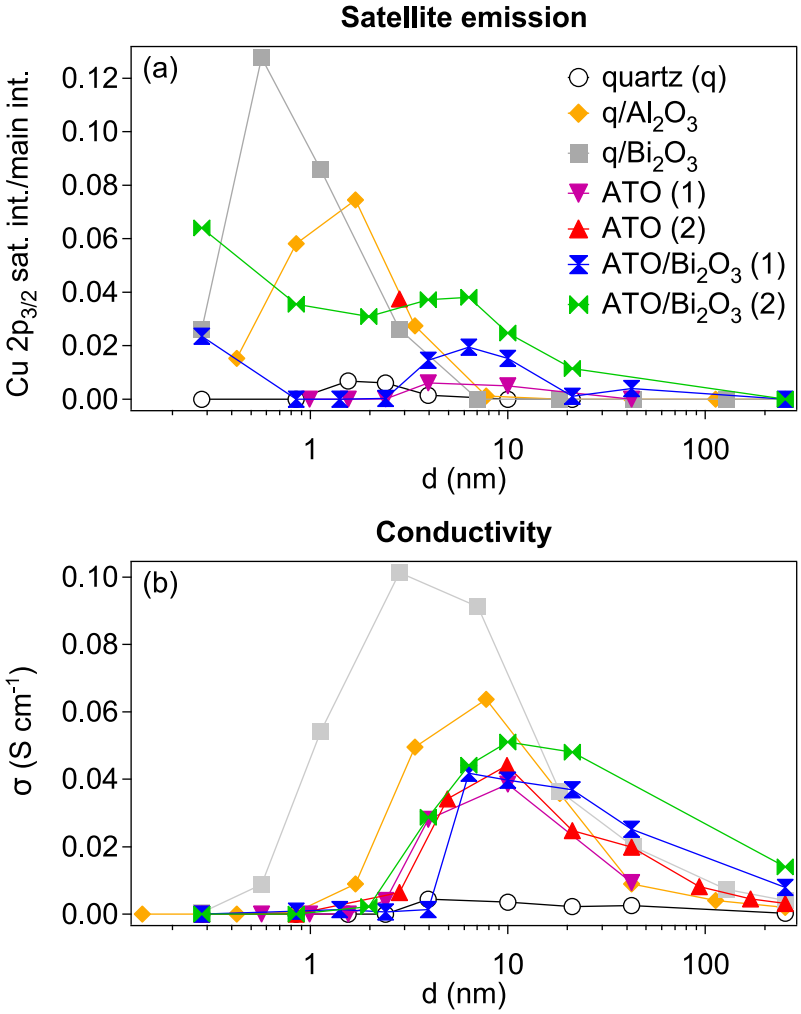

Figure 5.3: (a) The relative amount of Cu $2p_{3/2}$ satellite emission is displayed with respect to Cu_2O film thickness. XPS data of intermediate film thicknesses on ATO (2) has been acquired only at a thickness of 2.8 nm. (b) Conductivity with respect to Cu_2O thickness as calculated from reduced conductance data.

5.1.3 Morphology

There is a relationship between the excess conductivity and the Cu(II)-related satellite intensity, observed at low and intermediate Cu_2O thicknesses. In order to investigate whether grain boundaries have an effect on conductivity, the morphology of Cu_2O is included into the analysis. XRD has shown the material to be of polycrystalline cuprite structure without preferential crystallographic orientation, similar to previous work.[189] No CuO phase could be detected by XRD (not shown here). Cross-sectional SEM images of Cu_2O on corning glass and q/Al_2O_3 are displayed in Figure 5.4. A fibrous grain structure is found, with a lateral grain size which increases with thickness.[46] AFM topographies have been used to obtain a rough estimate of the grain size at the surface after complete film deposition. An average value of 35 ± 15 nm was obtained, without systematic dependency on the substrate material.

Conductive atomic force microscopy (CAFM) was measured to obtain direct evidence for an increased grain boundary conductivity. The best results were obtained on a 100 nm thick sample deposited on ITO-coated glass in a commercial stand-alone sputtering chamber by AJA International. On these samples, Cu_2O phase purity without preferential crystallographic orientation was confirmed by XRD (see Appendix A) and optical transmittance spectroscopy (not shown here). Topography and current map are presented in Figure 5.5. The thin bright lines of increased current between the grains are clear evidence for an increased grain boundary conductivity.

5.1.4 Discussion

When the lateral grain size L_{grain} increases with thickness according to Equation 2.20, the volume fraction of grain boundaries decreases with increasing thickness. Consequently, if a grain boundary effect is at play, enhanced conductance at low thicknesses can only be explained by the existence of more conductive grain boundaries with respect to the grain interior. Göbel *et al.* have described the increase in grain boundary conductance for the columnar morphology of their samples by a model of cuboid grains of horizontal dimensions L_{grain} and a vertical extension equal to the film thickness d.[65] Grain boundaries perpendicular to the current flow are neglected. The total reduced conductance Y with

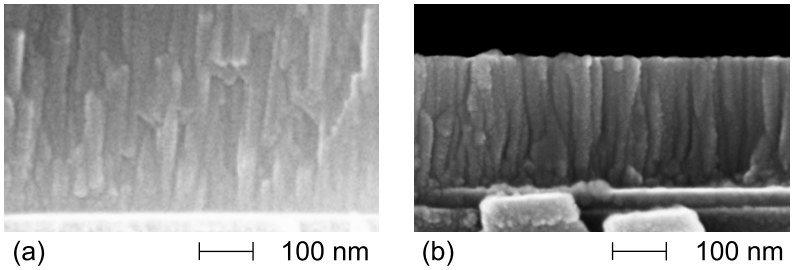

Figure 5.4: Cross-sectional SEM images of Cu_2O (a) on corning glass and (b) on q/Al_2O_3.

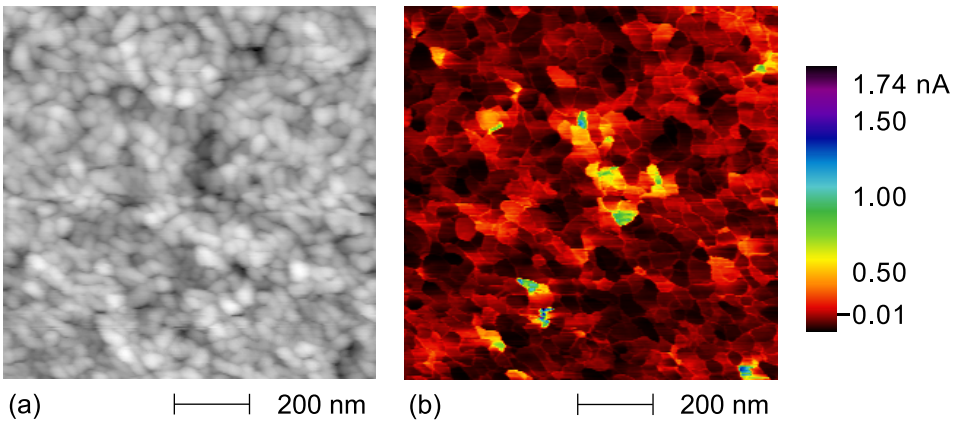

Figure 5.5: (a) Topography and (b) current map of Cu_2O on ITO-coated glass.

respect to thickness is expressed as parallel connection of grain conductance Y_{grain} and grain boundary conductance Y_{GB}.

$$Y = Y_{\text{grain}} + Y_{\text{GB}} \tag{5.2}$$

The situation is illustrated in Figure 5.6 (a). Figure 5.6 (b) shows a schematic representation of a film morphology with linear cone faces. This grain structure corresponds to Equation 2.20 with an exponent $n = 1$. Upon an increase in average grain size L_{grain} with d, regions close to the substrate interface remain at smaller L_{grain} than regions close to the film surface. For this reason, the total conductance needs to be integrated over thickness.

$$Y(d) = \int_0^d \sigma^*(z)\,\mathrm{d}(z) \tag{5.3}$$

When dividing $Y(d)$ by the film thickness d according to Equation 5.1, an average value for conductivity of the inhomogeneous thin film is obtained. An expression for $\sigma^*(z)$, which satisfies the interpretation by Göbel *et al.*, is given in Equation 5.4.

$$\sigma^*(z) = \sigma_{\text{grain}} \frac{L_{\text{grain}}(z)}{L_{\text{grain}}(z) + L_{\text{GB}}} + \sigma_{\text{GB}} \frac{L_{\text{GB}}}{L_{\text{grain}}(z) + L_{\text{GB}}} \tag{5.4}$$

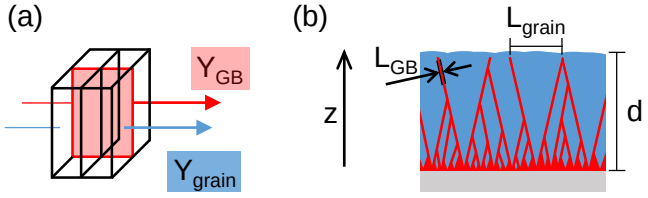

Figure 5.6: (a) The two parallel currents through the grain boundary (red) and through the grains (blue) are illustrated, together with the respective reduced conductances. (b) Schematic representation of the film morphology, where L_{grain} is the grain size, L_{GB} the width of the grain boundary and d the film thickness along z.

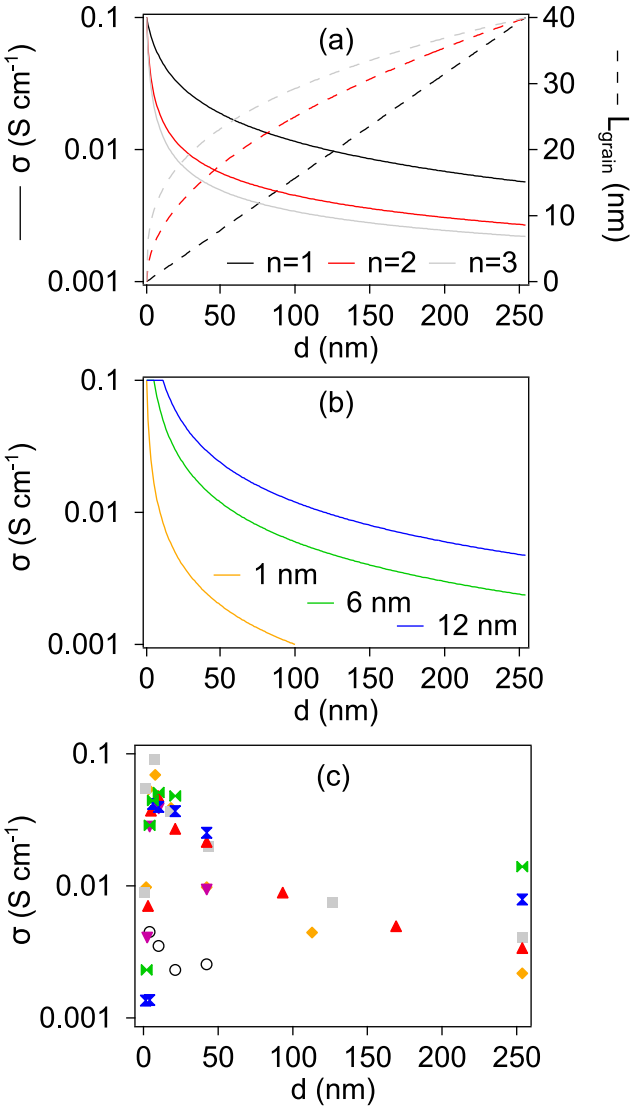

Figure 5.7: Effective conductivity from calculation for different (a) grain growth models $L_{grain}(z)$ and (b) interface layer thicknesses. The final grain size of $L_{grain} = 40\,nm$ is similar to the experimentally obtained values. (c) Conductivities from the experiment are shown with the same symbol coding as in Fig. 5.1 and 5.3.

The symbols σ_{GB} and σ_{grain} are the respective conductivities of grain boundary and grain. The grain boundary width L_{GB} is below a nanometer, since it describes a rather highly doped region.[65] Figures 5.7 (a) and (b) show results from the model, calculated with $L_{GB} = 0.5\,nm$. In the calculation, the grains begin to grow laterally only at a thickness of 1 nm, which is supposed to account for an interface layer of high conductivity, equal to σ_{GB}. The conductivity inside the grains is chosen equal to monocrystalline Cu_2O and the grain boundary conductivity is within the range of typical values for CuO ($0.01\,S\,cm^{-1}$ as single crystal and $1\,S\,cm^{-1}$ as thin film, sputtered-deposited at room temperature).[9, 18, 57] All curves have been calculated with $\sigma_{grain} = 10^{-6}\,S\,cm^{-1}$ and $\sigma_{GB} = 0.1\,S\,cm^{-1}$. For comparison, Fig. 5.7 (c) reproduces the measured conductivities on the same scale. Due to the limited amount of data points at different thicknesses for each substrate material, a reliable fitting of the data could not be conducted.

Fig. 5.7 (a) illustrates the effect of different $L_{grain}(z)$ on the calculated conductivity. Apart from of the linear relation (Equation 2.20 with $n = 1$), a square dependency ($n = 2$)

in red and a cubic one ($n = 3$) in gray are displayed. The more drastic the initial increase in L_{grain}, the stronger is the conductivity decay with increasing thickness. Fig. 5.7 (b) shows that a similar change in σ can be obtained by considering an interface layer with a conductivity equal to σ_{GB} and a monocrystalline bulk material of σ_{grain}.

It is apparent from Figure 5.7 that thickness-dependent analysis of conductance alone cannot distinguish whether an enhanced conductivity at low thickness is due to an interface or a grain boundary effect.[65] For this reason, additional experimental evidence needs to be considered. In a previous study, conductivity measurements on CuO thin films of different grain sizes with respect to temperature and atmosphere revealed the existence of more conductive grain boundaries in this material.[57] In the light of the present discussion, this corresponds well to the initially enhanced conductivity in CuO displayed in Figure 5.1 (c) and (f). For bulk samples of Cu_2O, there is evidence in literature to support the idea of an increased grain boundary conductivity.[14, 15] Hall effect measurements on Cu_2O thin films by Lee *et al.* confirm this, although not discussed by the authors: As the average grain size is reduced by two orders of magnitude, (1) carrier concentration increases while mobility decreases up to the point that no stable Hall voltage is obtained. Simultaneously, (2) the concentration of ionized impurities increases, which dominate charge carrier scattering at low temperatures.[46] An increasing impurity concentration gradually changes the electrical properties of Cu_2O to be rather similar to CuO. Given the possibility of highly conductive grain boundaries, a segregation of defects in the grain boundary can correlate observation (1) with observation (2). Consequently, grain boundaries are concluded to be the cause for the increased conductivity at low film thickness, as presented in this article. The results presented here show that XPS is able to detect the relevant change in cation oxidation state to prove the existence of Cu(II). The increased Cu(II)-related intensity at low film thickness, where grain size is expected to be relatively small, suggests that Cu(II) is present at the grain boundaries of Cu_2O. It is important for this assignment that the analysis is carried out in dependence on thickness, non-destructively and in vacuum, which prevents surface oxidation.

The Cu_2O films are rich in oxygen at low thickness, despite no sign for non-stoichiometry at high thickness (see Table 5.1). Under more reducing deposition conditions, the formation of Cu(0) becomes more likely. The width of the depletion layer, caused by the Cu/Cu_2O Schottky junction is 0.5–1 µm.[17] In case Cu(0) segregates in the grain boundaries, grains of similar size as in the present study would be fully depleted and no thickness dependence of conductivity could be observed by the here applied experimental procedure.

Given that Cu(II) is present at the grain boundaries in Cu_2O thin films, the film may be approximated by Cu_2O grains separated by CuO grain boundary phases. Transmission electron microscopy could confirm the existence of a CuO phase between Cu_2O grains, however an in situ sample preparation procedure would be required to prevent additional oxidation by exposure to ambient air, which was not available. In case any CuO phase is formed, the interface between Cu_2O and CuO is important for determining the grain

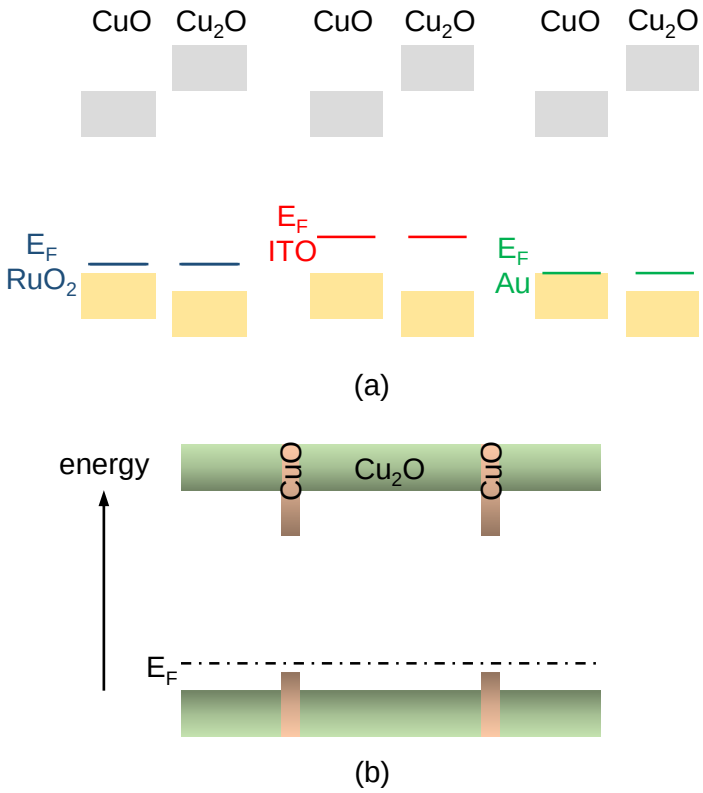

Figure 5.8: (a) Fermi energies in the band gap of CuO and Cu_2O at the contact to different metals. Valence band and conduction band are designated as VB and CB, respectively. (b) Schematic energy band alignment between grains of Cu_2O and grain boundaries of segregated CuO.

boundary properties. As a direct determination of the energy band alignment between Cu_2O and CuO is not possible using photoemission, the corresponding alignment is derived here using the transitivity rule according to $\Delta E_{VB}(Cu_2O, CuO) = \Phi_B(Cu_2O, M) + \Phi_B(M, CuO)$. Φ_B is the Schottky barrier for holes at the corresponding interface. M represents a common metal. This procedure has been successfully applied to interfaces of semiconducting oxides.[222, 223] Figure 5.8 (a) schematically shows Fermi energies in Cu_2O and CuO at the contacts to RuO_2, ITO and Au. The data have been obtained by photoemission according to the method by Kraut *et al.*[172] and are partially taken from previous studies.[57, 139, 189] The valence band discontinuity between CuO and Cu_2O is 0.2 eV. In the case of a grain boundary segregation of CuO in Cu_2O, a schematic energy band alignment as sketched in Figure 5.8 (b) will occur. The higher valence band maximum at the grain boundaries immediately explains the higher carrier concentration and therefore the higher conductivity of the grain boundary.

5.2 Carrier concentration and mobility in the grain boundaries

The highly conductive grain boundaries in Cu_2O are due to the occurrence of Cu(II). If the grain boundaries have electrical properties similar to CuO, the local conductivity should be caused by the corresponding charge carrier concentration and mobility.[18] In order to analyze the impact of Cu(II) on the electrical properties of Cu_2O further, Section 5.2.1 reports and discusses both Hall carrier concentration and mobility at different temperatures. In Section 5.2.2, Hall effect data of sputter-deposited Cu_2O samples with different grain sizes are compared and tentatively represented by the composite sphere model by Mathew *et al.*.[62]

5.2.1 Hall effect measurements at low temperature

A Cu_2O sample on corning glass, which had been deposited at TU Darmstadt and annealed for 1 h in air at 200 °C was measured in the commercial Hall effect system at UNL.[2] The thickness of the film was 1380 nm.

Carrier concentration

Figure 5.9 graphically displays the conductivity σ and carrier concentration p with respect to the absolute temperature, a well as a fit of the carrier concentration, which is descried further below.

The conductivity drops with a decrease in temperature, which is typical for a semiconductor. This is predominantly due to the carrier concentration, which follows the Boltzmann equation (in case of a non-degenerate semiconductor) given in Equation 2.4. In the presence of dopants, charge neutrality governs the amount of charged dopants according to Equation 2.15, which makes use of Equations 2.16 and 2.17. If only one active

[2] Prior to the annealing, no stable Hall voltage could be measured.

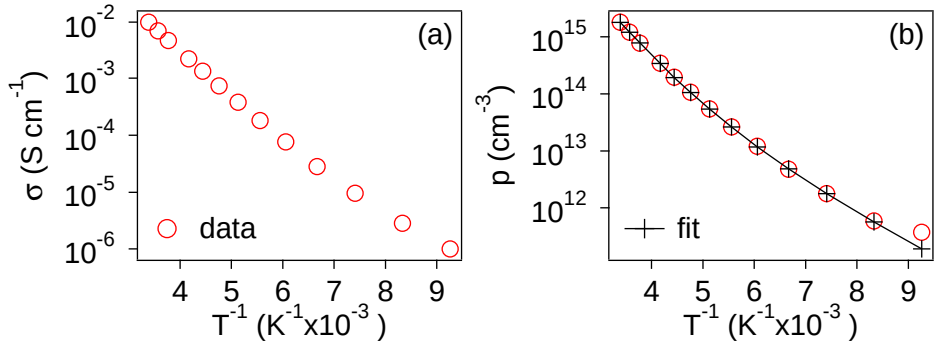

Figure 5.9: Graphical representation of (a) conductivity and (b) hole concentration of Cu_2O with respect to temperature between 108 K and 295 K, together with results from data fitting (black crosses and line).

dopant exists,[3] the Arrhenius plot of the carrier concentration exhibits a single slope. In the case of the data of Figure 5.9 (b), the slope is not constant. Similar observations have been reported for Cu_2O deposited by sputtering at relatively low temperatures.[46, 87] In order to fit the temperature-dependent carrier concentration as shown by the black line, three acceptor levels and a compensating donor level are assumed. The procedure is shortly outlined in the following: Due to the complete ionization of the donor, the respective transition level in the band gap is not relevant for the analysis. Adding more than one active dopant to Equation 2.15 (which is quadratic in case of one active dopant) increases its dimension successively. For this reason, the here represented situation of three active dopant levels is solved iteratively. A certain initial set of input parameters is assumed comprising the transition level and the concentration of each acceptor according to Equation 2.16. Similar to Figure 2.1, the charge concentrations of all charged acceptors, the completely ionized donors and the free hole charge concentration are graphically displayed with respect to the Fermi energy. After calculating the total charge of the system, the Fermi energy at charge neutrality is determined for all temperatures used in the experiment. From the Fermi energy at charge neutrality the free hole carrier concentration is calculated at each temperature using Equation 2.4. The plot against temperature allows for a comparison to the experimental data, followed by appropriate manual adjustment of the input parameters for subsequent calculation runs. This procedure is repeated until the best fit is obtained. Note, that the results can only be regarded as an approximation, since the evaluation of the fit quality is performed by manual comparison to the experimental data.

The fit represented in Figure 5.9 (b) is achieved with the following parameters shown in Table 5.2. The highest acceptor concentration is found at an energy above the valence band maximum of 0.1 eV. With successively lower defect concentrations, acceptor levels are further identified at 0.34 eV and 0.23 eV. The material is highly compensated, since N_D/N_{A1} is close to unity.

Table 5.2: Defect energies and concentrations used for the fitting of carrier concentration in Figure 5.9 (b).

E_{A1} (eV)	E_{A2} (eV)	E_{A3} (eV)	N_{A1} (cm^{-3})	N_{A2}/N_{A1}	N_{A3}/N_{A1}	N_D/N_{A1}
0.1	0.23	0.34	10^{18}	10^{-3}	0.2	0.99965

Discussion of the activation energies

The energy levels given in Table 5.2 correspond well to the values reported in literature (see Figure 2.12). Since nanocrystalline metallic copper precipitates are unlikely to be present in the material due to the annealing in air, the observed range of activation energies is not related to a depletion by Cu/Cu_2O Schottky barriers.[120] Note, that the

[3] A dopant is active when the energy of charge transition is in a range of $< 3kT$ from the Fermi energy.

main defect level is found at 0.1 eV which is rather low for Cu_2O, but similar to the value of CuO (0.12–0.15 eV).[18] This could be an indication for the formation of CuO in the grain boundary. But even if no CuO phase is formed, the occurrence of Cu(II) in the film is likely to cause additional shallow defect levels, which give rise to an activation energy similar to CuO: As mentioned in Section 2.6.1, divalent metal ions such as Mg(II) and Sr(II) form a complex with two copper vacancies, which has an acceptor level in the Cu_2O band gap at 0.1 eV.[101–103] It is proposed here, that Cu(II) can have a similar effect on the acceptor doping of Cu_2O as other divalent metals ions have. The formation of the defect complex between Cu(II) and two copper vacancies possibly leads to the CuO-like electrical properties in the grain boundary and is thus and an alternative explanation to the formation of nanocrystalline or amorphous CuO.

Carrier mobility

The mobility is shown in Figure 5.10 together with a reprint of data from Lee *et al.* on sputter deposited Cu_2O,[46] which in addition featured several data sets on monocrystalline Cu_2O.[9, 89, 224–226] Lee *et al.* have shown two scattering processes which limit the mobility of their samples: At high temperatures, scattering at longitudinal-optical phonons dominates.[75] At low temperatures, scattering at ionized impurities is the main mechanism, which is described by Equation 3.17.[47] Our data confirms the occurrence of both scattering mechanisms in the material.

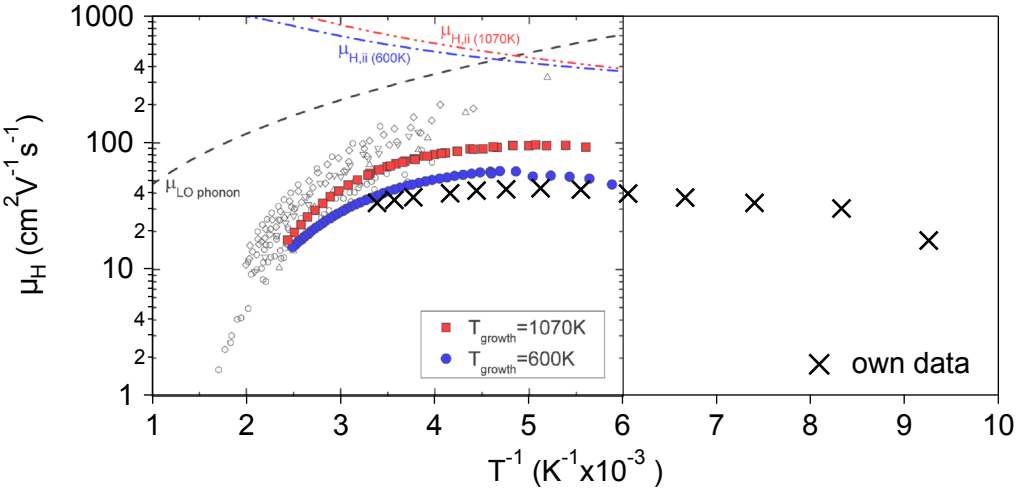

Figure 5.10: Hole mobility of Cu_2O with respect to temperature between 108 K and 295 K is shown by black crosses and compared to a compilation of results from literature on sputter-deposited Cu_2O (red squares and blue circles),[46] and data sets on monocrystalline Cu_2O (empty symbols).[9, 89, 224–226]

5.2.2 Hall effect measurements with different grain sizes

It was mentioned in Section 5.1.4, that electrical properties measured by the Hall effect method are reported in literature, which showed a dependence on grain size of polycrystalline Cu_2O.[46, 74] The existence of a grain boundary with high carrier concentration and low carrier mobility, similar to CuO, shall be verified here by a representation of experimental Hall effect data of sputter-deposited polycrystalline Cu_2O samples with respect to grain size.

In Section 2.5.2, the composite sphere model by Mathew *et al.* was introduced as the only formalism reported in literature, which provides equations for the interpretation of Hall effect measurements of a composite material with highly resistive particles in a highly conductive matrix phase. The parameters used for the calculation are equivalent to the ones used for the evaluation of the thickness-dependence of conductivity in Section 5.1.4. The results of the calculation according to the composite sphere model are graphically displayed in Figure 5.11 as black lines and compared to experimental data: The tilted squares and crosses represent results from this work, which are equivalent to the results shown in Table 4.1. In black, Cu_2O without post-deposition annealing is shown and in red after 1 h at 200 °C in air. For the grain size at the surface, a value of 45 nm was found, which did not change considerably during the annealing. The upright squares and crosses show results published in literature (in blue and green).[46, 74]

The grain sizes of the samples reported in the here cited literature have been determined from SEM images of the respective surfaces. Either SEM or AFM measurements of the surfaces of the samples prepared in this work were used to obtain a measure of the grain size which allows the comparison to the data from literature. Note, that the grain size at the sample surface is used and not an average grain size. The eventually decreased grain size from the surface towards the interface with the substrate is disregarded.

The experimental data show a clear trend of decreasing carrier concentration and increasing carrier mobility with increasing grain size. An exception is the Hall mobility obtained in this work prior to post-deposition annealing, which is comparatively small. Comparing the calculated black curves to the experimental data shows, that the carrier concentration is generally overestimated and the Hall mobility underestimated by the model by Mathew *et al.*. Since the correspondence of the model to the experimental data is not satisfactory, an empirical fitting is performed by a power law $y = A \cdot x^k$, with y being either the carrier concentration or the mobility and x the grain size L_{grain}. The power law fit to the experimental data results in exponents of $k = -0.88$ for the hole concentration and $k = 0.33$ for the mobility.[4] A power law fit to the modeled data according to Mathew *et al.* yields $k \approx -2$ for the hole concentration and $k \approx 1$ for the mobility.

[4]Since the experimental mobility of the as deposited sample of this work is significantly lower compared to the samples from literature, the corresponding data point is excluded from the fitting.

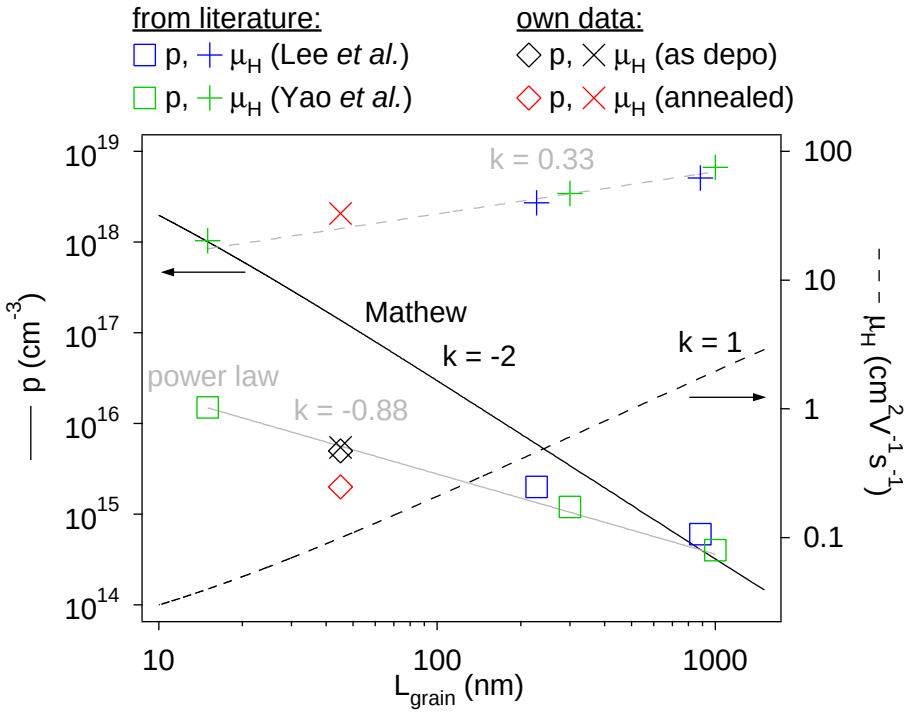

Figure 5.11: Experimental Hall concentration and mobility from this work as well as of Lee *et al.* [46] and Yao *et al.* [74] with respect to grain size. Predicted data according to the model by Mathew *et al.* is shown by the black lines.[62] In addition, an empirical fit by a power law is shown by the gray lines. The solid lines represent the concentration and the broken lines the mobility.

Discussion

The clear trends described by the experimental Hall effect data with increasing grain size confirm the existence of a high carrier concentration and a low carrier mobility inside the grain boundaries of Cu_2O with respect to the grain interior.

The experimental hole concentration and Hall mobility of this work after the post-deposition annealing correspond to the trend described by the data from literature. Only the Hall mobility before the annealing is significantly lower than the general trend. This lower mobility is possibly related to a higher degree of disorder in the grain boundary of the material, which causes additional charge carrier scattering. A less disordered structure in the grain boundary of the samples from literature could be due to the generally higher temperatures during fabrication, compared to the present work. Another possible explanation for the lower mobility could be the increased grain size towards the interface to the substrate. However, in this case the carrier concentration of the as deposited films produced in the present work would have to be higher than of the literature samples. Since the carrier concentration follows the trend of the literature data, the decreased grain size is discarded as explanation.

The comparison of the model by Mathew *et al.* to the experimental data from literature shows, that the model is not adequate to describe the experimental results from Hall effect measurements on polycrystalline Cu_2O. The model overestimates the charge carrier concentration and underestimates the mobility towards low grain sizes. This is probably because the composite sphere model assumes isotropic grains, whereas the film morphology is clearly anisotropic. The grains of the polycrystalline thin film are considerably more extended in the direction orthogonal to the substrate surface, than parallel to the surface. This can cause the more pronounced increase of the grain boundary fraction with decreasing grain size in the composite sphere model compared to the experimental data.

Apart from the differences in the shape of the grains, the restrictions to the model geometry in order to obtain the analytic expressions, as described in Section 2.5.2, do not apply for the experimental morphology. In a polycrystal, the grain boundary volume fraction decreases with the grain growth while the grain boundary width stays constant. Instead, in the composite sphere model by Mathew *et al.*, the grain boundary volume fraction decreases when the ratio between shell radius and core radius becomes smaller. For a given volume fraction, the sample space is assumed to be filled with spheres of the same ratio between shell and core radii, but of different absolute size. This variable absolute grain size in the model is possibly another reason, why the experimental carrier concentration and mobility of the Cu_2O polycrystals cannot be described. The density of conductive paths through the grain boundary (i.e. the shells of the composite spheres) towards lower grain sizes increases more strongly than it does in the experimental morphology.

Note, that differences in the absolute values can always be caused by a wrong choice of parameters. However, the discrepancy between model and experiment in the exponents of the power law fits prove the failure of the model independently on the absolute values of concentration and mobility.

5.3 Conclusion

The analysis of conductance with respect to the film thickness in UHV conditions has shown increased conductivity in polycrystalline Cu_2O thin films at low thicknesses. By simultaneous XPS measurements, this could be related to the occurrence of Cu(II), giving rise to a rather oxygen-rich region at low thickness, even in case of ideal stoichiometry at the surface of the final film. These extrinsic defects are likely to be segregated in the grain boundaries, causing the electrical properties of the same to be similar to CuO and masking the low carrier concentration and high hole mobility of Cu_2O thin films. As grains grow with increasing thickness, the strongest conductivity enhancement occurs at the interface to the substrate. Additional effects at the interface also have to be considered, as they cannot be ruled out by this method. One requirement for fabrication of

low-cost transparent electronics is a thin p-type semiconducting oxide, deposited at low temperature.

The evaluation of the Arrhenius plot of carrier concentration with respect to temperature revealed a range of activation energies instead of a single value. The energies corroborate previously reported results on Cu_2O. However, the defects with the highest concentration were found to have an acceptor state at 0.1 eV above the valence band maximum. Such a low acceptor energy is rather typical for CuO than for Cu_2O. This indicates the presence of Cu(II) in a sample of polycrystalline Cu_2O structure and shows its impact on the effective charge carrier concentration of the material.

The mobility at low temperatures enabled to identify the main scattering mechanism as ionized impurity scattering. With the clear trend of decreasing carrier concentration and increasing mobility with increasing grain size found for the experimental data, a segregation of Cu(II) in the grain boundary is confirmed.

The composite sphere model by Mathew *et al.* is not capable of reproducing carrier concentration and mobility obtained by the Hall effect method on the samples with different grain sizes. This supports the validity of the choice of the model by Göbel *et al.* in order to describe the influence of morphology on the inhomogeneous conductivity of polycrystalline Cu_2O.

Chapter 6

Energy band alignments at the nanoscale

As mentioned in the introduction, the interface between dielectric and semiconductor is significant for the performance of a TFT device. The preceding chapter investigated electrical and chemical properties of Cu_2O growing on different substrates, including Al_2O_3 and Bi_2O_3. In this chapter, the corresponding energy band alignments are presented, which were evaluated based on the method by Kraut and co-authors.[172] Substrates of Al_2O_3 by ALD are studied both as part of the multi-layer dielectric ATO (having 25 nm of pure aluminum oxide at the surface) as well as deposited as individual layer on ITO. Another type of substrate is sputter-deposited Bi_2O_3. The respective spectra are shown in the first section, including the evaluation of their chemical information. This is followed by a comparative resume of the respective energy band alignments at the interface. The discussion includes considerations on the usefulness of the Auger parameter in this type of analysis in order to decrease the necessary film thickness for the determination of the valence band offset below 1 nm.

The film thickness was controlled by the deposition time. The thickness can be evaluated by the damping of substrate intensities by the additional film material as described by Equation 3.10. This analysis requires a layer-by-layer growth. As this was not explicitly verified here, and thus an evaluation of thickness by XPS intensities could be subjected to error, the typical growth rate of stoichiometric Cu_2O as presented in Section 4.5 was simply assumed to be linear down to zero thickness.

6.1 Detail spectra

6.1.1 ATO/Cu_2O

In order to determine changes in the Fermi energy due to contact formation, core levels of both materials are measured after step-wise deposition. The obtained spectra of Cu 2p,

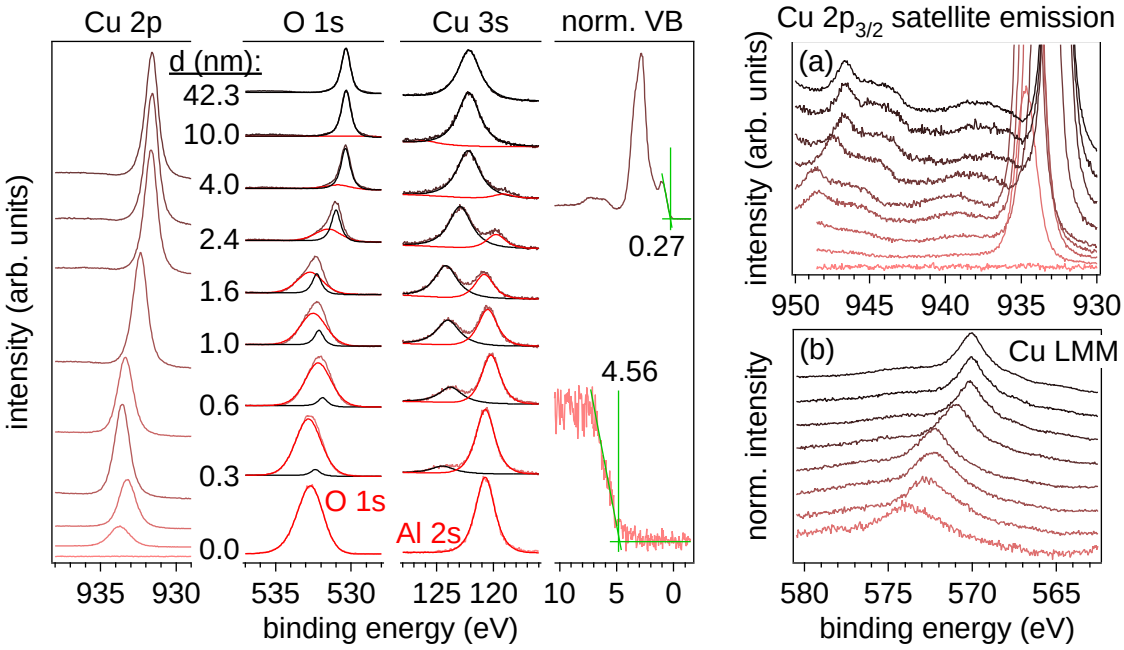

Figure 6.1: (left side) XPS data of core level lines (Cu 2p, O 1s, Cu 3s/Al 2s) and the valence band region for the interface ATO/Cu_2O. The thickness is given with the O 1s emissions. Fittings of O 1s, Cu 3s and Al 2s by Gauss/Lorentz profile are included. The graphical determination of the valence band maximum is schematically shown, together with the obtained values. (a) Cu $2p_{3/2}$ region, extended towards higher binding energy to show a potential satellite emission due to Cu(II) and (b) Cu LMM emission, both with increasing film thickness towards the top of the graph.

O 1s, Cu 3s, Al 2s and the valence band region are displayed in Figure 6.1. The intensity decrease of substrate emission lines and the increase of film emissions with increasing film thickness is clearly observed. Furthermore, significant binding energy shifts occur as more and more material is deposited.

In order to obtain reliable information on the energy band alignment at the interface, the chemical integrity of substrate and film needs to be ensured. The substrate is unlikely to react with the film material, since Al_2O_3 was deposited at 500 °C whereas the Cu_2O film deposition is carried out at room temperature. The Al 3s in Figure 6.1 is fitted with a single Gauss/Lorentz profile. Also the film material shows a single emission component both for Cu 3s and Cu 2p. However, as described in Section 3.3.1, the chemical shift with respect to the Cu(I) is too small to detect small amounts of other oxidation states, especially in case of a reduction to Cu(0).[171] The spectral features, which help to qualitatively judge on the copper oxidation state (Cu 2p satellite emission, Cu LMM Auger emission) are displayed in Figure 6.1 (a) and (b). The satellite intensity caused by the occurrence of Cu(II) ions is difficult to notice in Fig. 6.1 (a). Nevertheless, a semi-quantitative evaluation with respect to thickness can be made, which has been described in Section 5.1.2. The respective data in Figure 5.3 (a) is designated as ATO (1) and shows

that indeed a rather small amount of Cu(II) is found in this sample, compared to the Cu_2O samples on other substrates. The Cu LMM Auger emission in Fig. 6.1 (b) shows no sign of either Cu(0) or Cu(II).

The binding energy shifts are analyzed in Section 6.2 and will be discussed there. It shall be noted here, that at intermediated Cu_2O thicknesses, artifacts due to charging occurred, whereas the spectra of the substrate and the film at final thickness where free of charging artifacts.

6.1.2 ALD-Al_2O_3/Cu_2O

The preparation of an additional ALD-Al_2O_3 substrate had two purposes: The interface ATO/Cu_2O could not be prepared free from adventitious carbon, since the dielectric is a commercially available substrate by the company Planar systems. Furthermore, charging artifacts could be avoided by depositing the aluminum oxide on a conductive ITO-coated glass substrate. The top-most layer in ATO consists of 25 nm Al_2O_3, consequently the same thickness has been deposited for an in situ approach in a chamber connected to the DAISY-MAT System. The resulting detail spectra are displayed in Figure 6.2. With respect to the ATO/Cu_2O interface, the Cu 3p/Al 2p binding energy region has been measured in addition.

The core levels did not show the same charging effects at intermediate thicknesses as on ATO. The binding energy shifts, which give rise to changes in the Fermi energy $E_F - E_{VB}$ in the respective materials, are evaluated in Section 6.2. Unfortunately, copper ions were found to be partially oxidized to Cu(II), even at the final film thickness of around 250 nm, which was most likely due to na excess of oxygen in the process gas during deposition. This can be observed in the binding energy region of the Cu 2p satellites, displayed in Figure 6.2 (a) together with the Cu LMM emission (b). The green curve is a pure Cu_2O reference. Since the film at final thickness is not stoichiometric Cu_2O, the procedure of semi-quantification of Cu(II) satellite intensity of Section 5.1.2 was not applied to this data.

6.1.3 Bi_2O_3/Cu_2O

Bi_2O_3 is another substrate material, which was investigated in Chapter 5. As mentioned there, in addition to the ATO/Bi_2O_3 substrate a second substrate was included on the sample holder, which consisted of 45 nm Bi_2O_3, deposited on ITO-coated glass. This allowed for XPS measurements of the interface formation between Bi_2O_3 and Cu_2O without charging artifacts. The nomenclature is adapted from Chapter 5, which means the ITO-based substrate corresponding to ATO/Bi_2O_3 (1) is here referred to as **ITO/Bi_2O_3 (1)** and the same holds for **ITO/Bi_2O_3 (2)**. Figure 6.3 shows the detail spectra of the Cu_2O on ITO/Bi_2O_3 (1).

The binding energy shifts are discussed in Section 6.2. Since the Cu(II)-related satellite intensity has been evaluated in Section 5.1.2, the respective spectra are not included here.

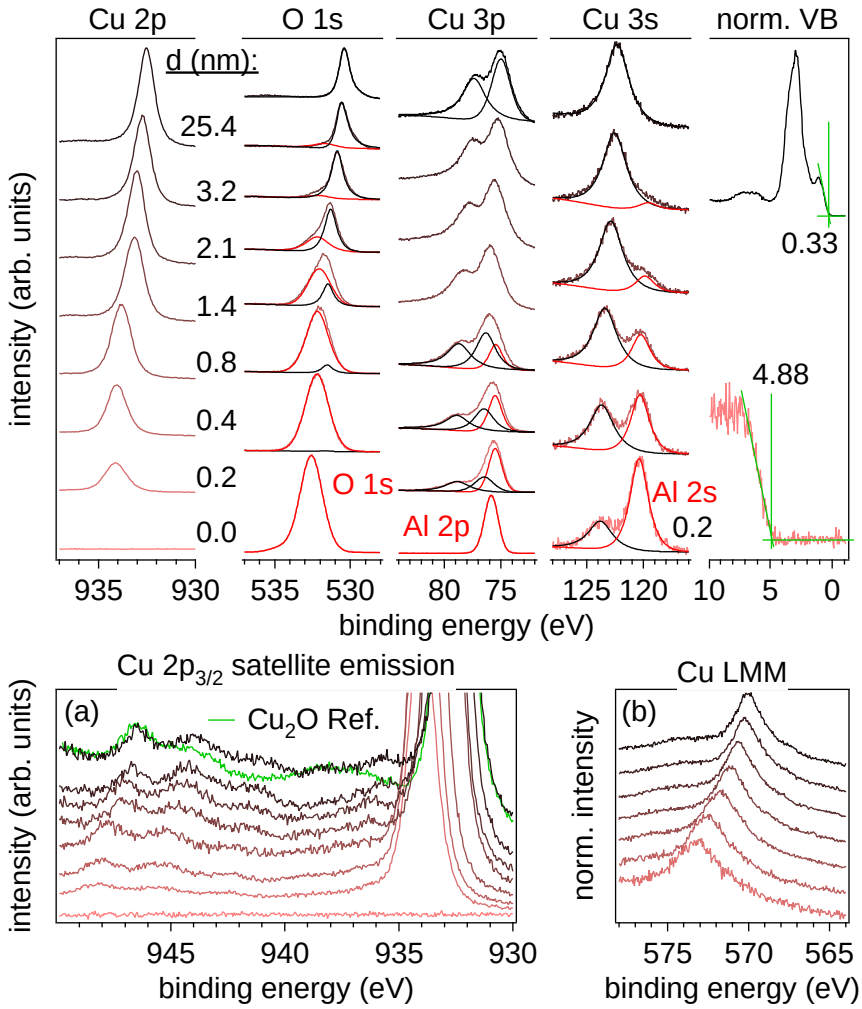

Figure 6.2: (top) XPS data of core level lines (Cu 2p, O 1s, Cu 3p/Al 3p, Cu 3p/Al 3p) and the valence band region for the interface ALD-Al_2O_3/Cu_2O. The thickness is given with the Cu 2p emissions. Fittings of O 1s, Cu 3p, Al 2p, Cu 3s and Al 2s by Gauss/Lorentz profile are included. The graphical determination of the valence band maximum is schematically shown, together with the obtained values. (a) Cu $2p_{3/2}$ region, extended towards higher binding energy to show a potential satellite emission due to Cu(II) and (b) Cu LMM emission, both with increasing film thickness towards the top of the graph.

A noteworthy observation was made comparing in situ spectra immediately after the Bi_2O_3 deposition with ex situ data after exposure to ambient air for the deposition of the gold contacts. This data is shown in Figure 6.4. There is a considerable shift in Fermi energy from 1.8 to 1.3 eV after the Bi_2O_3 surface is exposed to ambient atmosphere. The additional component in the O 1s emission at $\geq$ 531 eV is explained by hydroxides and oxygen bonds to adventitious carbon at the surface.[171] The FWHM of the Bi 4f emission remains unchanged upon air exposure. Since all binding energies in Bi_2O_3 change in parallel, it may be suspected that a surface band bending towards lower $E_F - E_{VB}$

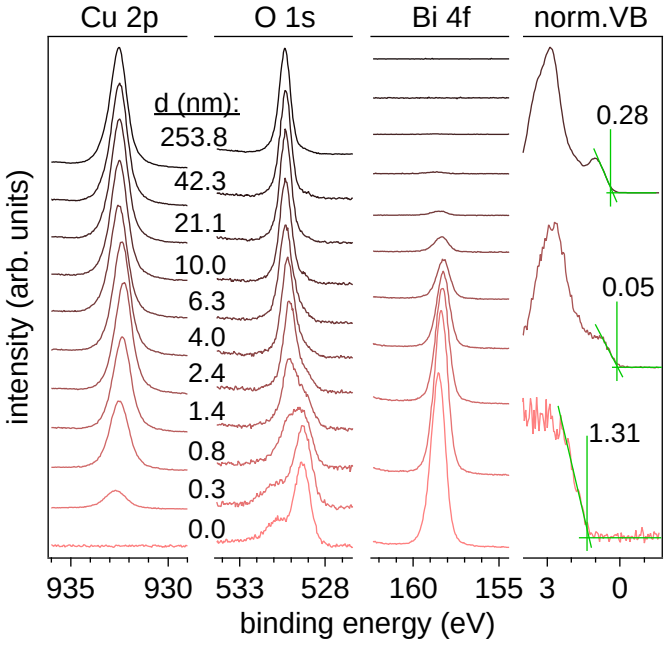

Figure 6.3: XPS data of core level lines (Cu 2p, O 1s, Bi 4f) and the valence band region for the interface ITO/Bi_2O_3/Cu_2O (1). The thickness is given with the O 1s emissions. No line shapes have been fitted in this experiments. The graphical determination of the valence band maximum is schematically shown, together with the obtained values.

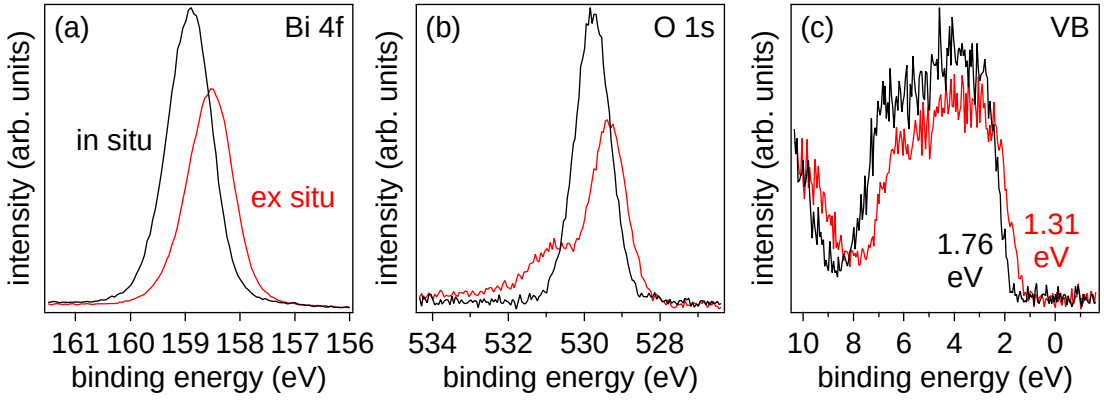

Figure 6.4: Comparison of in situ and ex situ (after exposure to ambient air) surfaces of Bi_2O_3.

is responsible for the observed binding energy shift. The work function has not been measured to conclude on the ionization potential.

6.2 Energy band alignments

The difference between Fermi energy and valence band maximum $E_F - E_{VB}$ is evaluated from the relative core level binding energy shift at each film thickness. The results for the samples presented in this chapter are displayed in Figure 6.6. The core levels used for the calculation are indicated in the general legend above the plots. In addition to $E_F - E_{VB}$, the shift in the Auger parameter $\Delta\alpha'$ was evaluated for Cu_2O and is included as the extra-atomic relaxation ΔR according to Equation 3.7. In this section, the discussion is integrated in the description of the results.

Extra-atomic relaxation at interfaces

Figure 6.5 schematically shows how $\Delta\alpha'$ manifests in the binding energy shifts of Cu_2O close to the interface to any of the substrates presented in this work. The Auger parameter α' is proportional to the difference between the binding energy of the photoelectron and the *apparent* binding energy of the Auger electron in the spectrum, when calculated from its kinetic energy. This difference becomes more negative towards the interface, since the kinetic energy of Auger electron is more affected by the additional extra-atomic relaxation in vicinity to the substrate than the energy of the photoelectron (see Section 3.3.1 for further details). The photoelectron binding energy E_B is affected only by $\Delta R = \Delta\alpha'/2$ according to Equation 3.6. Equation 6.1 gives an expression for a binding energy shift, corrected for this extra-atomic relaxation.

$$\Delta E_B^{corr} = \Delta E_B + \Delta R = \Delta\epsilon - \Delta E_F + e\Delta\Phi \tag{6.1}$$

When a change of the copper oxidation state $\Delta\epsilon$ as well as charging $e\Delta\Phi$ can be neglected, then ΔE_B^{corr} should be equal to the change in Fermi energy at the interface. Under these circumstances a correction of the binding energy shift for extra-atomic relaxation can improve the accuracy of estimation of the valence band discontinuity, especially at low film thicknesses where a different polarizability than in the bulk occurs. The approach will be evaluated in the discussion of the data in the following paragraphs.

Cu_2O on Al_2O_3 by ALD

Figures 6.6 (a) and (b) show the results for the interfaces of Cu_2O on Al_2O_3 by ALD. On the ATO substrate, a rough accordance between shifts of substrate and film emissions is observed. At intermediate thicknesses, charging effects due to the limited substrate conductance appear. However, the contribution $e\Delta\Phi$ is the same for both substrate and film emissions. Since artifacts due to charging were absent both in the measurement of the clean substrate and the film at final thickness, the evaluation of the valence band

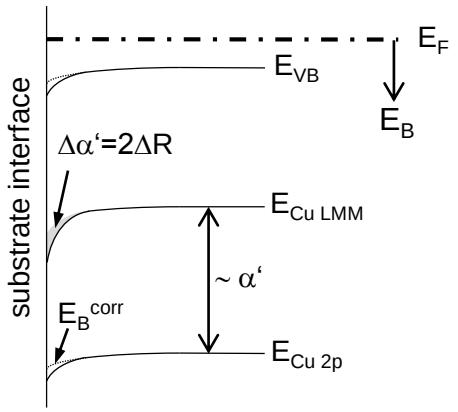

Figure 6.5: Schematic representation of extra-atomic relaxation in Cu_2O at the interface to the substrate. The measured binding energies Cu 2p and Cu LMM (and the corresponding valence band maximum) are represented as solid lines. The additional shift in Cu LMM $\Delta\alpha'$ is shown in gray. When $\Delta R = \Delta\alpha'/2$ is added to the photoelectron binding energy, the broken line E_B^{corr} is obtained.

discontinuity ΔE_{VB} is possible. The respective value is found to range between 2.2 and 2.6 eV, when the measured Cu 2p binding energy is used for the calculation, as shown in the figure by vertical solid lines. Using ΔE_B^{corr} corrected for the extra-atomic relaxation shown by the broken lines leads to a constant value of $\Delta E_{VB} = 2.6$ eV between 0.6 and 4 nm.

The interface between ALD-Al_2O_3 and Cu_2O shown in Figure 6.6 (b) reveals no sign of charging artifacts. This is probably due to a presumably better substrate conductivity and a higher conductivity of the copper oxide film than in the experiment on ATO, since part of the copper ions are Cu(II). Although all core levels of substrate and film individually show consistent shifts, there is some irregularity in the core level binding energies of the film material at 1.8 nm. The origin of this is not clear. ΔE_{VB} ranges from 2.6 to 3.2 eV when calculated from the measured binding energy shifts. The value corrected for extra-atomic relaxation is in the range of 3.1 ± 0.1 eV.

The valence band offset to ALD-Al_2O_3 from the DAISY-MAT chamber is 0.5 eV higher than to the ATO substrate, although the material at the substrate surface in both cases is Al_2O_3 by ALD. The similar Fermi energy $E_F - E_{VB}$ in Al_2O_3 before film deposition does not indicate pronounced differences between the two substrate materials. This is reasonable, as in both cases the main defect level responsible for Fermi level pinning should be due to hydrogen.[152] The hydrogen most likely originates from incomplete reactions during the ALD cycle. Since ATO is deposited at 500 °C substrate temperature, compared to 200 °C during ALD of Al_2O_3 in the DAISY-MAT chamber, a lower hydrogen concentration may be present in ATO. This can explain the weaker Fermi level pinning in ATO than in ALD-Al_2O_3 (Figure 6.6 (a) and (b)) which results in a lower valence band discontinuity to Cu_2O.

Besides an influence of the substrate, the partial oxidation of Cu(I) to Cu(II) may be another reason for the observed difference in ΔE_{VB} between Fig. 6.6 (a) and (b). Siol *et al.* showed, that Cu_2O is able to incorporate higher values of band bending at the interface to ZnO, when it is partially oxidized.[227] The authors compared slightly oxidized $Cu_{2-x}O$ ($x > 0$, Cu/O = 1.85 – 1.90) with a low Fermi energy of ≤ 0.25 eV to almost stoichiometric Cu_2O of high Fermi energy (≥ 0.45 eV). The high Fermi energy is explained by bulk

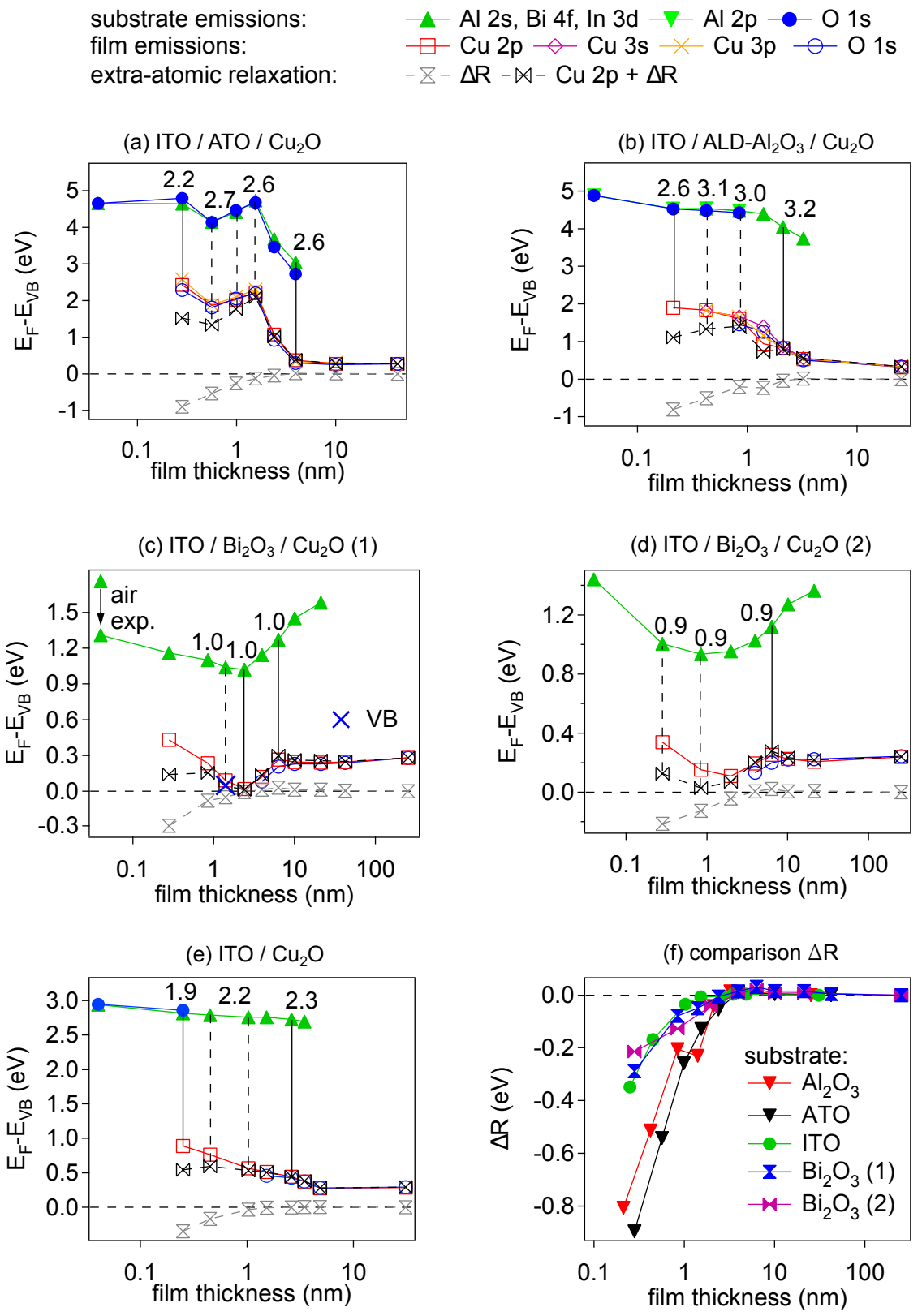

Figure 6.6: (a)–(e) Overview of valence band alignments of Cu_2O film on different substrates. The evaluation of extra-atomic relaxation in Cu_2O is included as ΔR and as corrected $E_F - E_{VB}$, derived from the Cu 2p emission. (f) Comparison of ΔR on all substrates.

Fermi level pinning at metallic copper precipitates. Applied to the data of Figure 6.6 this would mean, that the oxygen-rich copper oxide in (b) should result in a comparatively low valence band discontinuity. However, the stoichiometric Cu_2O on ATO in Fig. 6.6 (a) does not contain metallic copper precipitates, so the band bending is not limited by the bulk Fermi level pinning. Hence, in order to obtain an unambiguous result for the valence band discontinuity between ALD-Al_2O_3 and stoichiometric Cu_2O, the value from the experiment on ATO may safely be considered, giving rise to $\Delta E_{VB} = 2.6\,eV$. The oxygen-rich $Cu_{2-x}O$ on ALD-Al_2O_3 in Fig. 6.6 (b) is in fact significantly more oxidized (Cu/O = 1.71) than the oxygen-rich films in the work by Siol *et al.*.[227] This can be an indication, that further oxidation of Cu(I) to Cu(II) imposes an additional limit to the band bending in Cu_2O.

Cu_2O on Bi_2O_3

The two interfaces between Bi_2O_3 and Cu_2O shown in Figures 6.6 (c) and (d) are rather similar, so they will be discussed together. The value of $E_F - E_{VB}$ after exposure to ambient air is used for the calculation of the offset between valence band maximum and core levels in Bi_2O_3 (see Fig. 6.4). The O 1s emissions are not fitted here due to the strong impact of exposure to ambient air. It is not clear how the secondary O 1s component at higher binding energy is affected by the Cu_2O deposition. Nevertheless, the O 1s binding energy in Cu_2O is estimated from the respective binding energy of maximum intensity. Similar to the analysis of Cu_2O on Al_2O_3, the consistency of ΔE_{VB} estimation with respect to film thickness can be improved, when the binding energy shift is corrected for extra-atomic relaxation at the interface. For unknown reasons this approach works better on the data from the experiment on ITO/Bi_2O_3/Cu_2O (2) than on ITO/Bi_2O_3/Cu_2O (1), with a valence band discontinuity of 0.9 eV. This value is observable in a film thickness range between 0.3 and 6.3 nm. On ITO/Bi_2O_3/Cu_2O (1), the valence band discontinuity is found to be 1.0 eV.

Cu_2O on ITO

The data in (e) is taken from a previously published work and shows Cu_2O on ITO, where both materials have been deposited at room temperature.[189] In the original publication, the Auger parameter has not been evaluated. Here, it appears to be useful in order to determine the valence band discontinuity between the two materials. Removing the additional extra-atomic relaxation caused by the substrate at low film thickness leads to a valence band offset of $\Delta E_{VB} = 2.2\,eV$.

Comparison of the substrate materials

A comparison of the different substrate materials in terms of their influence on ΔR with increasing thickness is given in Figure 6.6 (f). It is observed, that Al_2O_3 as substrate has a more severe effect on extra-atomic relaxation at low thicknesses of Cu_2O than Bi_2O_3

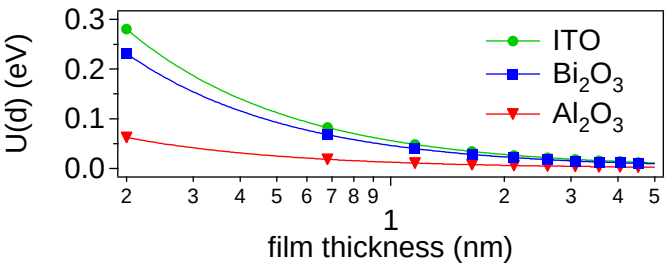

Figure 6.7: Polarization energy with respect to Cu_2O thickness on different substrate materials, according to Equation 3.9.

and ITO, the latter showing no significant difference between each other. As outlined in Section 3.3.1, many effects at interfaces can cause a contribution to ΔR, which are all related to a change in electron density not at the photoemitting ion/atom but in its vicinity. This has an effect on polarizability, in other words on the screening of the photohole. Equation 3.9 allows to estimate the polarization energy $U(d)$ with respect to film thickness. Bi_2O_3 has a dielectric constant of 40,[228] compared to 9 of Al_2O_3,[229] which is rather similar to Cu_2O.[72] Although ITO is not degenerately doped when deposited at room temperature, its dielectric constant is assumed to be infinite, similar to a metal. The resulting values are graphically displayed with respect to thickness in Figure 6.7.

Since $U(d)$ is positive whereas ΔR is negative, the different dielectric constants of substrate and film materials are not the main cause for the observed negative ΔR. However, since the effect is undoubtedly present, it may simply counteract a more prominent relaxation phenomenon at the interface. Such a compensation of a negative ΔR would be stronger for Cu_2O on ITO and Bi_2O_3 than for Cu_2O on Al_2O_3. This interpretation is supported by a study in which Cu_2O was deposited on SiO_2 and ZrO_2.[230] SiO_2 has a lower dielectric constant than Cu_2O, whereas ZrO_2 a higher one.[229] $\Delta\alpha'$ towards low film coverages was found to be negative in both cases and to decrease more strongly on the less polarizable substrate (SiO_2) than on the one with higher polarizability (ZrO_2). Consequently, the main contribution to ΔR is probably due to the chemical bonds between substrate and film material.[185] If the bonds to the substrate caused a change of copper oxidation state from Cu(I) to Cu(II), local relaxation at the copper ion would occur, which in principle should affect the change of Auger parameter with increasing thickness.[180] However, based on the data of Fig. 6.6 no systematic influence of the amount of Cu(II) on ΔR could be identified.

Particularities of Cu_2O on Bi_2O_3

Both experiments on Bi_2O_3 represented in Figures 6.6 (c) and (d) show two noteworthy particularities, which have not been mentioned so far:

- At a thickness of around 2 nm, the Fermi energy in Cu_2O is decreased to 0.02 eV (c) and 0.11 eV (d), respectively (0.03 eV at 1 nm, when ΔR is considered).
- The binding energies of substrate and film emissions cease to change in parallel above a film thickness of 6 nm.

The correlation of relative Cu(II) satellite intensity and conductivity, as displayed in Figure 5.3 shall be considered for possible explanations. The data is reproduced in Figure 6.8 for direct comparison.

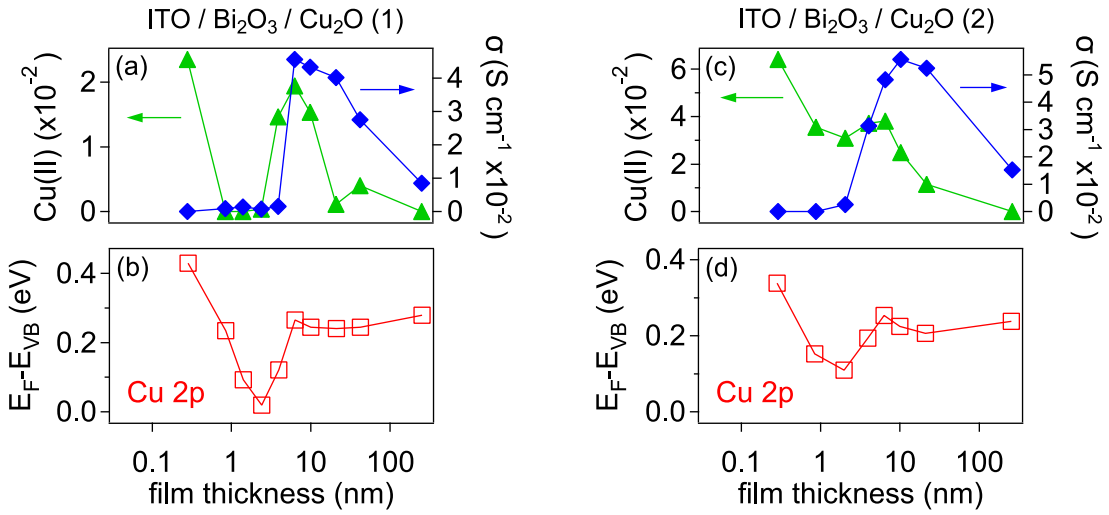

Figure 6.8: Comparison of Cu(II)-related satellite intensity and conductivity with Fermi energy in Cu_2O on the two Bi_2O_3 substrates.

The interesting observation here is, that the highest satellite intensity (neglecting the sub-nanometer region, where the low intensity of film emissions induces a rather large error to the procedure for satellite quantification) does not occur at the same thickness as the low Fermi energy in Cu_2O. Hence, the presence of Cu(II) is not responsible for the observed low Fermi energy. The data does not provide any other explanation for the unusually low Fermi energy, so the reason remains elusive.

The thickness of highest Cu(II) satellite intensity corresponds roughly to the onset of continuous conduction observed by the peak in conductivity, especially for the film on ITO/Bi_2O_3/Cu_2O (1). This is also the thickness beyond which the Cu 2p core level does not follow the further increasing Bi 4f binding energy anymore but stabilizes roughly at the bulk value of Cu_2O. Towards higher Cu_2O thicknesses, the Bi 4f binding energy appears to become like the value at the in situ surface of Bi_2O_3. The reason for this is unknown.

As mentioned in Section 2.6.1, the Fermi energy in Cu_2O is limited to values close to the valence band maximum by the mechanism of self-compensation. The latter could be the reason for the observed limitation of the Cu_2O Fermi energy beyond a thickness of 4 nm. The occurrence of Cu(II) at the same film thickness supports this interpretation, since it is a sign that the material surpasses the limits of thermodynamic stability. Furthermore, it may be an indication for the complex formation between Cu(II) and two copper vacancies, which was discussed in Section 5.2.1. Such a complex with a divalent cation has an acceptor state in the band gap at 0.1 eV, which is lower than the intrinsic acceptor levels of Cu_2O.[102] Hence, additional charge carriers are created upon complex

formation, which is why this mechanism possibly contributes to the self-compensation of the material.

6.3 Conclusion

The valence band discontinuities between Cu_2O and Al_2O_3 by ALD (2.6 eV) as well as Cu_2O and Bi_2O_3 (0.9-1.0 eV) have been determined in this chapter. Additional extra-atomic relaxation ΔR due to the vicinity to the substrate interface has been taken into account by measurement of the Auger parameter. In the absence of a chemical shift, the binding energy shift in the film can be corrected for ΔR, which allows a measurement of ΔE_{VB} at film thicknesses far below what is usually possible. Since extra-atomic relaxation is an inherent effect of the photoemission process, it is concluded that the valence band offset between two materials is already fully developed at a film thickness of a few Ångström. This validates the discussion of Cu(II)-containing grain boundaries in Cu_2O by taking into account the energy band alignment to CuO (see Chapter 5). The exact origin of extra-atomic relaxation at the interface could not be elucidated. However, a sole contribution of polarizability due to different dielectric constants of substrate and film material is only of subordinated importance.

Relevance for bottom-gate TFTs

The Fermi energy of the semiconductor is related to the concentration of charge carriers in the channel region, which is generally modulated by the gate potential of a TFT. In the absence of a gate bias and with a defect-free dielectric, the Fermi energy at the interface to the dielectric is determined by the work function of the metallic gate contact. By the choice of different gate metals, the band alignment between semiconductor and dielectric could be deliberately altered. However, the dielectric Al_2O_3 deposited by ALD contains a significant amount of fixed charges, which pin the Fermi energy of Al_2O_3 to values above 4.5 eV. This is schematically shown for Al_2O_3 on ITO in Figure 6.9.

According to the common anion rule, the valence band offset between Al_2O_3 and Cu_2O is around 2 eV.[231] However, the Fermi level pinning in Al_2O_3 causes the value to be increased to at least 2.6 eV. This is schematically shown in Figure 6.9. Both contacting materials ITO and Cu_2O exhibit high Fermi energies at the interface to Al_2O_3,[152] which directly shows the existence of positively charged defects in the dielectric.

The Fermi level pinning has an influence on the valence band offset and thus on the value of $E_F - E_{VB}$ in the p-type semiconductor at the interface to the dielectric. A high Fermi energy in a p-type semiconductor may lead to self-compensation by the formation of intrinsic acceptor dopants (see Section 2.4.3). Such dopants (copper vacancies) would increase the hole carrier concentration in the material and decrease the ON/OFF current ratio of a respective TFT.

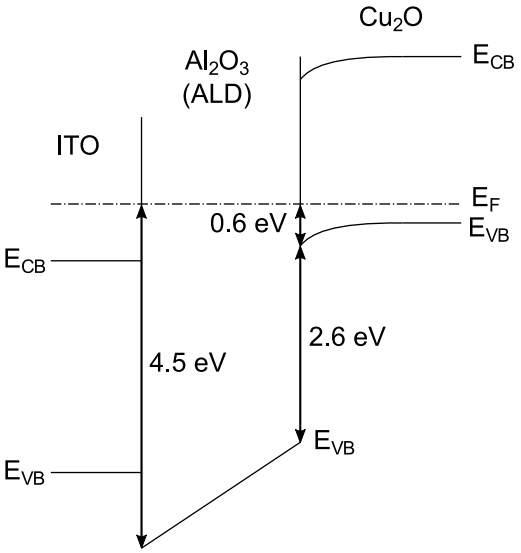

Figure 6.9: The energy band alignment in a bottom-gate stack of a TFT is schematically shown, using ITO as gate, Al_2O_3 by ALD as dielectric and Cu_2O as p-type semiconductor. The interface ITO/Al_2O_3 is taken from previous work.[152] The partial depletion of Cu_2O at the interface is illustrated by the comparatively high Fermi energy of $E_F - E_{VB} = 0.6\,eV$.

It is possible that the defects created by self-compensation lead to a destabilization of the Cu_2O structure. With a high concentration of copper vacancies the material becomes oxygen-rich. When the Cu_2O structure becomes instable due to this copper deficiency, the coordination of copper ions changes, which possibly results in the formation of Cu(II), which could be observed on substrates of Bi_2O_3.

In Chapter 5 and later in the discussion of TFT characteristics of Chapter 8, the valence band offset between grain boundaries and grains in Cu_2O is assumed to be the same as the offset between CuO and Cu_2O. The results of the present chapter could show, that the valence band offset between two materials is already established at film thicknesses below 0.5 nm. Consequently, the effect of a 0.5 nm wide grain boundary on macroscopic electrical properties can be discussed in the light of the energy alignment between CuO and Cu_2O.

CHAPTER 7

CHEMICAL STABILITY OF Cu_2O DURING POST-DEPOSITION PROCESSING

As described in Chapters 4 and 5, the electrical properties of Cu_2O are affected by the occurrence of secondary cation oxidation states. The present chapter shows that a reduction or oxidation of copper cations in Cu_2O can be induced by subsequent process steps during the fabrication of a device. Section 7.1 is concerned with the chemical alterations in Cu_2O induced by the deposition of the typical dielectric layer Al_2O_3. Section 7.2 shows how electrical and structural properties of copper oxide are altered by post-deposition heat treatments in different atmospheres.

7.1 Reactivity of Cu_2O as the substrate material

In order to fabricate a TFT or a solar cell, several thin layers of different materials are typically deposited on top of each other. In a top-gate approach, the dielectric is deposited on the semiconductor. This section focuses on the reduction of copper ions by atomic layer deposition of Al_2O_3 but also shows how Cu(I) becomes oxidized to Cu(II) when Al_2O_3 is deposited by sputtering. The results were obtained by angle-resolved in situ X-ray photoelectron spectroscopy in the DAISY-MAT system at TU Darmstadt. Al_2O_3 layers of different thicknesses were deposited in a step-wise manner on sputter-deposited Cu_2O substrates and subsequently analyzed by XPS. The study confirms, that the Fermi level in Cu_2O is pinned at the contact to metallic copper. Such a pinning would not allow a modulation of the charge carrier concentration in the Cu_2O layer of a TFT.

The results of this section have been published in the journal *Materials Research Express*.[193]

7.1.1 Chemical analysis

Core level and valence band spectra recorded during the stepwise deposition of ALD-Al_2O_3 onto Cu_2O are shown in Figure 7.1. The deposited thickness of Cu_2O was 93 nm, measured by profilometry. The intensities of the substrate emissions decrease and those of the film increase with the number of deposition cycles. No Cu 2p satellite emission, associated with Cu(II),[173] is observed at any thickness. The Cu_2O film is clearly not oxidized during the ALD process. However, a shoulder appears in the Cu LMM Auger emission at around 2.3 eV lower binding energy than the main emission, which indicates the occurrence of Cu(0).[188] This shoulder is clearly observed after 3 cycles but already weakly present after the first deposition cycle. As pointed out by Gharachorlou *et al.*, the low Cu(0) intensity after the first full cycle is due to the re-oxidation of the metallic copper, which has formed after the first half-cycle of TMA.[158] Our data shows the re-oxidation to Cu(II) to be only partial, which may be related to the usage of water as oxidative precursor instead of oxygen. Since the initial Cu_2O surface is free of hydroxyl-groups, the mechanism proposed by Gharachorlou *et al.*, in which $CuAlO_2$ and Cu are formed during the TMA half-cycle is a possible scenario.[158] The occurrence of the aluminate is discussed further below.

In order to investigate whether the metallic copper is localized at the interface, additional samples were produced by the same procedure and measured with a lower emission angle of 15°, as depicted in Figure 7.2. Graph (a) shows a sample after 9 ALD cycles (0.81 nm nominal Al_2O_3 thickness, according to the typical GPC) and clearly reveals a more intense LMM emission from Cu(0) when measured with enhanced surface sensitivity. Graph (b) displays the data of another sample after 30 ALD cycles (2.7 nm nominal thickness) and shows a similar intensity of metallic copper at an emission angle of 15°. Consequently, it is concluded that the metallic copper is concentrated at the interface and remains unchanged upon further Al_2O_3 deposition beyond 9 cycles. The effect of air exposure shown in the figure will be discussed further below.

The film thickness was evaluated by the damping of the Cu $2p_{3/2}$ intensity by the overlying layer according to

$$I_\mathrm{d} = I_0 \cdot \mathrm{e}^{-d/(\lambda_\mathrm{e} \sin\theta)}. \tag{7.1}$$

I_d is the substrate copper core level intensity measured through the additional layer on the surface, I_0 is the intensity of the clean substrate, d is the thickness of the layer, λ_e is the mean free path of photoelectrons in Al_2O_3 (1.28 nm for Cu 2p),[232] and θ is the emission angle. Between 0 and 3 cycles, the thickness increases proportionally to the number of cycles with a GPC of ≈ 0.2 nm/cycle. Between 3 and 9 cycles, the typical GPC of Al_2O_3 by ALD of 0.09 nm/cycle is observed. This analysis is formally only valid when the substrate is inert towards the film deposition, since the intensity is related to the atomic density of the respective element.[154] However, in the presented case, a reduction of copper occurs, which rather increases the copper density at the interface,

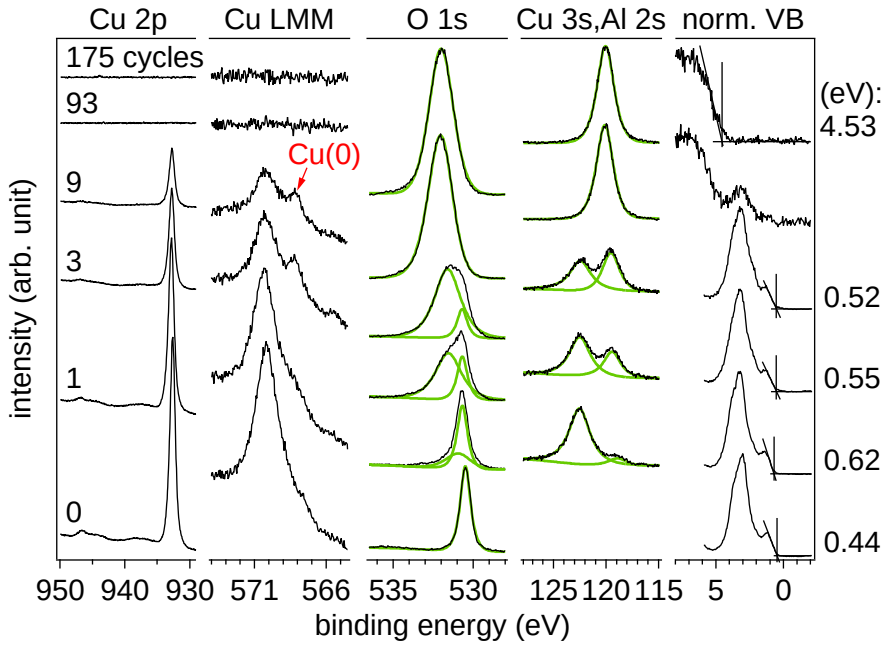

Figure 7.1: XP core level and valence band (VB) spectra are graphically displayed. Going from bottom to top starting with the uncoated substrate, the layer thickness increases with the number of cycles given on the left-hand side. The Cu LMM Auger emission is included to show reduction of Cu(I) to Cu(0). The binding energy range of Cu $2p_{3/2}$ is extended to show the eventual satellite emission. The O 1s, Cu 3s and Al 2s spectra were fitted by a Gauss/Lorentz profile in order to identify individual lines of surface and film emissions. The Cu 3s emission of the uncoated substrate was not measured. The intensities of the valence band spectra were normalized. The graphical evaluation of $E_F - E_{VB}$ is shown together with the corresponding values.

compared to the parent material Cu_2O. This results in an underestimation of the real value and consequently supports the conclusion of an initially enhanced GPC.

Figure 7.2 (b) shows the effect of air exposure on a Cu_2O sample with 30 cycles (nominally 2.7 nm) ALD-Al_2O_3 deposited. The Cu LMM emission related to Cu(0) is decreased after exposure, which means that oxygen from the atmosphere diffuses through the Al_2O_3 film. If ALD-Al_2O_3 forms a weak diffusion barrier to oxygen, this raises the question why the GPC ceases to be enhanced after 3 cycles. Since the ratio Cu(0)/Cu(I) at the interface remains constant beyond 9 ALD cycles, it has to be concluded that the reduction to metallic copper saturates at the Cu_2O surface after a few ALD cycles, which inhibits further oxygen from being released from the substrate bulk. The oxygen has to originate from the Cu_2O bulk, since Gharachorlou *et al.* did not observe the initial GPC enhancement on thin Cu_2O on copper.[158]

For comparison, reactive magnetron sputter deposition of Al_2O_3 was done on the same substrate material. The spectra are shown in Figure 7.3. After Al_2O_3 sputter deposition, a partial oxidation of the substrate is observed in the Cu 2p satellite emission.

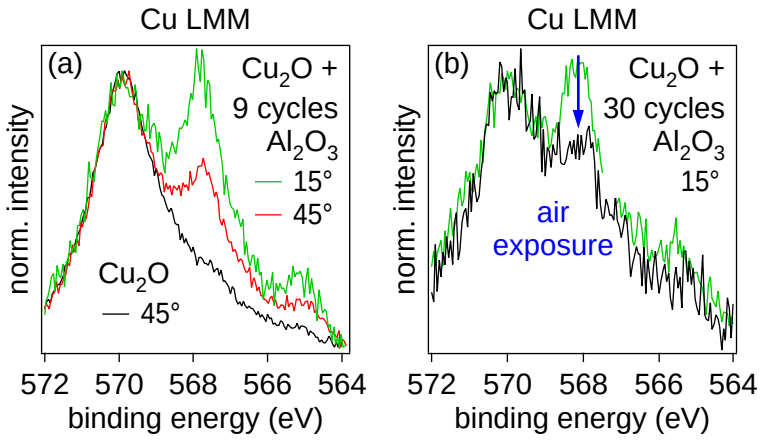

Figure 7.2: Cu LMM emission of copper oxide surfaces which are covered with ALD-Al_2O_3 of different thicknesses. Intensities were normalized to the Cu(I) peak and binding energies were shifted to coincide with the spectra of the Cu_2O surface. (a) The spectra were obtained with emission angles of 45° and 15° to show the localization of the metallic copper at the interface to Al_2O_3. (b) The change in relative intensity of the shoulder in the LMM emission related to Cu(0) after exposure to ambient air is shown compared to the in situ surface.

The Cu(II) may additionally be observed as a secondary peak in the Cu LMM emission at a binding energy approximately 1 eV lower.[188] On an ITO substrate, reactive magnetron sputtering of Al_2O_3 has been reported to lead to the implantation of oxygen.[233] Substrate oxidation occurs, since a fraction of the oxygen in the process gas is negatively ionized in the plasma and accelerated towards the substrate by the electric field in the plasma sheath region at the target surface.[234]

7.1.2 Fermi level pinning due to partial reduction

The binding energy shifts of the Cu_2O substrate in the course of deposition are displayed in Figure 7.4 by means of $E_F - E_{VB}$ of the substrate and final film material Al_2O_3. The atomic ratio of aluminum to oxygen in the film was calculated from integral peak intensities and atomic sensitivity factors provided for the instrument. The original Fermi energy of 0.4 eV in the Cu_2O increases to 0.6 eV already after the first ALD cycle. This shows the formation of the Cu_2O/Cu Schottky junction.[17, 120] The Fermi level pinning is clearly observed in the binding energies of the substrate emissions, which do not follow the ones of the film emissions. A valence band offset between Cu_2O and Al_2O_3 can therefore only be approximated from the data. Since the Cu_2O film in the work by Gharachorlou *et al.* is a thin layer on a copper substrate, the authors cannot observe the effect of the Schottky barrier.[158]

The Fermi energy in thick ALD-Al_2O_3 is detected at $E_F - E_{VB} = 4.5$ eV, confirming previous studies.[152] Furthermore, our data shows reported indications for the existence

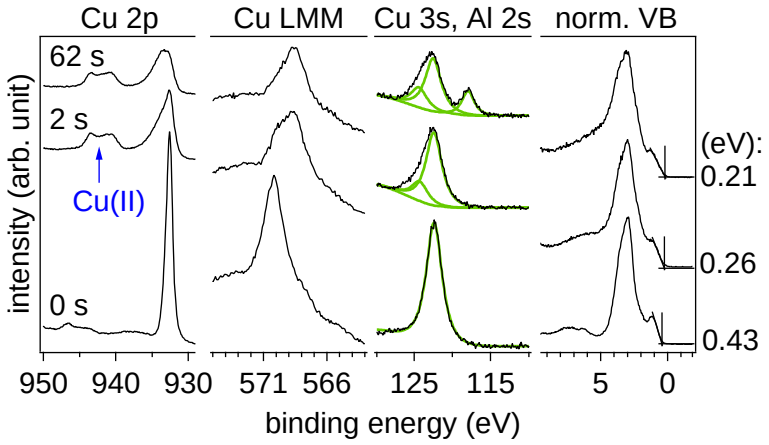

Figure 7.3: Al_2O_3 by sputtering: XP core level and valence band spectra are shown in a similar manner as in Figure 7.1, with the Al_2O_3 deposition time given on the left. The fitting of the Cu 3s emission partly used two components in order to accommodate Cu(I) and Cu(II).

of $CuAlO_2$.[158] Below 10 cycle, the stoichiometry of the film phase is rather poor in aluminum, with respect to Al_2O_3. In addition, the binding energy difference between film emissions Al 2s and O 1s is lower than of the final Al_2O_3 film. As $E_F - E_{VB}$ is calculated for Al_2O_3, the value obtained from the Al 2s core level is slightly lower for less than 10 cycles, than when calculated from O 1s. The presence of $CuAlO_2$ is consequently confirmed by our data.

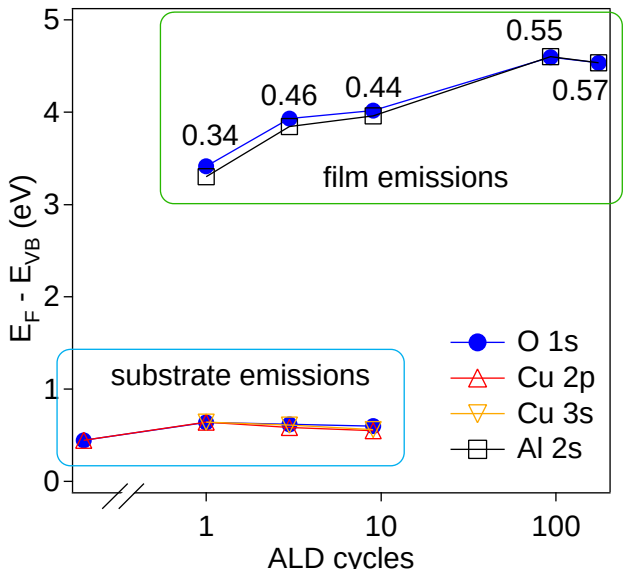

Figure 7.4: Valence band maxima with respect to Fermi energy are shown for each deposition step. The numbers next to the film emissions represent the atomic ratio Al/O in the film.

The Al 2s binding energy increases during initial film formation, so it could be argued that charging is involved. When charging occurs during XPS, the binding energy typically depends linearly on the dielectric thickness, provided the chemical state of the material remains unchanged.[235] The Al_2O_3 binding energies in Figure 7.4 after 93 and 175 cycles are constant and the atomic ratio of aluminum to oxygen does not change. For these reasons, charging is concluded to be irrelevant.

7.1.3 Conclusion

In situ XPS confirmed the partial reduction of a Cu_2O substrate to metallic copper by ALD of Al_2O_3. Figure 7.5 (a) shows a schematic illustration of the method. The use of a homogeneous Cu_2O substrate instead of a thin Cu_2O layer on metallic copper[158] allows for the observation of Fermi level pinning in the semiconductor by the Cu_2O/Cu Schottky barrier formation (Figure 7.5 (b)). The precursor TMA reacts with lattice oxygen originating from regions lying deeper than just the first few layers of the surface, which is schematically depicted in Figure 7.5 (c). This leads to an initially enhanced GPC. The oxygen extraction from the substrate is limited to the first few cycles, which is found to be due to a saturated copper reduction, rather than the oxygen diffusion barrier of Al_2O_3. Observations from Al_2O_3 deposited by magnetron sputtering on a Cu_2O substrate indicate that this technique provides no alternative to ALD when an inert Cu_2O surface is required since the copper oxide surface becomes oxidized in this case. The chemical instability of Cu_2O when it is used as a substrate for the deposition of other materials is the primary reason for the choice of a bottom-gate TFT architecture in this thesis.

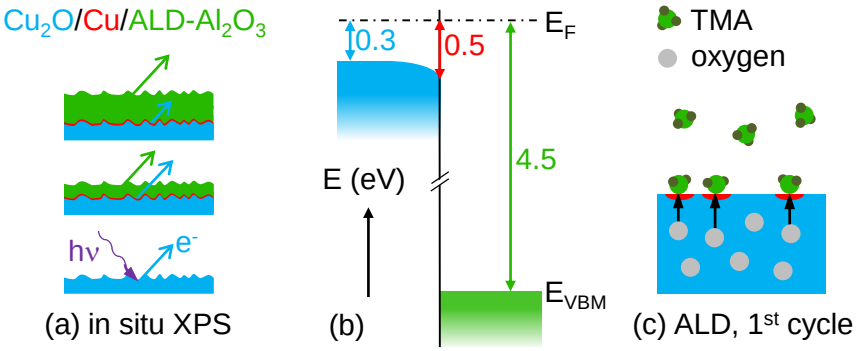

Figure 7.5: (a) In situ XPS after step-wise deposition allows for (b) the analysis of $E_F - E_{VB}$ in Cu_2O and Al_2O_3. (c) TMA reacts with lattice oxygen of Cu_2O by forming Cu(0) at the Cu_2O surface.

7.2 Post-deposition heat treatments

As described in Section 2.6.2, post-deposition annealing is widely applied to improve the electrical properties of thin-film transistors. However, it may also induce oxidation or reduction depending on the atmosphere in which the annealing is conducted. In order to understand the mechanisms during such heat treatments, this section presents Hall effect measurements at different temperatures above room temperature and in three different atmospheres. Since the degradation of the electrical properties of Cu_2O is related to the presence of oxidation states other than Cu(I), mainly effects of oxidation and reduction are discussed as well as as whether they are localized or homogeneous, respectively. The experiments including the film deposition were performed at TU Darmstadt. Furthermore, an XRD study of the influence of annealing at 200 °C in air is presented, which is a post-deposition annealing frequently applied in TFT fabrication.[127, 128] In the latter case, film deposition and measurements were conducted at UNL.

7.2.1 Relaxation Hall effect measurements

The experiments reported in this section consisted of repetitive Hall effect measurements of a sample under controlled temperature and atmosphere. 1.5 µm thick Cu_2O and 2.5 µm thick CuO films on quartz glass were studied. The conditions were kept constant for a certain time, in order to observe the transient *relaxation* of the sample's electric properties. Three different atmospheres were evaluated concerning their oxidative or reductive effect on Cu_2O at elevated temperatures. Figures 7.6 (a) and (b) show hole concentration and mobility in a gas flow of an argon/oxygen mixture with a ratio of 8/2 at atmospheric pressure, corresponding roughly to the oxygen amount in ambient air. This atmosphere is referred to as "simulated air" or simply air and the sample is designated as **Cu_2O A**. Figures 7.6 (c) and (d) represent similar data obtained on **Cu_2O B** in a flow of argon at atmospheric pressure (with a residual oxygen partial pressure of approximately 6×10^{-3} mbar). Finally, Figures 7.6 (e) and (f) show the results on **Cu_2O C** at low total pressure of 10^{-6} mbar, referred to as vacuum. In each experiment the temperature was increased from room temperature to 100 °C, 200 °C and 300 °C. In addition, the temperature was decreased back to room temperature between each temperature step. The relaxation time at each temperature step, meaning the time a certain sample condition was held constant, was sufficient to gain qualitative information on the occurring processes. Due to time constraints, full relaxation was not reached in most cases. The sharp peaks in the measured data are artifacts from the measurement during the time of temperature stabilization and eventual adjustment of the measurement current after changing the sample temperature.

The electrical properties at room temperature after each relaxation step are summarized in Figure 7.7. Despite the varying measurement time during the relaxations, the effect of the different atmospheres is compared. The partial relaxation attained in all measurements is sufficient for the qualitative discussion presented here. In addition, the

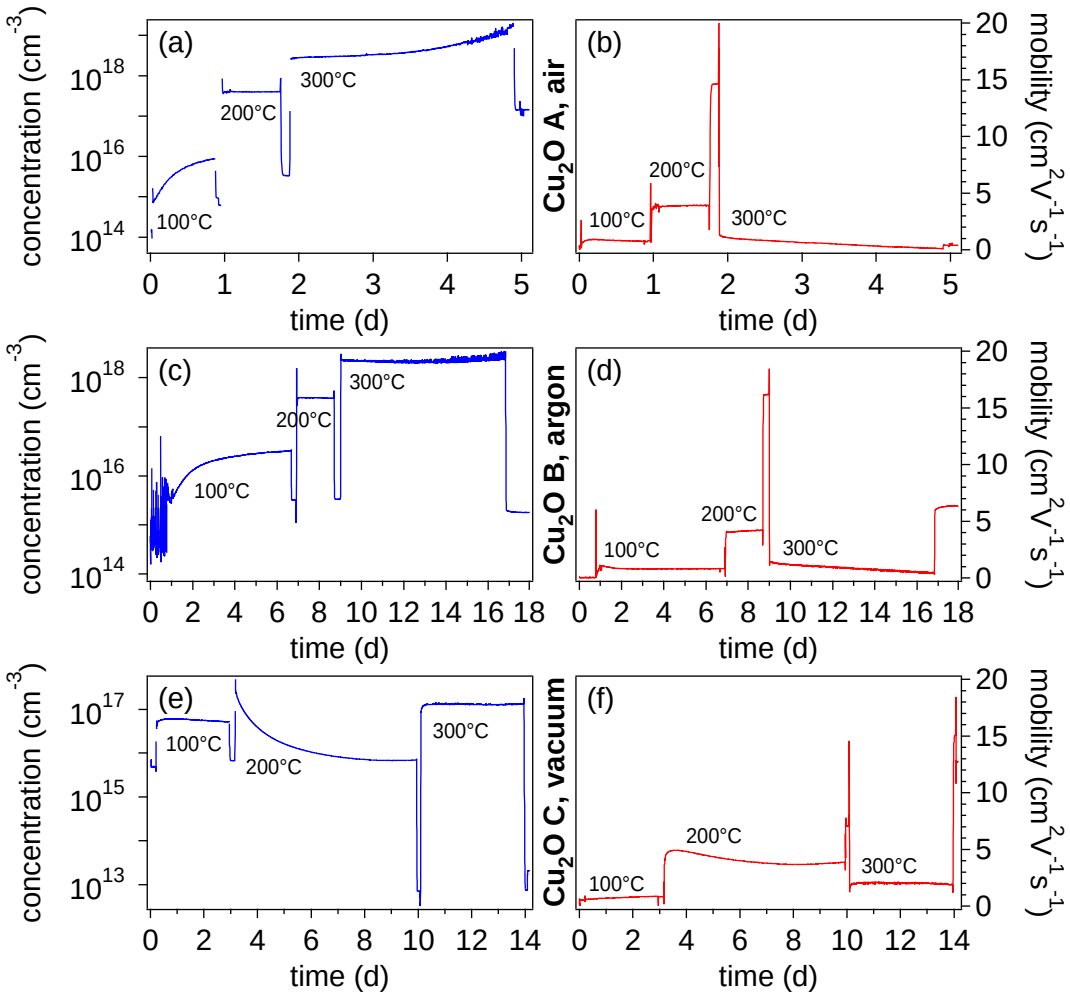

Figure 7.6: The relaxation of Hall carrier concentration and mobility is shown (a), (b) in simulated air; (c), (d) in argon; (e), (f) under vacuum. The temperature is indicated in each plot, without mentioning the room temperature steps in between.

conductivity of two CuO samples in simulated air and under vacuum are included. The CuO samples were measured parallel to the Cu_2O samples presented in Figure 7.6 (a),(b) and (e),(f). Due to the known low mobility of CuO,[18] the respective samples could not be measured by the Hall effect method and only conductivity data is shown.

The obtained results in air and argon atmosphere shall be described first. Whether the atmosphere is air or argon does not have a significant impact on electrical properties when heating Cu_2O up to 200 °C. At 100 °C, conductivities of both Cu_2O A and B increase partially due to an increase in carrier concentration. At 200 °C, no further change in concentration is observed. However, the room temperature mobility is substantially improved under both atmospheric conditions. After relaxation at 300 °C, the mobility is decreased in both atmospheres. The mobility attenuation is more pronounced in air than in argon.

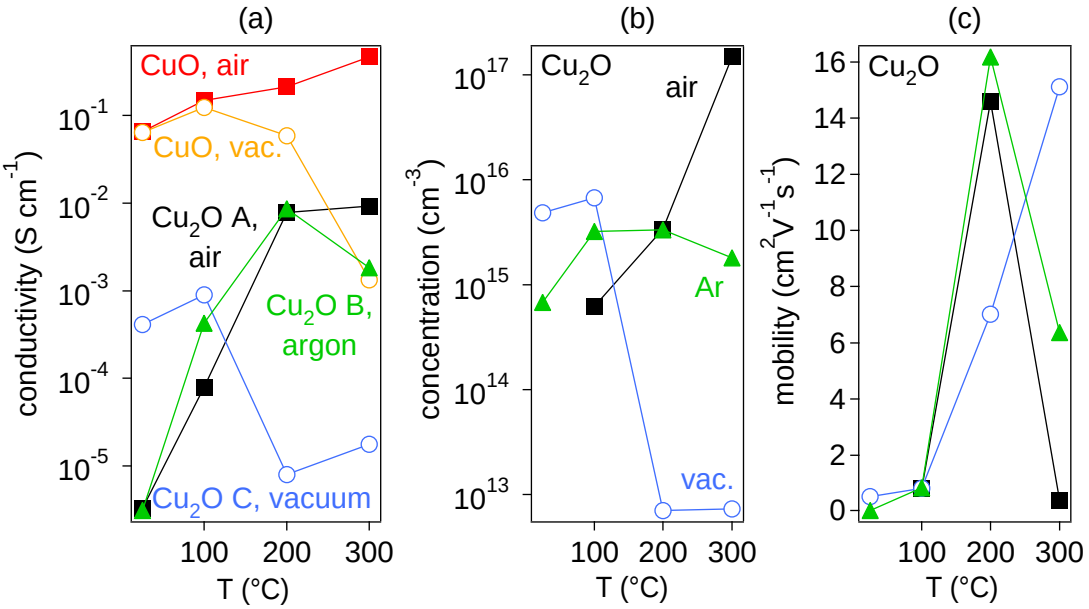

Figure 7.7: Summary of results from Hall effect measurements at variable temperatures (above RT) and atmospheres, showing (a) conductivity, (b) hole concentration and (c) mobility.

The changes in electrical properties are different under vacuum. No pronounced alteration occurs at 100 °C, whereas a significant drop in hole concentration at 200 °C is observed, which causes the conductivity to decrease accordingly. On the contrary, the trend in mobility shows an increase once the sample has been heated to 200 °C. At 300 °C, no additional decrease in charge carrier concentration occurs, however the mobility is further improved.

At the temperatures where rather slow changes in carrier concentration occur (in air and argon at 100 °C, in vacuum at 200 °C) it can be observed in Fig. 7.6, that the mobility changes more rapidly than the carrier concentration.

The conductivity of CuO increases after heating both in air and vacuum at 100 °C, which is shown in Figure 7.7 (a). Differences due to the atmosphere are observed after the samples have been heated above 200 °C. In air, the conductivity increases continuously, whereas under vacuum a decrease is observed. The latter is more pronounced after relaxation at successively higher temperatures.

7.2.2 X-ray diffraction measurements

In order to obtain information on structural changes in the samples, the films were measured by X-ray diffraction after the Hall effect measurement and some of the samples also before it. Figure 7.8 summarizes the results. The XRD measurements of two Cu_2O samples (A and B) before the Hall experiment are shown in Fig. 7.8 (a). The intensity ratio between the most intense reflections (111) and (200) indicates a tendency for preferential

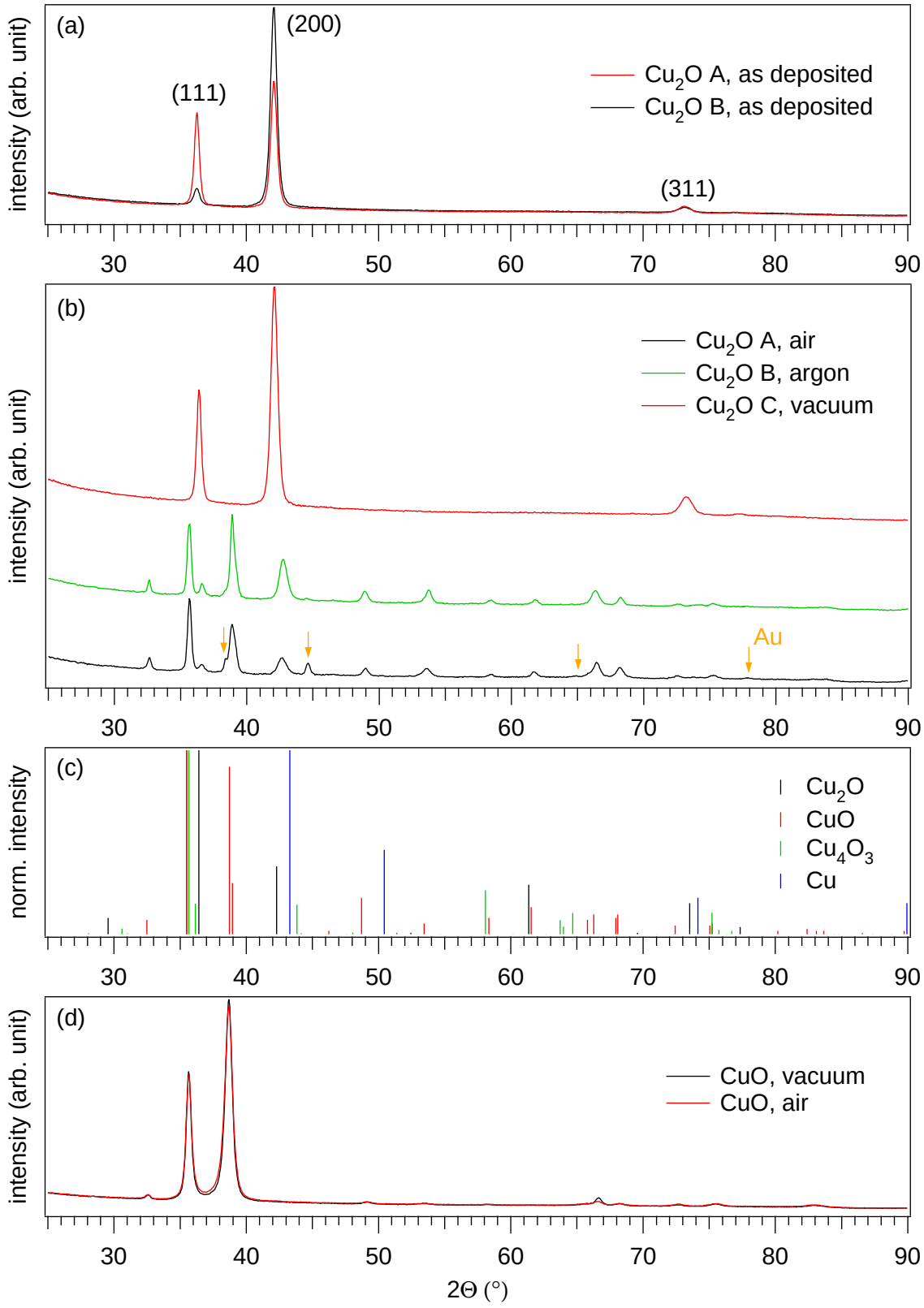

Figure 7.8: (a), (b), (d) X-ray diffraction on samples measured by the Hall effect method at elevated temperatures. The reflection angles and intensities of gold are taken from PDF 00-004-0784. (c) Relevant PDF from ICDD.

orientation along (200) in both samples, similar to the data shown in Fig. 4.4. Although the depositions were carried out with identical parameters, this ratio is not the same for both samples. The sample Cu_2O C was not measured by XRD before the Hall effect experiment due to time constraints. Fig. 7.8 (b) shows the three Cu_2O samples after the experiments in the Hall furnace. Cu_2O A and Cu_2O B are partially oxidized to CuO after heating in air and argon atmosphere. The degree of oxidation in argon is similar to the one in air. The reflections from gold originate from the contacting material. After the experiment in vacuum, no crystallographic structure other than Cu_2O is observed. In order to analyze the patterns further, a comparison of the grain size determined with the Scherrer equation, as well as the lattice plane distance d_{hkl}, is displayed in Figure 7.9.

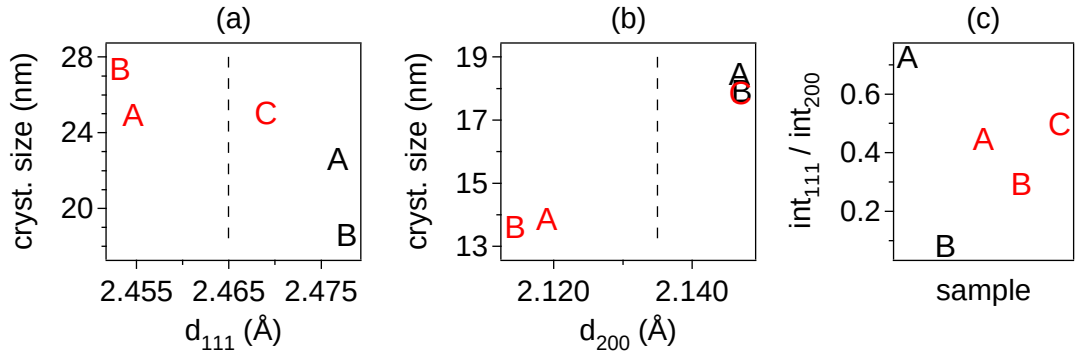

Figure 7.9: Crystallite size (a) in (111) direction and (b) in (200) direction with respect to the distance between the respective lattice planes. (c) Intensity ratio of (111) and (200) reflections. Samples A and B are shown before the Hall effect measurement in black. The data obtained afterwards is represented in red (A: air, B: argon, C: vacuum). The literature value of d_{hkl} is shown by the broken line.

Both for the analysis of the FWHM and of the diffraction angle, it is important that no reflections are overlapping without being recognized by the peak fitting routine. In case a secondary Cu_4O_3 phase is present, an additional reflection would occur in close proximity to the Cu_2O (111) reflection. However, this phase could not be detected in any of the samples shown in Fig. 7.8. The Cu (111) reflection might cause an asymmetry in the Cu_2O (200) reflection. However, a metallic copper phase was not detected in the samples due to the absence of the reflection at 50.434°.

Cu_2O crystallites oriented in (111) direction perpendicular to the sample surface grow during the heating experiments independently on partial oxidation and reduction, which can be observed in Fig. 7.9 (a). Crystallites oriented in (200) are affected in a different way, as shown in Fig. 7.9 (b). It appears, that an oxidizing environment and/or the occurrence of a secondary CuO phase causes Cu_2O crystallites to shrink in the (200) direction. Another effect of partial oxidation on the remaining Cu_2O phase is the conversion of tensile strain (in the as deposited film) to compressive strain. In other words, the material

becomes compacted by heating treatment. Fig. 7.9 (c) shows, that the oxidative atmospheres do not have a significant effect on the intensity ratio between Cu_2O (111) and (200) reflections. The initially different values of int_{111}/int_{200} of Cu_2O samples A and B as deposited become alike by the heating, resulting in an average value around 0.4.

Time-dependence of post-deposition annealing in air

The XRD measurements of Figure 7.8 could only be performed either before or after the complete Hall effect measurement since the atmosphere during the Hall effect measurement had to remain unchanged. Hence, transient phase changes could not be recorded. In order to investigate the time-dependence structural changes caused by post-deposition annealing, Cu_2O samples from UNL were successively annealed for different periods, each time followed by an XRD measurement. The annealing conditions were chosen identical to the ones applied in TFT fabrication, reported in the subsequent chapter (200 °C on a commercial hotplate in ambient air). In Section 4.3 it was mentioned, that after 1 h annealing the Hall mobility is increased whereas the carrier concentration increased only slightly. The main objective of this section is to clarify if and after which duration of annealing a secondary phase of either Cu_4O_3 or CuO is formed.

Figure 7.10 shows XRD patterns of Cu_2O films deposited at UNL and annealed in air for different durations. In addition, an annealing was conducted inside the deposition chamber in the same atmosphere as during the deposition. For this particular sample, this corresponds to 5 % oxygen flow. After 1 h annealing in air, the material is exclusively of Cu_2O structure within the detection limits of XRD.[1] After longer annealing times a secondary CuO phase is detected ($\geq$ 5 h). The annealing in the deposition chamber at 5 % oxygen in the gas flow is shown by the green curve, which reveals that the formation of CuO phase is related to the presence of oxygen in the atmosphere. Since the oxygen partial pressure in the chamber at a flow ratio of 5 % is lower than in ambient atmosphere, the formation of CuO phase is suppressed. No Cu_4O_3 structure is formed during any of the annealing steps.

The inset of Fig. 7.10 shows an enlarged representation of the Cu_2O (111) reflections, which are the most intense ones in these samples. The data is now stacked by increasing annealing time. The other Cu_2O reflections roughly shift in parallel with (111), which indicates that the materials is isotropically strained. The data indicates that the annealing partially releases compressive strain in the material and brings the distance between the lattice planes closer to the database value. This can be observed with greater detail in the representations of crystallite sizes by using the Scherrer equation with respect to lattice plain distances d_{hkl} for the (111) and the (200) Cu_2O reflections shown in Figure 7.11.

The most pronounced change in both d_{111} and d_{200} is observed already after 1 h annealing. The data point after annealing in 5 % oxygen flow and 5×10^{-3} mbar pressure

[1] Note, that the presence of nanocrystalline CuO or Cu_4O_3 cannot be fully excluded based on XRD data.

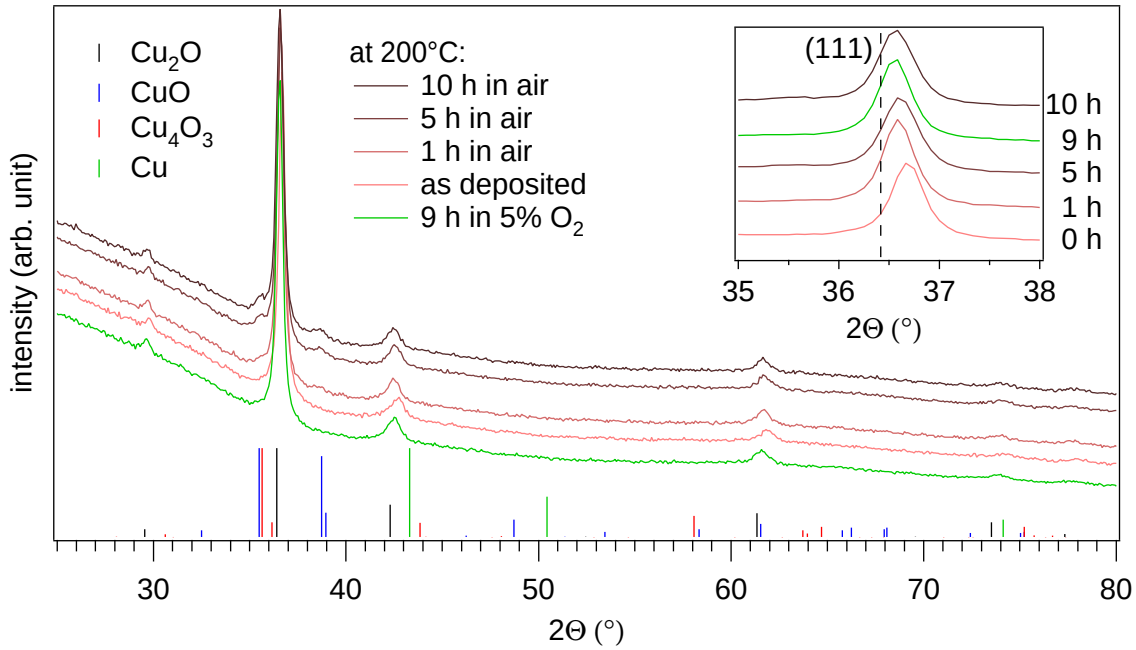

Figure 7.10: Diffraction patterns of Cu_2O samples from UNL after annealing at 200 °C in air for different durations as well as in the deposition atmosphere for 9 h. The inset shows a magnified view of the Cu_2O (111) reflection. Horizontal lines represent data from the PDF.

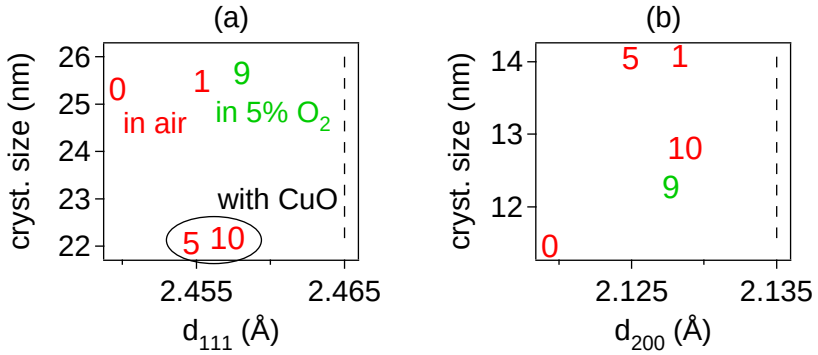

Figure 7.11: Crystallite size (a) in (111) direction and (b) in (200) direction with respect to the distance between the respective lattice planes. The numbers indicate the time of annealing in units of hours. The literature value of d_{hkl} is shown by the broken line.

suggests, that the partial oxidation to CuO has no influence on the strain release. However, the partial oxidation seems to affect the crystallite size. In the (111) direction shown in Fig. 7.11 (a), the crystallite size decreases significantly upon formation of the secondary CuO phase. In the (200) direction of Fig. 7.11 (b), rather a general increase of crystallite size is observed without systematic dependence on the presence of CuO. This may simply be due to an artifact in the evaluation of the FWHM of the most intense Cu_2O reflection

($2\Theta = 36.419°$), caused by the most intense CuO reflection at a similar diffraction angle ($2\Theta = 35.496°$). However, both reflections have been taken into account according to the procedure for qualitative phase analysis outlined in Section 3.3.6.

7.2.3 Discussion

A pronounced dependence on heating time is observed in the Hall effect data of Fig. 7.6 as well as in the XRD results after different annealing times presented in Fig. 7.10. According to the stability regions of compounds formed by copper and oxygen shown in Fig. 2.13, an oxygen partial pressure of less than 10^{-14} bar is needed to be in the stability region of Cu_2O at 600 K.[116] Hence, all the here reported experiments were performed on a metastable Cu_2O phase, which is kinetically stabilized. Consequently, the oxidation and reduction of Cu_2O is inherently time-dependent.

It could be observed by the Hall effect method, that the carrier mobility generally changes faster than the carrier concentration. By XRD measurements it was shown, that a partial release of compressive strain in the material happens already after 1 h of annealing. After longer annealing times, a partial oxidation to CuO takes place, which does not influence the strain of the Cu_2O grains. Hence it is concluded, that the mobility increase due to the annealing is related to the strain release in the material, whereas an increase of carrier concentration is caused by the partial oxidation to CuO.

The tensile strain, which exists in the Cu_2O samples from TU Darmstadt is converted into compressive strain, when the material is partially oxidized to CuO. This happens both in the (111) direction as well as in the (200) direction. Furthermore, a decrease of grain size due to the formation of CuO could be observed. The crystallographic orientation along which the grain size is reduced depends on the preferential orientation of the sample and was observed both along (111) and along (200) for the samples from UNL and TU Darmstadt, respectively. This is in line with literature, which reports no preferred orientation relationship of CuO precipitates in a Cu_2O matrix.[12] The isotropic compression of Cu_2O grains due to the formation of CuO indicates, that the partial oxidation during heating occurs in the grain boundary of the material.[2] This confirms the localization of Cu(II) inside the grain boundaries of Cu_2O, which was concluded based on the results of Chapter 5.

The drop in carrier concentration of Cu_2O in samples heated at $\geq 200\,°C$ in vacuum can be explained as a combination of two processes: First the CuO surface layer is reduced to Cu_2O,[21, 190] then a partial reduction of Cu(I) to Cu(0) occurs. Since the thickness of the Cu_2O films is rather high, the first effect is believed to be of minor importance. As mentioned in Section 2.6.1, metallic copper precipitates are able to deplete the semiconductor Cu_2O by Cu/Cu_2O Schottky barriers.[9, 89, 120, 124] Note, that there is no Cu

[2]Note, that after the heating experiments on the TU Darmstadt samples, the amount of CuO phase compared to Cu_2O is significantly higher than in the UNL samples after the post-deposition annealing (see Fig. 7.8 (b) and Fig. 7.10). It is assumed, that the principle mechanism of partial oxidation is not altered by the amount of CuO but simply causes its effects to be more pronounced.

structure detected by XRD. In the dissertation by Sebastian Siol,[139] SEM images of sputter-deposited Cu_2O after an annealing step in vacuum at 300 °C are shown. These images reveal metallic copper particles at the film surface. The temperature was 100 °C higher than in the Hall effect experiment presented here. However, the changes of electrical properties at 200 °C are slow – a stabilization occurs only after 7 days – with no significant change induced by the subsequent heating step at 300 °C (see Fig. 7.6 (e)). Hence, the presence of similar metallic precipitates at the surface of Cu_2O C after 7 days heating at 200 °C is likely. With a diameter of around 50 nm,[139] it is surprising, that no trace of Cu phase is found in the respective diffractogram (Fig. 7.8 (b)). This could mean, that copper precipitates are mainly present at the surface and the bulk contains only smaller copper crystallites or none at all. Note, that the CuO surface layer on air-exposed Cu_2O is also not detectable by XRD. The width of the depletion region at a Cu_2O/Cu Schottky barrier is reported to be 0.5–1 µm, [17] so even when copper is only present at the surface of the material, the bulk charge carrier concentration of thin films is depleted effectively.

The decrease in conductivity of CuO under vacuum may involve a partial reduction of Cu(II) to Cu(I), which would induce a decrease in carrier concentration. There is however no evidence in Fig. 7.8 (d) for the formation of a Cu_2O phase in the CuO samples heated in vacuum. This is surprising, because 300 °C in vacuum has been reported to reduce CuO to Cu_2O.[191] Since the authors of the referenced study used XPS to determine the oxidation state of the material, it is most likely that not the complete film is reduced to 200 °C, but only regions close to the surface. This could explain the absence of a Cu_2O phase in the respective diffractogram in Fig. 7.8 (d). Further proof is needed to confirm this assumption. Another important point to consider is the increased grain boundary conductivity in CuO.[57] It is possible, that primarily the carrier concentration in the grain boundary is reduced. However, without additional knowledge on the nature of the defects in the grain boundaries of the material, it is not possible to draw further conclusions at this point.

7.2.4 Conclusion

This section provided insight into processes occurring during the annealing of copper oxide films. An improved charge carrier mobility is most likely related to the isotropic release of residual strain. Oxidation and reduction are sensitive to the oxygen amount in the atmosphere during annealing and are primarily responsible for changes of the carrier concentration. During a heat treatment, the mobility changes faster (≤ 1 h) than the carrier concentration. For this reason, post-deposition annealing in order to increase mobility can be conducted in an oxidative atmosphere without causing a significant increase of carrier concentration.

The reduction of Cu_2O to metallic copper under an oxygen-poor atmosphere occurs primarily at the surface. The conclusion is based on the absence of XRD reflections

from the structure of metallic copper and conclusions from SEM images of previous work.[139] In an oxygen-rich atmosphere, the formation of a large amount of CuO in polycrystalline Cu_2O of low density can cause an isotropic compression of the Cu_2O grains. This shows, that an oxidation to CuO primarily occurs at the grain boundaries of Cu_2O. The conclusion corroborates the results of Chapter 5, which revealed the presence of Cu(II) in the grain boundary of nominally stoichiometric Cu_2O.

With the aim to keep the maximum temperature during fabrication as low as possible, an annealing in air or argon at 200 °C is found to lead to the highest values of mobility. Since the differences in electrical properties between heating in air and argon atmosphere are small, ambient air may be chosen as post-deposition atmosphere for practical reasons and to keep fabrication costs low. Heating in vacuum at 300 °C is excluded as possible post-deposition annealing, although the high mobility and low carrier concentration appear beneficial for an application in TFTs. However, the low carrier concentration is caused by a partial depletion due to Cu/Cu_2O Schottky barriers. The resulting Fermi level pinning would not allow a modulation of the carrier concentration by the gate field in a respective TFT device. Furthermore, a substrate temperature of 300 °C does not allow the usage of flexible organic substrates.

Chapter 8

Properties of thin-film transistors

In the first section of this chapter, a presentation and discussion of p-type Cu_2O TFT characteristics is given. The main mechanisms which hinder an accumulation and depletion of the channel by the field-effect are discussed. In order to obtain a deeper understanding of the interplay between defects and electrical field, a study of TFT transfer characteristics under depletion stress and in dependence on temperature was conducted, which is presented in the second section.

8.1 Electrical characteristics

The structure of TFT devices in bottom-gate, top-contact geometry has been described in Sections 2.3.2 and 3.2.1. Figure 8.1 shows transfer curves of devices with different Cu_2O thicknesses on n-Si/SiO_2 and ITO/ATO. The data presented in Fig. 8.1 (b) confirms, that the gate leakage current is generally at least two orders of magnitude smaller than the drain current. Independent of the substrate material, a low ON/OFF current ratio is observed. In the OFF state, the channel conductivity corresponds to 2.5 $S\,cm^{-1}$, when estimated by using Equation 5.1, which is within the range of Cu_2O conductivities reported in Table 5.1. Changing the semiconductor thickness between 10 nm and 20 nm, as well as the usage of different dielectric materials does not have a significant effect on the drain current modulation. However, the leakage current is higher through the SiO_2 dielectric due to its lower thickness compared to ATO.

The effect of the post-deposition annealing in air during 1 h at 200 °C is shown in Figure 8.2 for devices on the ATO bottom-gate dielectric. This post-deposition annealing procedure was chosen based on the results of Section 7.2. The ON/OFF current ratio is increased and the hysteresis becomes smaller after the annealing in air. From the output characteristics of the annealed device shown in Figure 8.2 (c), the absence of

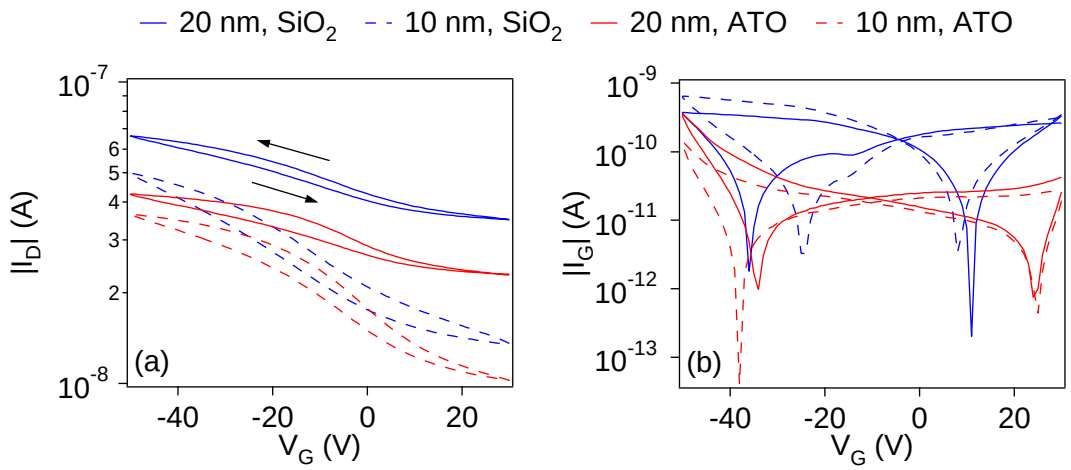

Figure 8.1: Transfer curves (a) and leakage current (b) of TFTs with different Cu_2O thicknesses on n-Si/SiO_2 and ITO/ATO (all currents absolute and on logarithmic scale). Devices with $w/l = 80/20$ were measured at $V_D = -1$ V.

both drain current saturation and pinch-off at $V_D >> V_G$ is observed. Consequently, a saturation mobility according to Equation 2.13 may not be calculated. At $V_D = 1$ V an operation in the linear regime can be confirmed. In this case the drain current depends linearly on the gate voltage, according to the classic equation for thin-film transistors given in Equation 2.11. By using Equation 2.13 the field-effect mobility can be calculated, which is shown in Figure 8.2 (d). The capacitance per unit area was evaluated at 10 kHz on an ITO/ATO/Au MIS structure, giving a value of $C_{di} = 5.92 \times 10^{-8}\,\mathrm{Fcm^{-2}}$, which corresponds to a relative permittivity of ATO of $\epsilon_r = 16.7$. From positive to negative gate voltages, the field-effect mobility of the annealed TFT first increases to a peak value of $\mu_{lin} = 1.3 \times 10^{-3}\,\mathrm{cm^2V^{-1}s^{-1}}$. This value is an order of magnitude higher than of the device before the annealing. With further increasing gate voltage in the range $V_G > -10$ V the field-effect mobility decreases.

8.1.1 Discussion

Since the drain current modulation by the field-effect is small, the assumption of a high density of localized states is reasonable.[123] These states pin the Fermi energy at a certain energetic distance from the Cu_2O valence band. As explained in Chapter 2, the application of a gate potential changes the charge of these localized states instead of creating free charge carriers in the Cu_2O valence band. The nature of these localized states in the Cu_2O channel layers of the here presented TFT devices is discussed in the following.

Based on the data of Chapter 5 it is known, that copper ions in the oxidation state Cu(II) are present at the interface and in the grain boundary. For the discussion it shall be assumed here that a nanocrystalline CuO phase is formed in the boundary regions surrounding the Cu_2O grains, which is schematically shown in Figure 8.3 (a). The results

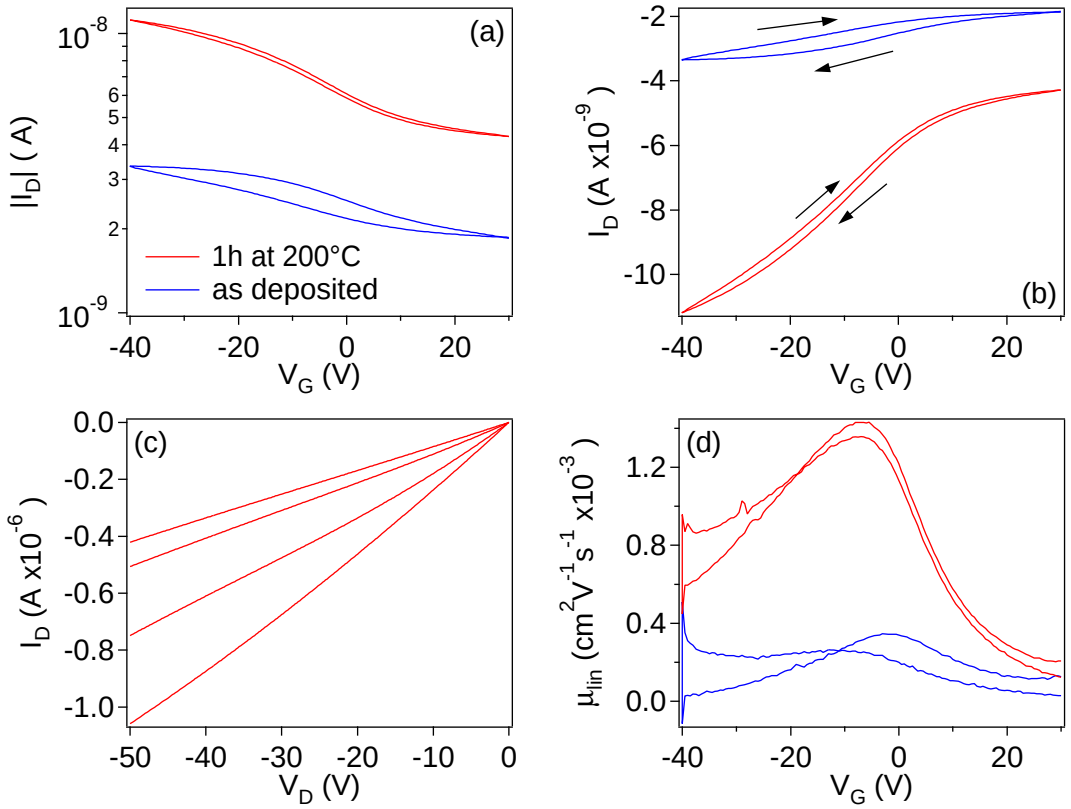

Figure 8.2: TFT characteristics of a device as deposited at room temperature and after a post-deposition annealing in air at 200 °C. The Cu_2O film thickness was 12 nm and the channel geometry was $w/l = 40/20$. Transfer characteristics at $V_D = -1$ V (a) on logarithmic scale and (b) on linear scale with indication of hysteresis; (c) Output characteristics from $V_G = 30$ V to $V_G = -40$ V; (d) linear field-effect mobility from transfer characteristics.

of Chapter 6 could show, that the energy band alignment between two materials is already fully developed at a film thickness in the range of 0.5 nm. Hence, the contact between the grain boundary material and the grain material can be discussed by taking into account the corresponding valence band offset. The valence band maximum of CuO lies at 0.2 eV above the valence band maximum of Cu_2O and thus represents a high density of states inside the band gap of Cu_2O. These states lie slightly below the intrinsic Fermi energy of Cu_2O ($E_F - E_{VB} \approx 0.23$ eV). In Figure 8.3 (b) a schematic energy band diagram from gate electrode to semiconductor is shown, with the CuO band edges superimposed to the ones of Cu_2O.

Upon the application of a negative gate voltage, first the CuO valence states become "charged" with holes. The word *charged* is put in parenthesis here, because is does not mean a change in atomic charge, but an accumulation of holes in the valence states of CuO. The hole mobility of CuO is approximately four orders of magnitude lower than of Cu_2O.[9, 18] This limits the field-effect mobility of the device. In addition, the here assumed nanocrystalline or amorphous structure of CuO presents a disturbance to the

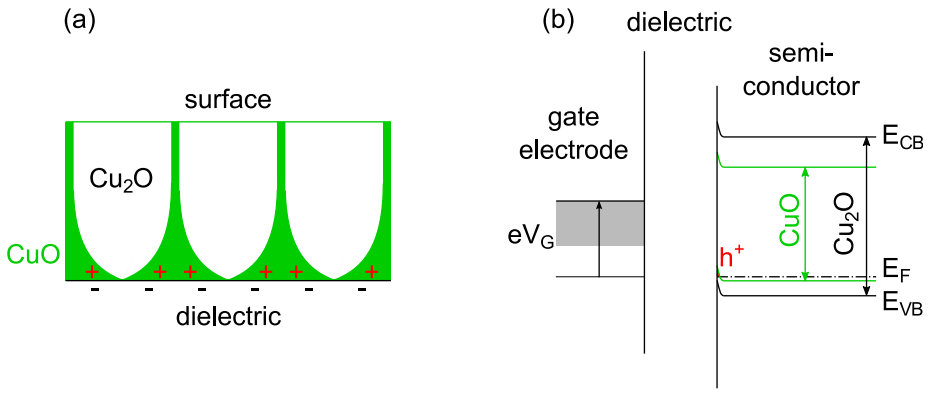

Figure 8.3: A TFT of polycrystalline Cu_2O with CuO in the grain boundary under negative gate bias (accumulation) is schematically shown by (a) a cross-sectional view of the semiconducting channel and by (b) the energy band alignment from gate electrode to the semiconductor. The valence band offset between CuO and Cu_2O is assumed to remain unchanged upon application of the gate bias.

periodicity of the CuO lattice. Consequently, the change in density of valence states at the CuO band edge is not sharp like in a perfect crystal and a high density of localized tail states exists. These tail states further limit the hole carrier mobility in the Cu(II)-containing regions.

Upon the application of a positive gate bias, the channel layer should become depleted from hole carriers. However, the localized valence states of CuO cause Fermi level pinning. Consequently, by the application of a positive gate bias the drain current cannot be decreased below a level which corresponds to the conductivity of the material without gate bias. In other words, the TFT cannot be turned OFF.

As indicated by the arrows in Figure 8.2 (b), the device characteristics corrrespond to a clockwise hysteresis. Hence, mobile ion migration in the channel does not cause the observed hysteresis, since in this case it should be counter-clockwise.[236] This is true for all TFTs produced in this work. With multiple measurements, the hysteresis retraces itself, which means a *non-equilibrium*, *steady-state* is reached.[236] Wager has interpreted this as a manifestation of traps located remotely from the channel-insulator interface, since the capture and emission processes are faster than the sweep time. Hence, the Cu(II) oxidation state in the grain boundary and also at the surface of a Cu_2O layer exposed to ambient air can explain the hysteresis.

It cannot be assumed that a reduction of Cu(II) to Cu(I) or of Cu(I) to Cu(0) occurs during the annealing, due to the high amount of oxygen in ambient air. Hence, the field-effect mobility is increased by the annealing due to a reduction of charge carrier scattering. Comparing the transfer characteristics after annealing to the results from Hall measurement of Section 7.2, the improved Hall mobility and a slightly increased carrier concentration corroborate the encountered changes in the device properties. Since the drain current mainly flows through the interface and grain boundary layers, it can be concluded that the hole mobility of these Cu(II)-containing region is increased by the

annealing.

It should be noted, that the mobility of oxide TFTs of polycrystalline n-type ZnO is generally monotonically increasing with gate voltage bias.[11] This is due to a lowering of the energy barrier at grain boundaries in ZnO, which is induced by the increased carrier concentration in the channel.[237, 238] The energy barriers at ZnO grain boundaries are caused by immobile charges in the boundary, which provoke a depletion layer around it. The decrease in mobility at high gate voltages shown in Fig. 8.2 (d) confirms, that the grain boundaries of Cu_2O are not depleted with respect to the grain interior and that there is no potential barrier for holes between Cu_2O and CuO. Instead, the barrier of 0.2 eV for holes traveling from CuO to Cu_2O possibly contributes to a confinement of charge carriers inside the grain boundary.

8.2 Transfer characteristics under depletion stress at different temperatures

Charge carrier accumulation in an oxide TFT takes place in a very thin region close to the interface to the dielectric. The preceding section could clarify the relevant mechanism, which impede an accumulation and depletion of holes in Cu_2O. In case of an operation in depletion mode (the device is ON at 0 V gate bias) a positive gate bias is needed to turn the p-type device OFF. From the TFT characteristics it is observed that the OFF drain current is particularly high. The Fermi level pinning at the high density of localized states is responsible, that the device cannot be switched OFF. This section intends to explore the TFT under depleting gate bias stress in order to gain further insight into mechanism which impede the depletion of the channel layer.

The typical response of TFTs to gate voltage stress is caused by charge trapping mechanisms. Under accumulation stress, a large threshold voltage shift in the direction of the stressing polarity occurs. A corresponding shift under depletion stress is comparatively small due to the low carrier concentration in the channel. In the absence of other responses of the device to gate stress, the shape of the transfer curve (e.g. sub-threshold swing, field-effect mobility, OFF drain current) does not change significantly under depletion stress.[239]

The following conditions were applied in the experiments: The TFT channel layer was 10 nm thick and had a width of 80 µm and a length of 20 µm. The device was not annealed after fabrication. During the test it was kept in the dark under vacuum at approximately 10^{-3} mbar. Gate voltage stress was 30 V in all stress tests with a recording of transfer characteristics every 30 min. A curve after recovery was measured once before the subsequent test (when applicable). The protocol of the test procedure comprised the following steps:

(a) Depletion stress at room temperature for 3 h

(b) Annealing at 200 °C for 105 min with simultaneous readings of transfer characteristics

(c) Depletion stress at −23 °C for 3 h after annealing

(d) Depletion stress at room temperature for 3 h after annealing

(e) Depletion stress at 100 °C for 3 h after annealing

The results are given in Figure 8.4 (a)–(e), corresponding to the steps mentioned above. The top row shows the transfer characteristics. The hysteresis is in all cases clockwise, confirming that migration of ionic species is not relevant.[236] The threshold voltage shift is not evaluated like in typical stress tests, since the value cannot be determined reliably due to the non-linear transfer curve. Alternatively, the absolute drain current is plotted with respect to time in the plots of the middle row. The drain current is shown at gate voltage steps of −10 V in forward direction up to the maximum (negative) voltage. Lastly, the bottom row shows the ON/OFF drain current ratio at each time step, taken from the transfer characteristics at most negative and most positive gate voltage. The description of the results is partially accompanied by a short discussion of specific observations in order to focus on the processes under depletion stress in the main discussion of this section.

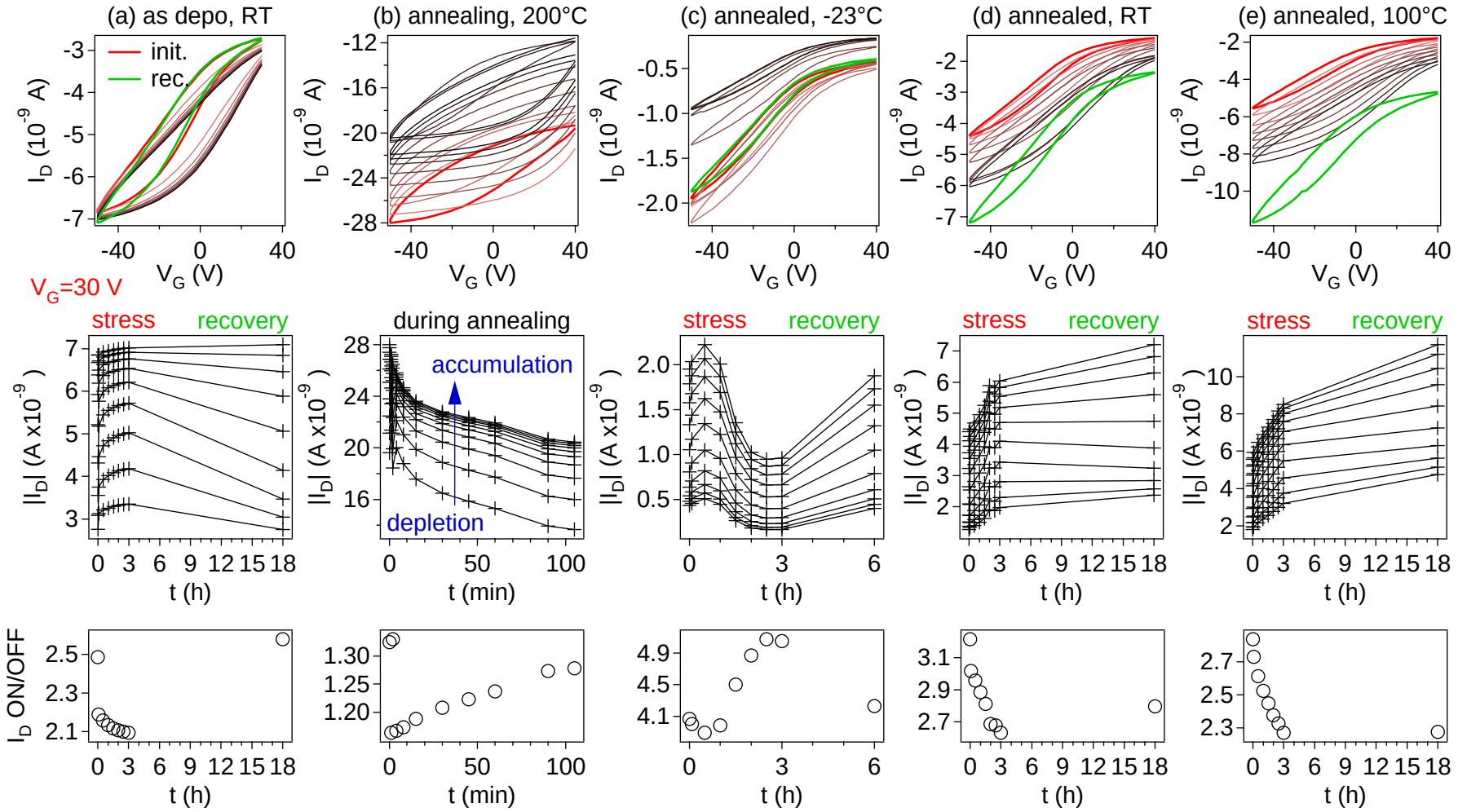

Figure 8.4: Influence of depletion stress and temperature on transfer characteristics. Under stress or annealing: red to black curves, recovered: green (when applicable).

Fig. 8.4 (a): Depletion stress at room temperature of the as-deposited TFT results in comparatively fast changes to the transfer characteristics and full recovery. A shift is observable in the same polarity as the gate stress. Considering a conventional interpretation of gate voltage stress, these observations suggest that charge trapping occurs at the semiconductor/dielectric interface.[239] Due to the considerable drain current in the OFF state, a large number of carriers are present in the channel even under positive gate voltage bias (compared to an ideal TFT in depletion). These carriers then become trapped and cause a shift in the transfer curve.

Fig. 8.4 (b): At 200 °C (without application of gate stress), a considerable increase in drain current and hysteresis width, as well as a decrease in ON/OFF drain current is observed, which is probably both due to the thermally induced higher charge carrier concentration. The hysteresis width increases further after the first few measurements showing more severe trapping of charge carriers. During the annealing, a relative decrease in drain current is observed together with a slight increase of the ON/OFF current ratio. This is most likely related to a reduction of copper cations, which reduces the carrier concentration.

Fig. 8.4 (c): After the annealing, gate bias stress is applied at −23 °C substrate temperature. The drain current initially increases slightly and the ON/OFF ratio decreases under stress. This may be relates to a threshold voltage shift to the positive side, which could be explained by the trapping of hole carriers at the channel-dielectric interface.[239] However, after 30 min the drain current decreases and the ON/OFF ratio increases. This trend appears to saturate after a total stress time of 3 h. Full recovery of the initial characteristics is observed after another 3 h without gate stress.

Fig. 8.4 (d): At RT, the initial curve after annealing compared to the initial curve before annealing of Fig. 8.4 (a) confirms that the total drain current is decreased by the annealing. Furthermore, a decrease in hysteresis width is observed. Under depletion stress, the drain current as well as the hysteresis increase continuously while the ON/OFF ratio decreases. No recovery is reached after 15 h without gate stress. Instead, the characteristics after stress are very similar to the initial curve before annealing, except for the smaller hysteresis width.

Fig. 8.4 (e): Stress at 100 °C results in a similar behavior like at RT, however with a generally higher drain current level due to the higher temperature. Accordingly, also the magnitude of changes during gate stress is increased with respect to the measurement at RT.

8.2.1 Discussion

The impact of heating in vacuum on the carrier concentration in comparatively thick samples has been discussed in Section 7.2. The main processes are a reduction of Cu(II) which has formed at the surface in contact with ambient air and subsequently a formation of metallic copper at the surface. The hole concentration data shown in Figure 7.6 (e)

is relevant in this context. After 105 min, which is equivalent to the annealing time of the TFT in Fig. 8.4 (b), the concentration in the Hall samples is decreased by at least 40 %. The drain current shown in Fig. 8.4 (b) decreases by a similar amount, neglecting the changes in the ON/OFF current ratio. Hence, it seems plausible that a reduction of hole carriers due to cation reduction takes place in the TFTs during the annealing at 200 °C in vacuum. A temperature of 100 °C is not sufficient to provoke cation reduction, as both thick films for Hall effect measurements and thin film in TFTs show no decrease in carrier concentration and drain current at that temperature, respectively. Given that effects due to temperature are comparatively small in vacuum below 100 °C, the findings of Fig. 8.4 (c)–(e) may be interpreted as being mainly due to the gate bias stress.

The increase in drain current under depletion stress, which is observed at room temperature and 100 °C, but not at −23 °C shall now be discussed. Two types of processes can be responsible for changes in drain current under depletion stress in a homogeneous semiconductor: Defect creation and defect migration. Pure rearrangement of charged defects during stress would have no effect on the OFF current, as no new charge carriers are created. Instead, only an increase of the ON current would be observed, since the channel is formed in the vicinity to the dielectric interface. From the plots in the middle and bottom row of Figure 8.4 it is observed, that an increase in drain current is generally accompanied by a decrease in ON/OFF ratio and vice-versa. Hence, an increase in charge carriers takes place in the semiconductor, and not only a rearrangement of the charges due to mere electromigration of defects. Defect creation has an effect on both ON and OFF drain current, causing an overall increase of I_D, which corresponds to the experimental observation. Further cation oxidation is unlikely due to the low total pressure during the experiment. Hence, possible processes which lead to an increase in carrier concentration during gate voltage stress have to be discussed. At first the behavior of homogeneous Cu_2O shall be discussed, when it is forced into depletion by the gate voltage stress. In subsequent paragraphs, the role of the grain boundary is discussed.

Depleting an intrinsically doped semiconductor likely induces *self-compensation*. The mechanism is described in Section 2.4.3 and applies to materials in thermodynamic equilibrium. Note, that Cu_2O is metastable at room temperature and in ambient atmosphere which means that – theoretically – the concept of self-compensation cannot be applied. However, the equilibrium conditions of a device under gate voltage bias are different from a device without bias. Hence, any dynamic change of a device under stress has to occur towards the new equilibrium, which is imposed by the gate voltage. Depletion stress on a p-type semiconducting channel forces the Fermi energy to rather high levels in the band gap. With an equilibrium in the channel region at a negative potential, the intrinsically p-type material Cu_2O has to compensate this negative potential by providing positive charge carriers. This is accomplished by the creation of intrinsic acceptor defects (mainly copper vacancies). In other words, the Fermi energy is constrained to a region close to the valence band maximum. The relation of the defect concentration and the Fermi level is described by Equation 2.18. When comparing Figures 8.4 (c), (d) and (e) with each other,

the increase in drain current is more pronounced at elevated temperatures and does not occur at −23 °C. This temperature effect is possibly related to the Boltzmann term of Equation 2.18.

The role of the grain boundary

The grain boundary contains a high carrier concentration with respect to Cu_2O and acts like a shunting path for conduction through the grain. A constant valence band offset between CuO and Cu_2O and the large depletion width in Cu_2O suggest, that an increase in $E_F - E_{VB}$ by the positive gate bias affects the grain boundaries and the grains by the same amount. Since an increase in Fermi energy is limited by pinning to the valence states of CuO, the Fermi energy in the Cu_2O grains is not significantly increased by the positive gate voltage. Hence, the effects of depletion stress should rather be discussed for CuO than for Cu_2O. A discussion of intrinsic defect reactions related to self-compensation, for example according to the defect complex mechanism outlined by Mittiga *et al.* would not be relevant (see Section 2.6.1).[106] However, a discussion of defect mechanisms in CuO is difficult due to the limited knowledge on intrinsic defects in the material. Compared to Cu_2O, the literature on electronic structure and defect states of CuO is much more scarce. Nevertheless, CuO is known to be intrinsically p-type with copper vacancies being the main acceptor state.[240] Hence, self-compensation most likely plays a role also in CuO.

8.3 Conclusion

The low modulation of the hole carrier concentration by the field-effect in a TFT based on Cu_2O is a sign of the Cu(II) oxidation state occurring in the grain boundary and at the interface. The Fermi energy is pinned to the valence states of CuO. The external gate field mainly has an effect on the Cu(II) interface region, causing a low ON/OFF ratio and low mobility since the charge carrier concentration of the Cu_2O grains is hardly changed. A higher field-effect mobility is achieved by annealing in air. However, the higher device mobility is most likely due to an improved hole mobility in the interface and grain boundary regions.

Results from gate bias stress in depletion at different temperatures were interpreted under consideration of self-compensation by intrinsic defects. The existence of the highly conductive grain boundary and interface layers suggests, that the relevant processes occur in these regions rather than inside the grains. Being comparable to the intrinsically p-type material CuO in terms of electrical properties, self-compensation under depletion likely occurs in the Cu(II)-containing regions. However, for a discussion of defect mechanisms in depleted CuO, further knowledge on intrinsic defects in this material is required.

Chapter 9

Summary and conclusions

This study investigated Cu_2O for an application in p-type thin-film transistors. Following the approach of a moderate temperature route ($T \leq 200\,°C$) in order to enable deposition on low-cost and flexible organic substrates, an inhomogeneous and metastable polycrystalline semiconductor is obtained. The relevant mechanisms which limit the electrical performance of this material were identified. It is proposed, that the presence of oxidation states other than Cu(I) is responsible for the non-ideal behavior of Cu_2O, which is observed in the presented experimental data as well as in literature. By sputter-deposition at room temperature it is practically impossible to obtain a TFT channel layer of Cu_2O with low charge carrier concentration, high mobility and without a pinned Fermi level. This is illustrated by a schematic representation of the Fermi energy with respect to stoichiometry in Figure 9.1. Detailed explanations are given in the subsections below.

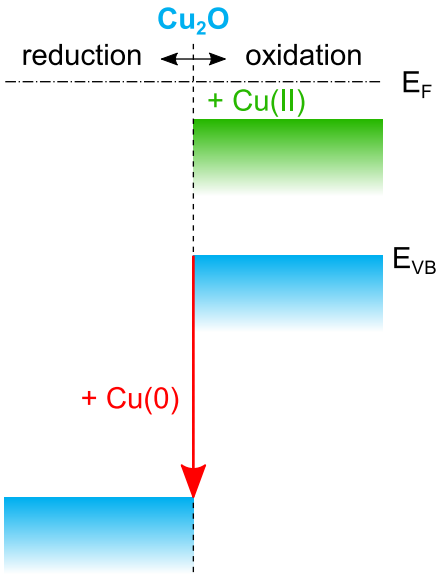

Figure 9.1: Schematic representation of the valence band maxima in Cu_2O with inhomogeneous oxidations states. The Schottky barrier Cu/Cu_2O pins the Fermi level of Cu_2O to 0.5–0.6 eV. Cu(II) in the grain boundaries causes additional states between the Fermi level and the valence band maximum of Cu_2O.

Cu(II) in the grain boundaries of Cu_2O

Like in other polycrystalline semiconductors the grain boundary has severe influence on macroscopic electrical properties. However, instead of a barrier due to a local depletion, a higher charge carrier concentration with respect to the grain interior is observed in Cu_2O. This is due to the occurrence of Cu(II) in the grain boundary, even when the material is stoichiometric according to XRD results and XPS data of the film surface. Theses results are partially published in Reference [221].

Most of the existing models which describe inhomogeneous electrical properties of polycrystals are limited to materials with low grain boundary conductivity with respect to the grain interior. A material with highly conductive grain boundaries requires a new formalisms. An adequate model was proposed in this thesis in order to describe the conductivity with respect to grain size for the typical polycrystalline film growth of columnar grains. Related to the film growth, the grain boundary density is highest in vicinity to the substrate surface. Hence, the thinner a film the more severe is the increase of conductivity with respect to monocrystalline Cu_2O. In oxide TFTs, the semiconducting layers are typically less than 50 nm thick and thus contain a high volume fraction of grain boundaries.

The bonds between Cu(II) ions and oxygen in the grain boundary probably have a similar geometry like in the CuO structure. However, the grain boundary layer can only be amorphous or nanocrystalline due to its limited width. The question of energy band alignment between the grains and the grain boundary needed to be answered. It could be shown, that a thickness of 0.5 nm is enough, to obtain the same valence band offset between two materials like at the contact between the bulk materials. This conclusion was drawn from an XPS analysis of the energy band alignments between thin Cu_2O films to different substrates. By the removal of the contribution of extra-atomic relaxation from the data, it could be shown that the valence band offset between two material is already established at a layer thickness of a few Ångström.

The valence band offset between Cu_2O and CuO was determined from transitivity to be $\Delta E_{VB} = 0.2\,\text{eV}$. The resulting barrier for holes between CuO and Cu_2O effectively contributes to a confinement of charge carriers inside the grain boundary and enhances the shunting effect on the current through the grains. With Cu(II) in the grain boundary of Cu_2O, the CuO valence states represent a high density of states at 0.2 eV above the valence band maximum of Cu_2O. The disordered structure inside the grain boundary and interface layers causes a high density of tail states. When a corresponding p-type channel layer of a TFT is switched from depletion to accumulation, hole charge carriers are introduced to the valence states of CuO instead of the valence band of Cu_2O. When the device is switched from accumulation to depletion, the Fermi energy remains low because it is pinned at these CuO tail states.

With the drain current modulation in polycrystalline Cu_2O happening predominantly in the Cu(II)-containing regions of the material, the corresponding ON/OFF drain current

ratio and field-effect mobility are severely limited. The OFF drain current is high due to the high intrinsic hole carrier concentration of CuO, compared to Cu_2O.[9, 18] The localization of the states at the valence band maximum of CuO limits the increase in drain current by the field-effect and correspondingly the field-effect mobility.

The carrier mobility of polycrystalline Cu_2O can be increased by post-deposition annealing in air at 200 °C. The mobility increase is related to the structural relaxations which occur during less than 1 h. Longer annealing times provoke a growth of the grain boundary region by the formation of CuO crystallites. Since the grain boundary width is increased after prolonged annealing, the effective hole carrier concentration of the material rises as well. By limiting the duration of the treatment, the simple post-deposition annealing at 200 °C in air improves the TFT device performance while being compatible with organic substrates.

Cu(0) and the depletion of Cu_2O

Cu(II) in the grain boundary appears to be unavoidable when intentionally stoichiometric Cu_2O is deposited by reactive sputtering at room temperature. Aiming to prevent the formation of Cu(II), a decrease of the oxygen content in the process readily leads to the formation of Cu(0). The Cu/Cu_2O Schottky barrier causes a depletion of the material, and results in electrical properties similar to a highly compensated semiconductor. The Fermi energy is pinned to $0.5\,\mathrm{eV} \leq E_F - E_{VB} \leq 0.6\,\mathrm{eV}$. The work by Siol *et al.* shows, that the Fermi level pinning limits the band bending in Cu_2O at the heterojunction to ZnO.[227]

Apart from the film deposition, the cation reduction to metallic copper can also occur by post-deposition processing. If the Cu_2O film is annealed in vacuum at temperatures $\geq$ 200 °C, metallic copper forms at the surface. If another material is deposited onto Cu_2O by a process which involves species that react with oxygen, the Cu_2O surface is also partially reduced to metallic copper. This could be shown for the atomic layer deposition of the dielectric Al_2O_3, which is published in Reference [193].

Outlook

Concerning an improvement of the characteristics of p-type TFTs below a maximum fabrication temperature of 200 °C, the usage of a polycrystalline Cu_2O channel layer remains challenging. The highly conductive grain boundaries need to be eliminated, which requires a single-crystalline material. However, epitaxial layers are only obtainable by the usage of high temperature.[10] Possibly, the segregation of Cu(II) into the grain boundary can be suppressed by the intentional incorporation of other divalent cations. In case the formation of the complex with the two copper vacancies is responsible for the high carrier concentration in the grain boundary,[101, 102] the substitution of Cu(II) by an isovalent cation may potentially suppress the formation of the complex or increase its

energy level in the band gap. Both could lead to a lower carrier concentration in the grain boundary.

From a fundamental point of view, a model which describes Hall effect data of a polycrystalline thin film with highly conductive grain boundaries is lacking. With such a model at hand, the contributions of charge carrier concentration and mobility on conductivity could be analyzed individually for grain and grain boundary regions. This would allow for a better localization of the respective mechanisms, which affect either of both electrical properties. Further experimental studies of electrical properties of a material with highly conductive grain boundaries could involve the deposition of Cu_2O in the different zones of the structure zone model in order to investigate various morphologies. The fabrication of these samples could be achieved by variation of the sputtering power, deposition temperature and total chamber pressure.

It should be noted, that the existence of oxidation states different from the parent material is not necessarily detrimental for the desired electrical properties of a TFT channel material. An example is given by the case of p-type SnO. On the one hand, the higher oxidation state Sn(IV) forms the n-type phase SnO_2. Hence, a partial oxidation of SnO-based TFTs decreases the hole carrier drain current[241, 242] and a tendency towards ambipolar behavior is observed under even more oxidizing conductions.[243] On the other hand, the inclusion of metallic Sn(0) in SnO appears to improve the hole mobility.[242]

Alternative materials are continuously researched, which promise good switching characteristics when applied in p-type TFTs. Calculations by density functional theory predicted multi-component oxides with half the effective hole mass than Cu_2O, for example $K_2Sn_2O_3$.[244] P-type conduction could be shown for bismuth-based multicomponent oxides.[245] However, experimental reports on thin films of these materials with electrical properties comparable to Cu_2O cannot be found in literature. Apart from oxides, other p-type materials like halides have been shown to produce working thin film devices, such as heterojunction diodes with CuI.[246]

The partial reduction of copper oxide can be beneficial for other applications than in thin-film transistors. For example, the occurrence of metallic copper at the interface between Cu_2O and Al_2O_3 by ALD led to further investigation for an application as resistive memory.[247] Working devices based on the layer sequence ITO/Cu_2O/Cu/Al_2O_3/Pt are shown in the Master thesis of José Rosa.[248][1] In order to clarify whether the metallic copper at the interface is beneficial for the resistive switching, a comparison to samples based on pure Cu_2O/Al_2O_3 and Cu/Al_2O_3 interfaces is required. Furthermore, with the drastic change in carrier concentration of copper oxides from depleted Cu_2O ($p \approx 10^{10}\,cm^{-3}$)[9] to CuO ($p \approx 10^{19}\,cm^{-3}$)[18], thin films of graded stoichiometry may be of potential interest for an application in valence-change resistive memory devices. Such films could be deposited by reactive sputtering simply by a variation of oxygen partial pressure in the process gas during the deposition.

[1] These results are not included in this thesis, because they are beyond its scope.

Bibliography

[1] P. Barquinha, R. Martins, L. Pereira, and E. Fortunato. *Transparent Oxide Electronics: From Materials to Devices*. Wiley-Blackwell, 2012. DOI: 10.1002/9781119966999 (cited on pages 1, 2).

[2] S. Brotherton. *Introduction to Thin Film Transistors*. Springer Science + Business Media, 2013. DOI: 10.1007/978-3-319-00002-2 (cited on pages 1, 7).

[3] H. Moon, H. Cho, M. Kim, K. Takimiya, and S. Yoo. "Towards Colorless Transparent Organic Transistors: Potential of Benzothieno[3,2-*b*]benzothiophene-Based Wide-Gap Semiconductors". *Advanced Materials* 26 (2014), pages 3105–3110. DOI: 10.1002/adma.201305440 (cited on page 1).

[4] URL: http://www.lg.com/us/tvs/lg-OLED77G6P-oled-4k-tv (cited on page 2).

[5] URL: http://www.sharp-world.com/products/professional-monitors/products/pn-h801/specifications.html (cited on page 2).

[6] URL: http://www.planar.com/products/transparent-displays/planar-lo55/?f=Planar%20LO55.pdf (cited on page 2).

[7] J. F. Wager, D. A. Keszler, and R. E. Presley. *Transparent Electronics*. Springer Science + Business Media, 2008. DOI: 10.1007/978-0-387-72342-6 (cited on page 2).

[8] H. Kawazoe, M. Yasukawa, H. Hyodo, M. Kurita, H. Yanagi, and H. Hosono. "p-Type Electrical Conduction in Transparent Thin Films of $CuAlO_2$". *Nature* 389 (1997), pages 939–942. DOI: 10.1038/40087 (cited on pages 2, 22).

[9] E. Fortin and F. L. Weichman. "Hall effect and electrical conductivity of Cu_2O monocrystals". *Canadian Journal of Physics* 44 (1966), pages 1551–1561. DOI: 10.1139/p66-128 (cited on pages 2, 3, 32, 36, 37, 96, 101, 134, 139, 149, 150).

[10] K. Matsuzaki, K. Nomura, H. Yanagi, T. Kamiya, M. Hirano, and H. Hosono. "Epitaxial growth of high mobility Cu_2O thin films and application to p-channel thin film transistor". *Applied Physics Letters* 93 (2008), page 202107. DOI: 10.1063/1.3026539 (cited on pages 2, 3, 32, 34, 37, 70, 85, 149).

[11] E. Fortunato, P. Barquinha, and R. Martins. "Oxide Semiconductor Thin-Film Transistors: A Review of Recent Advances". *Advanced Materials* 24 (2012), pages 2945–2986. DOI: 10.1002/adma.201103228 (cited on pages 3, 141).

[12] M. Martinez-Clemente and R. D. Schmidt-Whitley. "A TEM study of precipitates in Cu_2O". *Journal of Materials Science* 10 (1975), pages 543–546. DOI: 10.1007/bf00543701 (cited on pages 3, 134).

[13] B. K. Moss, P. Goodman, and A. W. S. Johnson. "Investigation of mineralogical and synthetic Cu_2O by HREM and CBED". *Journal of Solid State Chemistry* 73 (1988), pages 268–273. DOI: 10.1016/0022-4596(88)90078-3 (cited on pages 3, 36).

[14] F. L. Weichman. "Grain-Boundary Conductivity of Cu_2O Polycrystals and Rectifiers". *Journal of Applied Physics* 41 (1970), page 3491. DOI: 10.1063/1.1659447 (cited on pages 3, 24, 32, 97).

[15] S. Aggarwal. "Point defects and transport in binary and ternary, non-stoichiometric oxides". *Solid State Ionics* 101-103 (1997), pages 321–331. DOI: 10.1016/s0167-2738(97)84048-9 (cited on pages 3, 24, 97).

[16] W. Schottky and W. Deutschmann. "Zum Mechanismus der Richtwirkung in Kupferoxydulgleichrichtern". *Physikalische Zeitschrift* 30 (1929), pages 839–846. DOI: 10.1007/978-94-009-0657-0_3 (cited on page 3).

[17] W. H. Brattain. "The Copper Oxide Rectifier". *Reviews of Modern Physics* 23 (1951), pages 203–212. DOI: 10.1103/revmodphys.23.203 (cited on pages 3, 32, 97, 124, 135).

[18] A. A. Samokhvalov, N. A. Viglin, B. A. Gizhevskij, N. N. Loshkareva, V. V. Osipov, N. I. Solin, and Y. P. Sukhorukov. "Low-mobility charge carriers in CuO". *Journal of Experimental and Theoretical Physics* 76 (1993), pages 463–468 (cited on pages 3, 31, 84, 96, 99, 101, 128, 139, 149, 150).

[19] B. K. Meyer, A. Polity, D. Reppin, M. Becker, P. Hering, P. J. Klar, T. Sander, C. Reindl, J. Benz, M. Eickhoff, C. Heiliger, M. Heinemann, J. Bläsing, A. Krost, S. Shokovets, C. Müller, and C. Ronning. "Binary copper oxide semiconductors: From materials towards devices". *Physica Status Solidi B* 249 (2012), pages 1487–1509. DOI: 10.1002/pssb.201248128 (cited on pages 3, 31, 33, 38, 81, 82).

[20] K. Matsuzaki, K. Nomura, H. Yanagi, T. Kamiya, M. Hirano, and H. Hosono. "Effects of post-annealing on (110) Cu_2O epitaxial films and origin of low mobility in Cu_2O thin-film transistor". *Physica Status Solidi A* 206 (2009), pages 2192–2197. DOI: 10.1002/pssa.200881795 (cited on pages 3, 33, 36, 37, 72).

[21] A. Rosencwaig and G. Wertheim. "X-ray photoemission satellites; surface or bulk effect?" *Journal of Electron Spectroscopy and Related Phenomena* 1 (1972), pages 493–496. DOI: 10.1016/0368-2048(72)80019-7 (cited on pages 3, 64, 134).

[22] F. Ran, H. Hiramatsu, H. Hosono, T. Kamiya, and M. Taniguti. "Detection of dead layers and defects in polycrystalline Cu_2O thin-film transistors by x-ray reflectivity and photoresponse spectroscopy analyses". *Journal of Vacuum Science & Technology B* 33 (2015), page 051211. DOI: 10.1116/1.4929445 (cited on pages 3, 32, 33, 39, 70, 88).

[23] F. Ran, M. Taniguti, H. Hosono, and T. Kamiya. "Analyses of Surface and Interfacial Layers in Polycrystalline Cu_2O Thin-Film Transistors". *Journal of Display Technology* 11 (2015), pages 720–724. DOI: 10.1109/jdt.2015.2432752 (cited on pages 3, 39).

[24] H. Ibach and H. Lüth. *Solid-State Physics*. Springer Science + Business Media, 2009. DOI: 10.1007/978-3-540-93804-0 (cited on pages 7, 22).

[25] A. Klein. *Semiconductor Interfaces*. Lecture notes. Technische Universität Darmstadt. 2008 (cited on page 7).

[26] S. M. Sze. *Physics of Semiconductor Devices*. 3rd edition. John Wiley & Sons, 2007 (cited on pages 7, 19).

[27] A. C. Tickle. *Thin-Film Transistors, A New Approach to Microelectronics*. John Wiley & Sons, 1969 (cited on pages 7, 14).

[28] K. Albe, P. Ágoston, and J. Pohl. "Ab-Initio Modeling of Defects in Semiconductors". *Advanced Characterization Techniques for Thin Film Solar Cells*. Edited by D. Abou-Ras, T. Kirchartz, and U. Rau. Weinheim, Germany: Wiley-VCH Verlag GmbH & Co. KGaA, 2011. DOI: 10.1002/9783527636280 (cited on pages 7, 19).

[29] M. Ohring. *Material Science of Thin Films*. 2nd edition. Stevens Institute of Technology, NJ, U.S.A.: Academic Press, 2001 (cited on pages 7, 22, 42, 43, 50, 55, 63, 74, 75).

[30] W. Heisenberg. "Über den anschaulichen Inhalt der quantentheoretischen Kinematik und Mechanik". *Zeitschrif für Physik* 43 (1927), pages 172–198. DOI: 10.1007/bf01397280 (cited on pages 8, 57).

[31] W. Pauli. "Über den Zusammenhang des Abschlusses der Elektronengruppen im Atom mit der Komplexstruktur der Spektren". *Zeitschrift für Physik* 31 (1925), pages 765–783. DOI: 10.1007/bf02980631 (cited on pages 8, 57).

[32] E. Fermi. "Sulla quantizzazione del gas perfetto monoatomico". *Rendiconti Lincei* 3 (1926), pages 145–149 (cited on page 9).

[33] P. A. M. Dirac. "On the Theory of Quantum Mechanics". *Proceedings of the Royal Society A: Mathematical, Physical and Engineering Sciences* 112 (1926), pages 661–677. DOI: 10.1098/rspa.1926.0133 (cited on page 9).

[34] J. E. Lilienfeld. "Method and apparatus for controlling electric currents". Patent. 1930 (cited on page 12).

[35] H. Borkan and P. K. Weimer. "An Analysis of the Characteristics of Insulated-Gate Thin-Film Transitors". *RCA Review* 24 (1963), pages 153–165 (cited on page 14).

[36] G. G. Roberts, N. Apsley, and R. W. Munn. "Temperature dependent electronic conduction in semiconductors". *Physics Reports* 60 (1980), pages 59–150. DOI: 10.1016/0370-1573(80)90046-0 (cited on page 15).

[37] D. K. Schroder. *Semiconductor Material and Device Characterization*. 3rd edition. Wiley-Blackwell, 2006. DOI: 10.1002/0471749095 (cited on page 18).

[38] J. Robertson and S. J. Clark. "Limits to doping in oxides". *Physical Review B* 83 (2011). DOI: 10.1103/physrevb.83.075205 (cited on pages 18, 33).

[39] P. Stallinga. *Electrical Characterization of Organic Electronic Materials and Devices*. Wiley-Blackwell, 2009. DOI: 10.1002/9780470750162 (cited on page 19).

[40] J. W. Orton and M. J. Powell. "The Hall effect in polycrystalline and powdered semiconductors". *Reports on Progress in Physics* 43 (1980), pages 1263–1307. DOI: 10.1088/0034-4885/43/11/001 (cited on pages 20, 21, 24, 25, 28).

[41] F. Greuter and G. Blatter. "Electrical properties of grain boundaries in polycrystalline compound semiconductors". *Semiconductor Science and Technology* 5 (1990), pages 111–137. DOI: 10.1088/0268-1242/5/2/001 (cited on page 20).

[42] C. R. M. Grovenor. "Grain boundaries in semiconductors". *Journal of Physics C: Solid State Physics* 18 (1985), pages 4079–4119. DOI: 10.1088/0022-3719/18/21/008 (cited on page 20).

[43] A. Oprea, E. Moretton, N. Bârsan, W. J. Becker, J. Wöllenstein, and U. Weimar. "Conduction model of SnO_2 thin films based on conductance and Hall effect measurements". *Journal of Applied Physics* 100 (2006), page 033716. DOI: 10.1063/1.2229802 (cited on page 21).

[44] M. Frischbier. "Die elektrischen Eigenschaften von Indiumoxid-Dünnschichten: in-situ Hall-Effekt-Messungen zur Aufklärung des Einflusses von Punktdefekten und Korngrenzen". PhD thesis. Technische Universität Darmstadt, 2015 (cited on pages 21, 71).

[45] J. Y. W. Seto. "The electrical properties of polycrystalline silicon films". *Journal of Applied Physics* 46 (1975), page 5247. DOI: 10.1063/1.321593 (cited on page 21).

[46] Y. S. Lee, M. T. Winkler, S. C. Siah, R. Brandt, and T. Buonassisi. "Hall mobility of cuprous oxide thin films deposited by reactive direct-current magnetron sputtering". *Applied Physics Letters* 98 (2011), page 192115. DOI: 10.1063/1.3589810 (cited on pages 21, 23, 30, 32, 34, 70, 94, 97, 100–103).

[47] D. Chattopadhyay and H. J. Queisser. "Electron scattering by ionized impurities in semiconductors". *Review of Modern Physics* 53 (1981), pages 745–768. DOI: 10.1103/revmodphys.53.745 (cited on pages 21, 101).

[48] K. Nomura, H. Ohta, A. Takagi, T. Kamiya, M. Hirano, and H. Hosono. "Room-temperature fabrication of transparent flexible thin-film transistors using amorphous oxide semiconductors". *Nature* 432 (2004), pages 488–492. DOI: 10.1038/nature03090 (cited on pages 21, 22).

[49] H. Hosono, M. Yasukawa, and H. Kawazoe. "Novel oxide amorphous semiconductors: transparent conducting amorphous oxides". *Journal of Non-Crystalline Solids* 203 (1996), pages 334–344. DOI: 10.1016/0022-3093(96)00367-5 (cited on page 22).

[50] M. Orita, H. Ohta, M. Hirano, S. Narushima, and H. Hosono. "Amorphous transparent conductive oxide $InGaO_3$ $(ZnO)_m$ ($m \leq 4$): a Zn4s conductor". *Philosophical Magazine Part B* 81 (2001), pages 501–515. DOI: 10.1080/13642810110045923 (cited on page 22).

[51] Y. Ogo, H. Hiramatsu, K. Nomura, H. Yanagi, T. Kamiya, M. Kimura, M. Hirano, and H. Hosono. "Tin monoxide as an s-orbital-based p-type oxide semiconductor: Electronic structures and TFT application". *Physica Status Solidi A* 206 (2009), pages 2187–2191. DOI: 10.1002/pssa.200881792 (cited on page 22).

[52] B. A. Movchan and A. V. Demchishim. "Study of the structure and properties to thick vacuum condenates of nickel, titanium, tungsten, aluminum oxide and zirconium dioxide". *The Physics of Metals and Metallography* 28 (1969), page 83 (cited on page 22).

[53] J. A. Thornton. "High Rate Thick Film Growth". *Annual Review of Materials Science* 7 (1977), pages 239–260. DOI: 10.1146/annurev.ms.07.080177.001323 (cited on page 23).

[54] R. Messier. "Revised structure zone model for thin film physical structure". *Journal of Vacuum Science & Technology, A* 2 (1984), page 500. DOI: 10.1116/1.572604 (cited on pages 23, 188).

[55] R. Messier. "Toward quantification of thin film morphology". *Journal of Vacuum Science & Technology A* 4 (1986), page 490. DOI: 10.1116/1.573866 (cited on page 23).

[56] B. Yang, B. L. Walden, R. Messier, and W. B. White. "Computer Simulation Of The Cross-Sectional Morphology Of Thin Films". *Proc. SPIE*. Volume 0821. Modeling of Optical Thin Films. International Society for Optics and Photonics. 1988, pages 68–76. DOI: 10.1117/12.941843 (cited on page 23).

[57] J. Morasch, H. F. Wardenga, W. Jaegermann, and A. Klein. "Influence of grain boundaries and interfaces on the electronic structure of polycrystalline CuO thin films". *Physica Status Solidi A* 213 (2016), pages 1615–1624. DOI: 10.1002/pssa.201533018 (cited on pages 24, 31, 96–98, 135).

[58] A. Y. Shik. *Electronic Properties of Inhomogeneous Semiconductors*. Edited by D. de Cogan. 1995, page 153 (cited on page 24).

[59] J. Volger. "Note on the Hall Potential Across an Inhomogeneous Conductor". *Physical Review* 79 (1950), pages 1023–1024. DOI: 10.1103/physrev.79.1023 (cited on page 24).

[60] K. Lipskis, A. Sakalas, and J. Viščakas. "On the interpretation of Hall and thermoelectric effects in polycrystalline films". *Physica Status Solidi (a)* 4 (1971), K217–K220. DOI: 10.1002/pssa.2210040341 (cited on page 24).

[61] J. Heleskivi. "On the Hall Voltage in an Inhomogeneous Material". *Journal of Applied Physics* 43 (1972), page 740. DOI: 10.1063/1.1661193 (cited on page 24).

[62] M. G. Mathew and K. S. Mendelson. "Hall effect in the "composite sphere" material". *Journal of Applied Physics* 45 (1974), page 4370. DOI: 10.1063/1.1663060 (cited on pages 25, 99, 103).

[63] C. Rajagopal and M. Satyam. "Studies on electrical conductivity of insulator-conductor composites". *Journal of Applied Physics* 49 (1978), page 5536. DOI: 10.1063/1.324474 (cited on page 26).

[64] M. Nakamura. "Effective conductivity of regular conducting channeling textures in two dimensions". *Journal of Applied Physics* 54 (1983), page 7012. DOI: 10.1063/1.331965 (cited on page 26).

[65] M. C. Göbel, G. Gregori, X. Guo, and J. Maier. "Boundary effects on the electrical conductivity of pure and doped cerium oxide thin films". *Physical Chemistry Chemical Physics* 12 (2010), page 14351. DOI: 10.1039/c0cp00385a (cited on pages 27, 28, 30, 94, 96, 97).

[66] L. O. Grondahl. "Theories of a new solid junction rectifier". *Science* 64 (1926), pages 306–308. DOI: 10.1126/science.64.1656.306 (cited on page 31).

[67] F. Biccari. "Defects and Doping in Cu_2O". PhD thesis. Sapienza – University of Rome, 2010 (cited on page 31).

[68] H. Al-Jawhari. "A review of recent advances in transparent p-type Cu_2O-based thin film transistors". *Materials Science in Semiconductor Processing* 40 (2015), pages 241–252. DOI: 10.1016/j.mssp.2015.06.063 (cited on pages 31, 37).

[69] Z. Wang, P. K. Nayak, J. A. Caraveo-Frescas, and H. N. Alshareef. "Recent Developments in p-Type Oxide Semiconductor Materials and Devices". *Advanced Materials* 28 (2016), pages 3831–3892. DOI: 10.1002/adma.201503080 (cited on pages 31, 37).

[70] S. Nikitine, J. Grun, and M. Sieskind. "Etude spectrophotometrique de la serie jaune de Cu_2O aux basses temperatures". *Journal of Physics and Chemistry of Solids* 17 (1961), pages 292–300. DOI: 10.1016/0022-3697(61)90195-0 (cited on page 31).

[71] J. F. Pierson, A. Thobor-Keck, and A. Billard. "Cuprite, paramelaconite and tenorite films deposited by reactive magnetron sputtering". *Applied Surface Science* 210 (2003), pages 359–367. DOI: 10.1016/s0169-4332(03)00108-9 (cited on page 31).

[72] P. Dawson, M. Hargreave, and G. Wilkinson. "The dielectric and lattice vibrational spectrum of cuprous oxide". *Journal of Physics and Chemistry of Solids* 34 (1973), pages 2201–2208. DOI: 10.1016/s0022-3697(73)80067-8 (cited on pages 31, 116).

[73] J. W. Hodby, T. E. Jenkins, C. Schwab, H. Tamura, and D. Trivich. "Cyclotron resonance of electrons and of holes in cuprous oxide, Cu_2O". *Journal of Physics C: Solid State Physics* 9 (1976), page 1429 (cited on page 32).

[74] Z. Q. Yao, S. L. Liu, L. Zhang, B. He, A. Kumar, X. Jiang, W. J. Zhang, and G. Shao. "Room temperature fabrication of p-channel Cu_2O thin-film transistors on flexible polyethylene terephthalate substrates". *Applied Physics Letters* 101 (2012), page 042114. DOI: 10.1063/1.4739524 (cited on pages 32, 34, 39, 102, 103).

[75] H. Shimada and T. Masumi. "Hall Mobility of Positive Holes in Cu_2O". *Journal of the Physical Society of Japan* 58 (1989), pages 1717–1724. DOI: 10.1143/jpsj.58.1717 (cited on pages 32, 101).

[76] H. Dünwald and C. Wagner. "Untersuchungen über Fehlordnungserscheinungen in Kupferoxydul und deren Einfluss auf die elektrischen Eigenschaften". *Zeitschrift für Physikalische Chemie B* B22 (1933), pages 212–225 (cited on page 32).

[77] C. Wagner and H. Hammen. "Conductivity and oxygen excess in cuprous oxide". *Zeitschrift für Physikalische Chemie* 40 (1938), pages 197–206 (cited on page 32).

[78] Y. Tretyakov, V. Komarov, N. Prosvirnina, and I. Kutsenok. "Nonstoichiometry and defect structures in copper oxides and ferrites". *Journal of Solid State Chemistry* 5 (1972), pages 157–167. DOI: 10.1016/0022-4596(72)90024-2 (cited on page 32).

[79] O. Porat and I. Riess. "Defect chemistry of $Cu_{2-y}O$ at elevated temperatures. Part I: Non-stoichiometry, phase width and dominant point defects". *Solid State Ionics* 74 (1994), pages 229–238. DOI: 10.1016/0167-2738(94)90215-1 (cited on page 32).

[80] M. Yoshimura, A. Revcolevschi, and J. Castaing. "Thermogravimetric study of the non-stoichiometry of cuprite Cu_2O". *Journal of Materials Science* 11 (1976), pages 384–386. DOI: 10.1007/bf00551450 (cited on page 32).

[81] J. Xue and R. Dieckmann. "The non-stoichiometry and the point defect structure of cuprous oxide ($Cu_{2-\delta}O$)". *Journal of Physics and Chemistry of Solids* 51 (1990), pages 1263–1275. DOI: 10.1016/0022-3697(90)90003-x (cited on page 32).

[82] J. Park and K. Natesan. "Oxidation of copper and electronic transport in copper oxides". *Oxidation of Metals* 39 (1993), pages 411–435. DOI: 10.1007/bf00664664 (cited on page 32).

[83] R. Dieckmann. "Point defects and transport in non-stoichiometric oxides: Solved and unsolved problems". *Journal of Physics and Chemistry of Solids* 59 (1998), pages 507–525. DOI: 10.1016/s0022-3697(97)00205-9 (cited on page 32).

[84] J. Maluenda, R. Farhi, and G. Petot-Ervas. "Chemical diffusion measurements in single crystalline cuprous oxide". *Journal of Physics and Chemistry of Solids* 42 (1981), pages 697–699. DOI: 10.1016/0022-3697(81)90123-2 (cited on page 32).

[85] N. L. Peterson and C. L. Wiley. "Diffusion and point defects in Cu_2O". *Journal of Physics and Chemistry of Solids* 45 (1984), pages 281–294. DOI: 10.1016/0022-3697(84)90033-7 (cited on page 32).

[86] Z. Grzesik, M. Migdalska, and S. Mrowec. "Chemical diffusion in non-stoichiometric cuprous oxide". *Journal of Physics and Chemistry of Solids* 69 (2008), pages 928–933. DOI: 10.1016/j.jpcs.2007.10.014 (cited on pages 32, 35).

[87] G. Beensh-Marchwicka, L. Król-Stępniewska, and M. Słby. "Effect of the oxygen pressure during sputtering on the properties of thin CuO_x films". *Thin Solid Films* 88 (1982), pages 33–39. DOI: 10.1016/0040-6090(82)90347-9 (cited on pages 32, 100).

[88] M. O'Keeffe and W. J. Moore. "Electrical Conductivity of Monocrystalline Cuprous Oxide". *The Journal of Chemical Physics* 35 (1961), page 1324. DOI: 10.1063/1.1732045 (cited on page 32).

[89] H. McKinzie and M. O'Keeffe. "High temperature Hall effect in cuprous oxide". *Physics Letters A* 24 (1967), pages 137–139. DOI: 10.1016/0375-9601(67)90728-1 (cited on pages 32, 36, 101, 134).

[90] R. Kužel, C. D. Cann, S. S. Sheinin, and F. L. Weichman. "Hole mobility in Cu_2O. II. Scattering by defects". *Canadian Journal of Physics* 48 (1970), pages 2657–2660. DOI: 10.1139/p70-329 (cited on page 32).

[91] R. Kužel and F. L. Weichman. "Hole mobility in Cu_2O. I. Scattering by lattice vibrations". *Canadian Journal of Physics* 48 (1970), pages 2643–2656. DOI: 10.1139/p70-328 (cited on page 32).

[92] J. Bloem, A. Van der Houven van Oordt, and F. Kröger. "A new luminescence emission in Cu_2O". *Physica* 22 (1956), pages 1254–1256. DOI: 10.1016/s0031-8914(56)90217-8 (cited on page 33).

[93] J. Bloem. "Discussion of some optical and electrical properties of Cu_2O". *Philips Research Reports* 13 (1958), page 167 (cited on pages 33, 34).

[94] M. Zouaghi, B. Prevot, C. Carabatos, and M. Sieskind. "Near infrared optical and photoelectric properties of Cu_2O. III. Interpretation of experimental results". *Physica Status Solidi A* 11 (1972), pages 449–460. DOI: 10.1002/pssa.2210110207 (cited on pages 33, 38).

[95] M. Nolan and S. D. Elliott. "The p-type conduction mechanism in Cu_2O: a first principles study". *Physical Chemistry Chemical Physics* 8 (2006), page 5350. DOI: 10.1039/b611969g (cited on page 33).

[96] H. Raebiger, S. Lany, and A. Zunger. "Origins of the p-type nature and cation deficiency in Cu_2O and related materials". *Physical Review B* 76 (2007). DOI: 10.1103/physrevb.76.045209 (cited on page 33).

[97] D. O. Scanlon, B. J. Morgan, and G. W. Watson. "Modeling the polaronic nature of p-type defects in Cu_2O: The failure of GGA and GGA+U". *Journal of Chemical Physics* 131 (2009), page 124703. DOI: 10.1063/1.3231869 (cited on page 33).

[98] D. O. Scanlon, B. J. Morgan, G. W. Watson, and A. Walsh. "Acceptor Levels in p-Type Cu_2O: Rationalizing Theory and Experiment". *Physical Review Letters* 103 (2009). DOI: 10.1103/physrevlett.103.096405 (cited on pages 33, 34).

[99] D. O. Scanlon and G. W. Watson. "Undoped n-Type Cu_2O: Fact or Fiction?" *The Journal of Physical Chemistry Letters* 1 (2010), pages 2582–2585. DOI: 10.1021/jz100962n (cited on pages 33–35, 83).

[100] D. O. Scanlon and G. W. Watson. "Uncovering the Complex Behavior of Hydrogen in Cu_2O". *Physical Review Letters* 106 (2011). DOI: 10.1103/physrevlett.106.186403 (cited on pages 33–35).

[101] L. Y. Isseroff and E. A. Carter. "Electronic Structure of Pure and Doped Cuprous Oxide with Copper Vacancies: Suppression of Trap States". *Chemistry of Materials* 25 (2013), pages 253–265. DOI: 10.1021/cm3040278 (cited on pages 33, 35, 101, 149).

[102] S. Brochen, L. Bergerot, W. Favre, J. Resende, C. Jiménez, J.-L. Deschanvres, and V. Consonni. "Effect of Strontium Incorporation on the p-Type Conductivity of Cu_2O Thin Films Deposited by Metal-Organic Chemical Vapor Deposition". *The Journal of Physical Chemistry C* 120 (2016), pages 17261–17267. DOI: 10.1021/acs.jpcc.6b05479 (cited on pages 33, 35, 101, 117, 149).

[103] J. Resende, C. Jiménez, N. D. Nguyen, and J.-L. Deschanvres. "Magnesium-doped cuprous oxide (Mg:Cu_2O) thin films as a transparent p-type semiconductor". *Physica Status Solidi A* (2016). DOI: 10.1002/pssa.201532870 (cited on pages 33, 35, 101).

[104] C. G. Van de Walle and J. Neugebauer. "Universal alignment of hydrogen levels in semiconductors, insulators and solutions". *Nature* 423 (2003), pages 626–628. DOI: 10.1038/nature01665 (cited on page 33).

[105] R. Kužel. "The effect of oxygen on the electric conductivity of a cuprous oxide single crystal". *Czechoslovak Journal of Physics* 11 (1961), pages 133–140. DOI: 10.1007/bf01688616 (cited on page 34).

[106] A. Mittiga, F. Biccari, and C. Malerba. "Intrinsic defects and metastability effects in Cu_2O". *Thin Solid Films* 517 (2009), pages 2469–2472. DOI: 10.1016/j.tsf.2008.11.054 (cited on pages 34, 35, 146).

[107] S. Ishizuka, S. Kato, Y. Okamoto, and K. Akimoto. "Control of hole carrier density of polycrystalline Cu_2O thin films by Si doping". *Applied Physics Letters* 80 (2002), page 950. DOI: 10.1063/1.1448398 (cited on page 35).

[108] N. Kikuchi, K. Tonooka, and E. Kusano. "Mechanisms of carrier generation and transport in Ni-doped Cu_2O". *Vacuum* 80 (2006), pages 756–760. DOI: 10.1016/j.vacuum.2005.11.039 (cited on page 35).

[109] F. Biccari, C. Malerba, and A. Mittiga. "Chlorine doping of Cu_2O". *Solar Energy Materials and Solar Cells* 94 (2010), pages 1947–1952. DOI: 10.1016/j.solmat.2010.06.022 (cited on page 35).

[110] Y. S. Lee, J. Heo, M. T. Winkler, S. C. Siah, S. B. Kim, R. G. Gordon, and T. Buonassisi. "Nitrogen-doped cuprous oxide as a p-type hole-transporting layer in thin-film solar cells". *Journal of Materials Chemistry A* 1 (2013), page 15416. DOI: 10.1039/c3ta13208k (cited on page 35).

[111] K. Kardarian, D. Nunes, P. M. Sberna, A. Ginsburg, D. A. Keller, J. V. Pinto, J. Deuermeier, A. Y. Anderson, A. Zaban, R. Martins, and E. Fortunato. "Effect of Mg doping on Cu_2O thin films and their behavior on the TiO_2/Cu_2O heterojunction solar cells". *Solar Energy Materials and Solar Cells* 147 (2016), pages 27–36. DOI: 10.1016/j.solmat.2015.11.041 (cited on page 35).

[112] M. Nolan and S. D. Elliott. "Tuning the Transparency of Cu_2O with Substitutional Cation Doping". *Chemistry of Materials* 20 (2008), pages 5522–5531. DOI: 10.1021/cm703395k (cited on page 35).

[113] Y. Nakano, S. Saeki, and T. Morikawa. "Optical bandgap widening of p-type Cu_2O films by nitrogen doping". *Applied Physics Letters* 94 (2009), page 022111. DOI: 10.1063/1.3072804 (cited on page 35).

[114] N. Tabuchi and H. Matsumura. "Control of Carrier Concentration in Thin Cuprous Oxide Cu_2O Films by Atomic Hydrogen". *Japanese Journal of Applied Physics* 41 (2002), pages 5060–5063. DOI: 10.1143/jjap.41.5060 (cited on page 35).

[115] S. Nandy, A. Banerjee, E. Fortunato, and R. Martins. "A Review on Cu_2O and Cu^I-Based p-Type Semiconducting Transparent Oxide Materials: Promising Candidates for New Generation Oxide Based Electronics". *Reviews in Advanced Sciences and Engineering* 2 (2013), pages 273–304. DOI: 10.1166/rase.2013.1045 (cited on page 35).

[116] J. Maier. *Physical Chemistry of Ionic Materials: Ions and Electrons in Solids*. Wiley-Blackwell, 2004. DOI: 10.1002/0470020229 (cited on pages 35, 36, 134).

[117] M. Hansen and K. Anderko. *Constitution of Binary Alloys*. 2nd edition. New York: McGraw-Hill, 1958 (cited on page 36).

[118] R. A. Yund and G. Kullerud. "Stable mineral assemblages of anhydrous copper and iron oxides". *American Mineralogist* 49 (1964), page 689 (cited on page 36).

[119] A. Soon, X.-Y. Cui, B. Delley, S.-H. Wei, and C. Stampfl. "Native defect-induced multifarious magnetism in nonstoichiometric cuprous oxide: First-principles study of bulk and surface properties of Cu_2O". *Physical Review B* 79 (2009). DOI: 10.1103/physrevb.79.035205 (cited on page 36).

[120] F. L. Weichman. "Internal Schottky barriers in semiconductors". *Canadian Journal of Physics* 60 (1982), pages 269–272. DOI: 10.1139/p82-034 (cited on pages 36, 37, 63, 81, 100, 124, 134).

[121] W. Meyer and H. Neldel. "Über die Beziehungen zwischen der Energiekonstanten s und der Mengenkonstanten a in der Leitwertstemperaturformel bei oxydischen Halbleitern". *Zeitschrift für Technische Physik* 12 (1937), page 588 (cited on page 37).

[122] C. Noguet, M. Tapiero, and J. P. Zielinger. "A New Model for Interpreting the Electric Conduction Phenomena in Cu_2O Single Crystals". *Physica Physica Status A* 24 (1974), pages 565–574. DOI: 10.1002/pssa.2210240224 (cited on page 37).

[123] C. Jeong, J. Sohn, S. Song, I. Cho, J. Lee, E. Cho, and H.-I. Kwon. "Investigation of the charge transport mechanism and subgap density of states in p-type Cu_2O thin-film transistors". *Applied Physics Letters* 102 (2013), page 082103. DOI: 10.1063/1.4794061 (cited on pages 37, 38, 138).

[124] R. Boucher. "The electrical property dependence of disordered copper oxide on oxygen content". *Journal of Physics and Chemistry of Solids* 66 (2005), pages 1234–1239. DOI: 10.1016/j.jpcs.2005.04.003 (cited on pages 37, 81, 134).

[125] X. Zou, G. Fang, L. Yuan, M. Li, W. Guan, and X. Zhao. "Top-Gate Low-Threshold Voltage p-Cu_2O Thin-Film Transistor Grown on SiO_2/Si Substrate Using a High-κ HfON Gate Dielectric". *IEEE Electron Device Letters* 31 (2010), pages 827–829. DOI: 10.1109/led.2010.2050576 (cited on page 38).

[126] X. Zou, G. Fang, J. Wan, X. He, H. Wang, N. Liu, H. Long, and X. Zhao. "Improved Subthreshold Swing and Gate-Bias Stressing Stability of p-type Cu_2O Thin-Film Transistors Using a HfO_2 high-k Gate Dielectric Grown on a SiO_2/Si Substrate by Pulsed Laser Ablation". *IEEE Transactions on Electron Devices* 58 (2011), pages 2003–2007. DOI: 10.1109/ted.2011.2142313 (cited on page 38).

[127] E. Fortunato, V. Figueiredo, P. Barquinha, E. Elamurugu, R. Barros, G. Gonçalves, S. K. Park, C. Hwang, and R. Martins. "Thin-film transistors based on p-type Cu_2O thin films produced at room temperature". *Applied Physics Letters* 96 (2010), page 192102. DOI: 10.1063/1.3428434 (cited on pages 38, 127).

[128] V. Figueiredo, E. Elangovan, R. Barros, J. V. Pinto, T. Busani, R. Martins, and E. Fortunato. "p-type Cu_xO Films Deposited at Room Temperature for Thin-Film Transistors". *Journal of Display Technology* 8 (2012), pages 41–47. DOI: 10.1109/jdt.2011.2170153 (cited on pages 38, 127).

[129] D. Nam, I. Cho, J. Lee, E. Cho, J. Sohn, S. Song, and H. Kwon. "Active layer thickness effects on the structural and electrical properties of p-type Cu_2O thin-film transistors". *Journal of Vacuum Science & Technology B* 30 (2012), page 060605. DOI: 10.1116/1.4764110 (cited on page 38).

[130] J. Sohn, S.-H. Song, D.-W. Nam, I.-T. Cho, E.-S. Cho, J.-H. Lee, and H.-I. Kwon. "Effects of vacuum annealing on the optical and electrical properties of p-type copper-oxide thin-film transistors". *Semiconductor Science and Technology* 28 (2012), page 015005. DOI: 10.1088/0268-1242/28/1/015005 (cited on page 38).

[131] I.-J. Park, C.-Y. Jeong, M. U, S.-H. Song, I.-T. Cho, J.-H. Lee, E.-S. Cho, and H.-I. Kwon. "Bias-Stress-Induced Instabilities in P-Type Cu_2O Thin-Film Transistors". *IEEE Electron Device Letters* 34 (2013), pages 647–649. DOI: 10.1109/led.2013.2253758 (cited on page 38).

[132] H. Al-Jawhari and J. Caraveo-Frescsa. "Effect of Gate Dielectrics on the Performance of p-type Cu_2O TFTs Processed at Room Temperature". *Advanced Materials Research* 856 (2013), pages 215–219. DOI: 10.4028/www.scientific.net/amr.856.215 (cited on page 39).

[133] P. Pattanasattayavong, S. Thomas, G. Adamopoulos, M. A. McLachlan, and T. D. Anthopoulos. "p-channel thin-film transistors based on spray-coated Cu_2O films". *Applied Physics Letters* 102 (2013), page 163505. DOI: 10.1063/1.4803085 (cited on page 39).

[134] S. Y. Kim, C. H. Ahn, J. H. Lee, Y. H. Kwon, S. Hwang, J. Y. Lee, and H. K. Cho. "p-Channel Oxide Thin Film Transistors Using Solution-Processed Copper Oxide". *ACS Applied Materials & Interfaces* 5 (2013), pages 2417–2421. DOI: 10.1021/am302251s (cited on page 39).

[135] J. Yu, G. Liu, A. Liu, Y. Meng, B. Shin, and F. Shan. "Solution-processed p-type copper oxide thin-film transistors fabricated by using a one-step vacuum annealing technique". *Journal of Materials Chemistry C* 3 (2015), pages 9509–9513. DOI: 10.1039/c5tc02384j (cited on page 39).

[136] A. Müller. "The Background of Röntgen's Discovery". *Nature* 157 (1946), pages 119–121. DOI: 10.1038/157119a0 (cited on page 42).

[137] K. Ellmer. "Magnetron sputtering of transparent conductive zinc oxide: relation between the sputtering parameters and the electronic properties". *Journal of Physics D: Applied Physics* 33 (2000), R17 (cited on page 43).

[138] Y. Gassenbauer. "Untersuchung der elektronischen und chemischen Oberflächeneigenschaften von Zinn-dotiertem Indium-Oxid im Hinblick auf die Funktion in organischen Leuchtdioden". PhD thesis. Technische Universität Darmstadt, 2007 (cited on pages 45, 46).

[139] S. Siol. "Kupfer-Chalkogenide für photovoltaische Anwendungen". PhD thesis. Technische Universität Darmstadt, 2014 (cited on pages 45, 46, 98, 135, 136).

[140] A. C. Jones, H. C. Aspinall, P. R. Chalker, R. J. Potter, T. D. Manning, Y. F. Loo, R. O'Kane, J. M. Gaskell, and L. M. Smith. "MOCVD and ALD of High-k Dielectric Oxides Using Alkoxide Precursors". *Chemical Vapor Deposition* 12 (2006), pages 83–98. DOI: 10.1002/cvde.200500023 (cited on page 47).

[141] J. R. Bakke, K. L. Pickrahn, T. P. Brennan, and S. F. Bent. "Nanoengineering and interfacial engineering of photovoltaics by atomic layer deposition". *Nanoscale* 3 (2011), page 3482. DOI: 10.1039/c1nr10349k (cited on page 47).

[142] L. Goux, K. Opsomer, R. Degraeve, R. Müller, C. Detavernier, D. J. Wouters, M. Jurczak, L. Altimime, and J. A. Kittl. "Influence of the Cu-Te composition and microstructure on the resistive switching of Cu-Te/Al_2O_3/Si cells". *Applied Physics Letters* 99 (2011), page 053502. DOI: 10.1063/1.3621835 (cited on page 47).

[143] C. S. Hwang. "Atomic Layer Deposition for Microelectronic Applications". *Atomic Layer Deposition of Nanostructured Materials*. Edited by N. Pinna and M. Knez. Weinheim, Germany: Wiley-VCH Verlag GmbH & Co. KGaA, 2012. Chapter 8, pages 161–188. DOI: 10.1002/9783527639915 (cited on page 47).

[144] V. Miikkulainen, M. Leskelä, M. Ritala, and R. L. Puurunen. "Crystallinity of inorganic films grown by atomic layer deposition: Overview and general trends". *Journal of Applied Physics* 113 (2013), page 021301. DOI: 10.1063/1.4757907 (cited on pages 47, 48).

[145] A. M. Shevjakov, G. N. Kuznetsova, and V. B. Aleskovskii. "Interaction of titanium and germanium tetrachlorides with hydrated silica". *Proceedings of the Second USSR Conference on High-Temperature Chemistry of Oxides*. Chemistry of High-Temperature Materials. Leningrad, USSR, 1965, pages 149–155 (cited on page 47).

[146] T. Suntola and J. Antson. "Method for producing compound thin films". Patent. 1977 (cited on page 47).

[147] R. L. Puurunen. "Surface chemistry of atomic layer deposition: A case study for the trimethylaluminum/water process". *Journal of Applied Physics* 97 (2005), page 121301. DOI: 10.1063/1.1940727 (cited on pages 47, 49).

[148] A. Fuchs. "Der Frontkontakt der CdTe-Dünnschichtsolarzelle: Charakterisierung und Modifizierung von Puffer- und Fensterschichten und deren Grenzflächen". Phd thesis. Technische Universität Darmstadt, 2014 (cited on page 48).

[149] T. J. M. Bayer. "Atomic Layer Deposition von Al_2O_3-Schichten auf Indiumzinnoxid Aufbau einer Depositionseinrichtung und Untersuchung von Grenzflächeneigenschaften". Diploma. Technische Universität Darmstadt, 2009, page 90 (cited on pages 49, 50).

[150] J. W. Elam, D. Routkevitch, P. P. Mardilovich, and S. M. George. "Conformal Coating on Ultrahigh-Aspect-Ratio Nanopores of Anodic Alumina by Atomic Layer Deposition". *Chemistry of Materials* 15 (2003), pages 3507–3517. DOI: 10.1021/cm0303080 (cited on page 49).

[151] A. W. Ott, J. W. Klaus, J. M. Johnson, and S. M. George. "Al_2O_3 thin film growth on Si(100) using binary reaction sequence chemistry". *Thin Solid Films* 292 (1997), pages 135–144. DOI: 10.1016/S0040-6090(96)08934-1 (cited on page 49).

[152] T. J. M. Bayer, A. Wachau, A. Fuchs, J. Deuermeier, and A. Klein. "Atomic Layer Deposition of Al_2O_3 onto Sn-Doped In_2O_3: Absence of Self-Limited Adsorption during Initial Growth by Oxygen Diffusion from the Substrate and Band Offset Modification by Fermi Level Pinning in Al_2O_3". *Chemistry of Materials* 24 (2012), pages 4503–4510. DOI: 10.1021/cm301732t (cited on pages 49, 50, 113, 118, 119, 124).

[153] R. L. Puurunen and W. Vandervorst. "Island growth as a growth mode in atomic layer deposition: A phenomenological model". *Journal of Applied Physics* 96 (2004), page 7686. DOI: 10.1063/1.1810193 (cited on page 49).

[154] M. Tallarida, K. Kukli, M. Michling, M. Ritala, M. Leskelä, and D. Schmeisser. "Substrate Reactivity Effects in the Atomic Layer Deposition of Aluminum Oxide from Trimethylaluminum on Ruthenium". *Chemistry of Materials* 23 (2011), pages 3159–3168. DOI: 10.1021/cm200276z (cited on pages 49, 122).

[155] M. Tallarida, C. Das, D. Cibrev, K. Kukli, A. Tamm, M. Ritala, T. Lana-Villarreal, R. Gómez, M. Leskelä, and D. Schmeisser. "Modification of Hematite Electronic Properties with Trimethyl Aluminum to Enhance the Efficiency of Photoelectrodes". *The Journal of Physical Chemistry Letters* 5 (2014), pages 3582–3587. DOI: 10.1021/jz501751w (cited on page 49).

[156] C. L. Hinkle, A. M. Sonnet, E. M. Vogel, S. McDonnell, G. J. Hughes, M. Milojevic, B. Lee, F. S. Aguirre-Tostado, K. J. Choi, H. C. Kim, and et al. "GaAs interfacial self-cleaning by atomic layer deposition". *Applied Physics Letters* 92 (2008), page 071901. DOI: 10.1063/1.2883956 (cited on page 49).

[157] J. Kwon, J. M. Ducéré, P. Alphonse, M. Bahrami, M. Petrantoni, J.-F. Veyan, C. Tenailleau, A. Estève, C. Rossi, and Y. J. Chabal. "Interfacial Chemistry in Al/CuO Reactive Nanomaterial and Its Role in Exothermic Reaction". *ACS Applied Materials & Interfaces* 5 (2013), pages 605–613. DOI: 10.1021/am3019405 (cited on page 49).

[158] A. Gharachorlou, M. D. Detwiler, X.-K. Gu, L. Mayr, B. Klötzer, J. Greeley, R. G. Reifenberger, W. N. Delgass, F. H. Ribeiro, and D. Y. Zemlyanov. "Trimethylaluminum and Oxygen Atomic Layer Deposition on Hydroxyl-Free Cu(111)". *ACS Applied Materials & Interfaces* 7 (2015), pages 16428–16439. DOI: 10.1021/acsami.5b03598 (cited on pages 49, 122–126).

[159] B. Rai. "Cu_2O solar cells: A review". *Solar Cells* 25 (1988), pages 265–272. DOI: 10.1016/0379-6787(88)90065-8 (cited on page 51).

[160] T. J. Rinke and C. Koch. *Photolithography: Theory and Application of Photoresists, Etchants and Solvents*. MicroChemicals GmbH, 2012 (cited on pages 53, 54).

[161] S. Graubner. "Synthese und Charakterisierung von Kupferoxid-Dünnschichten". PhD thesis. Justus-Liebig-Universitä Giessen, 2010 (cited on page 53).

[162] H. Hertz. "Über einen Einfluss des ultravioletten Lichtes auf die elektrische Entladung". *Annalen der Physik* 267 (1887), pages 983–1000 (cited on page 55).

[163] A. Einstein. "Über einen die Erzeugung und Verwandlung des Lichtes betreffenden heuristischen Gesichtspunkt". *Annalen der Physik* 322 (1905), pages 132–148 (cited on page 55).

[164] K. Siegbahn and K. Edvarson. "β-Ray spectroscopy in the precision range of $1{:}10^{-5}$". *Nuclear Physics* 1 (1956), pages 137–159. DOI: 10.1016/s0029-5582(56)80022-9 (cited on page 55).

[165] D. Briggs. *Handbook of X-Ray and Ultraviolet Photoelectron Spectroscopy*. Heyden & Son, 1977 (cited on pages 55, 57).

[166] M. P. Seah and W. A. Dench. "Quantitative electron spectroscopy of surfaces: A standard data base for electron inelastic mean free paths in solids". *Surface and Interface Analysis* 1 (1979), pages 2–11. DOI: 10.1002/sia.740010103 (cited on page 56).

[167] M. Weidner. "Fermi Level Determination in Tin Oxide by Photoelectron Spectroscopy". PhD thesis. Technische Universität Darmstadt, 2015 (cited on page 56).

[168] H. Bubert and H. Jensen, editors. *Surface and Thin Film Analysis: Principles, Instrumentation, Applications*. Wiley-VCH Verlag GmbH, 2002. DOI: 10.1002/3527600167 (cited on page 56).

[169] J. C. Riviere and S. Myhra, editors. *Handbook of Surface and Interface Analysis: Methods for Problem-Solving*. 2nd edition. CRC Press, 2009 (cited on pages 56, 63).

[170] *Energy Resolution in X-ray Photoelectron Spectroscopy (XPS)*. Application Note 31068. Thermo Fisher Scientific Inc., 2008 (cited on page 57).

[171] J. F. Moulder, W. F. Stickle, P. E. Sobol, and K. D. Bomben. *Handbook of X-ray Photoelectron Spectroscopy*. Physical Electronics, Inc., 1995 (cited on pages 57, 59–63, 108, 110).

[172] J. R. Waldrop, W. Grant, S. P. Kowalczyk, and E. A. Kraut. "Measurement of semiconductor heterojunction band discontinuities by x-ray photoemission spectroscopy". *Journal of Vacuum Science & Technology A* 3 (1985), page 835. DOI: 10.1116/1.573326 (cited on pages 57, 65–67, 98, 107).

[173] D. Frost, A. Ishitani, and C. McDowell. "X-ray photoelectron spectroscopy of copper compounds". *Molecular Physics* 24 (1972), pages 861–877. DOI: 10.1080/00268977200101961 (cited on pages 60, 63, 122).

[174] C. D. Wagner. "Chemical shifts of Auger lines, and the Auger parameter". *Faraday Discussions of the Chemical Society* 60 (1975), page 291. DOI: 10.1039/dc9756000291 (cited on pages 60, 61).

[175] W. Egelhoff. "Core-level binding-energy shifts at surfaces and in solids". *Surface Science Reports* 6 (1987), pages 253–415. DOI: 10.1016/0167-5729(87)90007-0 (cited on page 60).

[176] T. D. Thomas. "Extra-atomic relaxation energies and the Auger parameter". *Journal of Electron Spectroscopy and Related Phenomena* 20 (1980), pages 117–125. DOI: 10.1016/0368-2048(80)85011-0 (cited on page 60).

[177] C. Wagner and A. Joshi. "The auger parameter, its utility and advantages: a review". *Journal of Electron Spectroscopy and Related Phenomena* 47 (1988), pages 283–313. DOI: 10.1016/0368-2048(88)85018-7 (cited on pages 60, 61).

[178] G. Hollinger. "Structures chimique et electronique de l'interface SiO_2-Si". *Applications of Surface Science* 8 (1981), pages 318–336. DOI: 10.1016/0378-5963(81)90126-4 (cited on page 61).

[179] S. Iwata and A. Ishizaka. "Electron spectroscopic analysis of the SiO_2/Si system and correlation with metal-oxide-semiconductor device characteristics". *Journal of Applied Physics* 79 (1996), pages 6653–6713. DOI: 10.1063/1.362676 (cited on page 61).

[180] A. R. González-Elipe and F. Yubero. *Spectroscopic characaterization of oxide/oxide interfaces, Handbook of Surfaces and Interfaces of Materials*. Edited by H. S. Nalwa. 2nd edition. Academic Press, San Diego, 2001 (cited on pages 61, 62, 116).

[181] R. Reiche, F. Yubero, J. Espinós, and A. González-Elipe. "Structure, microstructure and electronic characterisation of the Al_2O_3/SiO_2 interface by electron spectroscopies". *Surface Science* 457 (2000), pages 199–210. DOI: 10.1016/s0039-6028(00)00375-7 (cited on page 62).

[182] J. A. Mejías, V. M. Jiménez, G. Lassaletta, A. Fernández, and J. P. Espinós. "Interpretation of the Binding Energy and Auger Parameter Shifts Found by XPS for TiO_2 Supported on Different Surfaces". *The Journal of Physical Chemistry* 100 (1996), pages 16255–16262. DOI: 10.1021/jp960988c (cited on page 62).

[183] R. Reiche, D. Dobler, J. P. Holgado, A. Barranco, A. I. Martín-Concepción, F. Yubero, J. P. Espinós, and A. R. González-Elipe. "The Auger parameter and the study of chemical and electronic interactions at the Sb_2O_x/SnO_2 and Sb_2O_x/Al_2O_3 interfaces". *Surface Science* 537 (2003), pages 228–240. DOI: 10.1016/s0039-6028(03)00606-x (cited on page 62).

[184] J. G. Kirkwood. "Theory of Solutions of Molecules Containing Widely Separated Charges with Special Application to Zwitterions". *Journal of Chemical Physics* 2 (1934), page 351. DOI: 10.1063/1.1749489 (cited on page 62).

[185] J. Morales, J. P. Espinos, A. Caballero, A. R. Gonzalez-Elipe, and J. A. Mejias. "XPS Study of Interface and Ligand Effects in Supported Cu_2O and CuO Nanometric Particles". *Journal of Physical Chemistry B* 109 (2005), pages 7758–7765. DOI: 10.1021/jp0453055 (cited on pages 62, 116).

[186] S. Hüfner. *Photoelectron Spectroscopy: Principles and Applications*. 3rd edition. Springer Berlin Heidelberg, 2003. DOI: 10.1007/978-3-662-09280-4 (cited on pages 62, 63).

[187] D. Briggs and M. P. Seah. *Practical Surface Analysis, Auger and X-ray Photoelectron Spectroscopy*. 2nd edition. Practical Surface Analysis. John Wiley & Sons, 1990 (cited on page 63).

[188] P. E. Larson. "X-ray induced photoelectron and Auger-spectra of Cu, CuO, Cu_2O, and Cu_2S thin-films". *Journal of Electron Spectroscopy and Related Phenomena* 4 (1974), pages 213–218. DOI: 10.1016/0368-2048(74)80052-6 (cited on pages 63, 122, 124).

[189] J. Deuermeier, J. Gassmann, J. Brötz, and A. Klein. "Reactive magnetron sputtering of Cu_2O: Dependence on oxygen pressure and interface formation with indium tin oxide". *Journal of Applied Physics* 109 (2011), page 113704. DOI: 10.1063/1.3592981 (cited on pages 63, 64, 79–81, 85, 94, 98, 115).

[190] T. Novakov and R. Prins. "Band structure and the shakeup photoelectron spectra of copper and nickel halides and oxides". *Solid State Communications* 9 (1971), pages 1975–1979. DOI: 10.1016/0038-1098(71)90594-1 (cited on pages 64, 134).

[191] S. Lee, N. Mettlach, N. Nguyen, Y. Sun, and J. White. "Copper oxide reduction through vacuum annealing". *Applied Surface Science* 206 (2003), pages 102–109. DOI: 10.1016/s0169-4332(02)01239-4 (cited on pages 64, 135).

[192] M. V. Hohmann, P. Ágoston, A. Wachau, T. J. M. Bayer, J. Brötz, K. Albe, and A. Klein. "Orientation dependent ionization potential of In_2O_3: a natural source for inhomogeneous barrier formation at electrode interfaces in organic electronics". *Journal of Physics: Condensed Matter* 23 (2011), page 334203. DOI: 10.1088/0953-8984/23/33/334203 (cited on page 66).

[193] J. Deuermeier, T. J. M. Bayer, H. Yanagi, A. Kiazadeh, R. Martins, A. Klein, and E. Fortunato. "Substrate reactivity as the origin of Fermi level pinning at the Cu_2O/ALD-Al_2O_3 interface". *Materials Research Express* 3 (2016), page 046404. DOI: 10.1088/2053-1591/3/4/046404 (cited on pages 66, 121, 149).

[194] A. Franciosi and C. G. Van der Walle. "Heterojunction band offset engineering". *Surface Science Reports* 25 (1996), pages 1–140. DOI: 10.1016/0167-5729(95)00008-9 (cited on page 67).

[195] R. Anderson. "Experiments on Ge-GaAs heterojunctions". *Solid-State Electronics* 5 (1962), pages 341–351. DOI: 10.1016/0038-1101(62)90115-6 (cited on page 67).

[196] M. A. Tupta. *Instrumentation and Techniques for Measuring High Resisitvity and Hall Voltage of Semiconducting Material*. Technical report. Keithley Instruments Inc., 2005 (cited on page 68).

[197] M. Grundmann. *The Physics of Semiconductors*. Springer Berlin Heidelberg, 2010. DOI: 10.1007/978-3-642-13884-3 (cited on page 69).

[198] E. H. Hall. "On a New Action of the Magnet on Electric Currents". *American Journal of Mathematics* 2 (1879), pages 287–292. DOI: 10.2307/2369245 (cited on page 69).

[199] J. S. Blakemore. *Solid State Physics*. Cambridge University Press, 1985. DOI: 10.1017/cbo9781139167871 (cited on page 70).

[200] E. Rutherford. "LXXIX. The scattering of α and β particles by matter and the structure of the atom". *Philosophical Magazine Series 6* 21 (1911), pages 669–688. DOI: 10.1080/14786440508637080 (cited on page 70).

[201] E. Conwell and V. F. Weisskopf. "Theory of Impurity Scattering in Semiconductors". *Physical Review* 77 (1950), pages 388–390. DOI: 10.1103/physrev.77.388 (cited on page 70).

[202] H. Brooks. "Scattering by ionized impurities in semiconductors". *Physical Review* 83 (1951), page 879 (cited on page 70).

[203] F. Caupin and A. D. Stroock. "The Stability Limit and other Open Questions on Water at Negative Pressure". *Advances in Chemical Physics* (2013), pages 51–80. DOI: 10.1002/9781118540350.ch3 (cited on page 70).

[204] J. L. van der Pauw. "A method of measuring the resistivity and Hall coefficient of lamellae of arbirtrary shape". *Philips Technical Review* 20 (1958), page 220 (cited on page 71).

[205] M. V. Hohmann, A. Wachau, and A. Klein. "In situ Hall effect and conductivity measurements of ITO thin films". *Solid State Ionics* 262 (2014), pages 636–639. DOI: 10.1016/j.ssi.2013.10.004 (cited on page 71).

[206] A. Wachau. "Sauerstoffaustausch polykristalliner kathodenzerstäubter Indiumoxid-Dünnschichten". PhD thesis. Technische Universität Darmstadt (cited on page 71).

[207] J. Tauc, R. Grigorovici, and A. Vancu. "Optical Properties and Electronic Structure of Amorphous Germanium". *Physica Status Solidi B* 15 (1966), pages 627–637. DOI: 10.1002/pssb.19660150224 (cited on pages 72, 82).

[208] L. Spieß, G. Teichert, R. Schwarzer, H. Behnken, and C. Genzel. *Moderne Röntgenbeugung*. 2nd edition. Vieweg + Teubner, 2009. DOI: 10.1007/978-3-8349-9434-9 (cited on pages 72–74).

[209] M. Birkholz. *Thin Film Analysis by X-Ray Scattering*. Wiley-VCH Verlag GmbH & Co. KGaA, 2006. DOI: 10.1002/3527607595 (cited on pages 72, 74).

[210] W. H. Bragg and W. L. Bragg. "The Reflection of X-rays by Crystals". *Proceedings of the Royal Society A: Mathematical, Physical and Engineering Sciences* 88 (1913), pages 428–438. DOI: 10.1098/rspa.1913.0040 (cited on page 72).

[211] H. Krüger and R. X. Fischer. "Divergence-slit intensity corrections for Bragg-Brentano diffractometers with circular sample surfaces and known beam intensity distribution". *Journal of Applied Crystallography* 37 (2004), pages 472–476. DOI: 10.1107/s002188980400740x (cited on page 73).

[212] E. J. Sonneveld and J. W. Visser. "Automatic collection of powder data from photographs". *Journal of Applied Crystallography* 8 (1975), pages 1–7. DOI: 10.1107/s0021889875009417 (cited on page 74).

[213] A. Savitzky and M. J. E. Golay. "Smoothing and Differentiation of Data by Simplified Least Squares Procedures." *Anal. Chem.* 36 (1964), pages 1627–1639. DOI: 10.1021/ac60214a047 (cited on page 74).

[214] W. A. Rachinger. "A Correction for the α_1 α_2 Doublet in the Measurement of Widths of X-ray Diffraction Lines". *Journal of Scientific Instruments* 25 (1948), pages 254–255. DOI: 10.1088/0950-7671/25/7/125 (cited on page 74).

[215] R. Delhez and E. J. Mittemeijer. "An improved α_2 elimination". *Journal of Applied Crystallography* 8 (1975), pages 609–611. DOI: 10.1107/s0021889875011466 (cited on page 74).

[216] A. Walsh, J. L. F. Da Silva, S.-H. Wei, C. Körber, A. Klein, L. F. J. Piper, A. DeMasi, K. E. Smith, G. Panaccione, P. Torelli, C. Bourlange, and R. G. Egdell. "Nature of the Band Gap of In_2O_3 Revealed by First-Principles Calculations and X-Ray Spectroscopy". *Physical Review Letters* 100 (2008). DOI: 10.1103/physrevlett.100.167402 (cited on page 83).

[217] J. Grun, M. Sieskind, and S. Nikitine. "Etude spectrophotometrique des spectres continus de Cu_2O a diverses temperatures". *Journal of Physics and Chemistry of Solids* 19 (1961), pages 189–197. DOI: 10.1016/0022-3697(61)90028-2 (cited on page 83).

[218] P. W. Baumeister. "Optical Absorption of Cuprous Oxide". *Physical Review* 121 (1961), pages 359–362. DOI: 10.1103/physrev.121.359 (cited on page 83).

[219] T. Ito, H. Yamaguchi, K. Okabe, and T. Masumi. "Single-crystal growth and characterization of Cu_2O and CuO". *Journal of Materials Science* 33 (1998), pages 3555–3566. DOI: 10.1023/a:1004690809547 (cited on page 83).

[220] F. Biccari, C. Malerba, and A. Mittiga. "Chlorine doping of Cu_2O". *Solar Energy Materials and Solar Cells* 94 (2010), pages 1947–1952. DOI: 10.1016/j.solmat.2010.06.022 (cited on page 83).

[221] J. Deuermeier, H. F. Wardenga, J. Morasch, S. Siol, S. Nandy, T. Calmeiro, R. Martins, A. Klein, and E. Fortunato. "Highly conductive grain boundaries in copper oxide thin films". *Journal of Applied Physics* 119 (2016), page 235303. DOI: 10.1063/1.4954002 (cited on pages 89, 148).

[222] R. Schafranek, S. Li, F. Chen, W. Wu, and A. Klein. "$PbTiO_3/SrTiO_3$ interface: Energy band alignment and its relation to the limits of Fermi level variation". *Physical Review B* 84 (2011), page 045317. DOI: 10.1103/physrevb.84.045317 (cited on page 98).

[223] S. Li et al. "Intrinsic energy band alignment of functional oxides". *Physica Status Solidi (RRL) – Rapid Research Letters* 8 (2014), pages 571–576. DOI: 10.1002/pssr.201409034 (cited on page 98).

[224] M. Zouaghi, M. Tapiero, J. Zielinger, and R. Burgraf. "Hall mobility and hole density in photoactivated Cu_2O single crystals". *Solid State Communications* 8 (1970), pages 1823–1825. DOI: 10.1016/0038-1098(70)90325-x (cited on page 101).

[225] B. A. Tazenkov and F. A. Gruzdev. "Positive and negative photomemory in cuprous oxide". *Soviet Physics - Solid State* 16 (1974), page 460 (cited on page 101).

[226] G. P. Pollack and D. Trivich. "Photoelectric properties of cuprous oxide". *Journal of Applied Physics* 46 (1975), page 163. DOI: 10.1063/1.321312 (cited on page 101).

[227] S. Siol, J. C. Hellmann, S. D. Tilley, M. Grätzel, J. Morasch, J. Deuermeier, W. Jaegermann, and A. Klein. "Band Alignment Engineering at Cu_2O/ZnO Heterointerfaces". *ACS Applied Materials & Interfaces* 8 (2016), 21824––21831. DOI: 10.1021/acsami.6b07325 (cited on pages 113, 115, 149).

[228] J. Morasch, S. Li, J. Brötz, W. Jaegermann, and A. Klein. "Reactively magnetron sputtered Bi_2O_3 thin films: Analysis of structure, optoelectronic, interface, and photovoltaic properties". *Physica Status Solidi A* 211 (2014), pages 93–100. DOI: 10.1002/pssa.201330216 (cited on page 116).

[229] J. Robertson. "High dielectric constant oxides". *The European Physical Journal Applied Physics* 28 (2004), pages 265–291. DOI: 10.1051/epjap:2004206 (cited on page 116).

[230] J. P. Espinós, J. Morales, A. Barranco, A. Caballero, J. P. Holgado, and A. R. González-Elipe. "Interface Effects for Cu, CuO, and Cu_2O Deposited on SiO_2 and ZrO_2. XPS Determination of the Valence State of Copper in Cu/SiO_2 and Cu/ZrO_2 catalysts". *Journal of Physical Chemistry B* 106 (2002), pages 6921–6929. DOI: 10.1021/jp014618m (cited on page 116).

[231] A. Klein. "Energy band alignment at interfaces of semiconducting oxides: A review of experimental determination using photoelectron spectroscopy and comparison with theoretical predictions by the electron affinity rule, charge neutrality levels, and the common anion rule". *Thin Solid Films* 520 (2012), pages 3721–3728. DOI: 10.1016/j.tsf.2011.10.055 (cited on page 118).

[232] A. Akkerman, T. Boutboul, A. Breskin, R. Chechik, A. Gibrekhterman, and Y. Lifshitz. "Inelastic Electron Interactions in the Energy Range 50 eV to 10 keV in Insulators: Alkali Halides and Metal Oxides". *Physica Status Solidi B* 198 (1996), pages 769–784. DOI: 10.1002/pssb.2221980222 (cited on page 122).

[233] Y. Gassenbauer, A. Wachau, and A. Klein. "Chemical and electronic properties of the ITO/Al_2O_3 interface". *Physical Chemistry Chemical Physics* 11 (2009), page 3049. DOI: 10.1039/b822848e (cited on page 124).

[234] K. Ellmer and T. Welzel. "Reactive magnetron sputtering of transparent conductive oxide thin films: Role of energetic particle (ion) bombardment". *Journal of Materials Research* 27 (2012), pages 765–779. DOI: 10.1557/jmr.2011.428 (cited on page 124).

[235] M. Perego and G. Seguini. "Charging phenomena in dielectric/semiconductor heterostructures during x-ray photoelectron spectroscopy measurements". *Journal of Applied Physics* 110 (2011), page 053711. DOI: 10.1063/1.3624757 (cited on page 126).

[236] J. F. Wager. "Transfer-curve assessment of oxide thin-film transistors". *Journal of the Society for Information Display* 18 (2010), page 749. DOI: 10.1889/jsid18.10.749 (cited on pages 140, 142).

[237] J. Levinson. "Conductivity behavior in polycrystalline semiconductor thin film transistors". *Journal of Applied Physics* 53 (1982), page 1193. DOI: 10.1063/1.330583 (cited on page 141).

[238] F. M. Hossain, J. Nishii, S. Takagi, A. Ohtomo, T. Fukumura, H. Fujioka, H. Ohno, H. Koinuma, and M. Kawasaki. "Modeling and simulation of polycrystalline ZnO thin-film transistors". *Journal of Applied Physics* 94 (2003), page 7768. DOI: 10.1063/1.1628834 (cited on page 141).

[239] J. F. Conley. "Instabilities in Amorphous Oxide Semiconductor Thin-Film Transistors". *IEEE Transactions on Device and Materials Reliability* 10 (2010), pages 460–475. DOI: 10.1109/tdmr.2010.2069561 (cited on pages 141, 144).

[240] D. Wu, Q. Zhang, and M. Tao. "LSDA+U study of cupric oxide: Electronic structure and native point defects". *Physical Review B* 73 (2006), page 235206. DOI: 10.1103/PhysRevB.73.235206 (cited on page 146).

[241] E. Fortunato, R. Barros, P. Barquinha, V. Figueiredo, S. K. Park, C. Hwang, and R. Martins. "Transparent p-type SnO_x thin film transistors produced by reactive rf magnetron sputtering followed by low temperature annealing". *Applied Physics Letters* 97 (2010), page 052105. DOI: 10.1063/1.3469939 (cited on page 150).

[242] J. A. Caraveo-Frescas, P. K. Nayak, H. A. Al-Jawhari, D. B. Granato, U. Schwingenschlögl, and H. N. Alshareef. "Record Mobility in Transparent p-type Tin Monoxide Films and Devices by Phase Engineering". *ACS Nano* 7 (2013), pages 5160–5167. DOI: 10.1021/nn400852r (cited on page 150).

[243] K. Nomura, T. Kamiya, and H. Hosono. "Ambipolar Oxide Thin-Film Transistor". *Advanced Materials* 23 (2011), pages 3431–3434. DOI: 10.1002/adma.201101410 (cited on page 150).

[244] G. Hautier, A. Miglio, G. Ceder, G.-M. Rignanese, and X. Gonze. "Identification and design principles of low hole effective mass p-type transparent conducting oxides". *Nature Communications* 4 (2013), page 2292. DOI: 10.1038/ncomms3292 (cited on page 150).

[245] A. Bhatia, G. Hautier, T. Nilgianskul, A. Miglio, J. Sun, H. J. Kim, K. H. Kim, S. Chen, G. Rignanese, X. Gonze, and et al. "High-Mobility Bismuth-based Transparent p-Type Oxide from High-Throughput Material Screening". *Chemistry of Materials* 28 (2016), pages 30–34. DOI: 10.1021/acs.chemmater.5b03794 (cited on page 150).

[246] M. Grundmann, F. Schein, M. Lorenz, T. Böntgen, J. Lenzner, and H. von Wenckstern. "Cuprous iodide: A p-type transparent semiconductor, history, and novel applications". *Physica Status Solidi A* 210 (2013), 1671–1703. DOI: 10.1002/pssa.201329349 (cited on page 150).

[247] I. Valov, E. Linn, S. Tappertzhofen, S. Schmelzer, J. van den Hurk, F. Lentz, and R. Waser. "Nanobatteries in redox-based resistive switches require extension of memristor theory". *Nature Communications* 4 (2013), page 1771. DOI: 10.1038/ncomms2784 (cited on page 150).

[248] J. Rosa. "Synthesis of IGZO nanoparticles for memory application". Master's thesis. Universidade NOVA de Lisboa, 2016 (cited on page 150).

List of abbreviations

AC	alternating current
AFM	atomic force microscopy/microscope
ALD	atomic layer deposition
AMOLED	active matrix organic light emitting diode
AOS	amorphous oxide semiconductors
ATO	Al_2O_3-TiO_2 multi-layer
α	absorption coefficient
α'	Auger parameter
B	magnetic field
BSE	backscattered electrons
c	defect concentration
CB	conduction band
CBM	conduction band minimum
CVD	chemical vapor deposition
d	film thickness
DAISY-MAT	DArmstadt Integrated SYstem for MATerial research
DC	direct current
DFT	density functional theory
d_{hkl}	distance of lattice planes hkl
d_i	information depth
DNQ-sulfonate	DiazoNaphtoQuinone-sulfonate
e	elementary charge
EBE	electron beam evaporation
EDS	energy dispersive X-ray spectroscopy
E	energy
E_A	acceptor level
E_a	activation energy
E_B	binding energy
$E_\mathrm{B}^\mathrm{corr}$	binding energy corrected for extra-atomic relaxation

$\Delta E_{\mathrm{B}}^{\mathrm{corr}}$	binding energy shift corrected for extra-atomic relaxation
$\Delta E_{\mathrm{B}}(\mathrm{PE})$	binding energy shift of photoelectron
E_{CB}	conduction band
E_{core}	core level binding energy
E_{D}	donor level
E_{F}	Fermi energy
ΔE_{f}	energy of defect formation
$E_{\mathrm{F}} - E_{\mathrm{VB}}$	valence band maximum with respect to the Fermi energy
E_{g}	energy band gap
E_{ion}	ionization potential
$\Delta E_{\mathrm{kin}}(\mathrm{AE})$	kinetic energy shift of Auger electron
E_{kin}	kinetic energy
E_{SEE}	secondary electron edge
E_{VB}	valence band
E_{vac}	vacuum energy
ΔE_{VB}	valence band discontinuity
ESCA	electron spectroscopy for chemical analysis
ϵ_{r}	relative permittivity
ϵ_0	permittivity of vacuum
$\mathcal{E}$	electric field strength
$\Delta\epsilon$	initial state contribution
FEM	finite-element method
F_{L}	Lorentz force
FWHM	full width at half maximum
G	conductance
g	transconductance
g_{A}	ground-state degeneracy of acceptor level
g_{D}	ground-state degeneracy of donor level
ΔG_{f}	Gibbs free energy of defect formation
GPC	growth per cycle
γ	divergence angle
h	Planck constant
hkl	Miller indices
I	electrical current or intensity
I_0	unattenuated intensity
ICDD	International Center of Diffraction Data
I_{d}	intensity attenuated by an additional layer of thickness d

$I_{D,lin}$	drain current in the linear region
I_D	drain current
$I_{D,sat}$	drain current in the saturation region
IGZO	indium-gallium-zinc oxide
I_R	reflected light intensity
I_S	source current
I_T	transmitted light intensity
ITO	indium tin oxide
j	current density
k	Boltzmann constant
l	channel length
λ_e	inelastic mean free path of electrons
LCD	liquid crystal display
L_{GB}	grain boundary width
L_{grain}	lateral grain size
λ	wave length
m_0	free electron mass
m_e^*	effective electron mass
MFC	mass flow controller
m_h^*	effective hole mass
MIS	metal-insulator-semiconductor capacitor
MOSFET	metal-oxide-semiconductor field-effect transistor
μ	charge carrier mobility
μ_d	drift mobility
μ_{FE}	field-effect mobility
μ_{grain}	charge carrier mobility of grain
μ_H	Hall mobility
μ_I	mobility limited by ionized impurity scattering
μ_i	chemical potential of element i
μ_{lin}	charge carrier mobility in the linear region
μ_O	chemical potential of the oxygen component
μ_{sat}	charge carrier mobility in the saturation region
N	density of states
n	free electron carrier concentration
N_A	density of acceptors
N_A^-	density of ionized acceptors
N_D	density of donors

N_D^+	density of ionized donors
N_{GB}	number of parallel grain boundaries
N_i	density of ionized impurities
n_i	particle number of element i
p	free hole carrier concentration
PDF	Powder Diffraction File
PGMEA	propylene-glycol-mono-methyl-ether-acetate
PL	photolithography
PLD	pulsed laser deposition
PPC	persistent photoconductivity
PVD	physical vapor deposition
q	charge
R	resistance
r	goniometer radius
R_H	Hall coefficient
r_H	Hall factor
R_H^*	effective Hall coefficient
$R_{H,GB}$	Hall coefficient of grain boundary
$R_{H,grain}$	Hall coefficient of the grain
RMS	root mean square
rRF-MS	reactive radio-frequency magnetron sputtering
ρ	charge density
S	subthreshold swing
sccm	standard cubic centimeters per minute
SE	secondary electrons
SEM	scanning electron microscopy/microscope
STO	strontium titanate
σ	conductivity
σ_{GB}	grain boundary conductivity
σ_{grain}	grain conductivity
SZM	structure zone model
σ^*	effective conductivity
T	temperature
TCO	transparent conducting oxide
TFT	thin-film transistor
T_m	melting temperature
TMA	trimethylaluminum

T_s	substrate temperature
τ	scattering time
θ	emission angle (XPS) or diffraction angle (XRD)
θ_{hkl}	angle with respect to lattice planes hkl
$U(d)$	polarization energy by the Kirkwood model
UPS	ultraviolet photoelectron spectroscopy
V	voltage
v	charge carrier velocity
VB	valence band
VBM	valence band maximum
$\mathrm{V_{Cu}}$	copper vacancy
$\mathrm{V_{Cu}^{split}}$	copper split vacancy
V_D	drain voltage
V_G	gate voltage
V_H	Hall voltage
$\mathrm{V_O}$	oxygen vacancy
V_on	gate voltage required for the onset of conduction
V_S	source voltage
V_th	threshold voltage
Φ	work function
φ	electrostatic potential
Φ_B	Schottky barrier height
$\Phi_\mathrm{instrument}$	work function of the instrument
Φ_sample	work function of the sample
W	width of the space charge region
w	channel width
X	volume fraction of grain boundary
XPS	X-ray photoelectron spectroscopy
XRD	X-ray diffraction
χ	electron affinity
Y	reduced conductance
Z	charge state

List of figures

List of tables

APPENDIX A

Conductive atomic force microscopy: Supporting XRD data

The current map shown in Figure 5.5 (b) proofs the existence of an increased grain boundary conductivity in Cu_2O. However, the same could not be observed for the films, which were analyzed by the in situ XPS and conductance measurements of Section 5.1. Since the film which showed the increased grain boundary conductivity by CAFM had been deposited by Dr. Suman Nandy, the deposition conditions were partly different from the other samples produced in this thesis. A power of 60 W was used and the total process pressure was 3×10^{-3} mbar.[1] Figure A.1 shows data obtained by XRD measurements.

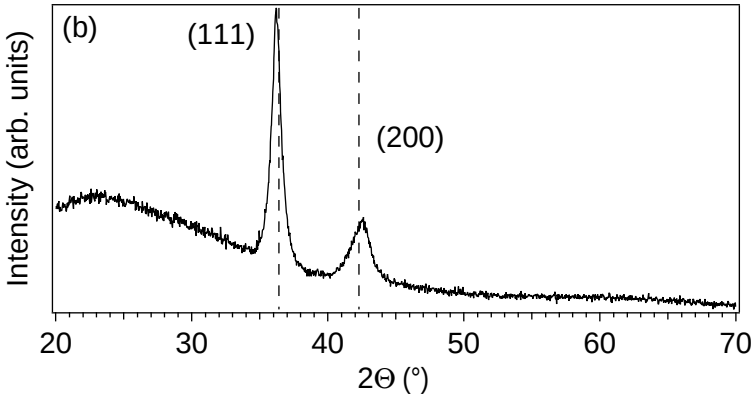

Figure A.1: X-ray diffraction pattern of the sample measured by CAFM.

The observed crystallographic structure is the one of Cu_2O. However, the CAFM samples might be slightly oxidized to Cu(II), since this leads to a decrease in the diffraction

[1] The deposition was done in the commercial system by AJA International of UNL.

angle for the (111) reflection and an increased angle for the (200) reflection (see Figure 4.4 (a)). The increased amount of Cu(II) in the grain boundaries probably caused the high conductivity region around the grain boundary to be wider than in stoichiometric Cu_2O samples. The wider grain boundary region probably enabled the observation of the highly conductive grain boundaries by CAFM on this particular sample.

As outlined in Section 2.5.1, the morphology of thin films depends on the kinetics of the deposited particles. The adatom mobility generally increases with sputtering power and decreases with the total pressure in the chamber due to a decreased number of collisions in the gas phase. Hence, it is possible that the higher particle energy as a result of the deposition conditions leads to a morphology rather similar to zone 2 or the transition zone T than zone 1.[54] In this case, the grains would be shaped like rods rather than inverted cones. This could further facilitate the detection of the increased grain boundary conduction by CAFM.

Acknowledgements

I would like to thank my supervisors Prof. Elvira Fortunato and Prof. Andreas Klein for giving me the opportunity to work on this thesis and providing inestimable scientific support. I am grateful that they accepted to collaborate on the subject of this work.

I would like to acknowledge the financial support by the Portuguese Foundation for Science and Technology (FCT) with the PhD grant SFRH/BD/ 77103/2011 and the German Science Foundation (DFG) within the collaborative research center SFB 595 (Electrical Fatigue of Functional Material).

I thank Prof. Andreas Klein, Prof. Lambert Alff and Prof. Wolfgang Donner for accepting to travel to Portugal in order to join the Examination Committee.

The work has been build up on the support by all involved colleagues at UNL and TU Darmstadt. The Portuguese group welcomed me in an extraordinary way. They were always helpful inside and outside the work environment. The strong bounds within the group got me through many difficulties. Despite the long periods of absence from Darmstadt, the links to the colleagues of the group at TU Darmstadt never became loose. I particularly enjoyed the scientific discussions in person and by email, since they could all so often provide new perspectives to a problem.

I would like to thank Hans Wardenga and Dr. Mareike Frischbier for the relaxation Hall effect measurements, Dr. Daniela Nunes for SEM measurements, Tomás Calmerio for AFM measurements and Dr. Suman Nandy for providing the CAFM images. Furthermore, I would like to acknowledge Dr. Nabiha Ben Sedrine of the Physics Department of the University of Aveiro for her help with the Raman and photoluminescence measurements.

I am grateful to my parents, which are my foundation to face with any of life's challenges. I thank Asal for her endurance and caring support. Most of all, I thank her for giving us Yassna.

Declaration of authorship

I hereby declare that this thesis is my own, unaided work. All information adapted from other literature is indicated and all direct and indirect sources are acknowledged as references. This work has not been previously submitted for examination purposes.

Almada, 23rd September 2016

Jonas Deuermeier

Curriculum vitae

Jonas Deuermeier

ORCID 0000-0002-2764-3124

Education

01/2012–12/2016	Doctoral dissertation in co-supervision by Prof. Elvira Fortunato and Prof. Andreas Klein at the Universidade NOVA de Lisboa, Portugal and the Technische Universität Darmstadt, Germany.
07/2014	ERASMUS-IP Summer School on Transparent Electronics, Chania, Greece
10/2012	ORAMA (FP7) Summer School, Heraklion, Greece
10/2004–10/2010	University degree Diplom-Ingenieur der Materialwissenschaft (equiv. Master of Science in Materials Science) from the Technische Universität Darmstadt with the grade "very good", corresponding to 17/20 (port. grading system)
04/2010–10/2010	Diplomarbeit (equiv. Master thesis) under supervision of Prof. Andreas Klein
09/2009–12/2009	Student Internship in the Diffraction Group of the Institute Laue Langevin, Grenoble, France under supervision of Dr. Thilo Pirling
10/2007–07/2008	Studies abroad as ERASMUS-student at the Università degli Studi di Sassari, Italy
2004	High school degree with the grade "very good"

Language skills

German	mother tounge
English	fluent
Portuguese	fluent
French	good
Italian	good
Persian	basic

List of publications

2016	S. Siol, J. C. Hellmann, S. D. Tilley, M. Grätzel, J. Morasch, J. Deuermeier, W. Jaegermann, and A. Klein. "Band Alignment Engineering

at Cu_2O/ZnO Heterointerfaces". *ACS Applied Materials & Interfaces* 8 (2016), pages 21824–21831. DOI: 10.1021/acsami.6b07325.

J. Deuermeier, H. F. Wardenga, J. Morasch, S. Siol, S. Nandy, T. Calmeiro, R. Martins, A. Klein, and E. Fortunato. "Highly conductive grain boundaries in copper oxide thin film". *Journal of Applied Physics* 119 (2016), page 235303. DOI: 10.1063/1.4954002.

J. Deuermeier, T. J. M. Bayer, H. Yanagi, A. Kiazadeh, R. Martins, A. Klein, and E. Fortunato. "Substrate reactivity as the origin of Fermi level pinning at the Cu_2O/ALD-Al_2O_3 interface". *Materials Research Express* 3 (2016), page 046404. DOI: 10.1088/2053-1591/3/4/046404.

K. Kardarian, D. Nunes, P. M. Sberna, A. Ginsburg, D. A. Keller, J. V. Pinto, J. Deuermeier, A. Y. Anderson, A. Zaban, R. Martins, and E. Fortunato. "Effect of Mg doping on Cu_2O thin films and their behavior on the TiO_2/Cu_2O heterojunction solar cells". *Solar Energy Materials and Solar Cells* 147 (2016), pages 27–36. DOI: 10.1016/j.solmat.2015.11.041.

2013 V. Figueiredo, J. V. Pinto, J. Deuermeier, R. Barros, E. Alves, R. Martins, and E. Fortunato. "p-Type Cu_xO Thin-Film Transistors Produced by Thermal Oxidation". *Journal of Display Technology* 9 (2013), pages 735–740. DOI: 10.1109/JDT.2013.2247025.

2012 T. J. M. Bayer, A. Wachau, A. Fuchs, J. Deuermeier, and A. Klein. "Atomic Layer Deposition of Al_2O_3 onto Sn-doped In_2O_3: Absence of Self-Limited Adsorption during Initial Growth by Oxygen Diffusion from the Substrate and Band Offset Modification by Fermi Level Pinning in Al_2O_3". *Chemistry of Materials* 24 (2012), pages 4503–4510. DOI: 10.1021/cm301732t.

2011 J. Deuermeier, J. Gassmann, J. Brötz, and A. Klein. "Reactive magnetron sputtering of Cu_2O: Dependence on oxygen pressure and interface formation with indium tin oxide". *Journal of Applied Physics* 109 (2011), page 113704. DOI: 10.1063/1.3592981.

Participation in international conferences

2016 European Materials Research Society (E-MRS) Spring Meeting, May 2–6, Lille, France (oral)

2014 10th International Thin-Film Transistor Conference (ITC), January 23–24, Delft, The Netherlands (poster)

2012 4th Transparent Conductive Materials (TCM), October 21–26, Heraklion, Greece (oral)

Materials Science Engineering (MSE), September 25–27, Darmstadt, Germany (oral)

8th International Thin-Film Transistor Conference (ITC), January 30–31, Lisbon, Portugal (oral)

2011	European Materials Research Society (E-MRS) Fall Meeting, September 19–23, Warsaw, Poland (oral)

Participation in projects

2012–2015	AllOxide PV "Novel composite oxides by combinatorial material synthesis for next generation All-Oxide-Photovoltaics", FP7-project N° 309018,
10/2011–12/2011	Collaborative Research Center 595 "Electrical fatigue of functional materials" by the German Science Foundation,
03/2011–09/2011	Advanced Amorphous Multicomponent Oxides for Transparent Electronics Ref: INVISIBLE – ERC N° 228144,
	POINTS – Printable Organic-Inorganic Transparent Semiconductor Devices Ref: FP7-NMP-2010-SMALL-4,

Almada, 23rd September 2016